Homogeneous Macroporous Oxide Supported Nanoparticle Assemblies: Synthesis, Characterisation and their Application as Photocatalysts for Hydrogen Evolution

Robert William Mitchell

Doctor of Philosophy

University of York

Chemistry

September 2014

Abstract

A general method is presented to deposit ligand-stabilised nanoparticles of TiO_2, Fe_3O_4 and CdS in photonic macroporous materials (SiO_2, ZrO_2, FTO) and mesoporous SiO_2. Composites of this type have application in catalysis and solar fuel technology. Established literature methods to form supported nanoparticle composites are often material specific, and cannot simultaneously control nanoparticle size, loading, and crystal phase whilst attaining a homogeneous distribution of particles within the pores. These factors are controlled in this work, and homogenous materials containing high loadings (3 – 65 wt%) of nanoparticles have been prepared. Nanoparticle-support interactions are enhanced by simple modifications to the support surface. The method can be applied to a variety of nanoparticles and substrates.

Nanoparticle loading in photonic materials caused a predictable red shift of the stop band position as a function of the loading amount and refractive indices of the components of the system. The potential for control over the optical properties of materials is of interest for sensing applications.

CdS loaded 3DOM ZrO_2 powders have been used as photocatalysts for hydrogen evolution from sacrificial reagents under visible light irradiation. The position of photonic stop bands relative to the electronic absorption of CdS was varied between composites. By colocating the blue edge of a photonic stop band with the absorption edge of CdS, a maximum 4.7 times enhancement in activity was observed in comparison to a non-porous composite, due to scattering and slow photon effects. Twofold enhancement was observed by partial overlap with the red edge of a stop band. This demonstrates the possibility to enhance the activity and efficiency of a photocatalyst by independent modification of the structural and optical properties of materials. No literature studies have reported the enhancement of reactions relevant to water splitting by overlap of electronic absorption with the blue edge of a stop band.

Table of Contents

Chapter 3 - Nanoparticle Deposition in Porous Materials

Experimental

Table of Figures

Table of Tables

Acknowledgements

There are a number of people I wish to thank for their support throughout this project. Firstly, I would like to thank all my family, for being supportive throughout my studies, and always being there when I needed them. Especially thanks to my parents for providing me with a roof over my head! I am extremely grateful for everything they have done for me, and for shaping me to be the person I am today.

I would like to thank my supervisor Richard Douthwaite for his academic support and guidance, and always being approachable with any problems. I am grateful to my second supervisor Rik Brydson for helpful discussions and for valuable microscopy advice. I would also like to thank my IPM Victor Chechik, for always being a friendly face and for useful discussions and advice in TAP meetings. I am extremely grateful to the White Rose Consortium for funding my research, and within the White Rose University network I would like to thank Robin Perutz, Stephanie Haywood, Julia Weinstein and Rolf Crook for helpful suggestions with research. I would especially like to thank Jay Wadhawan for helpful discussions and his general scientific enthusiasm, in addition to support outside research, and my Masters supervisor Grazia Francesconi for continual support and encouragement that pushed me to undertake research as a career.

In terms of instruments, numerous people provided me with training which was invaluable to my research. For all of their assistance, I would like to thank Sasha Borisova, Paul Elliott, Laurence Abbot, Adrian Whitwood, Ian Wright, Gonzalo Vallejo Fernandez, and Leonardi Lari. Thank you to Stephen Cowling and Graeme McAllister for low angle PXRD and CHN respectively, to Michael Ward in Leeds for TEM analysis, and also to Nicole Hondow and Yothin Chimupala in Leeds. I would like to thank all the admin and technical staff in the department, in particular to Simon Grist for his role as long term RED technician. I would also like to express gratitude to all the staff in stores and workshops, for always being helpful no matter the obscurity of the request.

Around the lab and the office, I would like to thank all past and present members of the RED group, especially Rob Thatcher, for his support in acclimatising to York and around the lab, and Natalie for both her continual support and for helping to keep the lab running smoothly. Thank you also to John, who generously donated electrodes when I needed to make samples at short notice and to Danielle and Nathan for brightening up the office lobe. Outside of the RED group, I am especially grateful to the AKDK/AR groups, in particular Dan and Abeda, for hosting us in their office after the infamous fire of ’11 and being extremely welcoming and a good laugh. I am also grateful to Luisa for being a good housemate, a font of knowledge and for invaluable advice on Endnote and thesis layout, and to Lucy for support during thesis times. Thanks also to everyone in E002 and the lunch group for making work an enjoyable place.

Special thanks have to go out to a series of individuals who made the last four years incredible. In no particular order, massive thanks to Chris Windle, Richard Falk, Martin Blake, Anthony Woodhead, James Robinson and Rob Thatcher for some amazing times in and out of chemistry. Finally, I am indebted to Rob Smith for the many lessons on how to enjoy life, for making everything a positive, and for being the funniest person I know. Without all this support this work would not have been possible.

Declaration

The work presented in this thesis is to the best of my knowledge original. The work contained within is entirely my own, with the following exceptions:

- Low angle PXRD was performed by Dr Stephen Cowling
- Elemental Analyses (CHN) were performed by Dr Graeme McAllister
- TEM EDX mapping and HAADF STEM imaging was obtained with assistance from Dr Michael Ward (University of Leeds).
- The 3DOM FTO films used for deposition of CdS and CdSe in chapter 3 were prepared by PhD student Menglong Zhang.

The deposition of TiO_2 and Fe_3O_4 in 3DOM SiO_2 and ZrO_2 presented in chapter 3 has been published in the journal Nanoscale, with reference: R. Mitchell, R. Brydson and R. E. Douthwaite, *Nanoscale,* 2014, **6**, 4043.

The photocatalysis of CdS and TiO_2 loaded 3DOM ZrO_2 presented in chapter 4 has been published in the journal Physical Chemistry Chemical Physics, with reference: R. Mitchell, R. Brydson, R.E. Douthwaite, *Phys. Chem. Chem. Phys.*, 2015, **17,** 493.

This thesis has not been submitted for any other degree at this or any other University.

Chapter 1

Introduction

1.1: Overview

Composite materials in which nanoparticles are homogeneously loaded onto a support are of interest for a variety of fields including catalysis,[1] solar energy,[2, 3] photoelectrochemistry,[4] and as sensors.[5] In this work, an *ex situ* approach to composite design is presented based on independent fabrication of an ordered porous support and ligand-stabilised nanoparticles, which are then combined. The overall aim of this work is to investigate the effect of an ordered porous photonic support, which can influence the propagation of light of certain wavelengths within its structure, on the hydrogen evolution activity of a photocatalyst material loaded within the pores.

1.1.1: Solar Energy Storage

Increasing concerns over use of fossil fuels as an energy source have led to widescale research into increasing and optimising our use of renewable energy. Of the options available, solar energy is an attractive prospect, as it is plentiful, carbon neutral, and potentially available to all. Global power consumption in 2001 was 13.5 TW, a small fraction of the 120 PW of solar energy received at the earth's surface.[6, 7] Silicon solar panels can be used to convert the suns energy directly into electricity, but storage of this energy for later use is problematic, typically achieved in expensive and inefficient batteries. Alternatively, solar energy can be stored in chemical bonds, using solar fuels produced by photocatalysis or electrolysis. Semiconductor photocatalysts have been used for redox transformations to form solar fuels, due to the ability of the photoexcited state to act simultaneously as a strong oxidising and reducing agent. This chapter will describe the mechanisms involved, and give a brief review of methods to improve activities of semiconductor photocatalysts by structural modification reported in the literature.

1.1.2: Semiconductor Photocatalysis

1.1.2a: Exciton Formation

Photocatalysis can be used to produce solar fuels, for example hydrogen from water. Water splitting is an endoenergetic reaction, requiring energy input to break the O-H bonds and form H-H and O-O bonds, as shown in Equation 1. By combining a light absorbing material with catalysts for product formation, the energy needed for this transformation can be supplied by light, and some of the photon energy is stored in the chemical bonds of the products.

Equation 1 $H_2O \xrightarrow{h\nu} H_2 + \frac{1}{2}O_2$ *ΔG° = 237.1 kJ mol^{-1} (Haynes)*[8]

Semiconductor materials can absorb electromagnetic radiation to form an excited electron/hole pair, also known as an exciton, which can be used for redox reactions. The photoelectrochemical splitting of water was first demonstrated in 1972 by Fujishima and Honda, using a TiO_2 photoelectrode under UV light irradiation for oxidation and a platinum electrode for reduction.[2] Ten years later, powdered Pt coated TiO_2 was used as a heterogeneous photocatalyst to split water.[3] Since these reports, a variety of oxide and non-oxide materials have been used as photocatalysts or for fabrication of photoelectrodes.

Contact between any two phases results in an equilibration of the Fermi levels of the two components. In the case of heterogeneous semiconductor photocatalysis, solid particles in solution are in contact with reagents in the liquid or gaseous phase. For micrometer sized particles, equilibration of the Fermi levels causes excess charge to accumulate on the semiconductor in a space charge region near the surface. The opposite charge builds up in the solution, creating an electric field, and resulting in band bending at the semiconductor/liquid interface. On excitation of a semiconductor with electromagnetic radiation of wavelength equal to or greater than the band gap (E_g), an electron is promoted from the valence band to the conduction band, leaving behind a positive hole. The electric field causes opposite movement of the photoexcited electron and hole. For nanoparticulate materials, including those studied in this work, the size of the space charge layer is

comparable to the particle size.[9] The effect of band bending is reduced, and instead transport of e^-/h^+ pairs is driven by diffusion.[10]

If the charge carriers reach the surface, redox transformation of adsorbed reagents can occur. However, thermal and radiative relaxation of e^-/h^+ pairs competes with this process.[11] Co-catalysts for oxidation and reduction are often employed to trap holes and electrons respectively, minimising recombination in addition to providing a surface for reaction. A visual representation of the process is shown in Figure 1.

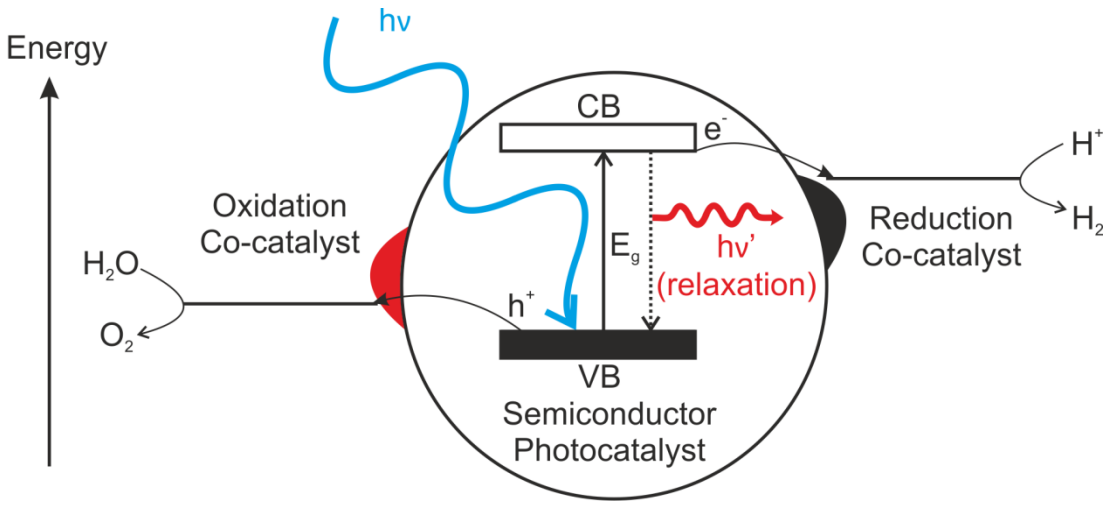

Figure 1: Schematic of photocatalysis using semiconductor materials. Absorption of a photon generates an excited e^-/h^+ pair. Co-catalysts can simultaneously act as e^-/h^+ traps to reduce recombination by thermal or radiative relaxation of the excited state, provide a surface for adsorption, and catalyse redox reactions.

1.1.2b: Band Structure

For a semiconductor to act as a photocatalyst for a redox reaction, the conduction band (CB) must be at a more negative potential than the reduction potential of the reaction. This permits donation of an excited electron to the lower energy state to achieve reduction of the reagent. Similarly, the valence band (VB) must be at a more positive potential than the oxidation potential of the reaction. This allows regeneration of the semiconductor by acceptance of an electron transferred during oxidation of the substrate. In addition, since the oxidation/reduction potentials are

Nernstian, solution pH is important for defining their position versus NHE. For water, $\Delta G° = 237$ kJ mol^{-1} which corresponds to an energy of 1.23 eV under standard conditions. Consequently, the band gap of a semiconductor must be greater than this value to be used for overall water splitting. For a typical metal oxide, the top of the valence band consists of oxygen 2p orbitals, and the bottom of the conduction band is composed of metal d, s or p orbitals. The band positions of several semiconductors at pH 0 relative to the potentials for water splitting are shown in Figure 2. The most active photocatalysts for overall water splitting involve ions with either d^0 or d^{10} electronic states, such as Ti(IV), Ta(V) or Ga(III).[12] Metal ions with partially filled d subshells tend to have lower photocatalytic activities as the d electrons are isolated on the metal centre, and may not form an effective conduction band which prevents recombination. In addition, transition metal cations with incomplete d shells can act as recombination centres for photogenerated holes. $NiTa_2O_6$ can show photoactivity for water splitting under UV light as the Ni(II) does not act as a recombination centre, however the observed activity is poor (11 μmol H_2 h^{-1} g^{-1}).[13]

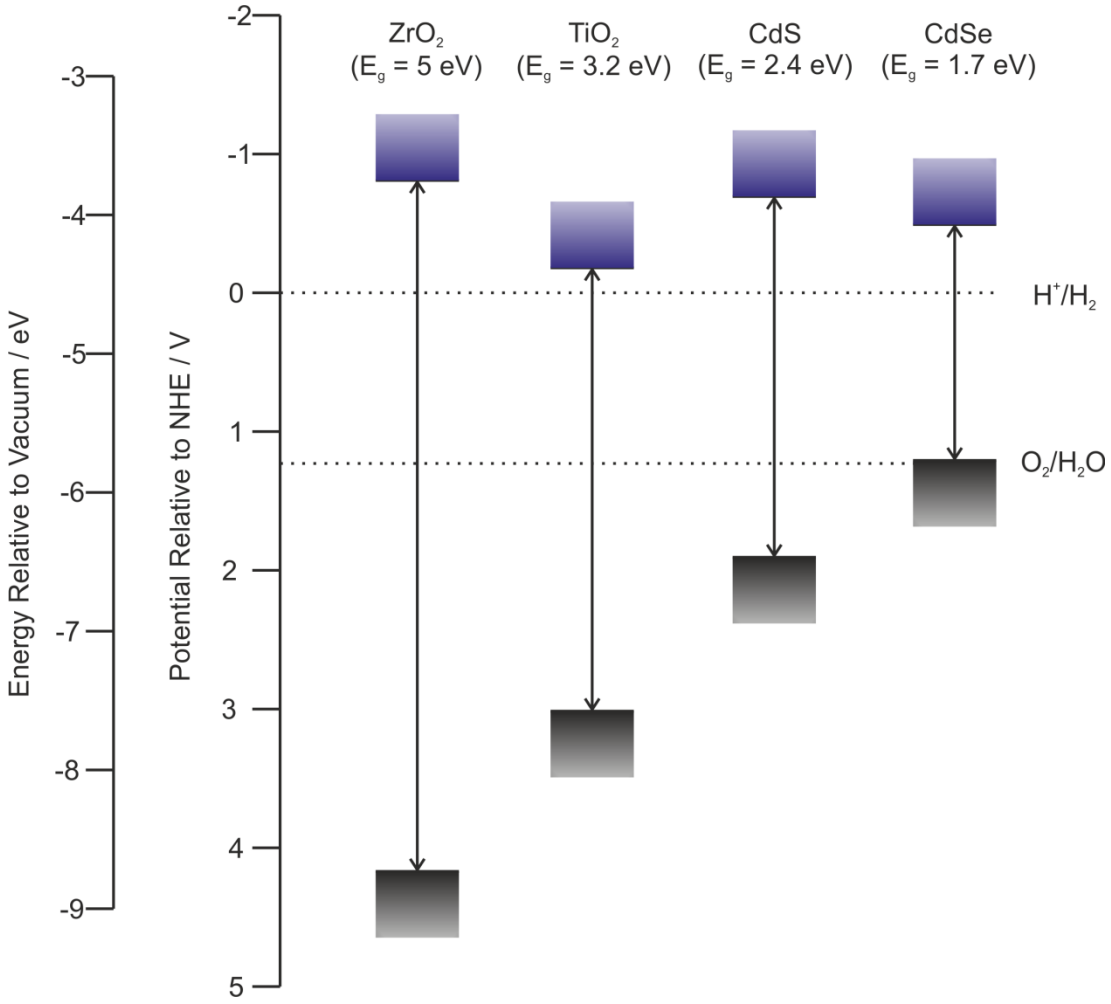

Figure 2: Valence band (black) and conduction band (blue) edge positions of selected semiconductor materials relative to proton reduction and oxygen oxidation potentials. Band positions at pH 0 were obtained from the literature.[14-18] *Unit increases in pH shift the band position upwards by 59 mV.*

1.1.2c: Sacrificial Reagents

Due to the high thermodynamic and kinetic energy cost to drive overall water splitting, sacrificial reagents, which have lower thermodynamic and kinetic barriers to reaction, are often used to test water oxidation or proton reduction half reactions. Using methanol as a sacrificial reagent, holes in the valence band oxidise methanol instead of water, and excited electrons reduce protons to form hydrogen. Using $AgNO_3$ or $Na_2S_2O_8$ as a sacrificial reagent, excited electrons reduce Ag^+ to Ag

metal or $S_2O_8^{2-}$ ions to SO_4^{2-}, and photogenerated holes oxidise water to O_2.[19] Sacrificial reagents can also be used to prevent photocorrosion of materials. The reactions involved in these processes will be discussed further in chapter 4 (section 4.1a).

1.1.2d: Visible Light Photocatalysis

Many groups are actively researching improved visible light photocatalysts. For oxide materials, the top of the valence band consists of O 2p orbitals, and the bottom of the conduction band metal s or d orbitals, typically leading to wide band gaps with energies corresponding to UV absorption. Modification of metal oxides by ion doping can be used to reduce the band gap energy into the visible range. For example, nitrogen doping in Ta_2O_5 reduces the band gap from 3.9 eV to 2.4 eV in TaON and 2.1 eV in Ta_3N_5.[19] As N^{3-} ions replace O^{2-} in the crystal lattice, N 2p electronic contributions raise the position of the valence band maximum. The bottom of the conduction band is fixed as the Ta 5d orbitals, hence the band gap decreases from the oxide to oxynitride and nitride.[20]

TaON and Ta_3N_5 show high oxygen evolution under visible light from sacrificial $AgNO_3$.[21, 22] Other examples of anion doped compounds which can produce hydrogen or oxygen (or both) from sacrificial donors under visible light irradiation are $LaTiO_2N$, $CaTaO_2N$, and $Y_2Ta_2O_5N_2$.[23-25] The oxysulfide $Sm_2Ti_2S_2O_5$ has a band gap of 2 eV, with a higher valence band position compared to the parent pyrochlore due to S 3p contributions. $Sm_2Ti_2S_2O_5$ shows activity for visible light hydrogen evolution from sacrificial methanol with Pt as co-catalyst and oxygen from sacrificial $AgNO_3$ with IrO_2 as co-catalyst.[26]

Doping of TiO_2 with nitrogen and other elements has been used to introduce absorption in the visible region. N-doped TiO_2 has been used as a photocatalyst for 2-propanol decomposition under UV and visible light irradiation.[27] However, in many cases the dopant introduces defect states in the band gap which can act as surfaces for recombination, reducing the quantum efficiency. For example, methyl

orange and 2-mercaptobenzothiazole can be photodegraded under visible light using N-doped TiO_2, but the photoactivity under UV light is observed to decrease with increasing N content.[28]

Cation doping can also be used to modify the band gap of a semiconductor material. $SrTiO_3$ has a band gap of 3.2 eV and can be used as a photocatalyst under UV light.[29] By simultaneous Na(I) and Mo(VI) doping, the conduction band minimum of $SrTiO_3$ is lowered by introduction of Mo 4d character, enabling absorption of visible light.[30] Cu(II) co-catalyst loaded materials showed activity for 2-propanol photodegradation under visible light.

1.1.2e: Photocatalyst Efficiency

The efficiency of a photocatalyst can be expressed in many ways. Generally, the useful output of a material (for example product formed or current produced) is related to the number of photons absorbed by the material. The quantum yield (QY) of a photocatalyst material is expressed by Equation 2:[31, 32]

Equation 2 $$QY\ \% = \frac{Number\ of\ moles\ product\ formed}{Number\ of\ moles\ photons\ absorbed} x100$$

The quantum yield of a material varies with the wavelength of light absorbed, and hence values are often quoted for a specific wavelength range. A related term, quantum efficiency (QE), is used when the action spectrum of the irradiation source is not known. The apparent quantum yield (AQY) for water splitting reactions relates the number of moles H_2 formed to the incident photon flux.[33] For electrochemical processes the efficiency is often described by the incident photon to current conversion efficiency (IPCE), as defined by Equation 3:

Equation 3 $$IPCE\ \% = \frac{Number\ of\ moles\ charge\ carriers\ collected}{Number\ of\ moles\ photons\ absorbed} x100$$

The efficiency of photoelectrochemical devices discussed below is reported in terms of the efficiency of fuel formation, which is based on the IPCE but takes into account the number of electrons involved in the chemical process. For solar cells, efficiency

is described by the external quantum efficiency (EQE) or internal quantum efficiency (IQE), which are defined as the probability that an incident photon will generate an electron which is collected by the cell. For EQE measurements, all light that enters the cell is considered, whereas for IQE measurements, photons which are reflected or not absorbed are discounted.

1.1.2f: State of the Art Materials

In powdered photocatalyst materials, the most active material reported for overall water splitting using UV irradiation is La-doped $NaTaO_3$ with NiO co-catalyst, exhibiting an apparent quantum yield of 56 % at 270 nm.[34] Using sacrificial reagents, a quantum yield approaching unity has been reported for ZnS (90 % QY, 313 nm) in aqueous Na_2SO_3 solution under UV light.[35]

For visible light photocatalysis, the oxynitride GaN:ZnO solid solution coated with $Rh_{1-x}Cr_xO_3$ nanoparticles exhibits the highest reported apparent quantum yield for overall water splitting of 5.9 % at 420 – 440 nm.[19, 36-38] Other oxide photocatalyst materials that have demonstrated visible light activity for overall water splitting include Ni-doped $InTaO_4$ with NiO co-catalyst (0.66 % QY, 402 nm),[39] and Pt/WO_3 coupled to Cr/Ta-doped $Pt/SrTiO_3$ (0.1 % QE, 420.7 nm).[40] Using sacrificial donors, much higher efficiencies have been reported, for example PdS-Pt co-catalyst loaded CdS (93 % QE, 420 nm) in aqueous Na_2S/Na_2SO_3 solution.[41, 42]

1.1.2g: Electrochemistry

Electrochemical methods can be used to evaluate potential semiconductor materials as photocatalysts. By supporting the material of interest on a conducting surface, in the absence of light a voltage can be applied to provide energy for chemical transformations. Redox catalysts are also often required to increase the reaction kinetics. Development of photoelectrochemical cells for production of solar fuels is of great interest for future energy applications.

For a semiconductor based electrode, two main mechanisms exist for product formation. In a similar fashion to heterogeneous photocatalysis, the semiconductor can act as both light harvester and catalyst, for example forming hydrogen with photogenerated electrons on the semiconductor surface and injecting holes into the electrode to perform oxidation at an external electrode. Alternatively, the semiconductor can be used as a light harvester, transferring photogenerated charge carriers into the electrode to provide a current which drives a reaction at an external electrode, for example formation of H_2 from H_2O at a platinum working electrode (Figure 3). Many semiconductors have small electron diffusion lengths (for example, α-Fe_2O_3),[43] which can be an issue for thick film electrodes (> 5 µm), resulting in recombination of electron hole pairs formed away from the contact. Nanostructuring of electrodes is of interest to decrease the recombination rate and enhance the efficiency of devices.

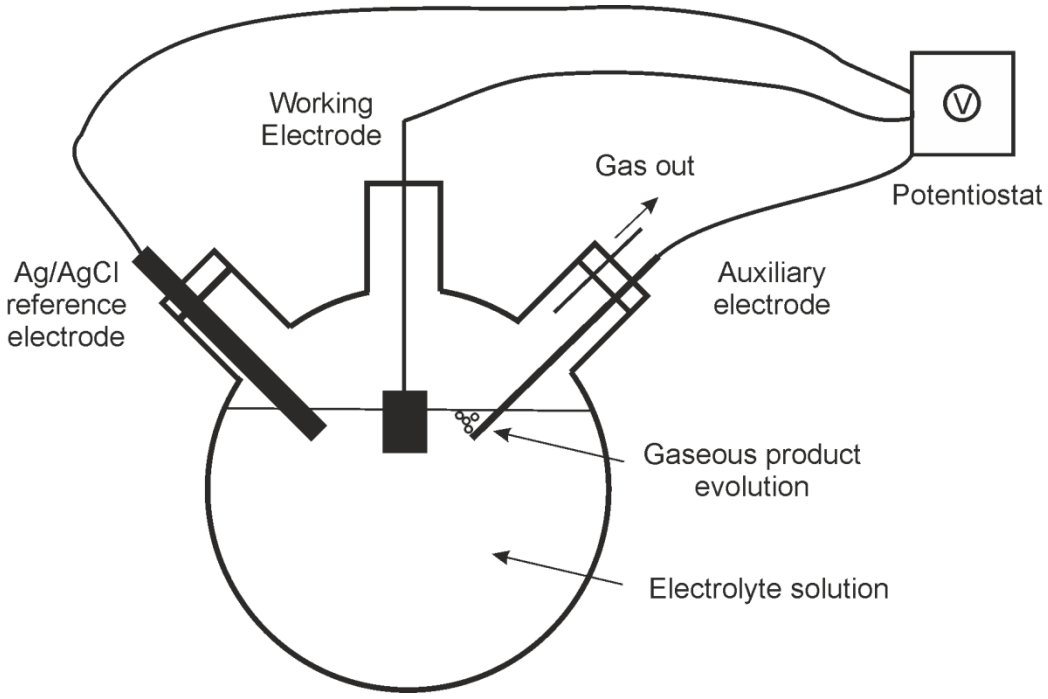

Figure 3: Schematic showing electrochemical setup for solar fuel production.

Transparent conducting oxide (TCO) materials are commonly used electrode materials for electrochemical testing of semiconductors. Tin-doped indium oxide (ITO) and fluorine-doped tin oxide (FTO) are two such materials with high electrical conductivity, and when cast as a thin film, optical transparency. Electrodes can be

fabricated from thin surface films of TCO materials on silica glass. Due to the transparency of the materials, rear illumination can be used to photoexcite materials deposited on the surface. ITO has a lower resistivity and higher free carrier density than FTO,[44] but is more expensive due to the comparative scarcity of indium. FTO is more thermally and chemically robust than ITO, in which leaching of indium ions is observed at high temperatures. The fabrication of porous FTO supported semiconductors for use as electrodes will be presented in the following chapters.

1.1.2h: Electrochemical Devices

Electrochemical devices based on multiple p-n junctions have been used for overall water splitting. An example from the literature is shown in Figure 4.[45, 46] The Si based triple junction absorbs light to form an excited e^-/h^+ pair. The doping in the triple junction is designed to separate the charges, with holes mediated to the Co based oxygen evolution catalyst and electrons to the NiMoZn hydrogen evolution catalyst. Gases are evolved by redox reactions at the surface, as shown in Figure 4a.

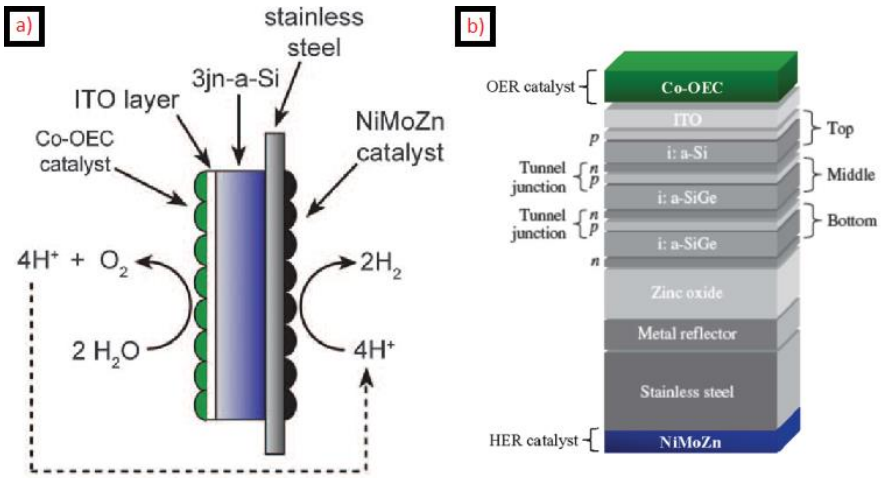

*Figure 4: Example of an electrochemical device for overall water splitting from the literature. (a) Wireless device operation and (b) layer design of Si based triple junction. Adapted from Reece **et al.** and Nocera.*[45, 46]

A similar study was reported previously with a CoMo hydrogen evolution catalyst and a separate anode coated with $NiFe_yO_x$ oxygen evolution catalyst.[47] Stable operation was observed over 300 days with 1 M KOH electrolyte (pH 14), with an efficiency of 7.8 % for hydrogen production. The device shown in Figure 4 has been run in a wired configuration with the NiMoZn layer on a separate electrode with 7.7 % efficiency for fuel production, operating at pH 7. The configuration without the wire in Figure 4 exhibits 4.7 % efficiency for fuel production.[45, 46]

The most efficient device currently reported consists of a monolithic p-$Ga_{0.52}In_{0.48}P$/n-GaAs/p-GaAs electrode with an external Pt counter electrode, which can achieve an efficiency of 12.4 % for H_2 production in 3 M H_2SO_4.[48] The combination of GaAs and $Ga_{0.52}In_{0.48}P$ absorbs the entire range of the solar spectrum. Stable photocurrent of 120 mA cm^{-2} was observed for 20 hours, after which degradation was observed.

1.1.3: Methods to Improve Photocatalyst Activity

Many attempts have been made to improve the activity of photocatalyst materials by miniaturisation and nanostructuring. Particle size is an important factor for a photocatalyst. Semiconductor materials have an intrinsic diffusion length, defined as the average distance a charge carrier travels before it recombines. This distance varies depending on the electronic band structure of a specific compound. For nanoparticles, the reduced dimensions increase the probability that charge carriers will reach the surface before recombining in comparison to a material of the same composition with larger particle size. If the charge carriers at the surface can be extracted, either by redox reactions with adsorbed reagents or via an external circuit, the recombination rate of the material will be decreased.

Surface area is another important factor for a photocatalyst. Highly efficient charge transport is irrelevant if recombination occurs at the surface due to limited adsorption/desorption of species. For nanoparticle materials, higher specific surface areas are inherent as a function of miniaturisation. Porous materials with high

surface areas are of great interest for catalysis applications. In addition, porosity and microstructuring of a material can also influence the propagation of light, offering enhanced light absorption properties. Interplay of all these effects is often present in real examples of photocatalyst materials. In this section, literature examples of photocatalytic activity enhancements by structural modifications will be analysed. Where available, photocatalytic activity of materials is presented in units of moles gas per hour, per gram of catalyst.

1.1.3a: Surface Area

Surface area is an important factor to consider for photocatalyst materials. Increased surface area implies an increased number of active sites for molecules to adsorb. High surface area photoactive materials can be prepared by loading of catalyst species into porous supports, or by fabrication of porous photocatalysts. TiO_2 loaded MCM-48 shows high activity for H_2 production from sacrificial aqueous methanol without the requirement for a co-catalyst. The highest activity observed was 12.75 mmol h^{-1} g^{-1} for a sample with surface area 1146 m^2 g^{-1}.[49] For comparison, with a Pt co-catalyst, activity of P25 TiO_2 has been reported as 16 mmol h^{-1} g^{-1} for a surface area of 48 m^2 g^{-1}.[50] Mesoporous silica loaded with Cu/TiO_2 shows activity for reduction of CO_2 to CO (60 µmol h^{-1} g^{-1}) and CH_4 (10 µmol h^{-1} g^{-1}) under UV irradiation without a co-catalyst.[51] Mesoporous N-doped TiO_2 has been used for rhodamine B degradation, showing higher activity as a function of increasing surface area.[52] One dimensional structures such as nanowires have also shown high activities for photocatalysis due to efficient charge transport, light collection and increased surface areas compared to bulk materials.[53, 54]

Zeolites loaded with CdS nanoparticles have been tested for H_2 production from sacrificial aqueous ethanol under visible light.[55] The order of activity and surface area of CdS loaded materials was Zeolite-Y (6.6 µmol h^{-1}, 380 m^2 g^{-1}) > SBA-15 SiO_2 (2.7 µmol h^{-1}, 351 m^2 g^{-1}) > Zeolite-L (1.7 µmol h^{-1}, 122 m^2 g^{-1}). However, the CdS loadings in these samples were not quantified, and hence the activity enhancement could be due to differences in adsorption of Cd(II) in the synthesis steps.

Comparison between photoactivity of similar composites of this type is not often made with respect to both nanoparticle loading and surface area. For crystalline mesoporous $La_2Ti_2O_7$ synthesised by hydrothermal reaction, rates of photocatalytic hydrogen evolution from aqueous methanol scaled with the sample surface area. Hydrogen evolution rates were observed to decrease from 209 μmol h^{-1} g^{-1} (50 m^2 g^{-1}), to 160 μmol h^{-1} g^{-1} (43 m^2 g^{-1}) to 20 μmol h^{-1} g^{-1} (5 m^2 g^{-1}) for $La_2Ti_2O_7$ prepared by solid state reaction (SSR).[56] Less crystalline materials exhibited a higher surface area but lower catalytic activity. Similar influence of crystallinity and surface area on photodegradation of rhodamine B was observed for mesoporous hollow shell TiO_2.[57] High crystallinity is important for photocatalysts, to minimise concentrations of defect sites and surface states which can act as recombination centres.[58]

1.1.3b: Particle Size and Morphology Effects

As mentioned above, nanoparticle-sized materials can be more active as photocatalysts than larger particles due to the increased surface area and the decreased distance to the surface for photogenerated charge carriers. Hydrogen evolution from aqueous methanol was measured for 30 – 50 nm sized and 300 – 500 nm sized Ta_3N_5 particles modified with Pt co-catalyst, with a rate three times higher in the smaller particles.[59] Other studies have demonstrated a threefold increase in methylene blue photodegradation using 18 nm Ta_3N_5 particles in comparison to 75 nm Ta_3N_5 particles.[60] Enhancements in hydrogen evolution activity from sacrificial methanol as a function of decreased particle size, and hence increased surface area, have been observed for $SrTiO_3$ and the sodium tungstates $NaTaO_3$ and $Na_2Ta_2O_6$.[29,61,62] For $NaTaO_3$, comparison was made between samples prepared by solid state reaction (SSR) and an exotemplating (ET) method, where particles are grown inside a porous carbon host which is then removed. Crystallite sizes were measured at 1 – 5 μm for SSR and 20 – 25 nm for ET prepared samples, with corresponding surface areas of 1.4 m^2 g^{-1} and 22.4 m^2 g^{-1} respectively. Rates of hydrogen evolution from sacrificial methanol under UV light were 0.34 mmol h^{-1} g^{-1}

(SSR) and 5.96 mmol h^{-1} g^{-1} (ET), reflecting the increased surface area for reaction and reduced distance to the surface for smaller particles. Addition of multilayer reduced graphene oxide and photodeposited gold nanoparticles increased the hydrogen evolution rate of ET $NaTaO_3$ to 13.78 mmol h^{-1} g^{-1}, due to efficient electron transfer and hence decreased recombination as confirmed by EPR studies.[62] Enhancement of visible light hydrogen evolution from sacrificial lactic acid has been demonstrated for Pt/CdS loaded graphene oxide.[63] Coupling of light absorbers with carbon nanotubes to facilitate increased charge separation has also been used in a variety of studies, including enhancement of photocatalytic degradation of phenol, 4-nitrophenol and rhodamine B.[64, 65]

Structures consisting of small ridged particles, or nanosteps, have demonstrated increased activity compared to bulk materials due to efficient charge separation. SEM images of Pt loaded $(AgIn)_{0.22}Zn_{1.56}S_2$ containing nanosteps from the literature are shown in Figure 5.[66] Thermal treatment of $Cd(OAc)_2$ formed sintered CdO nanoparticles, which were reacted with H_2S gas to form ridged CdS nanoparticles (100 – 300 nm).[67] Pt nanoparticles as co-catalysts were loaded onto the material, with EDX analysis showing a higher concentration of Pt on the edges of the step in comparison to the grooves. Photoexcited electrons migrate to the Pt co-catalyst particles on the edges of the steps and reduce surface adsorbed species, and photogenerated holes migrate to the grooves, with the close proximity of the two faces promoting multihole injection for oxidation.[34] Stable hydrogen production from sulfide/sulfite sacrificial donors was observed, at an increased rate of 5.4 mmol h^{-1} g^{-1} in comparison to 2.1 mmol h^{-1} g^{-1} for non-structured CdS formed by precipitation methods.[67] The apparent quantum yield at 420 nm was also increased from 11.7 % to 24.1 % for the nanostep structures. The improved activity is explained by the physical separation of the oxidation and reduction surfaces, decreasing the recombination rate of excitons. $(AgIn)_{0.22}Zn_{1.56}S_2$ with Pt co-catalyst (Figure 5) shows a rate of H_2 production of 3.15 mmol h^{-1} g^{-1} from sulfide/sulfite sacrificial donors and a quantum yield of 20 % at 420 nm, similarly attributed to nanostep structuring.[66] Nanosteps were observed in 2 % La-doped $NaTaO_3$, in addition to a decreased particle size relative to bulk $NaTaO_3$ by the same synthesis.

The materials were active for overall water splitting with a rate of hydrogen evolution from pure water of 0.45 mmol h^{-1} g^{-1} for La-doped $NaTaO_3$ compared to 0.17 mmol h^{-1} g^{-1} for $NaTaO_3$. Stoichiometric oxygen evolution was also measured. NiO co-catalyst deposition was observed preferentially on the step edges. With 0.2 weight % NiO loading, $NaTaO_3$:La produced hydrogen at a rate of 19.8 mmol h^{-1} g^{-1}, compared to 2.18 mmol h^{-1} g^{-1} for 0.05 weight % NiO loaded $NaTaO_3$.[34]

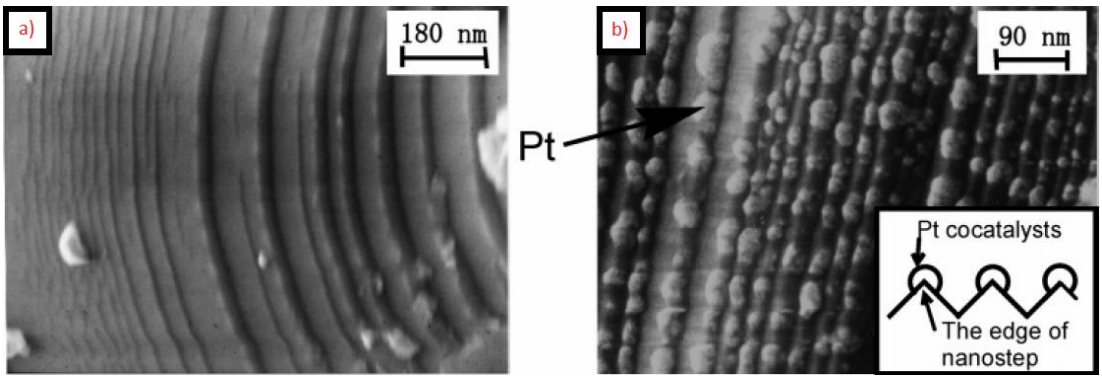

Figure 5: Literature SEM images of (a) uncoated $(AgIn)_{0.22}Zn_{1.56}S_2$ and (b) Pt loaded $(AgIn)_{0.22}Zn_{1.56}S_2$. Pt is deposited preferentially on the edges of the steps. Adapted from Tsuji ***et al.***[66]

Bulk CdSe is inactive for photocatalytic hydrogen production in water and sacrificial ethanol donors due to poor band alignment between the valence band, conduction band and redox potentials.[68] 1.4 nm thick CdSe nanoribbons have been fabricated, with an increased band gap of 2.7 eV compared to 1.7 eV in the bulk due to quantum confinement. The nanoribbons can produce hydrogen from water, sacrificial methanol solutions, and sacrificial sulfite/sulfide solutions under UV light. Using visible light, a hydrogen evolution rate of 0.4 mmol h^{-1} g^{-1} and apparent quantum efficiency of 13.4 % from 400 – 500 nm was observed from sacrificial sulfite/sulfide solutions.[69] CdSe quantum dots have also been used for photocatalytic hydrogen production from sulfite solutions. Activity decreased with increasing particle size from 1.75 to 3.05 nm, and for particles greater than 3.05 nm no activity was observed due to the decreased band gap. As the band gap widens the thermodynamic potential of excitons and hence electron transfer rate are increased, correlating with the higher activity observed for smaller particles.[70, 71] Mixtures of Pt loaded 3 nm mesoporous CdS particles and hollow CdS nanorods

have shown a hydrogen evolution rate of 27.3 mmol h^{-1} g^{-1} from sacrificial sulfide/sulfite solutions, with an apparent quantum yield of 60.34 % at 420 nm.[72] The catalysts show a high surface area of 112.8 m^2 g^{-1}, and the decreased distance to the surface for photogenerated charge carriers due to the nanoparticle size can reduce the recombination rate, contributing to the high efficiency of the material. In comparison, for a bulk CdS powder with surface area 0.26 m^2 g^{-1}, the quantum yield for photocatalysis with a Pt co-catalyst from sulfide/sulfite solutions has been reported as 25 % at 450 nm.[73]

1.1.3c: Layered Materials

Intrinsically layered structures can show high activity for photocatalysis due to the nanometre-scale separation of the structural moieties, which provides good contact for electron transfer, and efficient exciton transfer to the surface. Layered titanate nanosheets ($H_{0.67}Ti_{1.83}O_4$) with interlayer CdS have been used as photocatalysts for hydrogen production from sulfide/sulfite sacrificial donors, with the most active sample producing 1.02 mmol h^{-1} g^{-1} without a co-catalyst under visible light. Photoluminescence of CdS within the composites was observed to decrease to 5.3 % of the intensity of as prepared QDs, suggesting efficient charge transfer within the material and a reduced recombination rate for excitons.[74] $InFeO_3(ZnO)_m$ oxides have shown photocatalytic hydrogen evolution activity from aqueous methanol with a rate of 19.5 mmol h^{-1} g^{-1}.[58] The high rate is attributed to spatial charge separation within the structures, which consist of edge sharing InO_6 octahedra separated by a string of Fe and Zn occupied trigonal bypyrimidal and tetrahedral sites, with an increased separation of In layers as m increases. The band gap also increases with m, from 2.85 eV (n = 1) to 3.02 eV (n = 4). $InFeO_3(ZnO)_3$ showed the highest stable activity, due to interplay of the increased band gap (2.97 eV) in comparison to n = 1 and the decreased distance of exciton travel from the Zn/Fe layer to the In layers compared to n = 4.[58]

Layered perovskites with general formula $A(M_{n-1}Nb_nO_{3n+1})$, (A = alkali metal and M = La, Ca, Sr) are highly active for photocatalytic hydrogen evolution from aqueous

methanol.[75,76] For H^+ exchanged $KSr_2Nb_3O_{10}$, hydrogen is evolved at a rate of 8.9 mmol h^{-1} g^{-1}, which can be increased to 43 mmol h^{-1} g^{-1} by loading 0.1 weight % Pt as co-catalyst.[76] Migration of water and methanol into the interlayer spaces expands the sheet separation, and provides close contact between the generated excitons and reagents. Ni loaded $K_2La_2Ti_3O_{10}$ has been used as a photocatalyst for H_2 and O_2 generation in aqueous KOH.[77] Activity of 2.19 mmol h^{-1} g^{-1} H_2 and 1.13 mmol h^{-1} g^{-1} O_2 was observed for a sample with surface area 5 m^2 g^{-1}, and approximately half these values for a sample with 3 m^2 g^{-1}. Samples with higher surface area showed lower activity, however differences in crystallinity and morphology were observed.

1.1.3d: Light Collection

Enhancement of light collection and absorption is of great importance in solar devices. By increasing exciton formation a higher quantity of product can be formed. Reflective Ag back contacts and deposited light scattering Al_2O_3 nanoparticles on silicon nanowires have been used to demonstrate a photoelectrochemical cell with 90 % internal quantum efficiency from 400 – 900 nm.[78] Reflective surfaces have also been employed to increase the efficiency of dye sensitised solar cells (DSSCs).[79, 80]

Surface Plasmon Resonance (SPR) effects can have an influence on the light absorption of a photocatalyst.[81] Metal nanoparticles dispersed on the surface, most commonly gold, absorb electromagnetic radiation causing resonance of electrons and generation of an electric field at the surface. Enhancement of activity for photocatalysis is explained in the literature either by injection of excited electrons into the conduction band, or by enhanced exciton formation in strong local electric fields at the surface.[82] Au/TiO_2 composites have shown visible light hydrogen evolution from sacrificial methanol of 1.32 mmol h^{-1} g^{-1}, due to electron injection from Au to TiO_2.[83] Under simulated solar irradiation, 2 weight % Au/TiO_2 composites have shown hydrogen evolution of 7.2 mmol h^{-1} g^{-1} from 1 % methanol, in comparison to 1.08 mmol h^{-1} g^{-1} for 0.3 weight % Pt/TiO_2 from 25 % methanol, but

differences in methanol concentration and co-catalyst loading and identity cloud the SPR effect.[84] Au@SiO_2 core shell nanoparticles have been used to increase the IPCE of $BiVO_4$,[85] and the photocatalytic hydrogen evolution of CdS from 2-propanol.[86]

Periodic 1D, 2D or 3D structures can influence the propagation and velocity of electromagnetic radiation (Figure 6). In photonic crystals (PCs), modular variation in refractive index within the structure can be exploited to trap light and increase absorption to enhance the efficiency compared to an equivalent non-photonic structure. In addition, the microstructuring involved bestows an inherent increased surface area in comparison to a bulk material. Photonic crystals have been used to enhance the efficiency of solid DSSCs.[87-89] Photonic crystal based photocatalysts are the focus of this work, and will be described in more detail in the following section.

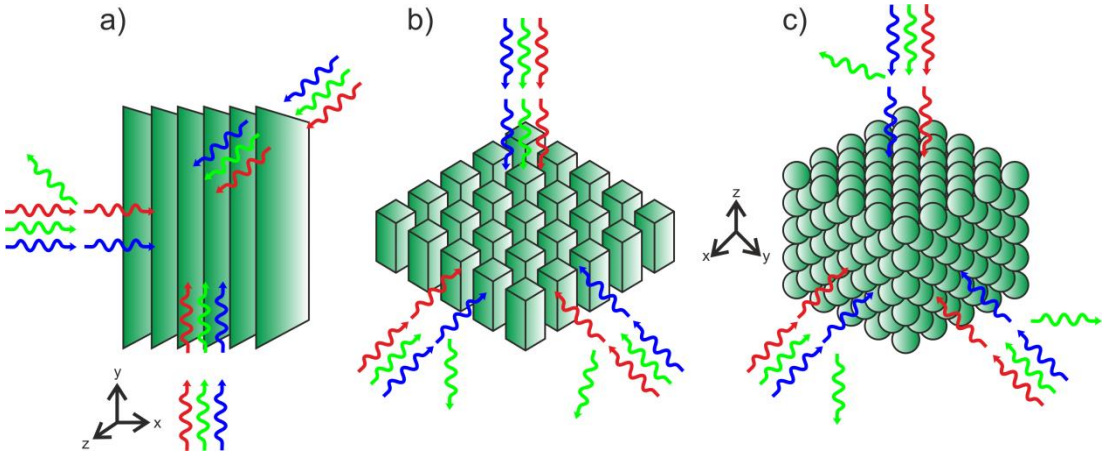

Figure 6: Examples of the effect of dimensionality in structures on light propagation. Photons of green light are reflected from photonic crystal planes within the structures. (a) 1D sheets, (b) 2D rods and (c) 3D opaline sphere arrays.

1.1.4: Photonic crystals

Three-dimensionally ordered macroporous (3DOM) materials can exhibit photonic properties, in which interaction of the material with certain frequencies of light is modified. These effects can be used to increase the efficiency of a photocatalyst. The following section presents a brief overview of the relevant theory, and a review

of literature examples incorporating photonic structures to achieve enhancements of photochemical and photoelectrochemical device activities.

1.1.4a: Photonic Effects

Photonic crystal materials can be observed to reflect light of certain wavelengths by Bragg diffraction.[90, 91] These materials consist of an ordered structure, comprising a regular array of objects of similar dimension to the wavelength of light of interest. Structures can include arrangements of rods or spheres or their inverse porous structures. A criterion for photonic behaviour is that there must be a difference in refractive index between at least two materials that comprise the photonic structure. In these materials, photonic behaviour prevents the propagation of certain light wavelengths within the structure, which are reflected if the source of illumination is external. Figure 7 shows a schematic of this reflection for the (111) planes in an opaline structure. The wavelengths of light reflected typically range over regions of around 20 – 100 nm known as photonic stop bands. In the case of 3DOM materials, the high refractive index walls and empty or solvent filled pores form a photonic crystal lattice. The (111) and (220) planes of 3DOM photonic crystals are shown in Figure 8. For most materials, partial photon reflection is observed due to imperfections in the photonic crystal lattice and because complete reflection within a 3DOM structure requires a refractive index ratio greater than 3.3 for the components of the lattice.

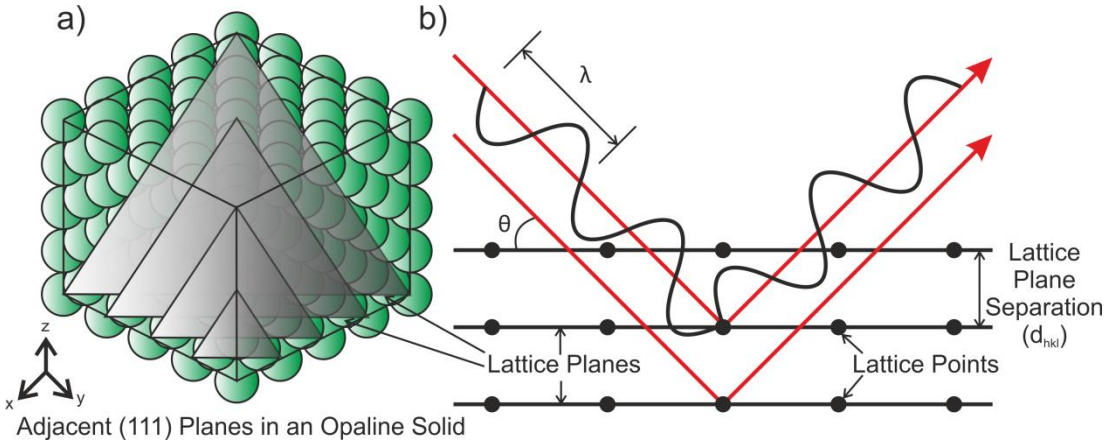

Figure 7: (a) Visualisation of adjacent (111) planes in an opaline sphere array, across multiple unit cells. (b) Bragg diffraction of electromagnetic radiation from lattice planes. Lattice points can be atoms (X-ray diffraction) or colloidal crystal spheres/3DOM walls (reflection from photonic materials).

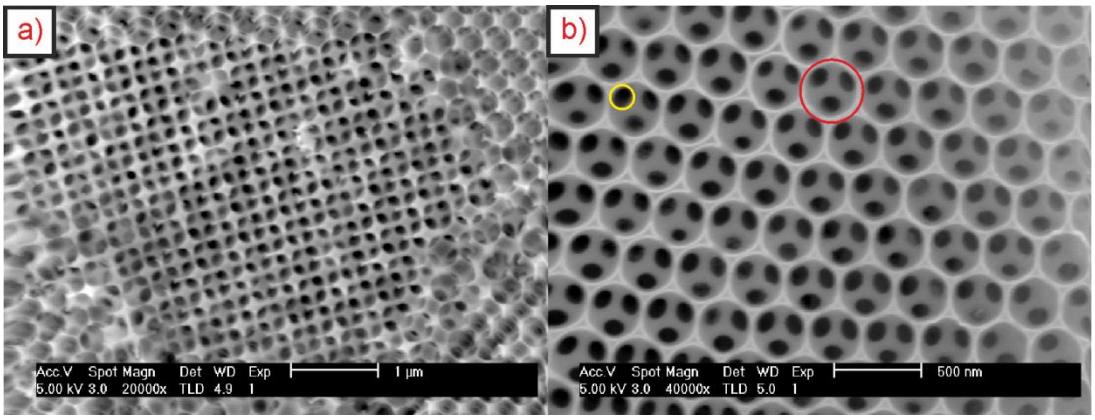

Figure 8: SEM images of 3DOM materials showing (a) 3DOM SiO_2 (220) planes and (b) 3DOM FTO (111) planes. Yellow circle represents a window between adjacent pores, red circle represents the pore size.

For a 3DOM semiconductor, or a 3DOM material containing semiconductor particles homogeneously loaded on the pore surface, overlap of the photonic stop band with the band gap can modify the absorption and emission properties of the semiconductor. If the band gap energy of the semiconductor coincides with the position of the photonic stop band, e^-/h^+ recombination can be inhibited. This effect is shown schematically in Figure 9. Propagation of light of energy equal to the band gap is forbidden within the photonic crystal (Figure 9a). Absorption of photons with greater energy than the band gap excites an electron to the middle of the

conduction band. After relaxation to the conduction band minimum, further radiative relaxation by band gap emission is suppressed by the photonic structure. Excited state lifetime enhancement from 2.8 ms to 4 ms has been reported in Tb(III)-doped LaF_3 nanoparticle loaded 3DOM SiO_2 by overlap of the emission band and photonic stop band.[92] 3DOM materials can also exhibit multiple light scattering effects, increasing the effective absorption of light in comparison to non-photonic materials.[93] Light trapping effects in 3DOM materials can lead to increased quantum efficiencies for photocatalysis.

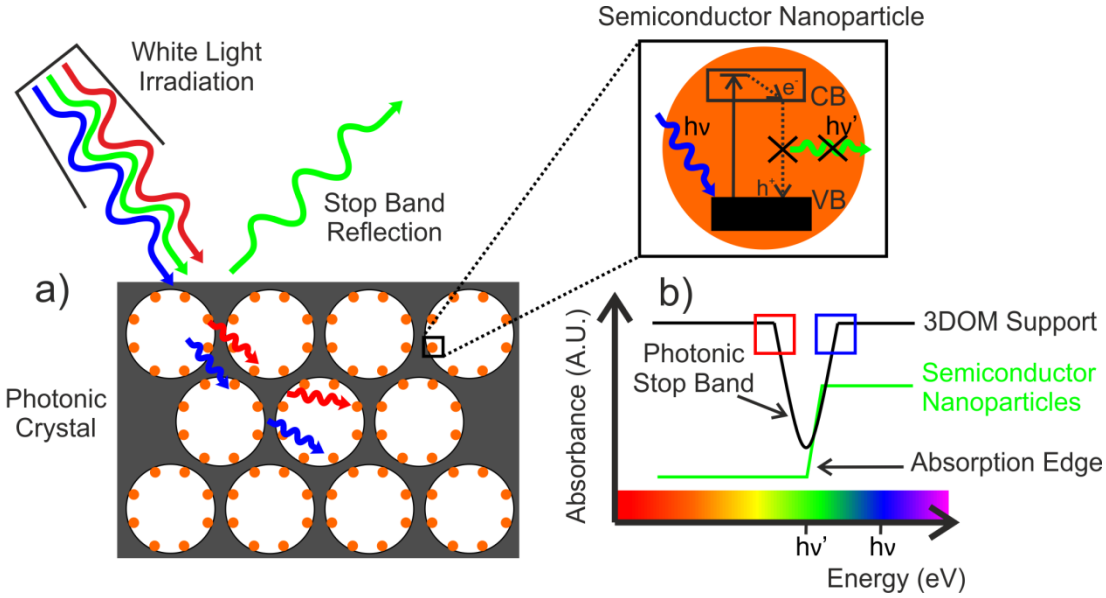

Figure 9: (a) Schematic showing inhibition of spontaneous e^-/h^+ recombination for semiconductor nanoparticles embedded in photonic crystals. Coloured lines represent approximate photon energies. The photonic stop band inhibits propagation of certain wavelengths within the structure. (b) Example UV-Vis absorbance spectra for the nanoparticle material and 3DOM support. Squares represent regions of slow photons at the red and blue edge of the stop band.

In addition to light trapping, the effective absorption of photons by the semiconductor can be increased by a photonic crystal. Photons of energy directly above and below the stop band positions in a photonic structure have their group velocity slowed within the lattice. The wavelengths affected are commonly referred to as slow photons. The effective path length of slow photons is increased, hence for a semiconductor material with band gap energy on the red or blue edge of the

photonic stop band, increased photon absorption is predicted.[94, 95] Practically, broad stop bands would be advantageous for slowing a greater range of wavelengths, and this has been demonstrated for the photocatalytic degradation of methylene blue using photonic TiO_2.[96]

Light at the edges of the photonic band gap can be described as a standing wave.[97, 98] At the red edge of the stop band, the wave maxima are localised in the walls, and the nodes in the voids. At the blue edge of the stop band, the wave maxima are localised in the voids. For effective enhancement of devices using slow photons at the edge of a stop band, the physical position of the light absorbing material within the photonic structure should be located to match the maximum intensity of the wave. This concept will be discussed further in chapter 4 (section 4.2.2b).

1.1.4b: Definition of Stop Band Positions

Bragg diffraction of electromagnetic radiation from the photonic crystal lattice shows stop bands corresponding to diffraction from different lattice planes, by the same principles as X-ray diffraction from an atomic lattice (Figure 7). For an oriented photonic crystal material, for example a thin film in which a specific crystal plane is grown normal to the surface, a singular stop band is observed. The position of the photonic stop band maximum (λ) has an angular dependence as defined by Equation 4:

$$\textit{Equation 4}^{99} \quad \lambda = \frac{2d_{hkl}}{m}\sqrt{{n_{avg}}^2 - sin^2\,\theta}$$

Where n_{avg} is the average refractive index of the walls and voids, θ is the angle of irradiation, m is the order of Bragg diffraction and d_{hkl} is the separation of the lattice planes. The Miller indices h, k and l define the crystal planes within the photonic crystal lattice. As θ → 90, sin θ → 1 and hence the value of the square root term decreases. The effect of this is to blue shift the stop band position. As an example, 230 nm polystyrene films show a blue shift in stop band from 570 nm to 450 nm when the angle of the reflectance probe to the surface is changed from 0 ° (surface normal) to 75 °.[100] For a powdered photonic crystal, a random assortment of crystal

planes can be present. Multiple photonic stop bands are observed if reflection from more than one of these crystal planes is constructive. Due to the random orientation of the crystal planes, the angular dependence of the stop band positions is relaxed, as defined by Equation 5:

$$\textit{Equation 5}^{99} \quad \lambda = \frac{2d_{hkl}}{m}[\phi n_{wall} + (1-\phi)n_{void}]$$

Where ϕ is the filling factor of the walls and n is the refractive index of the material composing the walls and void spaces. In opaline sphere arrays, a face centred cubic (FCC) arrangement of particles is observed. A 3DOM material shows the inverse of the opal structure, consisting of an FCC arrangement of air spheres encapsulated by the wall material. In an FCC lattice, only crystal planes consisting of all even or all odd h, k and l values show constructive interference of electromagnetic radiation, and hence a reflection.[101] Diffraction from the (111), (200), (220) and (311) planes are expected to produce stop bands in polycrystalline materials.[99] Equation 6 and Equation 7 relate the lattice plane separation to the unit cell parameter a and the periodicity of the photonic crystal lattice, D. In 3DOM materials, the periodicity of the structure is described by the pore size and wall thickness.

$$\textit{Equation 6} \qquad d_{hkl} = \frac{a}{\sqrt{h^2+k^2+l^2}}$$

$$\textit{Equation 7} \qquad D = \frac{a}{\sqrt{2}}$$

For a material of given refractive index, stop band positions can be controlled by varying the size of the pores and wall density. Of these, pore size is significantly easier to modify than wall thickness, and hence is the most common method for stop band modification. Stop band positions can be determined by diffuse reflectance UV visible spectroscopy (DRUVS). For a 3DOM heterogeneous photocatalyst in solution, the voids are filled with liquid which will typically have a refractive index greater than air (1.00029), resulting in a red shift of the stop band position. Measurement of the position of stop bands when the voids are filled with solvent is an important characterisation step in 3DOM photocatalyst design.

1.1.4c: Quantum Dot Emission Modification in Photonic Crystals

Inhibition and enhancement of spontaneous emission of CdTe quantum dots within 3DOM ZnO has been demonstrated as a function of the stop band energy (Figure 10).[102] A composite consisting of 3DOM ZnO was loaded with CdTe by atomic layer deposition (ALD), followed by growth of ZnO overlayers. Variation in the thickness of the overlayers was used to modify the position of the stop band.

Compared to a crushed photonic sample, photoluminescence was compared for samples with stop band positions centred on and at either side of the CdTe emission. The effect of the photonic structure is observed in Figure 10c. For the photonic samples, photoluminescence (PL) enhancement is observed compared to the crushed sample at the edges of the stop band due to slow photons. Enhancements of magnitude around 1.2 are observed due to slow photons at the red edge (left hand side) of the stop band, compared to 1.4 times enhancement at the blue edge (right hand side). In the centre of the stop band, the PL signal is reduced due to suppression of emission by the photonic crystal lattice, to around 0.6 – 0.7 times the intensity of the band in the crushed sample. Simultaneous inhibition and enhancement of emission has also been shown for CdS,[103] CdTe,[104] ZnS[105] and ZnS:Mn[106] in opal structures.

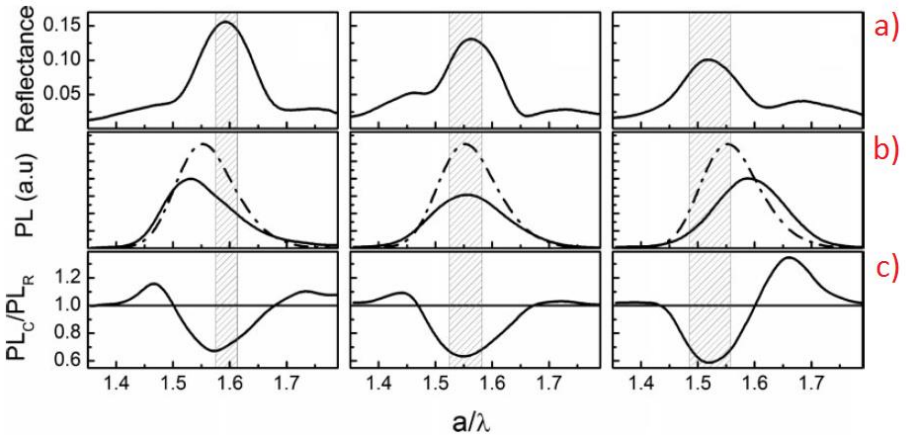

Figure 10: Literature photoluminescence spectra for ZnO/CdTe composites. Ordinate axis represents lattice parameter a/wavelength λ. From left to right, reflectance spectra (a) show red shift in the stop band position on increasing ZnO overlayer. (b) Photoluminescence (PL) trace (solid line) compared to crushed sample (dashed line). (c) Ratio of PL of sample to crushed sample. Adapted from Garcia ***et al.***[102]

The IPCE of CdS loaded 3DOM TiO_2 films on FTO glass electrodes has been studied as a function of the overlap between photonic stop bands and CdS emission. Maximum enhancements of IPCE by a factor of 4.7 were observed when the blue edge of the photonic stop band overlapped with the emission band, attributed to slow photon effects, compared to a factor of 1.8 for red edge overlap.[98] Modification of the excited state lifetimes of CdS quantum dots has also been observed within 3DOM TiO_2 due to the photonic structure.[107]

It should be noted that the emission suppression observed in all of these examples is achieved using a pseudo photonic band gap, in which complete reflection is not observed. The emission intensity depends on the angle of measurement in accordance with Equation 4. Improved emission suppression could be achieved with a full 3D photonic band gap which fully overlaps the photoluminescence band, but a 3DOM sample that displays this would require a refractive index contrast of 3.3 and a fill factor of 22.4 % in a 3DOM structure.[108] The emission lifetime of PbS quantum dots has been increased by a factor of 10 in a silicon inverse woodpile structure with a full 3D photonic band gap at 1.4 µm.[109] Non-radiative recombination can still contribute to photon loss. To the best of our knowledge, complete photonic band gap 3DOM materials have not yet been coupled with light emitters in the visible

region. High fill factor 3DOM GaP (n = 3.42 at 560 nm)[110] has been prepared by atomic layer deposition (ALD), and is calculated to have a full photonic band gap at 726 nm.[111] TiO_2 woodpile structures with a full 3D photonic band centred on 701 nm have also been fabricated.[112]

1.1.5: 3DOM Photocatalysts

1.1.5a: Photochemistry

TiO_2 is a commonly studied material in 3DOM photocatalysis. Photocatalytic activity of Pt loaded 3DOM TiO_2 has been evaluated as a function of the photonic stop band position. Enhanced hydrogen evolution and quantum yields from sacrificial aqueous methanol were reported for samples with overlap of TiO_2 absorption and (111) stop band position (247 μmol h^{-1}, QY = 11.9 %) compared to samples with overlap of TiO_2 absorption and (220) stop band positions, (128 μmol h^{-1} g^{-1}, QY = 6.2 %) and nanocrystalline TiO_2 (99 μmol h^{-1} g^{-1}, QY = 4.8 %), attributed to slow photon effects and multiple scattering in the 3DOM materials.[113] However, the reflectance spectra in this study do not indicate they were measured with solvent filled voids, and hence the position of the stop band may be shifted in the photocatalytic medium. The difference in activity observed could be due to variation in the loading of the platinum co-catalyst. Ag loaded 3DOM TiO_2 has shown a 1.25 times enhancement in methylene blue degradation in comparison to a disordered porous analogue.[114] Porous photonic TiO_2 spheres have also been used for methylene blue photodegradation, showing increased degradation rate constants (0.0685 min^{-1}) in comparison to P25 (0.0413 min^{-1}) due to slow photon effects.[115] The photocatalytic degradation of acid orange has been enhanced 4x in comparison to nanoparticle films using Pt loaded 3DOM TiO_2, due to slow photon effects and co-catalyst mediation of e^-/h^+ pairs.[96] Enhancement in photocatalytic efficiency due to slow photon effects have also been reported in mesoporous walled 3DOM Ti-Si oxide photonic crystal films for the degradation of rhodamine B,[116] and 3DOM TiO_2 films surface coated by poly(3-hexylthiophene) for methylene blue degradation under visible light.[117]

Modification of fill factors and the angle of irradiance have been used to influence photocatalysis in 3DOM films. 3DOM TiO_2 dispersions were tested for degradation of aqueous methylene blue to evaluate the slow photon effect in solution.[118] Observed decay rate constants were improved from nanocrystal TiO_2 (6.63 min^{-1} m^2) to 3DOM TiO_2 (11.3 min^{-1} m^2). By seeded TiO_2 growth from TiF_6^{2-}, the wall filling factor was increased, and the rate constant was increased to 15.9 min^{-1} m^2. The enhancements in activity in the 3DOM materials are attributed to slow photon effects, which are postulated to be increased for a higher filling fraction, however the corresponding shift in stop band position will also affect the overlap with the electronic absorption of TiO_2. 3DOM TiO_2 films have been studied as a photocatalyst for the degradation of methylene blue using monochromatic radiation (λ = 370 nm). Compared to TiO_2 nanocrystals, samples with a stop band centred on the illumination wavelength showed a decreased photodegradation rate at normal irradiation angle (0.85 times), due to restricted propagation of light within the photonic crystal. Variation of irradiance angle was used to blue shift the stop band such that the extent of overlap of the electronic absorption with the red edge of the stop band is adjusted, resulting in rate constant enhancements of 1.4 (10 °) and 2.4 (20 °). For samples in which slow photon effects were observed at normal incidence, the rate constant enhancements were reduced from 1.9 (surface normal) to 1.35 (10 °) and 1.25 (20 °) due to reduced overlap with the red edge of the stop band.[95]

3DOM Pt coated with TiO_2 has been used to photodegrade aqueous phenol. A conversion activity of 98.1 % over 4 hours was observed where slow photon wavelengths on the red edge of the stop band coincided with TiO_2 absorption, compared with 95 % for samples with non-optimised stop band overlap and 90 % for a non-photonic analogue.[119] 3DOM ZnO has demonstrated enhanced photocatalytic degradation of methyl orange in comparison to disordered porous and nanocrystal films.[120]

Bi_2WO_6 infiltrated SiO_2 opal arrays have been used for photodegradation of rhodamine B and phenol, showing enhanced activity in comparison to pure Bi_2WO_6 under visible light.[121] 3DOM Bi_2WO_6 films have also been used for methylene blue photodegradation. A maximum of 95 % degradation in 2 hours was observed using

a 55 ° angle of irradiance, compared to 83 % degradation at 30 ° and 63 % for a nanocrystal film.[122] 3DOM Ta_2O_5, TaON and Ta_3N_5 have also been studied as photocatalysts for H_2 evolution from aqueous methanol. 3DOM TaON showed an enhanced H_2 evolution rate (212.5 μmol h^{-1} g^{-1}) in comparison to the bulk material (30 μmol h^{-1} g^{-1}), attributed to a mixed phase composition of β/γ-TaON in the porous material.[123]

The rate of photoisomerisation of azobenzene has been studied in 3DOM SiO_2. Enhancements due to slow light at the edges of the stop bands were studied as a function of the thickness of the 3DOM layer. An increased rate was observed up to 1.35 times at the blue edge of the stop band with 27 layers of pores. On further increasing the thickness of the layer, the enhancement factor remained constant, attributed to scattering within the photonic crystal.[124]

1.1.5b: Photoelectrochemistry

Thin film photonic crystal arrays deposited on surfaces are of interest due to potential enhancement of activity of devices in numerous fields, including optics, electrochemistry, and solar fuel production.[87, 97, 125-127] 3DOM TiO_2 films on FTO glass infiltrated with CdS have been studied as photoelectrodes. Three pore sizes were investigated, with a maximum photocurrent of 4.84 mA cm^{-2} observed for a material with 288 nm diameter pores under simulated sunlight, with activity differences between samples attributed to the variation in surface area.[128] Architectures based on TiO_2 photonic crystals have been used to produce a device which can generate a photocurrent of 6.2 mA cm^{-2} at 0 V *vs.* Ag/AgCl, with 60 % IPCE at 460 nm. Electrodes consisted of ZnO nanowires grown in 3DOM TiO_2, sensitised with CdS QDs. The high efficiency was attributed to visible light scattering by the 3DOM structure.[129] Enhanced photocurrents have also been observed in 3DOM TiO_2/ZnO nanowire arrays in comparison to ZnO and 3DOM TiO_2.[130] Reduced TiO_2 nanotube/3DOM TiO_2 film composites have shown photocurrents of 2.5 mA cm^{-2} at 1.23 V *vs.* RHE and an IPCE of 79 % at 350 nm.[131] CdSe sensitised hybrid mesoporous/photonic crystal TiO_2 composite electrodes have shown high

photocurrents (14.2 mA cm^{-2} at 0.5 V *vs.* Ag/AgCl) under visible light, and increased IPCE at 575 nm (70.1 %) in comparison to CdSe/P25 (43.7 %).[132]

Disordered 3DOM antimony doped tin oxide (ATO) films as electrodes have been fabricated on FTO glass surfaces. The electrochemical activity of Fe_2O_3/3DOM ATO electrodes for water oxidation in the absence of light was compared to 3DOM Fe_2O_3 films, 3DOM ATO and 2D equivalents. Planar Fe_2O_3 films showed increased currents (11.7 mA cm^{-2} at 2 V *vs.* RHE) in comparison to 3DOM Fe_2O_3 (8.7 mA cm^{-2} at 2 V *vs.* RHE), due to poor charge transport in the porous material. The Fe_2O_3/3DOM ATO showed a higher current (31.7 mA cm^{-2} at 2 V *vs.* RHE) and earlier onset potential in comparison to Fe_2O_3/planar ATO (20.8 mA cm^{-2} at 2 V *vs.* RHE). The enhancements were attributed to light trapping effects of the porous film, increased surface area, and efficient charge transport through the conducting pore network.[126] Other studies have also demonstrated 3DOM α-Fe_2O_3 photoelectrodes for water oxidation, showing an earlier onset, increased photocurrent (3.1 mA cm^{-2} at 0.5 V *vs.* Ag/AgCl) and higher IPCE in comparison to planar films.[133]

3DOM $BiVO_4$ films with controlled pore and window sizes have been used as photoelectrodes. All 3DOM electrodes showed an increased photocurrent in comparison to a non-ordered reference sample (0.3 mA cm^{-2} at 1.2 V *vs.* Ag/AgCl), with a maximum of 1.35 mA cm^{-2} at 1.2 V *vs.* Ag/AgCl observed for a material with 180 nm pores. The effect of window size between adjacent pores was studied. Enhanced charge migration throughout the structure, and hence increased photocurrents were observed with smaller windows due to increased available surface area for reaction.[134]

The photocurrent of disordered porous and 3DOM WO_3 films has been studied with respect to the stop band position. By alignment of the red edge of a stop band and WO_3 absorption, observed photocurrents under UV and visible light were doubled in comparison to disordered porous WO_3 films due to the slow photon effect. IPCE values from 300 – 420 nm were also enhanced by 0.1 – 0.15 in the 3DOM samples.[125] Photoelectrochemical water splitting over 3DOM Bi_2WO_6 films has been demonstrated, showing a photon-to-hydrogen efficiency three times higher (0.13

%) than for nanocrystal Bi_2WO_6 films due to enhanced light penetration. Evolved gases at a rate of 4.5 μmol h^{-1} cm^{-2} (H_2) and 1.7 μmol h^{-1} cm^{-2} (O_2) were observed, with slightly lower O_2 yield than stoichiometry would suggest due to adsorption at the electrode.[122]

1.1.5c: Coupling of Plasmonics with Photonic Crystals

Photonic FTO nanocone arrays have been demonstrated as photoelectrodes. Photocurrents for Ti-doped Fe_2O_3 coated FTO increased from 1.2 mA cm^{-2}, to 2.24 mA cm^{-2} and 2.78 mA cm^{-2} for planar, 3D, and Au NP coated 3D electrodes respectively. Overall power conversion efficiency of 0.7 % at 0.88 V *vs.* RHE and photocurrent density of 3.39 mA cm^{-2} were observed on further addition of a Co-Pi co-catalyst.[4] Coupling of SPR and slow light effects to enhance efficiency has also been used in Ag/3DOM TiO_2 and Ag/3DOM TiO_2/nanorod TiO_2 composites.[135, 136] In the latter, photoelectrochemical water splitting to hydrogen (20 μmol h^{-1}) and oxygen (10 μmol h^{-1}) is observed, with a twofold enhancement in IPCE from 450 – 580 nm due to red edge slow photons.

CdS@Au core loaded 3DOM WO_3 composites have been tested for photocatalytic water splitting. Slow photons at the red edge of the stop band contributed to a 1.5 times enhancement in O_2 evolution (18.2 μmol h^{-1}) from sacrificial aqueous $AgNO_3$ for 3DOM WO_3 in comparison to crushed 3DOM WO_3. With the addition of CdS@Au nanoparticles, gas evolution rates of 32 μmol h^{-1} (H_2) and 42 μmol h^{-1} (O_2) were observed from sacrificial aqueous sulfide/sulfite and $AgNO_3$ respectively, in comparison to 20 μmol h^{-1} (H_2) and 26 μmol h^{-1} (O_2) for crushed samples.[137]

Photocatalytic decomposition of 2-propanol has been demonstrated over photonic Au/hollow TiO_2 nanosphere (Au/TiO_2-3DHNS) composites. Enhanced CO_2 evolution under polychromatic visible light was observed for Au/TiO_2-3DHNS samples (0.73 μmol h^{-1}) compared to a crushed sample (0.17 μmol h^{-1}) and non-ordered Au/TiO_2-HNS (0.24 μmol h^{-1}) of similar surface areas due to slow photon effects. Under monochromatic UV light (λ = 365 nm), CO_2 evolution rate of Au/TiO_2-3DHNS (9.4

μmol h^{-1}) was higher than the crushed sample (4.3 μmol h^{-1}) and Au/TiO_2-HNS (6.7 μmol h^{-1}). Slow photon effects were not observed at this wavelength, hence the enhancement in activity was attributed to multiple light scattering effects in the porous materials.[93]

1.1.6: Summary of Photocatalytic Activity Enhancements by Structural Modification

Direct comparison between the numerous literature reports of photocatalyst materials in the literature is difficult due to the multiple definitions of efficiency presented. In addition, the active mass of photocatalyst is not always specified, complicating comparison of product formation rates. However, an overarching theme towards efficiency enhancement by miniaturisation of components in devices can be seen. Numerous methods for enhancing the activity of materials are reported, and the observed enhancement factors vary greatly with the structuring of the material. In particular, a desired photocatalyst material would contain nanoparticle light absorbers, exhibit high surface area, and contain structural moieties that can influence the propagation of photons within the material to enhance absorption of light.

The aim of this work was to fabricate composite photocatalyst materials with these properties. 3DOM semiconductor materials have been shown to exhibit photoluminescence emission modification, enhanced photocurrents and IPCE, and enhancements in degradation rates of organic materials due to the photonic structure. In terms of photocatalytic hydrogen evolution, very few literature reports have studied the activity of 3DOM semiconductor materials.[113, 137]

Synthetic requirements restrict the formation of 3DOM semiconductors mostly to simple binary oxide materials, with some examples of ternary materials.[134, 138] Instead, the fabrication of composites consisting of nanoparticle photocatalysts deposited within photochemically inert 3DOM materials with intense stop bands was targeted. The main aim of the project was to evaluate the activity of these

composites for photocatalytic hydrogen evolution. The decreased distance to the surface for photogenerated charge carriers in nanoparticle materials combined with the effects of the photonic structure should effectively enhance the rate of photocatalysis. In addition, the confinement of photocatalyst species to the surface would reduce the amount of active material required in comparison to a 3DOM photocatalyst.

To ensure retention of the photonic structure on addition of nanoparticles, deposition must be homogeneous throughout the pores. In the following section, a brief literature review of techniques for deposition of nanoparticles will be presented. The relative strengths and weaknesses of each method will be considered, along with examples of their application for nanoparticle deposition in porous materials.

1.1.7: Techniques for Nanoparticle Deposition

1.1.7a: Chemical Bath Impregnation

The simplest and most commonly used method for deposition of nanoparticles is the chemical bath technique. A support is soaked in a precursor solution, for example metal nitrates or sulfates, allowing adsorption of metal ions on the surface. The sample is then removed, or the solution heated to evaporation. Depending on the material of interest, the sample may then be calcined to form the thermodynamically favoured oxide material, or placed in a second bath containing another precursor in a technique often referred to as successive ionic layer adsorption and reaction (SILAR). In some cases, multiple layers are built up by repeated dip/drying of the substrate.

Chemical bath techniques are often used for deposition of planar films on oxide surfaces, for example ZnO,[139] Co-doped CuO,[140] $BiVO_4$,[141] and CdSe.[142] Chemical bath methods have also been used for deposition of CoO and Co_3O_4 on $LaTiO_2N$,[143] and $Co(OH)_x$ species on Ta_3N_5,[144] showing the method is applicable to oxynitride and nitride materials in addition to oxides.

As examples in porous materials, Ag nanoparticles have been deposited in 3DOM TiO_2 films by the chemical bath method. Deposition of 5 – 10 nm particles was achieved by evaporation of aqueous $AgNO_3$ solutions containing ethanol at 50 °C for 5 hours.[114] The photonic stop band intensity drops on nanoparticle loading, accompanied by a slight red shift in the position as predicted by Equation 5. Au nanoparticles have also been deposited on 3DOM TiO_2 photonic crystals films by sequential dipping in aqueous $HAuCl_3$ and ethanol solutions,[136] or by hydrothermal methods.[135] Example TEM images from these literature works are displayed in Figure 11.[114, 136] SILAR techniques have been used to coat TiO_2 films, nanotubes and 3DOM TiO_2 with CdS, building up multiple layers by sequential dipping in solutions of cadmium acetate and sodium sulfide.[128, 145] The same approach has been used for deposition of CdS in the pore spaces of aluminosilicate zeolites.[55]

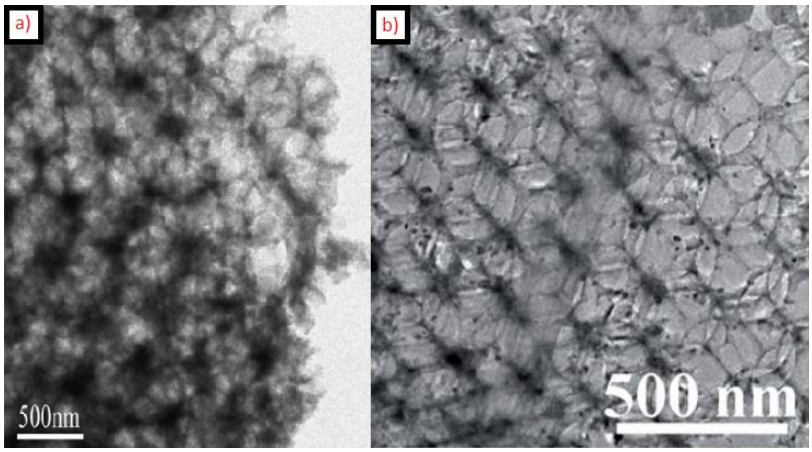

*Figure 11: Literature TEM images of 3DOM TiO_2 supported nanoparticles deposited by the chemical bath technique. (a) Ag loaded 3DOM TiO_2 and (b) Au loaded 3DOM TiO_2. Adapted from Zhao **et al.** and Zhang **et al.***[114, 136]

Chemical bath techniques are simple, and have been applied to deposit a wide variety of materials on planar, porous, and particulate surfaces. While versatile, control of the crystal phase of the particles formed is difficult, and the orientation of crystal planes is often dictated by the support. Direct control over the particle size is not possible, but can be influenced by the chemical composition and concentration of the precursor. In addition, aggregation of nanoparticles is unavoidable in some systems, and non-uniform adsorption of the precursor can

cause local variation in concentrations within the system. Adsorption of single to multiple monolayers of metal salt by repeated immersion/withdrawal of the substrate from solution can avoid these problems in some cases.

1.1.7b: Photodeposition

Nanoparticle deposition can be achieved by irradiating metal containing solutions (photodeposition). Typically used for deposition of metals on semiconductor materials, a high intensity light source is used to irradiate suspensions of metal salts in the presence of a support. Metal nanoparticles are formed by reduction of the metal salt by photoexcited electrons. An electron donor, such as acetic acid, is often present to prevent re-oxidation of the deposited metal species by the photoexcited holes. This technique is commonly used *in situ* to deposit co-catalysts for photocatalytic reactions by measuring gas evolution from an illuminated aqueous solution of sacrificial electron donor and photocatalyst in the presence of a metal precursor.

There are many literature examples of photodeposited metal nanoparticles. Well dispersed Pt nanoparticles around 2 nm in size can be deposited on CdS from an aqueous solution containing H_2PtCl_6 and acetic acid.[146] Using the same precursor, Pt nanoparticles have also been deposited on oxides, for example TiO_2,[147] and nitrides, for example Ta_3N_5.[148] Nanoparticles of Pt, Rh, Pd and Ir have been loaded onto Ag-$Sm_2Ti_2S_2O_5$ by both photodeposition and chemical bath techniques.[149] The observed activity for photocatalytic hydrogen evolution was higher for nanoparticles deposited by chemical bath approaches, attributed to a better quality of dispersion. Au nanoparticles have also been loaded on $NaTaO_3$ by photodeposition, with a wide size distribution of 2 – 10 nm.[62] The particle size of the support can govern the dispersion quality of photodeposited Au and Ag on TiO_2. For large particles, aggregates were observed, concentrated on grain boundaries and particle edges. In comparison, well dispersed 1 nm particles were deposited on TiO_2 nanoparticles.[150]

In addition to metal nanoparticles, deposition of metal oxides has also been reported by photodeposition. Ni_2O_3 nanoparticles were deposited on CdS as a co-catalyst for photocatalytic hydrogen production.[151] CdS powder was dispersed in an aqueous solution of nickel acetate and methanol, followed by irradiation with visible light to generate excitons, forming nanoparticles around 5 nm in size. A similar approach has been used for photodeposition of NiOOH films on TiO_2 substrates. The mechanism for this process involves band gap excitation of TiO_2 followed by transfer of photoexcited electrons to an external platinum electrode for oxygen reduction, coupled with oxidation of Ni(II) by photogenerated holes at the TiO_2 electrode.[152] Photogenerated holes have also been used to deposit RuO_2 on TiO_2 and CeO_2, followed by reduction in H_2 gas to form Ru metal nanoparticles.[153]

In porous materials, photodeposition has been used to deposit Au and CdS nanoparticles on meso-/macroporous N-doped TiO_2.[154] $HAuCl_3$ was used to photodeposit Au nanoparticles on the surface. A solution of S_8 and $Cd(NO_3)_2$ was added to the N-doped TiO_2/Au composite, forming S clusters preferentially on the Au particles. Further irradiation was used to generate excited electrons which are transferred to the Au particles, reducing S to S^{2-} ions and facilitating reaction with Cd(II) ions in solution to form CdS nanoparticles on the Au surface. Photodeposition has also been used for coating 3DOM TiO_2 with Ag,[155] and mesoporous TiO_2 with Ag, Cu and Ni nanoparticles.[156]

Compared to chemical bath techniques, control over the distribution of particles is difficult using photodeposition methods. Theoretically all of the precursor should be deposited on the support, however in practice material may also be deposited on the walls of the reaction vessel, and particles may form agglomerates. Despite these issues, the method is facile, and is commonly used for deposition of noble metal nanoparticles.

1.1.7c: Vapour Deposition Techniques

Various vapour phase deposition techniques exist in the literature. In basic chemical vapour deposition (CVD), a metal precursor in the gaseous state is passed over a substrate, followed by deposition on the surface. Solid or liquid precursors can be heated or exposed to plasma in order to form vapour, which is then transported to the substrate. In simple setups the precursor can be placed in the same chamber as the deposition target. Decomposition of the precursor can be induced by heat or introduction of a reducing or oxidising gas to form solid particles on the surface. More complex techniques such as atomic layer deposition (ALD) can be carefully controlled to build layers of a specific thickness. Sputtering is a related technique that can be used to form nanoparticle films. A precursor target is bombarded with high energy particles, releasing atoms which are then directed onto a substrate. This technique is also commonly used for coating non-conductive samples with films of carbon or gold prior to electron microscopy imaging.

In porous materials, tungsten, molybdenum and tantalum metals have been deposited on 3DOM carbon materials.[157] $W(CO)_6$, $Mo(CO)_6$ and $TaCl_5$ were used as precursors, and were heated to 300 – 500 °C in an evacuated chamber to form vapour, forming metal films by decomposition on the hot carbon surface. The films were observed to be uniform, penetrating depths of up to 20 µm within the sample.

Vapour phase deposition techniques are a powerful technique for formation of homogeneous surface films and nanoparticles. The major drawback of these techniques is typically the requirement of specialist equipment, which can be expensive. Simple thermal evaporation methods can be setup cheaply, but typically produce low quality films without extensive optimisation. For these methods, access to a precursor which can be vaporised is a requirement for deposition, which can be a problem for some materials. To produce higher quality nanoparticle films, techniques like ALD and sputtering can be used.

1.1.7d: Electrostatic Stabilisation

In chemical bath techniques, simple metal salts are employed as precursors to nanoparticle materials. In large concentrations, films of material are often produced. Formation of homogeneously distributed individual nanoparticle samples requires a low concentration of precursor, distributed evenly throughout the sample. Synthesis of stabilised nanoparticles, followed by deposition can be used to increase the homogeneity of the dispersion. Stabilisers such as EDTA and sodium citrate can be added to simple metal salts to form complexes which can cluster together to form charge stabilised nanoparticles. Deposition from these sols should favour homogeneously dispersed individual nanoparticles.

Platinum nanoparticles have been deposited from citrate complexes.[158-160] H_2PtCl_6 and sodium citrate were refluxed for 4 hours to form a platinum citrate sol. The citrate was then removed using an ion exchange resin, and replaced with polyethylene glycol protecting groups. The sol was dispersed across the surface of TiO_2 powder by sonication. Citrate stabilised Au nanoparticles have been deposited on methacrylate polymer surfaces, after previous modification with pendant amine and thiol groups.[161] Electrostatic stabilisation has also been used for deposition of PdNi nanoparticles on carbon.[162]

As an example of deposition within porous materials, $LaCoO_3$ perovskites have been dispersed in mesoporous silica using citrate precursors.[163] $La(NO_3)_3$ and $Co(NO_3)_3$ were mixed with citric acid in aqueous solution and allowed to react for 24 hours. The mixture was added to the mesoporous support, dried and calcined to form the loaded material. TEM analysis showed the deposition had occurred throughout the porous channels, but agglomerates and surface coatings were also observed.

Zeolite NaY has been loaded into 3DOM ZrO_2 by electrostatic interactions.[164] 3DOM ZrO_2 with surface sulfate groups was coated with multiple layers of polyelectrolyte with positive outer layer, to which a solution of zeolite NaY was added. Hydrothermal reaction was used to bond the particles to the support. Homogeneous coatings were achieved due to the strong attraction between the positively charged polyelectrolyte layer and the basic zeolite surface. The same

method has been used to homogeneously deposit TiO_2 nanoparticles in 3DOM carbon, TEM images of which are shown in Figure 12.[165]

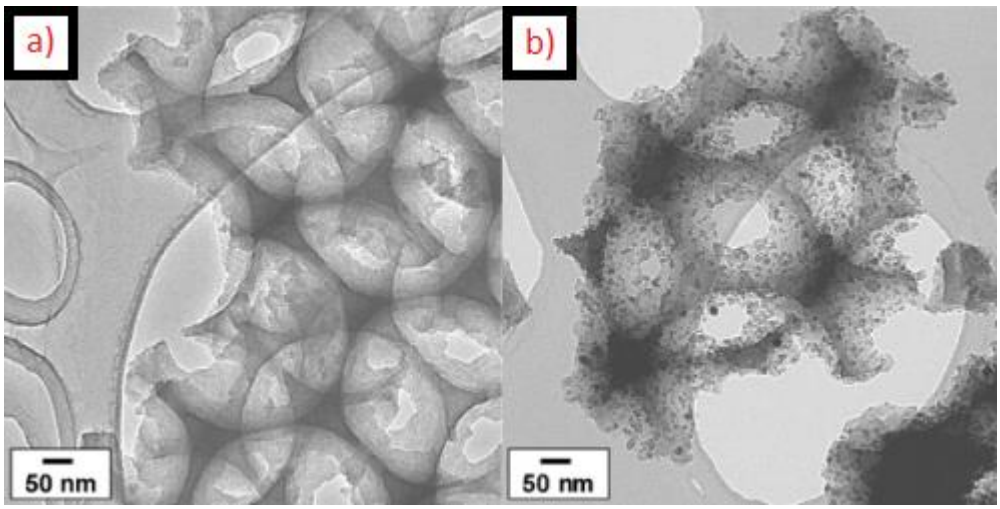

Figure 12: Literature TEM images of 3DOM carbon (a) and TiO_2 loaded 3DOM carbon (b) deposited using polyelectrolyte layers and charged precursors. Adapted from Wang ***et al.***[165]

Using charge stabilised nanoparticles, access to more complex ternary systems is possible, and formation of nanoparticles rather than films is preferred. However, agglomeration of particles is prevalent. High quality dispersions have been achieved with polyelectrolyte surface coatings, utilising strong ionic nanoparticle-support interactions to direct the deposition.

1.1.7e: Sterically Stabilised Nanoparticles

For electrostatically stabilised nanoparticles, dispersion is dependent on the choice of electrolyte, and is often difficult at high concentrations due to screening of the electrolyte charge. The surface charge of particles is also important, and can be sensitive to the pH of solution. As an alternative, long chain molecules grafted at the surface of a nanoparticle can be used to stabilise particles against aggregation.

The mechanism for steric stabilisation can be explained in terms of the free energy of solution. Considering two particles coated with long chain molecules, as they approach in solution the surface coatings will overlap. The movement of the chains

is restricted, resulting in a decrease in the entropy of the system. To counteract this unfavourable increase in the Gibbs free energy of the system, solvent floods in from around the particles to fill the void between them, and the particles are separated.[166]

Exploitation of strong Au-S and Au-N bonds has been used in a variety of the methods to deposit nanoparticles already described in this section. Depositions of ligand stabilised nanoparticles in the literature involve similar methods. Using preformed dodecanethiol functionalised Au nanoparticles, a general method for homogeneous deposition of up to 5 weight percent Au on a variety of oxide surfaces has been reported.[167] Calcination was used to remove the surface coating and anchor the particles to the support. Co nanoparticles have been deposited on Au/mica and Au/Si surfaces using long hydrocarbon chain thiols as anchors.[168]

In addition to Au particles and surfaces, colloidal techniques exist for formation of planar Fe_2O_3 films.[169] Stabilised nanoparticles were formed by dialysis against $HClO_4$. FTO coated glass slides were dipped in nanoparticle solution for 1 minute, then a carboxymethylcellulose solution for 1 minute to bind the particles together, growing larger films by multiple repetitions of this process. Fe_3O_4 nanoparticles have also been deposited on carbon surfaces.[170] Oleic acid stabilised nanoparticles have been deposited as thin films within polymer membranes by aerosol-assisted CVD (AACVD).[171] In porous materials, oleylamine stabilised Pd nanoparticles have been deposited on 3DOM SnO_2.[172]

1.1.8: Summary of Nanoparticle Deposition Techniques

Many other techniques exist for deposition of films and nanoparticles,[173] including aerosol based techniques[174] and electrochemical approaches.[175, 176] The examples presented above represent the most applicable methods to the systems of interest in this study. However, with all existing methods for deposition, simultaneous control of nanoparticle size, distribution, crystal phase and loading is difficult.

The nature and concentration of precursor used often plays a role in the final product. The thickness of the initial layer is controlled by the adsorption of the liquid or gaseous precursor onto the walls of the porous host, but this can vary wildly between different materials and multiple depositions may be required to build up a useful amount of material.

In general, multiple approaches exist for the synthesis of nanoparticle loaded materials. The homogeneity of the coating cannot be guaranteed, and for some materials has not been demonstrated. Composite materials with homogeneously distributed, space separated nanoparticles have application in a wide range of fields, limited only by the availability of a reliable synthetic route, hence the development of general methods to provide these materials is highly desirable.

1.2: Project Aims

As this chapter has discussed, increased efficiency for photocatalytic reactions using semiconductors can be achieved by controlling the size and structure of the material. Of particular interest are nanoparticle facets, which can show a higher surface area and exhibit reduced recombination due to the decreased distance to the surface for photogenerated charge carriers, in comparison to particles of micron size and above. In this study, composite photocatalysts consisting of semiconductor nanoparticles homogeneously distributed in photonic hosts will be fabricated, and the photocatalytic hydrogen evolution activity evaluated with respect to the optical properties of the support.

3DOM SiO_2 and ZrO_2 materials with a range of periodicities and stop bands in the visible region will be fabricated from polystyrene sphere templates. As discussed above, many techniques exist for deposition of nanoparticle materials, however the distribution of particles is not always homogeneous, and simultaneous control of the size and crystal phase is often problematic. Ligand stabilised nanoparticle materials will be synthesised, and a general method will be developed for their deposition in 3DOM powders. In addition, the generality of the method will be evaluated by its application to 3DOM films and mesoporous materials. The synthesis of ordered porous materials using established literature techniques will be described in chapter 2, and the subsequent deposition of nanoparticles within the pores will be presented in chapter 3.

Composite photocatalysts will be fabricated, consisting of CdS and TiO_2 nanoparticles deposited in 3DOM ZrO_2 with different stop band positions. The photocatalytic activity of these materials for hydrogen production from sacrificial electron donors will be investigated. The effect of overlap of the stop band position and the band gap of the semiconductor on the rate of hydrogen evolution will be analysed. This work will be presented in chapter 4.

Chapter 2

Synthesis of Ordered Porous Materials

2.1: Introduction

2.1a: Synthetic Approaches to Photonic Crystals

Fabrication of high quality photonic crystal architectures can be achieved by a variety of methods, including electron beam lithography and infiltration of colloidal templates by electrodeposition, ALD or capillary action.[99, 175, 177, 178] Electron beam lithography is typically used to etch a substrate to form a 2-dimensional structure with high precision. Electrodeposition, ALD and capillary infiltration can produce high quality 2D and 3D photonic crystal films on a planar substrate. In electrodeposition, a voltage is applied between an underlying conducting substrate and an auxiliary electrode to deposit a precursor from solution inside the voids. In an ALD experiment, sequential exposure to two or more precursors is used to build layers of material in a colloidal template. Structures with minimal defect concentrations can be fabricated by ALD. These methods are typically limited to the fabrication of photonic crystal films.

Three dimensionally ordered macroporous (3DOM) materials, or inverse opals, can show photonic properties as discussed in section 1.1.4a. Capillary infiltration of packed templates by liquid precursors can be used to form 3DOM powders and films.[99, 179-181] Common templates include monodisperse SiO_2 spheres synthesised by the Stöber method,[182] or polymer spheres such as polystyrene (PS) or poly-methylmethacrylate (PMMA) synthesised by emulsifier free emulsion polymerisation. Template spheres can be packed to form CCP arrays of spheres by convective self assembly or vertical capillary deposition at a planar interface to form films, or by centrifugation to form monolithic powders as shown in Figure 13.[99, 100, 183-185]

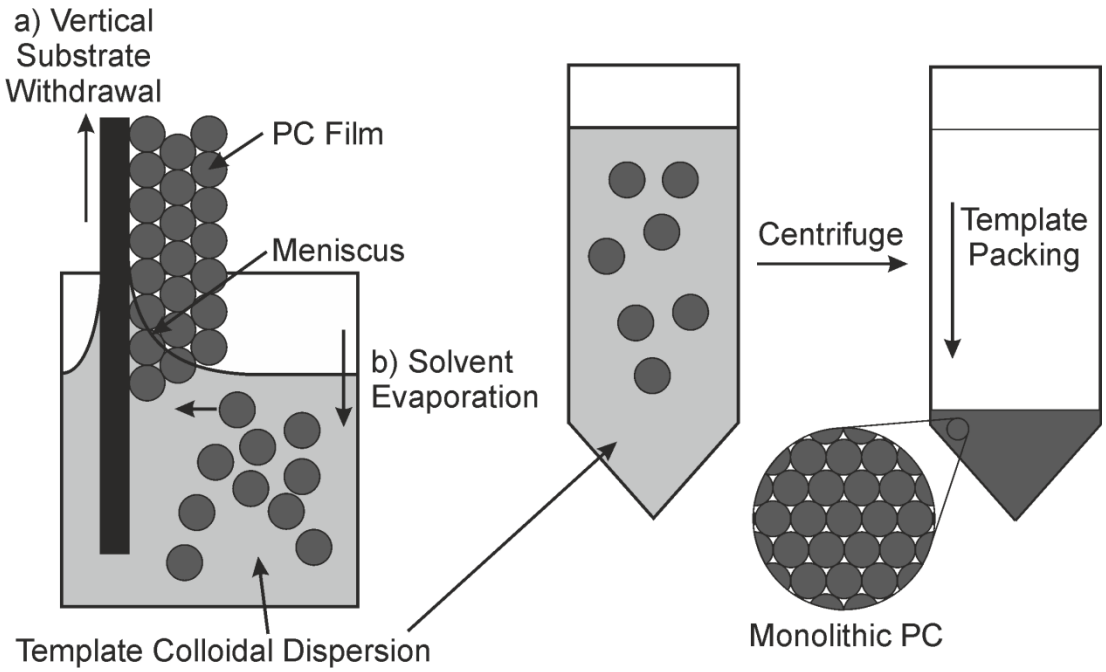

Figure 13: Packing of spherical templates, by assembly at a surface to form photonic crystal films (left) or by centrifugation to form powders (right).

The 3DOM structure is fabricated by infiltration of the interstitial volume between the colloidal spheres (Figure 14a). Precursors are typically metal alkoxides, nitrates or acetates, which are hydrolysed within the voids of the template to form a solid network. Fabrication of high quality photonic crystal structures requires a balance between the rate at which liquid is drawn into the template and the rate of hydrolysis of the precursors. Rates of hydrolysis are often controlled by additives and pH adjustment of the precursor solution. Template removal is achieved by calcination, electrochemical etching, or leaching with acid such as HF. Calcination creates windows between adjacent spheres which allow trapped gases to escape. These windows are advantageous for catalysis applications as they allow diffusion of reagents within the pores. However, for photonic crystal films template removal by calcination can cause contraction of the film, leading to cracks in the surface which are detrimental to the connectivity of the structure.

3DOM films can also be synthesised by co-deposition of precursor nanoparticles and template spheres as illustrated in Figure 14b. The colloidal particles self assemble at an interface to form 3DOM structures. This method is particularly

useful for ternary or higher phases in which synthesis by capillary infiltration is difficult due to variation in the hydrolysis rate of the precursors.

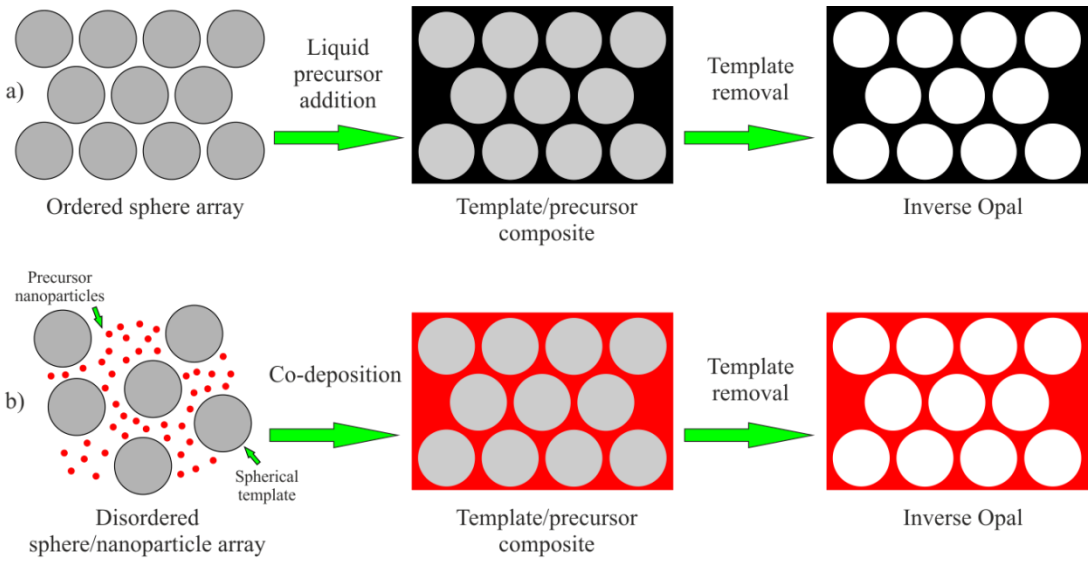

Figure 14: Methods for preparation of ordered porous structures. (a) Liquid infiltration of CCP spheres and (b) Co-deposition of nanoparticle precursors and spherical template particles. Template removal can be achieved by calcination, electrochemical etching, or by leaching with HF.[186]

Photonic crystal arrays can be fabricated from template spheres with a core-shell structure. After packing of the template, the core is removed, leaving the shell as a macroporous network of hollow spheres. In these systems, wall thickness can be directly controlled by variation of the shell thickness. Interpore windows in these materials are smaller,[186] which is of less benefit for photocatalysis as it can lead to increased tortuosity. Diffusion of products from within the pores to the surface may be an issue for small windows.

The relative ease of colloidal crystal templating methods allows for wide ranges of compositional flexibility. Functionalised 3DOM materials can be obtained by pre- or post- processing, for example mercaptopropyl functionalised 3DOM SiO_2 and poly(3-hexylthiophene) functionalised 3DOM TiO_2.[99, 117] 3DOM materials with mesoporous walls have been synthesised using surfactants in the precursor solution.[116, 187]

In this project, 3DOM powders and films were fabricated by liquid infiltration of CCP templates. Polystyrene spheres synthesised by emulsifier free emulsion polymerisation were used as templates. The mechanisms involved in this process will be discussed below.

2.1b: Emulsifier Free Emulsion Polymerisation of Styrene

To form high quality 3DOM materials, monodisperse template spheres must be used. The mechanism of polymerisation of styrene is an important consideration to achieve a monodisperse sphere distribution. At room temperature, styrene is sparingly soluble in water, and hence two phases will be present. On elevation of the temperature to 70 °C, the solubility of styrene in water increases to 4 g L^{-1}, allowing some monomer to dissolve in solution.[188] As styrene is consumed during reaction, more molecules diffuse into solution from the styrene droplets on the surface. $K_2S_2O_8$ (KPS) is used as an initiator, which when heated in solution forms $SO_4^{\cdot-}$ radical anions. On addition to styrene, oligomeric radicals are generated (Figure 15). Reaction of these radicals with further styrene molecules propagates the chain, forming surfactant like molecules with a hydrophobic carbon chain tail group and hydrophilic sulfate head group. The nucleation step begins when the hydrophobic chain reaches a critical size such that its interactions with water are energetically unfavourable.

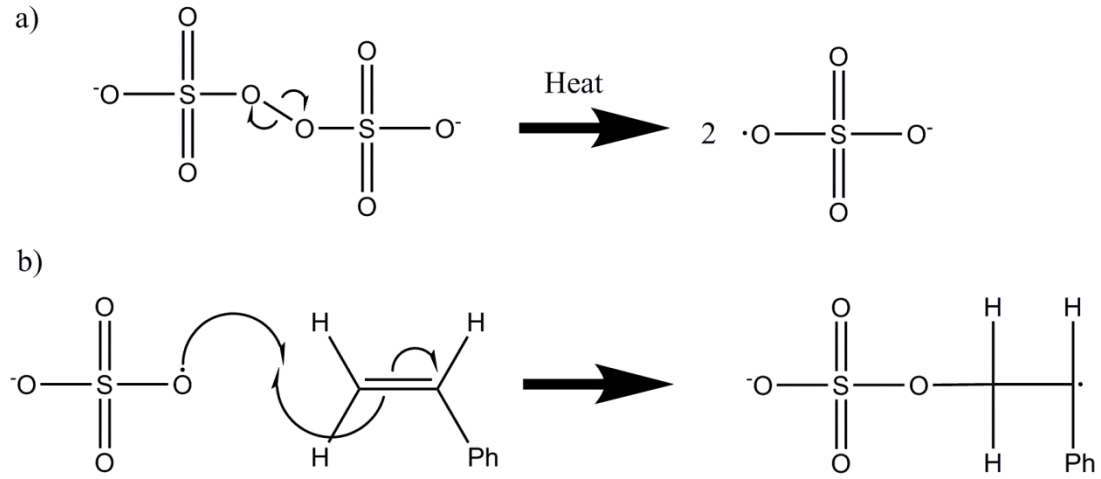

Figure 15: Polymerisation initiation steps using persulfate ions. (a) Formation of sulfate radicals from persulfate ions and (b) formation of an oligomeric radical.

There are two mechanisms by which nucleation can occur. As the oligomers become surface active, they can either precipitate out of solution or form micelles. Which effect takes place depends on the relative concentration of surfactant in solution. Below a critical micelle concentration (CMC) for the surfactant oligomers, homogeneous nucleation occurs, where the instability of the oligomers in solution leads to precipitation. Nuclei are formed as chains entangle each other and accumulate. Above the CMC, micellar nucleation occurs, where the surface active oligomers form spherical micelles with the sulfate head groups at the surface. In both cases the driving force is the increasing hydrophobicity of the growing chains. To form monodisperse spherical particles, micellar nucleation is preferred for isotropic growth, and the nucleation step must be fast such that it occurs before the particles begin to grow. For persulfate initiators, studies have shown that over time the activity of the initiator decreases,[189] hence the number of surface active oligomers in solution can decrease to zero if the rate of absorption of oligomers by the micelles is high enough. Thus, nucleation ends, and uniform growth of particles can occur.

Growth of particles proceeds by diffusion of styrene monomers into the nuclei. Growth can occur by coagulation of nuclei, capture of new oligomers and terminated polymer molecules from solution, or polymerisation of absorbed styrene within the growing particles. The latter is preferred for isotropic growth of

spheres. As the particles swell, any surface active oligomers remaining in solution will adsorb at the surface and further stabilise the micelle. The growing polymer particles are stabilised against aggregation by the electrostatic interaction between negatively charged sulfate groups on the surface. Growth of particles ends when all the monomer droplets are consumed, or can be stopped by addition of a polymerisation inhibitor.

The size of polystyrene sphere obtained is greatly dependent on the rate of diffusion of monomers into the growing droplets, the number of nucleation sites formed, and the growth time of the particles. Variation of these factors by adjusting reaction parameters were studied within our system to elucidate trends in the growth of polymer spheres, and form a wide size range of suitable templates for 3DOM materials.

2.1c: Chapter Aims

The synthesis and characterisation of porous supports will be reported in this chapter. The fabrication of these materials has been reported previously,[180] but was modified to produce specific support pore sizes. Deposition of nanoparticles within these materials to form novel composites will be presented in the following chapters.

The synthesis of polystryrene spheres by emulsifier free emulsion polymerisation is presented, with variation in the conditions used to modify the sphere size. Using PS templates, powdered 3DOM SiO_2 and ZrO_2, and 3DOM FTO films were synthesised. Mesoporous SiO_2 was synthesised using a triblock copolymer template. Powder XRD, SEM, TEM, porosimetry and DRUVS were used to probe the quality of all materials produced.

2.2: Results and Discussion

2.2.1: Polystyrene Template Synthesis

Attaining highly ordered packed sphere templates is an important factor for formation of good quality 3DOM materials. Templating from disordered spheres can lead to structures with local ordering, however due to the limited regularity on larger scales, little to no photonic properties will be observed from the 3DOM material.[180] Centrifugation can lead to well ordered arrays of spheres, as long as the spheres are perfectly spherical (Figure 13, above). A face centred cubic (FCC) close packed array of spheres is formed as the solvent is removed from between particles, and as a result of electrostatic repulsion of the sulfate groups on the surface of adjacent spheres.[180] Theoretically, FCC packing has been shown to be energetically preferred over hexagonal, and other close packing arrays.[190]

Polystyrene balls with sizes ranging from 200 – 600 nm were synthesised by emulsifier free emulsion polymerisation methods as described in the literature.[180, 191] The colloidal dispersion was centrifuged to pack the spheres into a close packed array. The supernatant was removed and the solid dried at 66 °C overnight to yield polystyrene spheres as a brittle white solid. Literature reports suggest centrifuging above 1000 rpm is necessary to avoid merging of spheres.[192] However, sedimentation from the dispersion takes much longer at slower speeds, often over 24 hours or more. Using a faster centrifuge speed of 4000 rpm the colloid was packed in a shorter time of 3 hours, with no discernible loss of quality or coalescence of polymer spheres observed via SEM. Typically, 4 g of packed monolithic PS spheres were obtained from 50 mL of colloidal dispersion.

The reaction conditions were modified to evaluate the effect of various reaction conditions on the quality and the sphere size obtained, in comparison to an initial set of control conditions. SEM imaging was used to determine the diameter D of the spheres, by averaging measurements of a minimum of 100 particles (N) from multiple images. The number average diameter D_n and weighted average diameter D_w were calculated from the following equations:[193]

Equation 8 $$D_n = \frac{\sum N_i D_i}{\sum N_i} \qquad D_w = \frac{\sum N_i D_i^4}{\sum N_i D_i^3}$$

The ratio of D_w/D_n was used to express the polydispersity of a polystyrene colloid batch. Typically in the literature values of D_w/D_n between 1.0 and 1.05 are considered to be monodisperse, however to ensure high quality 3DOM materials only batches with D_w/D_n less than 1.03 were used as templates. Batches with polydispersity > 1.03 were discarded. All latex suspensions were stable against sedimentation for at least 6 months, and in some cases up to a year.

Temperature, stir speed, reaction time, initiator concentration and addition of a stabiliser polyvinylpyrrolidone (PVP) were varied in a series of experiments. It has been reported that monomer concentration is proportional to the sphere size produced, however in this study monomer concentration was kept constant.[194] The purpose of this study was not to rigorously test the effect of each parameter on the sphere size, but to elucidate general trends in the reaction and allow synthesis of a range of sphere sizes as templates for 3DOM materials.

As an initial series of experiments, effect of variation in stir speed, reaction time and temperature were investigated. Table 1 summarises the effect of these parameters on the size of sphere obtained. The conditions for batch **PS-1** were found to reproducibly produce a particle size of around 500 nm by SEM, and were used as a baseline for comparison. SEM images showing the various particle sizes are displayed in Figure 16.

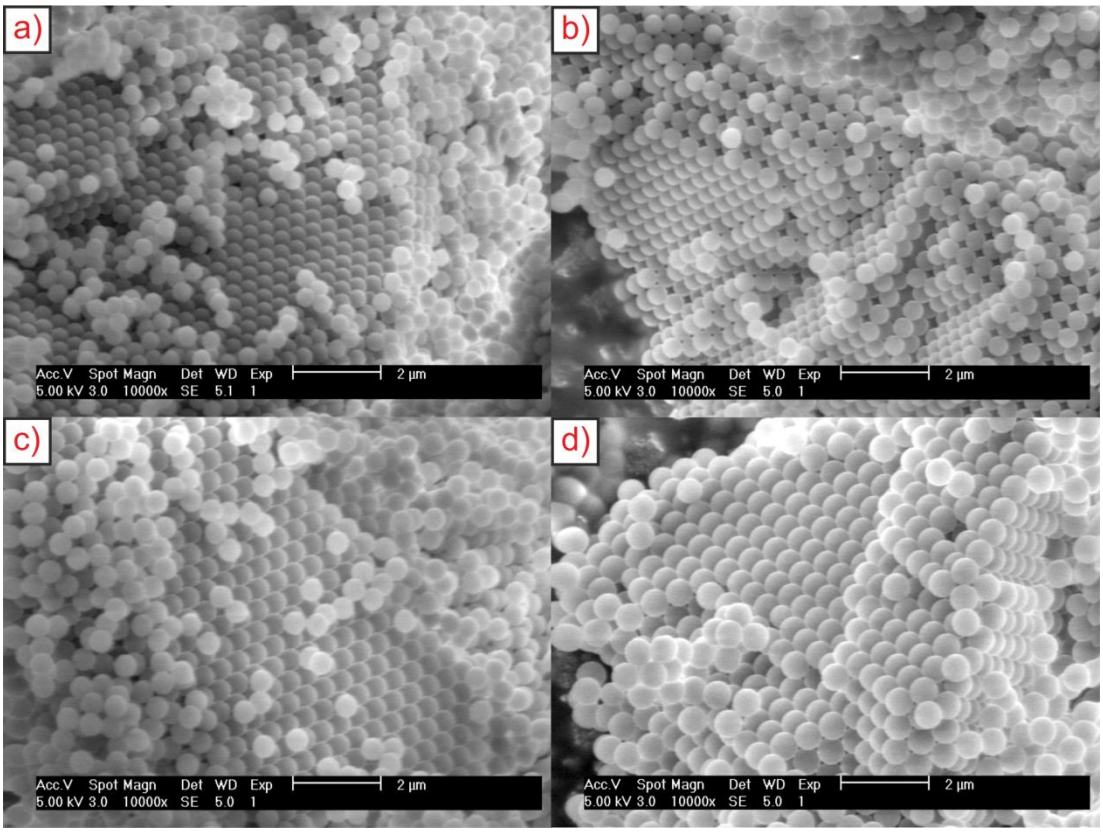

Figure 16: SEM images showing variation in polystyrene sphere size by modifying reaction stir speed, initiator concentration and temperature. (a) ***PS-3****, 402nm spheres, (b)* ***PS-7****, 436 nm spheres, (c)* ***PS-1****, 492 nm spheres, (d)* ***PS-2,*** *601 nm spheres.*

In batches **PS-2** and **PS-4**, the stir speed was modified. For **PS-2**, increasing the rate of stirring increased the size of the spheres obtained. A decreased stir speed slightly decreased the sphere size. High stir speeds would be expected to produce large spheres, as faster stirring ensures a well mixed solution, where surfactant oligomers diffusing at the surface of emerging nuclei are constantly being replaced from solution. This leads to less nucleation sites, and hence larger particles grow for the same monomer concentration. For lower stir speeds, it is likely that more nuclei form due to higher local concentrations of surfactant oligomers, forming micelles to reduce their surface tension. More nucleation sites result in less growth on individual sites, and hence smaller polymer spheres.

For batch **PS-3**, the reaction temperature was increased. In comparison to **PS-1**, smaller balls were observed, attributed to the higher reactivity of the initiator at

elevated temperatures. In a given period of time, a larger amount of smaller oligomer radicals are formed in comparison to lower temperature reactions. When the chains grow to a critical length, more micelles are formed, resulting in more nucleation sites. For a fixed monomer concentration, the final sphere size is therefore smaller.[195]

Batch	Temperature / °C	Stir speed / rpm	Reaction Time / h	D_n / nm[a]	D_w / nm	D_w / D_n
PS-1	70	245	28	492±21	494	1.006
PS-2	70	360	28	601±15	602	1.002
PS-3	80	245	28	402±12	403	1.003
PS-4	70	180	28	469±14	470	1.003
PS-5	70	245	48	496±10	497	1.001

Table 1: Effect of temperature, stir speed, and reaction time on the size of polystyrene spheres obtained. All syntheses used 1.23 mM $K_2S_2O_8$. The conditions for reaction 1 were used as a control experiment to evaluate the effect of each parameter. [a]Averaged over > 100 spheres, see Equation 8.

Reactions at higher temperatures of 85 °C and 90 °C produced smaller spheres of 350 nm and 250 nm respectively. However, after centrifugation disorder could be observed in the packing of spheres, which when templated to form 3DOM materials, resulted in low photonic stop band intensities. Polymerisation reactions at 95 °C have been reported in the literature, forming polydisperse spheres attributed to decomposition of the initiator.[196] Other methods were investigated to access sphere sizes below 400 nm.

For batch **PS-5**, the polymerisation reaction was allowed to continue for an additional 20 hours. SEM analysis shows a similar sphere size to batch **PS-1**, suggesting that further growth of the spheres does not occur after 28 hours due to total consumption of the monomer in solution. Images showed a disordered packing of spheres, in addition to some non-spherical particles (Figure 17). The colloidal dispersion obtained was more viscous in comparison to other reactions, suggesting non-isotropic growth and promoted reaction between adjacent spheres

after longer times at high temperature. It was concluded that 28 hours was sufficient time to produce well ordered spheres with good size distribution. Shorter reaction times have been reported by other groups to form well ordered spheres,[197] but were not investigated here.

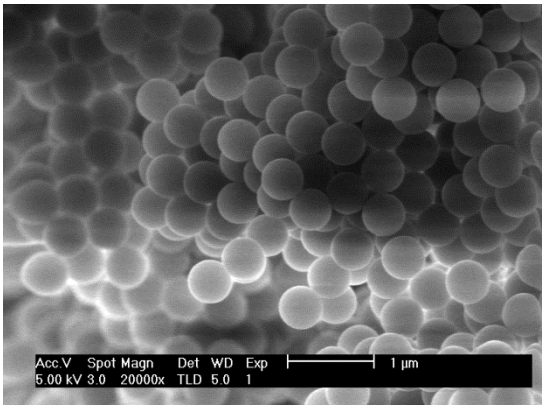

*Figure 17: SEM image of PS sphere batch **PS-5**, formed by reaction for 48 h. A disordered packing array and some elongated spheres can be observed.*

Variation in initiator concentration was also used to control the size of polystyrene spheres obtained. Table 2 lists the conditions used and resulting particle sizes. From the conditions for **PS-1**, the initiator concentration was reduced for **PS-6** and **PS-7**, and increased for **PS-8**. The particle size is seen to decrease with the initiator concentration, however for batches **PS-6** and **PS-7** the sphere sizes obtained are comparable, suggesting there is a lower limit to the effect of decreasing initiator concentration. A minimum sphere size obtainable by decreasing initiator concentration has also been observed in literature reports, attributed to insufficient conversion of reagents at low initiator concentration.[198]

Batch	$K_2S_2O_8$ initiator used / g	Initiator concentration / M	D_n / nm[a]	D_w / nm	D_w / D_n
PS-6	0.1105	3.07×10^{-4}	430±12	431	1.002
PS-7	0.221	6.13×10^{-4}	436±8	437	1.001
PS-1	0.442	1.23×10^{-3}	492±21	494	1.006
PS-8	0.663	1.84×10^{-3}	584±14	585	1.002

Table 2: Effect of initiator concentration on polystyrene sphere size. All reactions were operated at 70 °C for 28 hours, stirred at 245 rpm. [a] Averaged over > 100 spheres.

At constant aqueous phase ionic strength, a decrease in initiator concentration would be expected to increase the size of the resulting colloidal spheres.[198] However, if the only ions present in solution are from the initiator, changing initiator concentration will have a significant effect on the ionic strength of the solution. At high ionic strength, surface charges are screened by the electrolyte, allowing larger spheres to be formed by fusion of growing polymer particles. Conversely, at low ionic strength particle repulsion inhibits growth, leading to smaller spheres.[194] The trends in particle sizes obtained for **PS-6, PS-7** and **PS-8** suggest the effect of ionic strength is dominant, hence the particle size decreases with decreasing initiator concentration down to a limiting size of 430 nm in this system.

Synthesis of ordered polystyrene spheres of < 400 nm was not possible via the above methods. Instead, a modified literature method was used in which PVP is added to the reaction mixture.[191] PVP molecules can interact with growing PS spheres through a partial positive charge on the amide nitrogen, stabilising them against aggregation, and hence increasing the number of nucleation sites.[191] For a constant initiator concentration, the growth of individual particles will therefore be decreased, resulting in smaller spheres. Table 3 lists the reaction conditions and sphere sizes obtained.

Using **PS-11** as a base reaction, increasing the temperature for synthesis of **PS-12** decreased the size of the spheres as observed previously. For **PS-9** and **PS-10** the

PVP concentration was decreased, and larger spheres were obtained. The decreased stabilisation of the growing polymer particles results in the formation of fewer nuclei, leading to more growth on individual spheres. For **PS-13** and **PS-14** the amount of PVP in solution was increased, however the effect on the size of the spheres was minimal, in addition to causing a detrimental effect on the quality of the packing as observed by SEM. Using this method provided access to highly ordered spheres in the 200 – 400 nm size range.

Batch	PVP added / g	Temperature / °C	D_n / nm[a]	D_w / nm	D_w / D_n
PS-9	0.1	70	362±24	366	1.012
PS-10	0.25	70	251±23	257	1.024
PS-11	0.5	70	220±14	222	1.013
PS-12	0.5	80	185±14	188	1.017
PS-13	0.75	70	224±13	226	1.010
PS-14	1.0	70	210±20	217	1.031

Table 3: Effect of added stabiliser on polystyrene sphere size. All reactions were performed under N_2 and used 133 mL total solution, 300 rpm stir speed, 9.7 vol % styrene and 8.34 mM $K_2S_2O_8$. [a] Averaged over > 100 spheres.

2.2.2: Synthesis of Powdered 3DOM Materials

2.2.2a: Method Development

Polystyrene spheres of size 200 – 600 nm were used as templates to form 3DOM structures with periodicities ranging from around 150 – 500 nm.[99] By centrifugation, the spheres were packed into cubic close packed arrangements, and infiltrated with liquid precursors. The voids within the CCP opal structure are filled by capillary action of precursors, followed by hydrolysis and solidification. Silicon and zirconium hydroxides are formed by hydrolysis of the precursors. If hydrolysis is too fast, full penetration of the interstices in the template will not be achieved, hence control of

the hydrolysis rate is important for the formation of good quality photonic structures.[180] Adjusting the pH of a precursor mix can also be used to control the rate of condensation. On calcination, the template is removed and further condensation occurs to form the oxides, yielding coloured 3DOM SiO_2 and ZrO_2 materials as judged by SEM, TEM and DRUVS. Using 1 g PS powder and 3 mL Si/Zr precursor, yields were typically 50 – 150 mg for 3DOM SiO_2 and 150 – 250 mg for 3DOM ZrO_2.

By eye, all photonic samples exhibited colours, unlike their bulk counterparts. Reflectance measurements show photonic stop bands due to the ordered modulation of refractive index within the structure. A range of synthetic conditions were attempted in order to produce high quality 3DOM materials with intense stop bands.

A typical synthesis employs the impregnation of a layer of polystyrene by alkoxide diluted by alcohol, followed by calcination to remove the template. For 3DOM SiO_2 formation, tetraethyl-orthosilicate (TEOS) is used as Si source, with calcination at 500 °C for 10 hours (ramp rate 2 °C min^{-1}) to remove the template. Typical yields were 50 – 150 mg of opalescent 3DOM SiO_2 powders. Under these synthesis conditions, an amorphous microstructure is expected.[199] Literature reports suggest neat alkoxide can be used to form 3DOM materials,[180] however when this was attempted using TEOS no pores were observed after calcination. This is likely due to the viscosity of the liquid, preventing full penetration of the opal network over the timescales used. When processed, high local concentrations of alkoxide in and around the template form a thick layer of SiO_2 on the surface of the polystyrene.[180] This prevents escape of trapped gases, resulting in a non-porous material as judged by SEM. Further experiments utilised mixtures of TEOS with ethanol, water and HCl. Table 4 details the conditions used and the periodicities obtained from four precursor solutions. The quality of 3DOM structure was analysed by comparison of DRUVS spectra and SEM images (Figure 18 and Figure 19).

Method	Periodicity / nm	Wall Thickness / nm	λ_{111} position / nm	Precursors (ratio by volume)
SiO_2-A	N/A	N/A	N/A	TEOS
SiO_2-B	424±20	65±9	742	TEOS:EtOH, 1:1
SiO_2-C	407±16	69±8	719	TEOS:EtOH:H_2O:1M HCl, 6:4:3:1
SiO_2-D	415±16	59±9	702	TEOS:EtOH:H_2O:16M HCl, 6:4:3:1

Table 4: Reaction conditions for 3DOM SiO_2 formation using 492 nm PS spheres as a template.

The difference in precursor mix affects the rate of hydrolysis and polymerisation of the hydroxide network within the voids of the template. The methods **SiO_2-B**, **SiO_2-C** and **SiO_2-D** all produced porous samples, as judged by SEM and DRUVS analysis. The difference in the stop band position for these samples observed by DRUVS can be explained in terms of the differences in periodicity and wall thickness of the materials. Using method **SiO_2-D**, the material produced appeared disordered on the macroscale, displaying ordered porous regions 10 – 100's of microns wide interspersed with non-porous silica regions. The limited ordering of this sample is confirmed by the low-intensity stop band in the DRUVS spectrum. The non-porous regions result from premature hydrolysis of the TEOS before it fully permeates the interstices of the colloidal crystal, suggesting that this pH is not optimal for full penetration of the interstitial sites before precipitation of the alkoxide occurs. The methods **SiO_2-B** and **SiO_2-C** produce well ordered materials as judged by SEM analysis, with no discernible differences between them. From DRUVS, the intensity of the photonic stop band is enhanced for method **SiO_2-C** in comparison to **SiO_2-B**. Due to the surface characterising nature of SEM imaging it is impossible to probe the ordering in the centre of the particles, variation of which may explain the difference in the stop band intensity. The conditions described for method **SiO_2-C** were used in future syntheses of 3DOM SiO_2.

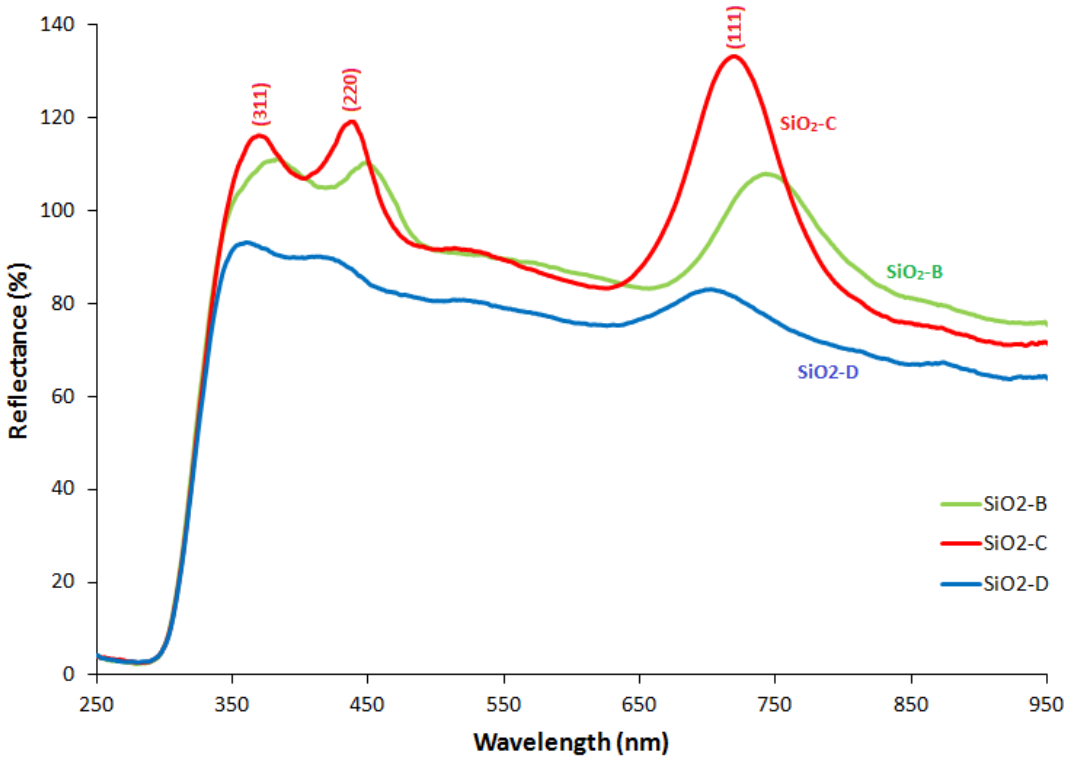

*Figure 18: DRUVS spectra of 3DOM SiO_2 prepared from different precursor mixes. The Miller indices of the photonic crystal planes for **SiO_2-C** are shown in brackets.*

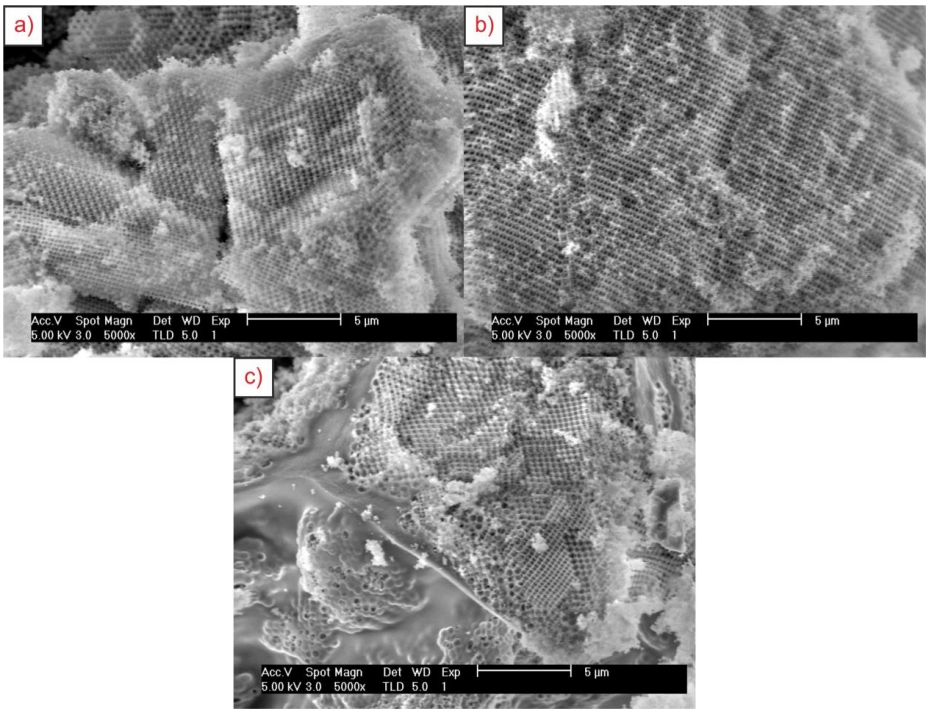

*Figure 19: SEM images of 3DOM SiO_2 prepared using different precursor mixes. (a) **SiO_2-B**, (b) **SiO_2-C**, (c) **SiO_2-D**.*

For synthesis of 3DOM ZrO_2, impregnation was achieved from a 1:1 volume ratio of zirconium acetate to methanol. Composites were calcined at 450 °C for 4 hours (ramp rate 1 °C min^{-1}). Typical yields were from 150 – 250 mg of coloured 3DOM ZrO_2 powder. As the template is removed, crystallisation of the precursors occurs to form a dense wall structure.[199] Higher ramp rates as with silica were used initially, but were found to cause collapse of the 3DOM structure. This method produced high quality photonic structures as evidenced by the intense colours of the powders (Figure 24b), SEM images (Figure 21) and intense stop bands (Figure 23b). Different precursor mixes involving addition of acid and water, and different ratios of methanol to zirconium acetate were investigated, but showed similar photonic architectures as judged by SEM and DRUVS.

Due to the amounts of 3DOM materials obtained in a typical synthesis, for nanoparticle deposition experiments multiple batches of 3DOM support were sometimes used to obtain a wide range of loadings. Batches with similar periodicity, photonic stop band position and wall fill factor were used. In the following chapters, full characterising data including these parameters will be included for the individual materials used for nanoparticle deposition. In the following section, characterising data is presented for individual batches of 3DOM SiO_2 and ZrO_2 based on 3 different sized templates.

2.2.3: Characterisation

2.2.3a: Powder X-Ray Diffraction

Powder XRD was used to characterise the crystal phases of the 3DOM materials (Figure 20). For SiO_2, no crystalline peaks are observed, but all samples analysed show a broad feature centred at 21.5 ° 2θ. This is typical of SiO_2 calcined at these temperatures. ZrO_2 PXRD patterns can be indexed to tetragonal ZrO_2, JCPDS file number 01-079-1763. The peaks show line broadening suggesting nanoparticle size.

The crystallite size of nanomaterials can be estimated from line broadening of PXRD peaks using the Scherrer equation (Equation 33, section 5.2.1). For the peak at 30.5

° 2θ, the FWHM of 1.6 ° was used to calculate an estimated crystallite size of 5.1 nm for 3DOM ZrO_2.

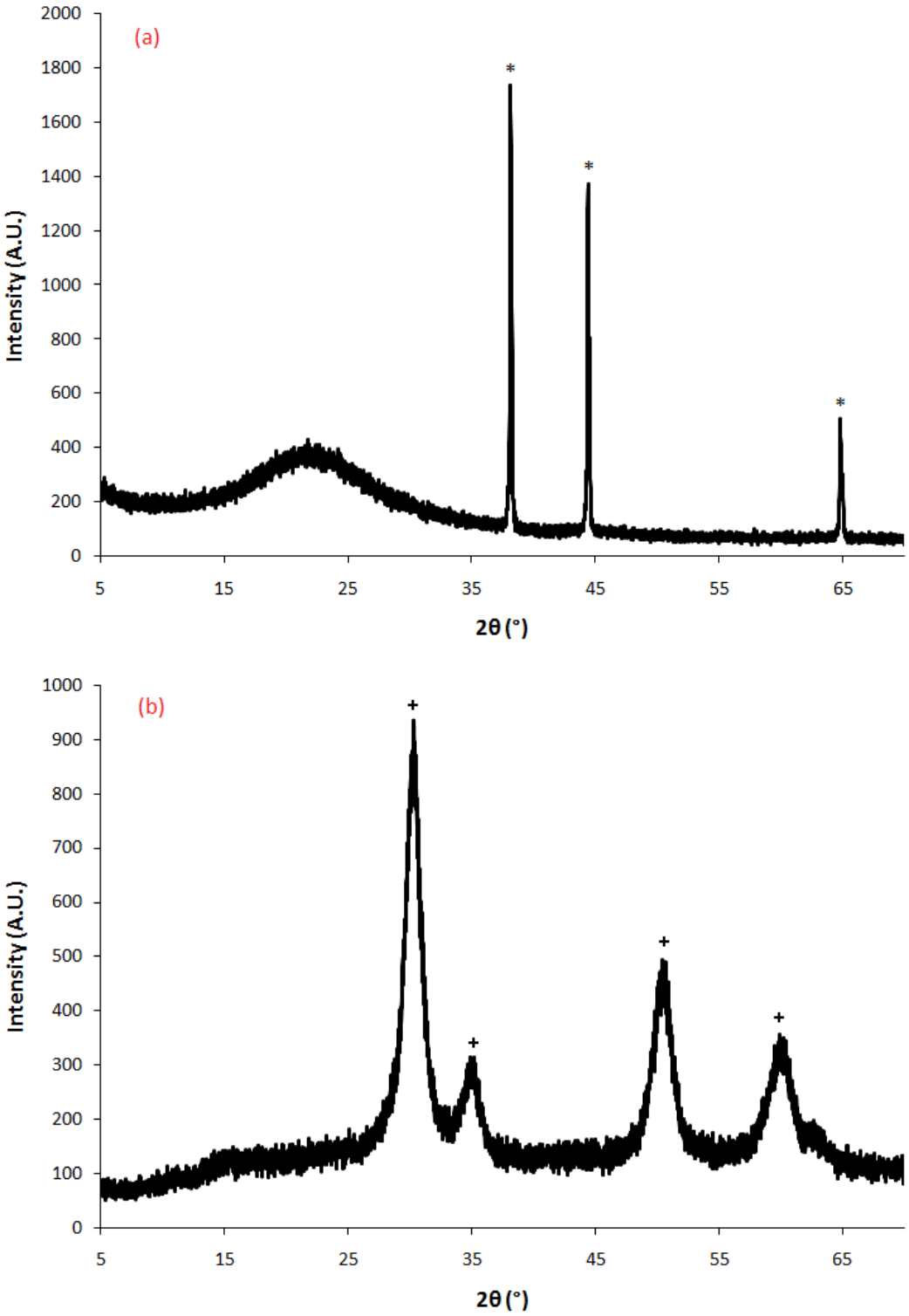

*Figure 20: Powder XRD patterns for 3DOM SiO_2 and ZrO_2. (a) 3DOM SiO_2, * = Al holder, (b) 3DOM ZrO_2, + = tetragonal ZrO_2, JCPDS 01-079-1763.*

2.2.3b: Electron Microscopy

SEM images of 3DOM SiO_2 and ZrO_2 templated from 402, 492 and 601 nm spheres are shown in Figure 21. The pores sizes, wall thicknesses and calculated filling factors of these materials are listed in Table 5. On calcination of the composite material, the silica/zirconia network in the voids of the material condenses and contracts, resulting in periodicities smaller than the diameter of template sphere used. The shrinkage is greater for 3DOM ZrO_2, due to sintering of the grains which compose the microcrystalline walls. The contraction observed is similar to values observed in the literature for SiO_2 (15 %) and ZrO_2 (34 %).[99] As the template size is increased, the wall size in the 3DOM material is also seen to increase as a result of the larger interstitial voids in the template. For all 3DOM SiO_2 samples used in this work, fill factors between 5 – 9 % were calculated, compared to 15 – 17 % for 3DOM ZrO_2 samples. Comparable wall fill factors are reported in the literature.[99] Samples were denoted yyy-MO_2, where yyy and MO_2 are the periodicity and chemical identity of the photonic crystal structure respectively.

Material	Template Sphere Size / nm	3DOM Periodicity / nm	Wall Thickness / nm	Fill Factor ϕ^a / %
SiO_2	402	351±15	56±9	6.8
SiO_2	492	395±12	58±10	8.0
SiO_2	601	503±16	67±10	8.2
ZrO_2	402	271±20	47±7	16.8
ZrO_2	492	343±17	60±9	17.0
ZrO_2	601	412±23	69±9	16.7

Table 5: Periodicity, wall thickness and fill factors of 3DOM SiO_2 and ZrO_2.

[a]calculated using Equation 9 (Section 2.2.3c).

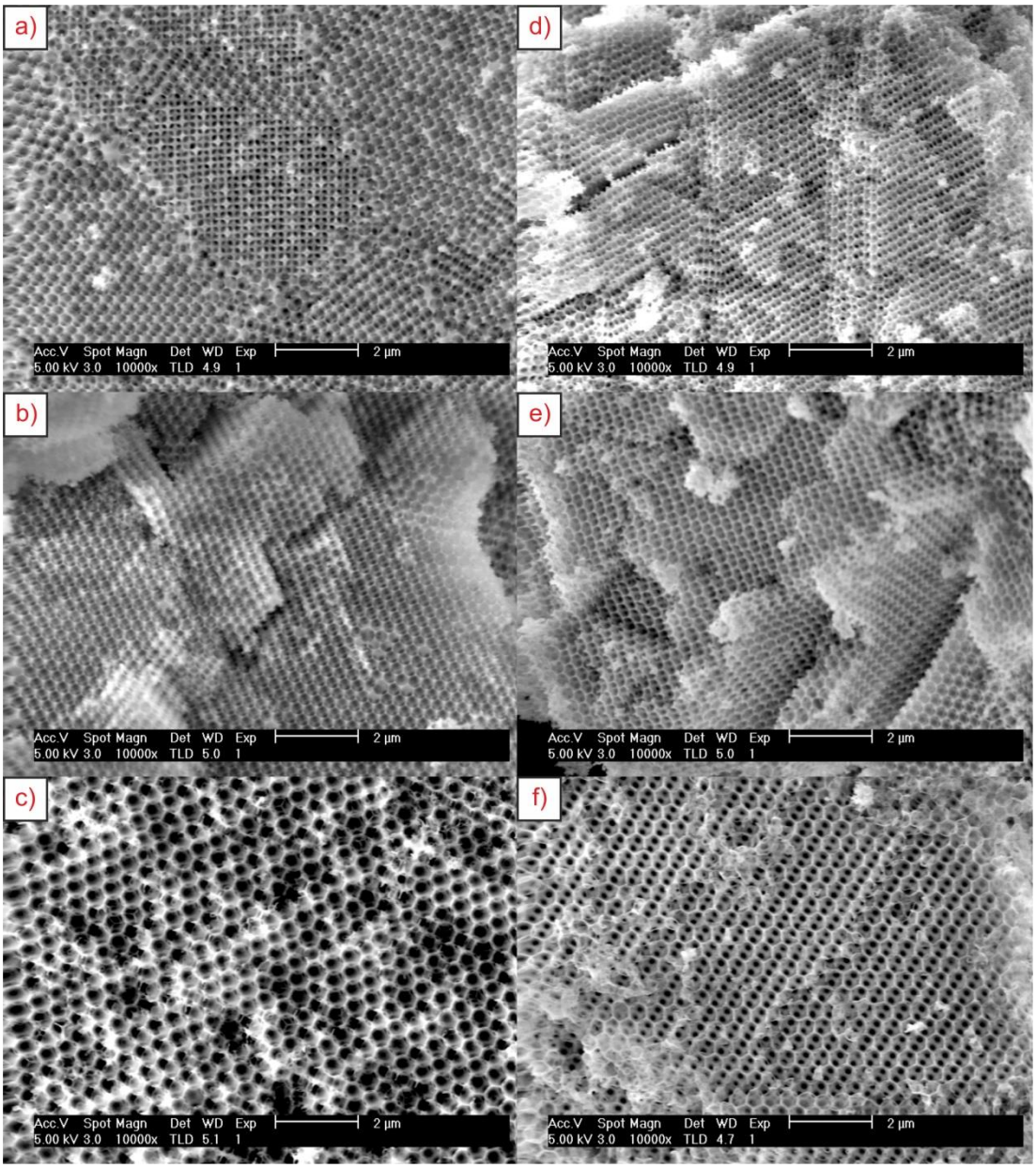

*Figure 21: SEM images of (a) – (c) 3DOM **351-SiO_2**, **395-SiO_2** and **503-SiO_2** templated from 402, 492 and 601 nm PS spheres respectively, (d) – (f) 3DOM **271-ZrO_2**, **343-ZrO_2** and **412-ZrO_2** templated from 402, 492 and 601 nm PS spheres respectively.*

TEM was also used to image the 3DOM materials (Figure 22). Consistent with the PXRD data, the walls in 3DOM SiO_2 are amorphous judged by both the absence of lattice fringes and the broad features in electron diffraction patterns. For 3DOM ZrO_2, single crystalline particles are observed at high magnification. The lattice spacings of the circled particles in Figure 22b were measured to be 2.59 Å, corresponding to the (200) crystal plane. An indexed electron diffraction pattern for

3DOM ZrO_2 is shown in Figure 22c. The average particle size over 200 particles was measured to be 3.47 ± 0.33 nm, similar to the crystallite size estimated by PXRD (5.1 nm). Literature studies have shown that small grain sizes are important for observation of powders coloured by Bragg diffraction of light due to minimisation of random scattering of light that occurs for larger grains.[99]

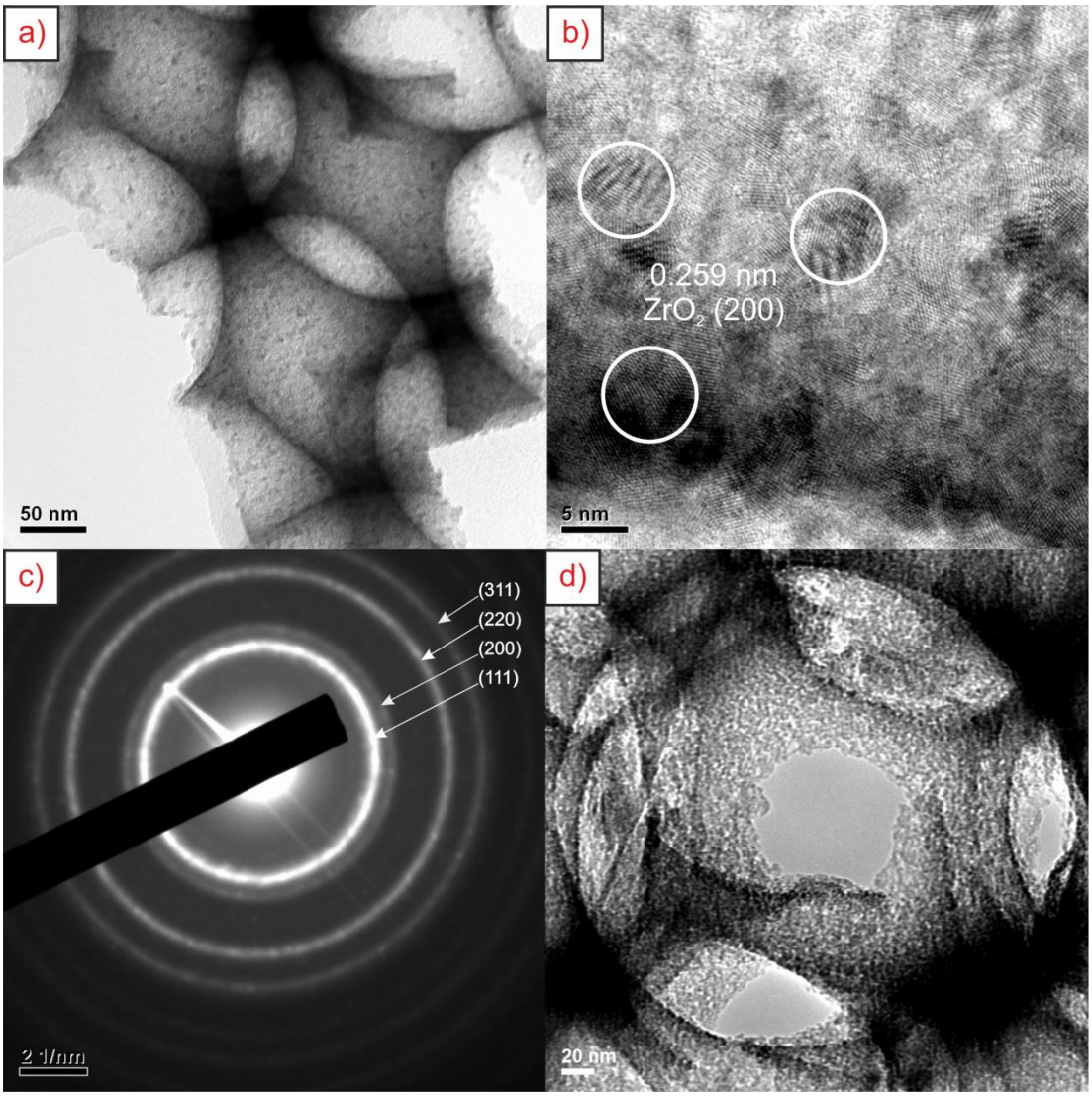

Figure 22: TEM images of 3DOM SiO_2 and ZrO_2. (a), (b) ***271-ZrO_2****, with circles showing indexed lattice fringes on crystalline walls, (c) electron diffraction pattern of region in (b), (d)* ***351-SiO_2****.*

2.2.3c: Diffuse Reflectance UV-Vis Spectroscopy

Diffuse reflectance spectroscopy was employed to characterise the photonic structure of these materials. Figure 23 shows the diffuse reflectance spectra for 3DOM SiO_2 and ZrO_2 as a function of increasing template size. The positions of the observed photonic stop bands are explained using the Bragg-Snell equation:

$$\textit{Equation 9} \qquad \lambda = \frac{2d_{hkl}}{m}[\phi n_{wall} + (1-\phi)n_{void}]$$

Where λ is the stop band position, m is the order of diffraction, d_{hkl} is the lattice plane separation for a plane with indices (hkl), ϕ is the fill factor of the walls, and n represents the refractive index of the walls and voids. The lattice plane separation is related to the periodicity D and unit cell parameter a for the material by Equation 10:

$$\textit{Equation 10} \qquad d_{hkl} = \frac{a}{\sqrt{h^2+k^2+l^2}} = \frac{D\sqrt{2}}{\sqrt{h^2+k^2+l^2}}$$

Table 6 lists the positions of the photonic stop bands observed in Figure 23. A red-shift of the stop band is observed for materials with larger pores, in agreement with Equation 9. The SiO_2 sample with a periodicity of 503 nm, denoted **503-SiO_2**, shows three stop bands at 454, 540 and 881 nm. These represent diffraction of light from different lattice planes within the photonic crystal.[99]

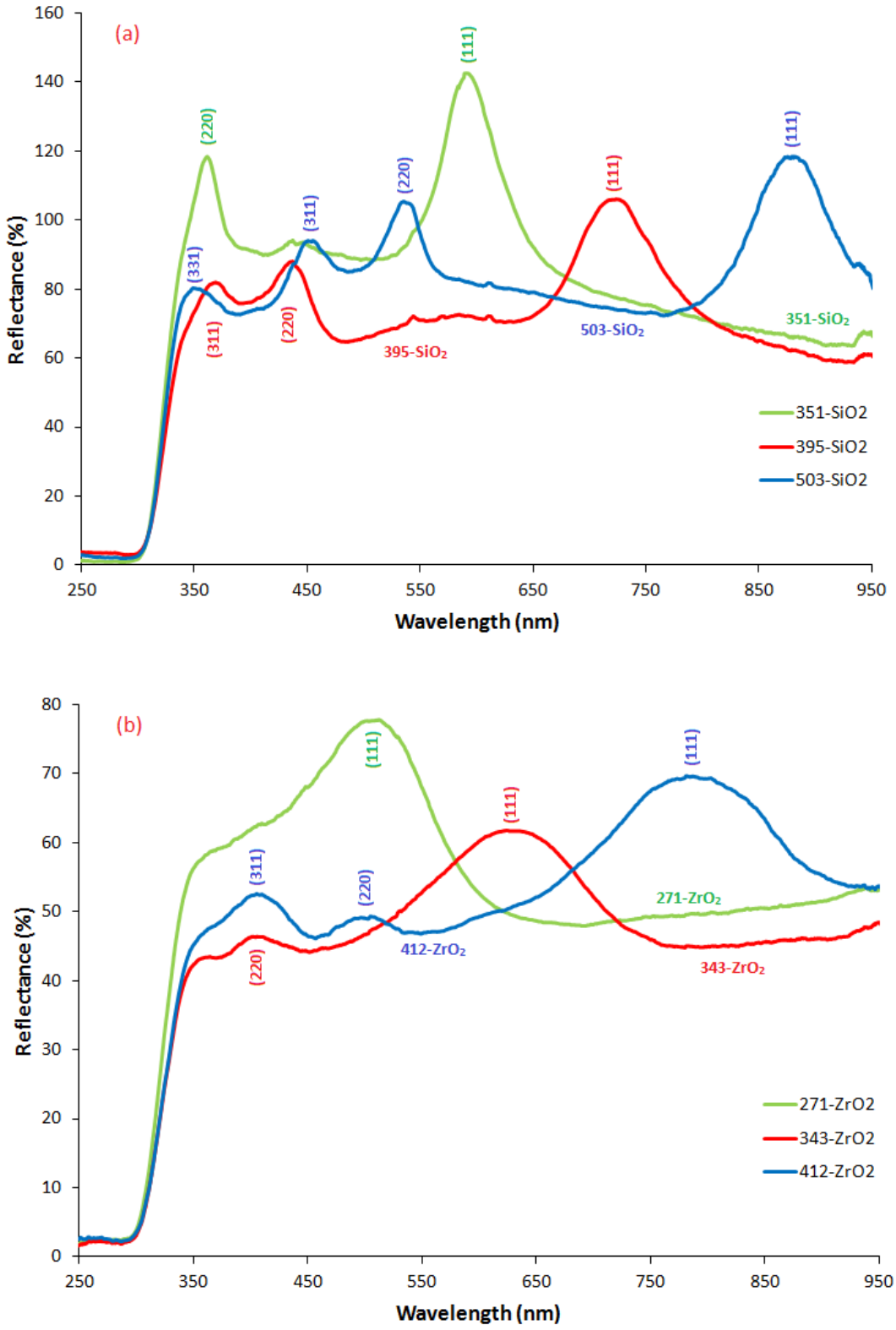

Figure 23: DRUVS spectra of (a) 3DOM SiO_2 and (b) 3DOM ZrO_2 samples with different periodicities. Numbers in brackets indicate the Miller indices of the crystal plane.

Material	Periodicity / nm	**(111)** stop band position / nm	Minor stop band positions / nm
351-SiO_2	351±15	591	363 **(220)**
395-SiO_2	395±12	724	370 **(311)**, 435 **(220)**
503-SiO_2	503±16	881	353 **(331)**, 454 **(311)**, 540 **(220)**
271-ZrO_2	271±20	510	N/A
343-ZrO_2	343±17	629	405 **(220)**
412-ZrO_2	412±23	790	408 **(311)**, 503 **(220)**

Table 6: Stop band positions for 3DOM SiO_2 and ZrO_2 templated from 406, 500 and 604 nm polystyrene spheres. Miller indices of the crystal planes are assigned in bold.

For an FCC packed array of pores, only reflections from planes with all even or all odd h, k, l, are allowed. For electromagnetic radiation interacting with other planes within the crystal, destructive interference occurs, and no reflection is observed. (111), (200), (220) and (311) are four possible Miller indices for planes which will show a reflection. From Equation 10, it follows that d_{hkl} is inversely proportional to the square root of the sum of the Miller indices. Compared to the (111) plane, the (200), (220), and (311) planes are expected to be observed at smaller wavelengths, with ratios as detailed in Table 7.

Miller indices	Theoretical ratio to (111) plane	**503-SiO_2** ratios to (111) plane
(111)	1	881nm, 1
(200)	$\sqrt{3}/\sqrt{4}$ = 0.866	N/A
(220)	$\sqrt{3}/\sqrt{8}$ = 0.612	540 nm, 0.612
(311)	$\sqrt{3}/\sqrt{11}$ = 0.522	454 nm, 0.515
(331)	$\sqrt{3}/\sqrt{19}$ = 0.397	353nm, 0.401

*Table 7: Miller index assignments for stop bands exhibited by **503-SiO_2** sample (see Figure 23)*

The Miller index assignments in Table 6 and Figure 23 were deduced using Equation 10. From the reflectance spectrum of **503-SiO_2**, the major stop band at 881 nm can be defined as the (111) plane, as it is the most intense and longest wavelength peak. The ratios of the positions of the minor stop bands to the position of the (111) reflection are 0.612 and 0.515, agreeing well with the theoretical values, hence the stop bands at 540 and 454 nm can be assigned as the (220) and (311) photonic crystal planes respectively. The stop bands in all other materials were assigned using the same method.

3DOM SiO_2 appears colourless in the bulk powder, due to diminished reflection of stop band wavelengths by random scattering of light from the amorphous walls. When illuminated, colours can be observed, which vary depending on whether the light is reflected or transmitted. In reflected light, colours corresponding to stop band wavelengths are observed. Scattering is also decreased for thin films, hence the colours observed in Figure 24a. In transmitted light, the perceived colour of the powder is that of the light which is allowed to propagate within the photonic crystal. These properties of 3DOM SiO_2 materials are of interest for optical filtering applications.[99]

In the images of 3DOM ZrO_2 shown, the colours of the samples are the same irrespective of light irradiation. This is due to the structure of the walls, consisting of packed nanoparticles which can scatter light in a non-random fashion.[99] This results in brightly coloured bulk powders as illustrated in Figure 24b. The small grain size is important for the observation of coloured samples, as described above.

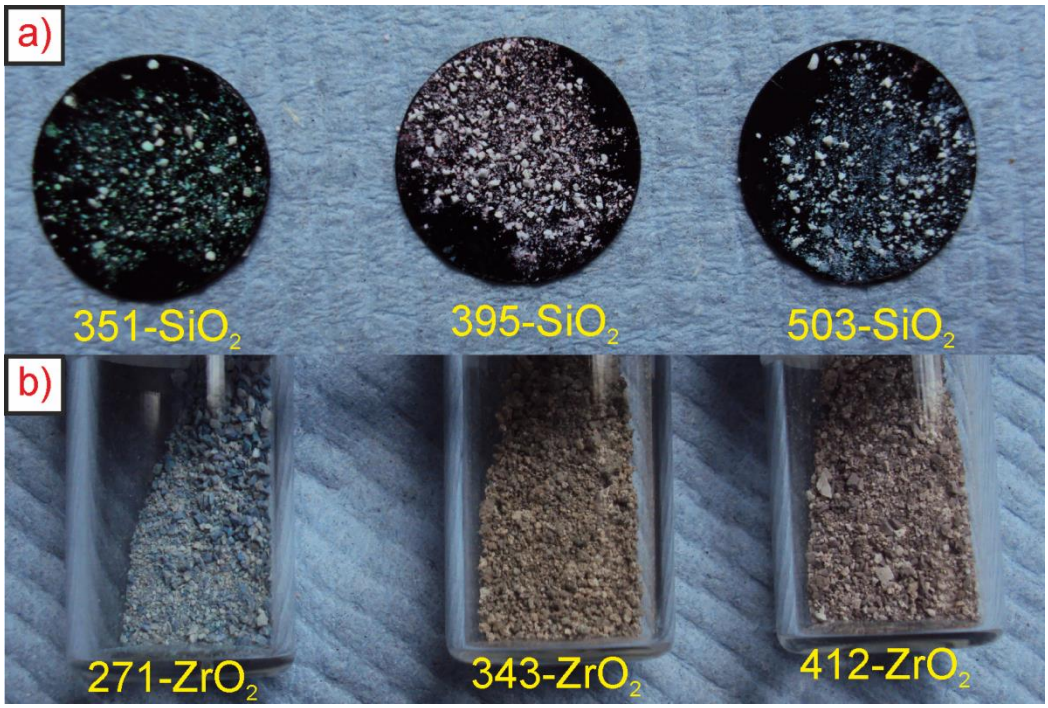

Figure 24: Photographs of (a) 3DOM SiO_2 and (b) 3DOM ZrO_2, showing vibrant colours due to the photonic structure.

2.2.3d: Effect of Solvents on the Reflectance Spectra

The refractive indices of the components within the photonic crystal system are an important factor in the position of the stop band, as described by Equation 9. In a dry powder the photonic stop band is well defined as the voids are filled with air, which has a refractive index of 1. By filling the voids with a liquid which has a greater refractive index, a red shift in stop band position occurs, along with a decrease in the intensity of the stop band due to the reduced refractive index contrast between the walls and the voids. As this shift is accompanied with a change in colour, addition of solvent can be used as a facile empirical test to determine whether a newly synthesised sample displays photonic properties. All photonic samples synthesised here show an instant colour change on addition of solvent. Figure 25 shows the diffuse reflectance spectra of a **319-ZrO_2** sample, templated from **PS-7** spheres, both dry and in the presence of ethanol. The stop band moves from 618 nm to 776 nm on addition of solvent. Using the periodicity of

this sample, 319 nm, and the refractive index of ZrO_2, n_{ZrO2} = 2.2, Equation 9 was used to calculate a fill factor (ϕ) of 15.6 %. Addition of ethanol with refractive index 1.36 would be expected to shift the stop band to 775.7 nm, in good agreement with the observed shift. Evolution of stop band position as a function of solvent refractive index has been reported for a variety of solvents in the literature, showing a linear relationship as predicted by Equation 9.[99, 200]

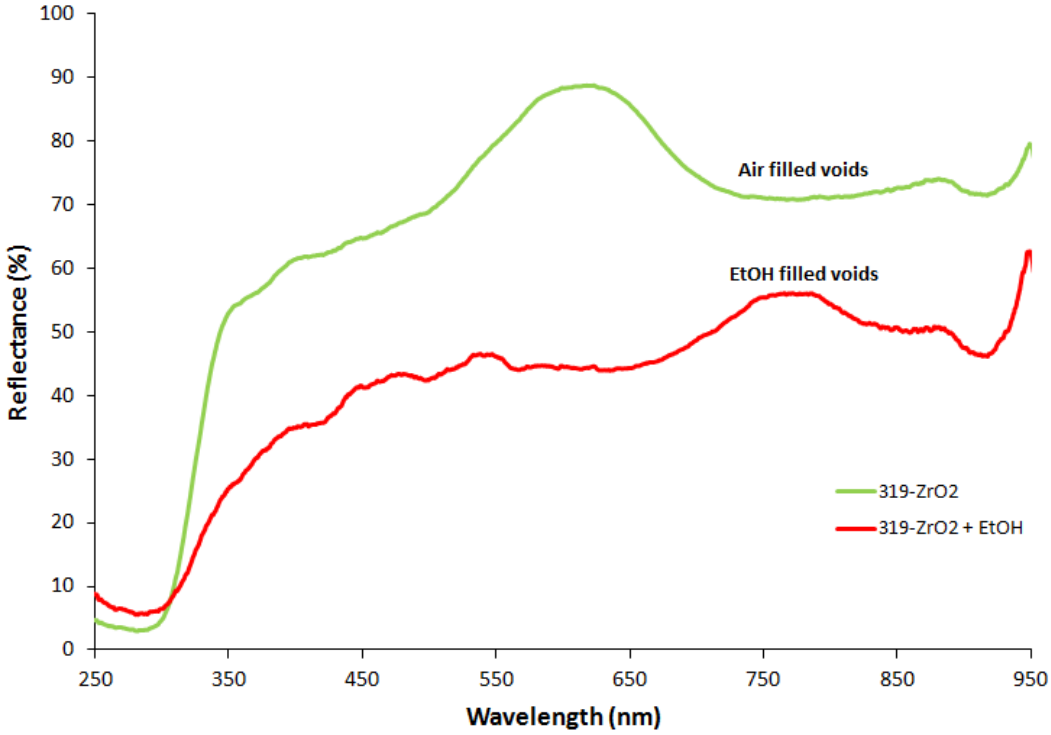

*Figure 25: DRUVS spectra of **319-ZrO₂** dry (green line) and wet (red line).*

2.2.3e: Surface Area Analysis

The surface areas of 3DOM SiO_2 and ZrO_2 were measured from nitrogen adsorption/desorption porosimetry using BET theory. In this technique, the adsorption and desorption of nitrogen molecules at the surface of materials is analysed as a function of pressure at a constant temperature of 77.4 K. Adsorption/desorption isotherms for SiO_2 and ZrO_2 are shown in Figure 26. The shapes of the graphs resemble a type II adsorption isotherm as defined by IUPAC.[201] The steady slope as the pressure increases corresponds to adsorption of a

monolayer of nitrogen onto the porous surface, with a sudden increase in adsorption due to capillary condensation of nitrogen as the pressure approaches saturation (P/P_0 = 1). The desorption trace follows that of adsorption, with no discerning features such as hysteresis loops as observed for mesoporous materials. This corroborates the presence of a network of larger pores as evidenced by SEM.

Surface areas of 3DOM SiO_2 and ZrO_2 were calculated from the volume adsorbed in the low relative pressure (P/P_0) region of the adsorption/desorption isotherm using BET theory (section 5.2.5), and are listed in Table 8. Multiple samples were tested and gave similar values regardless of the batch in which they were synthesised, showing the reproducibility of the method. The surface areas of 3DOM ZrO_2 samples are much lower than 3DOM SiO_2 samples, suggesting the amorphous walls in 3DOM SiO_2 have additional microporosity. The surface areas obtained were comparable to literature values. For some literature reported 3DOM SiO_2 materials higher surface areas are observed (173 – 231 $m^2\ g^{-1}$), however the adsorption/desorption isotherms show hysteresis implying mesoporous walls.[180] Similar values to this work have been reported in the literature for 3DOM ZrO_2, and other crystalline 3DOM materials.[180, 202]

Sample	BET Surface Area / $m^2\ g^{-1}$
395-SiO_2	91 ± 1
271-ZrO_2	20.6 ± 0.3

Table 8: BET surface areas of 3DOM SiO_2 and ZrO_2.

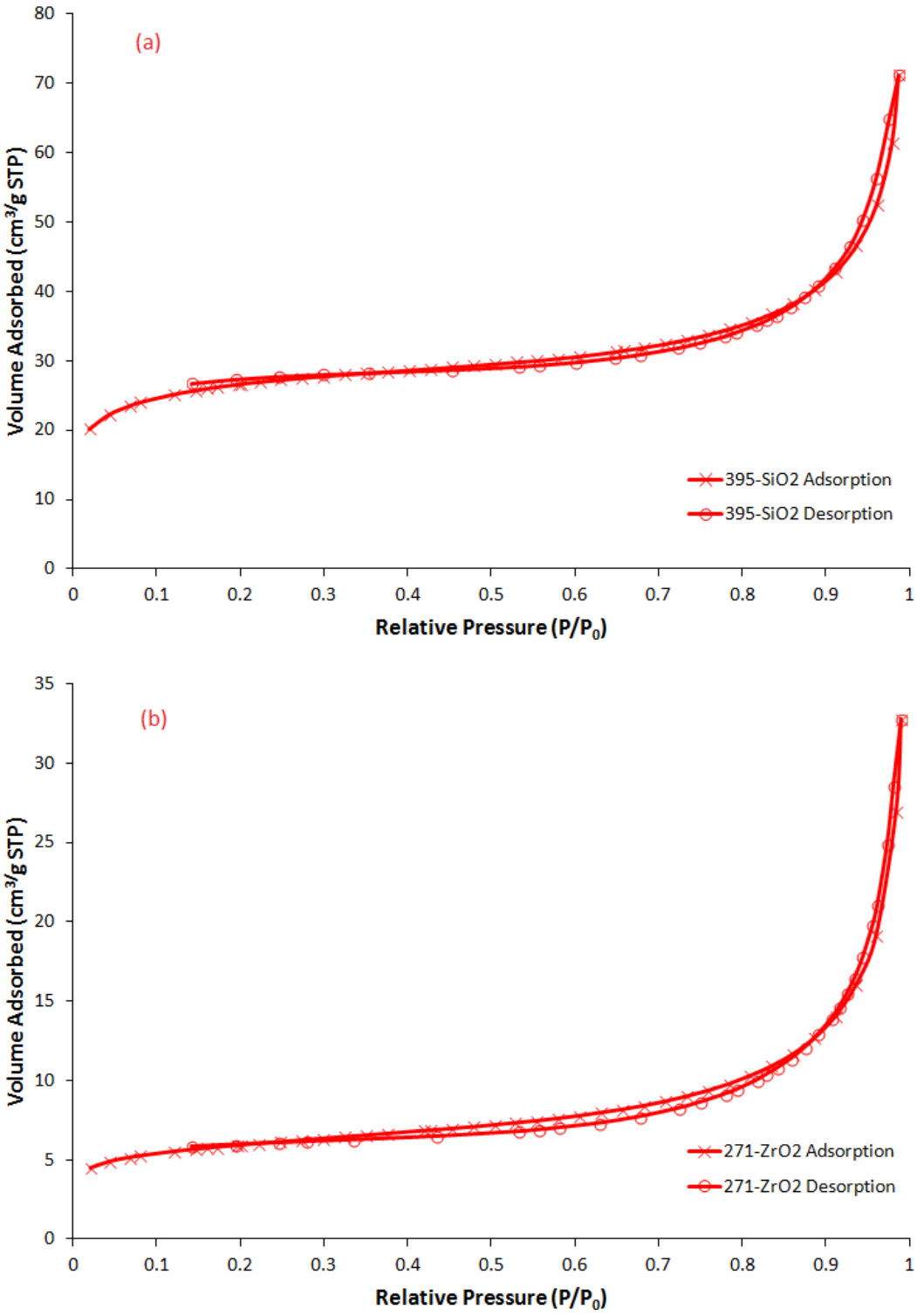

Figure 26: Nitrogen adsorption/desorption isotherm for (a) ***395-SiO_2,*** *and (b)* ***271-ZrO_2.***

With relevance to future chapters, fully characterised samples of **395-SiO_2** and **271-ZrO_2** were used for method development to study deposition of pre-synthesised nanoparticles within porous materials. 3DOM ZrO_2 materials with different periodicity and well defined photonic stop bands were identified as targets for CdS and TiO_2 deposition for photocatalysis.

2.2.4: Synthesis of 3DOM Transparent Conducting Oxides

As discussed in section 1.1.2g, recombination in semiconductors makes their use as macroscopic electrodes problematic. In the literature, 3DOM electrodes have been fabricated from transparent conducting oxide (TCO) materials.[126, 203] The deposition of nanoparticles on the surface of these materials is of interest for photoelectrochemical fuel production. Compared to a 3DOM semiconductor electrode, enhanced photocurrents can be produced due to efficient conductivity of the support, resulting in decreased recombination.

The synthesis of 3DOM fluorine doped tin oxide (3DOM FTO) glass has been reported in the literature.[204] This synthetic procedure was modified, with the aim of producing high quality 3DOM films as deposition targets for nanoparticle photocatalysts. The synthesis and characterisation of the 3DOM FTO films on FTO coated glass is presented in the following section.

2.2.4a: Deposition of PS films

Polystyrene films were deposited on fluorine doped tin oxide (FTO) substrates by a vertical deposition method. Colloidal polystyrene dispersions in water were evaporated at constant temperature over 1 – 3 days. As the solvent evaporates, the meniscus travels down the surface of the substrate, depositing polystyrene spheres by capillary forces as shown schematically in Figure 13 (section 2.1a). The attractive lateral capillary immersion forces between adjacent particles contribute to the formation of CCP sphere arrays.[205] The dispersion concentration was found to be

especially important for the deposition process. For high concentrations (>> 2 g L^{-1}), the films often flake off as they become too heavy due to gravity, whereas if the concentration is too low, the number of layers may be insufficient to form a photonic band gap which regulates light in all 3 dimensions. Dispersions containing around 2 g L^{-1} polystyrene were found to produce good quality films, and were further improved by addition of polyvinylpyrrolidone as per literature methods.[125] Photographs of polystyrene films are shown in Figure 27.

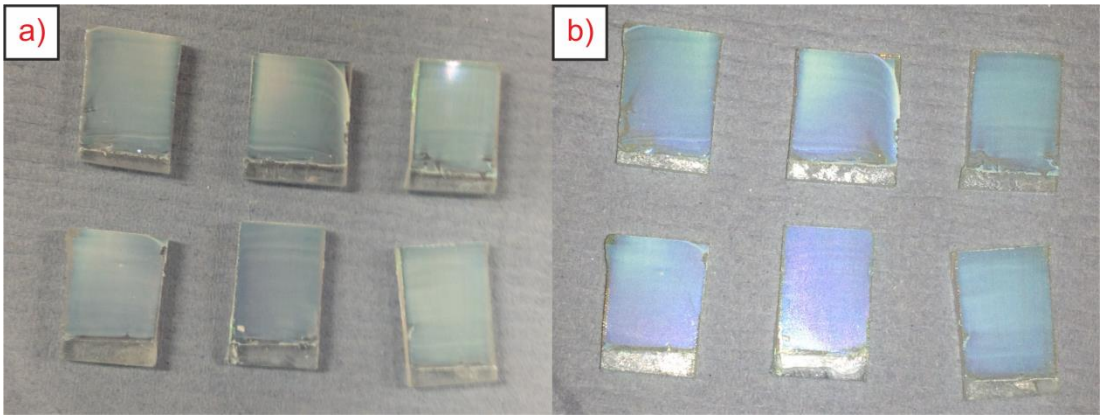

Figure 27: Photographs of polystyrene films on FTO glass. Taken (a) without flash and (b) with flash, showing opalescence of the film.

SEM images show the (111) plane is prevalent normal to the surface (Figure 28). Cracks can sometimes be seen on the film, which may be due to vibration or temperature fluctuations during film deposition, and is consistent with literature reports.[100] Samples were carbon coated prior to imaging, but charging of the surface under the electron beam is still prevalent. As a result, obtaining clear images of large areas is difficult, but the continuity of the film can be observed by scanning across the surface. By tilting the slides on the SEM stage, typical film thicknesses were measured to be around 10 – 12 µm, corresponding to around 20 – 24 layers of spheres.

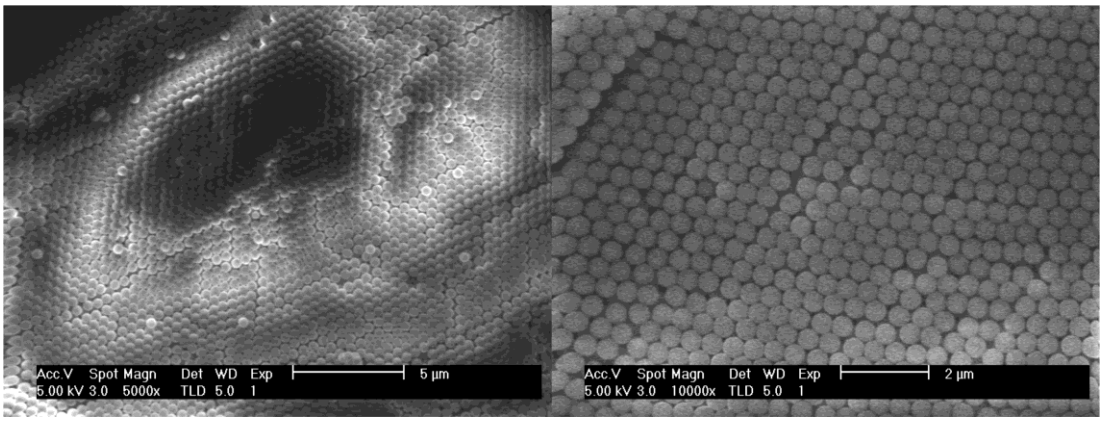

Figure 28: SEM images of polystyrene films on FTO glass. Lighting effects are due to charging of the surface under the electron beam.

2.2.4b: Infiltration of Polystyrene Films

Initial approaches to form 3DOM conducting films were attempted using indium doped tin oxide (ITO) nanoparticles, synthesised by literature procedures.[206] Packing of the nanoparticles into the interstitial sites of the polystyrene lattice was largely unsuccessful, occurring mostly due to gravity, with poor reproducibility across the slide. The inability to find a solvent which would disperse the hydrophilic PS spheres and organophilic ITO nanoparticles limited attempts at co-deposition approaches. Instead, liquid precursor routes were investigated for the synthesis of the more thermally stable FTO.

As FTO precursors, a mixture of ammonium fluoride and tin chloride pentahydrate was prepared as described in the literature.[204] Direct infiltration of the template was achieved by soaking the template film for 3 hours, followed by removal and calcination at 500 °C for 2 hours (1 °C min^{-1}) to form 3DOM FTO materials, as observed by eye and SEM (Figure 29 and Figure 30). Ordered porous regions were observed, within islands of around 10 – 20 µm in size. Islands are often observed in this type of film, forming due to contraction of the film on heating. Typically the separation between these regions is around 2 – 5 µm. The presence of a conducting layer beneath the film should allow transfer of charge across the electrode, making this a non-issue for the use of these materials in devices.

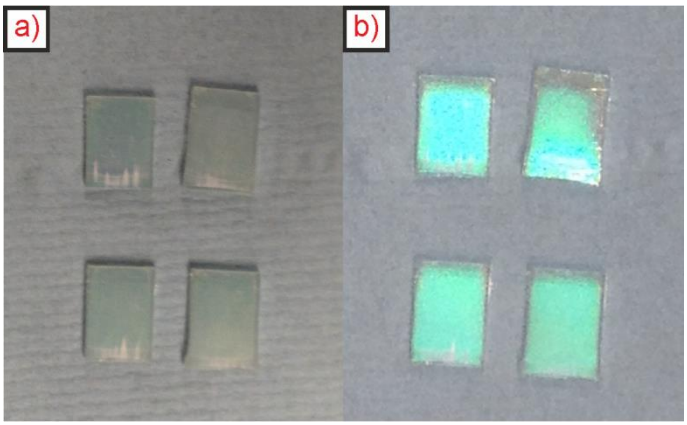

Figure 29: Photographs of 3DOM FTO films. Taken (a) without flash and (b) with flash, showing opalescence.

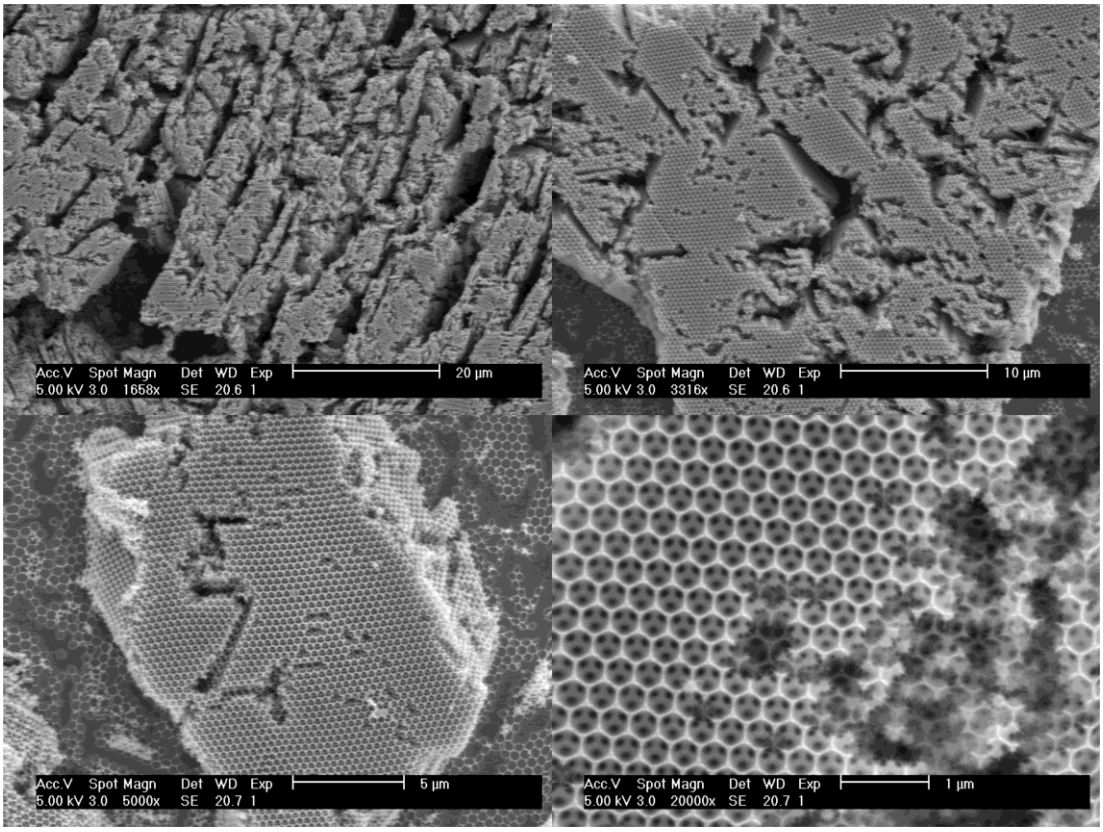

Figure 30: SEM images of 3DOM FTO films prepared by soaking PS films in ethanolic solution containing 0.1 M NH_4F and 0.2 M $SnCl_4$.[204]

To improve the quality of the films produced, a reduced pressure infiltration technique was utilised.[25,197] The colloidal crystal film was enclosed by another blank glass slide, and soaked in methanol prior to impregnation. The sandwiched slide was then placed directly into the precursor solution in a glass vial and soaked for 30 minutes. The vial was placed in a vacuum desiccator, and partially evacuated until

effervescence began to occur. At this point the tap was closed to leave a static atmosphere, and slowly draw the methanol out of the interstices in the packed polystyrene template, whilst in the process drawing in the precursor solution. Infiltration and hydrolysis of the precursor occurred over 3 hours, after which the vacuum was released, and the slides calcined at 500 °C for 2 hours (ramp rate 1 °C min^{-1}) to form 3DOM FTO films. Figure 31 shows SEM images of films produced via this method. Surface layers and grooves in the 3DOM film were visibly reduced in comparison to samples where soaking alone was used to infiltrate the interstices. The surface coverage in terms of the size and distance between the FTO islands was similar by both methods. By measuring the area of the islands in multiple SEM images, the fraction of surface covered with 3DOM FTO was determined to be approximately 65 %.

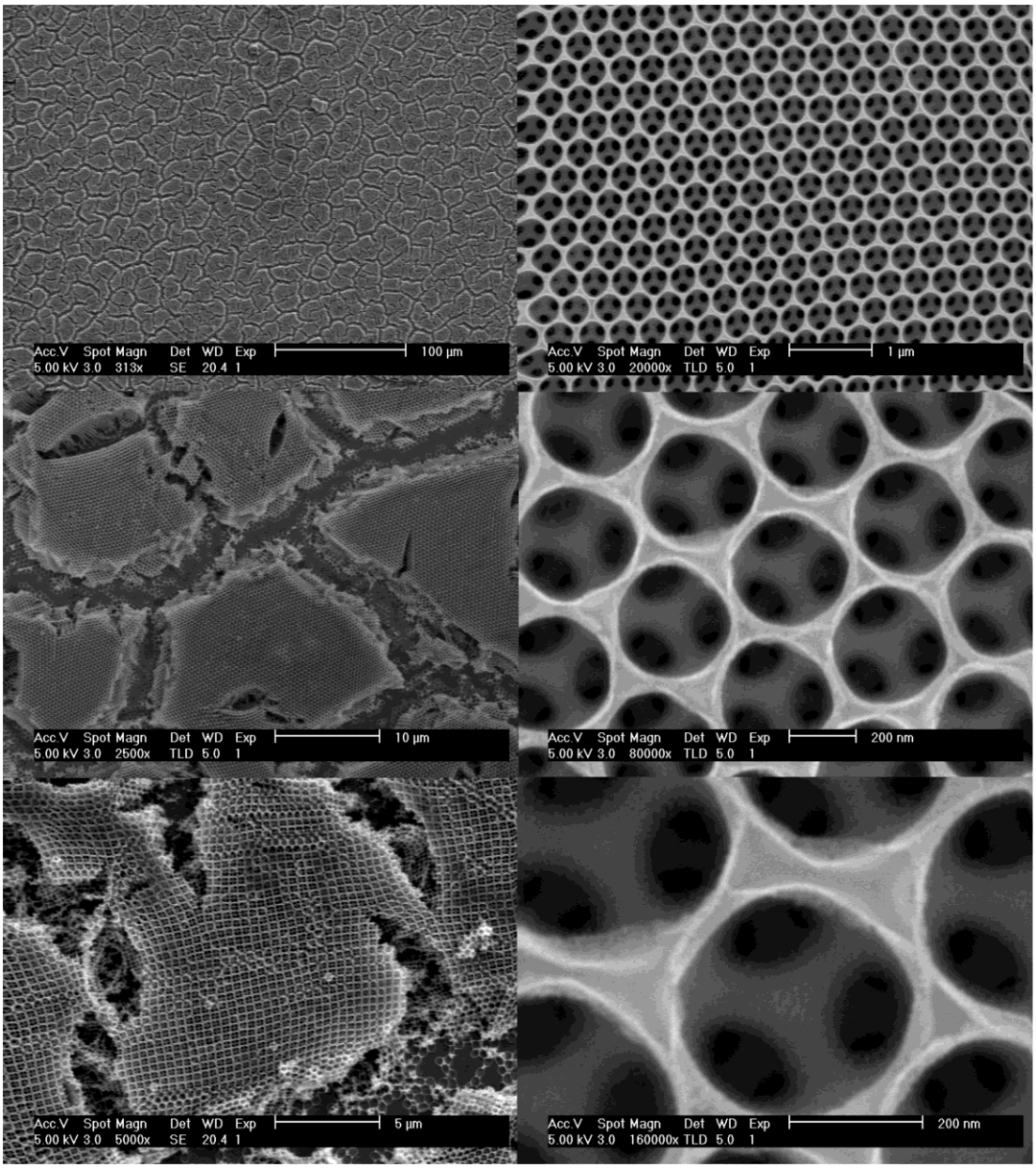

Figure 31: SEM images of 3DOM FTO films prepared by vacuum infiltration.

Figure 32 shows the DRUVS spectra of three 3DOM FTO films prepared in the same batch by vacuum infiltration. The stop band position and intensity is reproducible between samples. Only one peak is observed, corresponding to the (111) face which is aligned vertically in the majority of the sample. From the SEM images, in some regions (220) photonic crystal planes can be seen normal to the surface. The absence of a peak in the reflectance spectra in Figure 32 suggests that these defects are not widespread within these films, however in other samples peaks attributable to (220) photonic crystal planes have been observed.

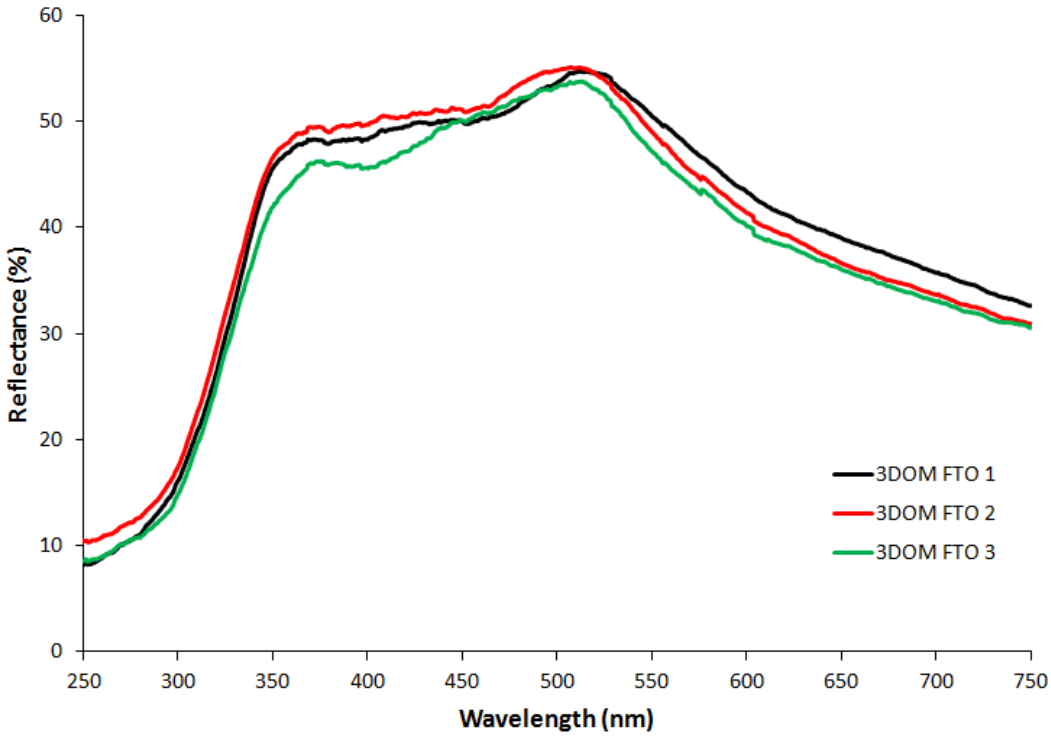

Figure 32: DRUVS spectra of three 3DOM FTO films on FTO glass, showing reproducibility of the stop band position.

The periodicity of these materials was measured to be 288 ± 14 nm. From this, the fill factor ϕ of 3DOM FTO samples was calculated to be 13 – 14 %. This is consistent with a larger contraction and increasing crystallinity in comparison to 3DOM SiO_2 samples, as observed in the synthesis of 3DOM ZrO_2.

TEM images of 3DOM FTO are displayed in Figure 33. The particle size of the grains composing the walls was measured to be 10.4 ± 1.8 nm. Electron diffraction showed diffraction rings with d_{hkl}-spacings matching tetragonal FTO (JCPDS file 5-0467).[204]

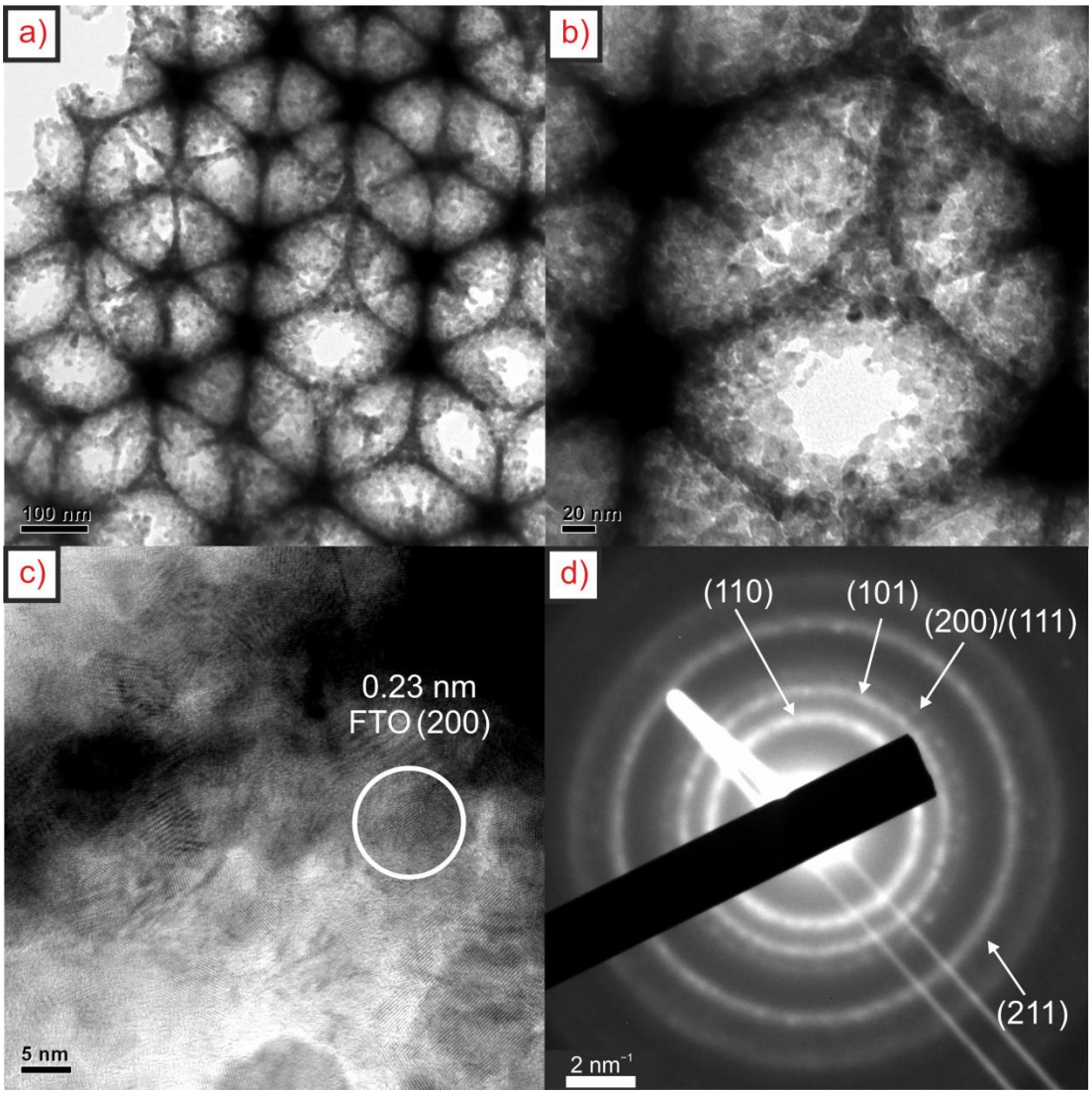

*Figure 33: (a) – (c) TEM images and (d) electron diffraction pattern of **288-FTO**. Assignments in (d) based on JCPDS 5-0467 and the literature.*[204]

2.2.5: Synthesis of Mesoporous Silica

The high surface area of mesoporous silica materials is attractive for applications in a variety of fields, including catalysis.[1, 163] The large surface areas provide more active sites for adsorption of reagents, which can result in an increased catalytic activity in comparison to a bulk material of similar composition. Nanoparticle loading in mesoporous materials has been used to form composite materials, typically from metal salts or vapour phase deposition processes as with 3DOM materials.[207, 208] In this study, mesoporous silica materials were fabricated in accordance with literature techniques.[209] Deposition of preformed nanoparticles within the mesopores was attempted, and will be detailed further in chapter 3. The synthesis and characterisation of these materials is discussed here.

Meso-SiO_2 was synthesised using TEOS as a silicon source, with Pluronic F127 as a template and ethylbenzene as a swelling agent. A yield of 1.13 g was obtained, corresponding to 87 % conversion of TEOS. Pluronic F127 is a triblock copolymer with formula $PEO_{106}PPO_{70}PEO_{106}$, where PEO is poly(ethylene oxide) and PPO is poly(propylene oxide), which can form micelles in solution due to the differences in solubility between the two blocks. Ethylbenzene infiltrates the hydrophobic PPO core and swells the micelles. Polymerisation of TEOS occurs in the aqueous phase around the micelles. Removal of the templating agent by calcination forms a highly ordered mesoporous material, with pore size reflective of the micelle diameter.

TEM imaging was used to analyse the materials (Figure 34), showing multiple layers of hexagonally packed pores. The average periodicity measured over 200 pores was found to be 16.9 ± 0.8 nm. Due to the 2D representations observed by TEM imaging, overlap of pore layers within the plane prevented the determination of wall thickness with high accuracy, however it was estimated to be around 4 nm.

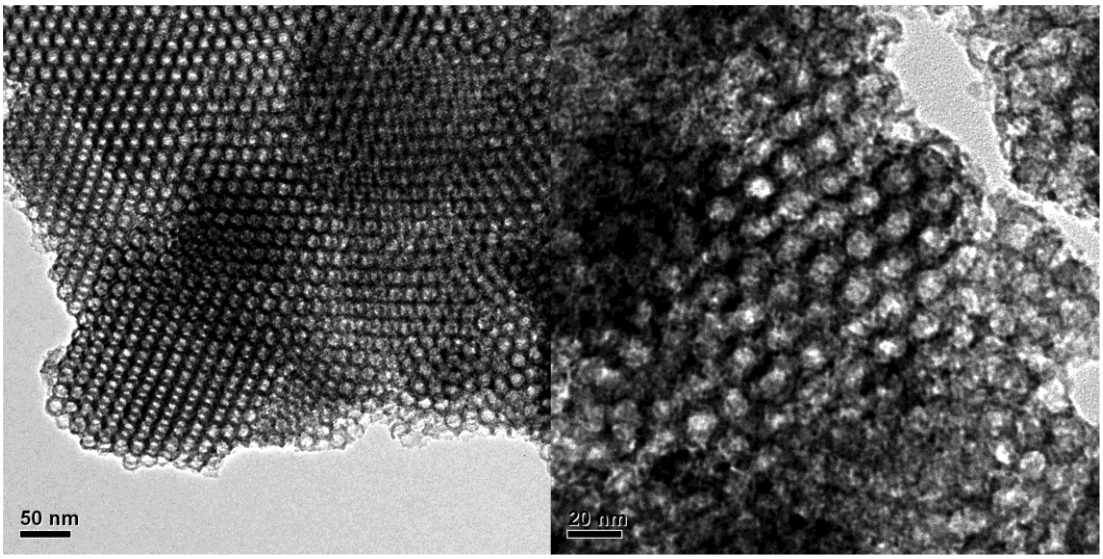

Figure 34: TEM images of ethylbenzene swollen ***Meso-SiO$_2$****.*

The surface area of **Meso-SiO$_2$** was measured by nitrogen adsorption/desorption porosimetry. The adsorption/desorption isotherm is shown in Figure 35, resembling a type IV isotherm with H2 hysteresis loop as classified by IUPAC.[201] As described above for 3DOM materials, the steady slope as the pressure increases corresponds to adsorption of a monolayer of nitrogen onto the porous surface, with a sudden increase in adsorption due to capillary condensation as the pressure approaches saturation. As the pressure is decreased, the volume adsorbed in the pores does not follow the adsorption trace, instead staying at a relatively steady state up until P/P_0 = 0.5. The sudden drop in adsorbed volume corresponds to emptying of the pores as the liquid evaporates.

The hysteresis loop observed in the adsorption/desorption isotherm is typical of mesoporous materials. An explanation for this effect is not fully known, however theories have been postulated based on the size and shape of the pores.[210, 211] For circular pores which are large in comparison to the windows between them, at high P/P_0 the pores are filled by capillary condensation. However, on desorption the small windows act as a bottleneck, and prevent emptying of the pores until the relative pressure is decreased. The surface tension of the liquid in the pores prevents the formation of bubbles at high relative pressure, and hence evaporation cannot occur.[211] The window size determines the relative pressure at which emptying of the pores occurs.[212] From the 0.05 to 0.3 P/P_0 region of the adsorption

branch, a surface area of 560.3 ± 7.4 m^2 g^{-1} was calculated using BET theory (see section 5.2.5). Similar surface areas have been reported in the literature.[209, 213]

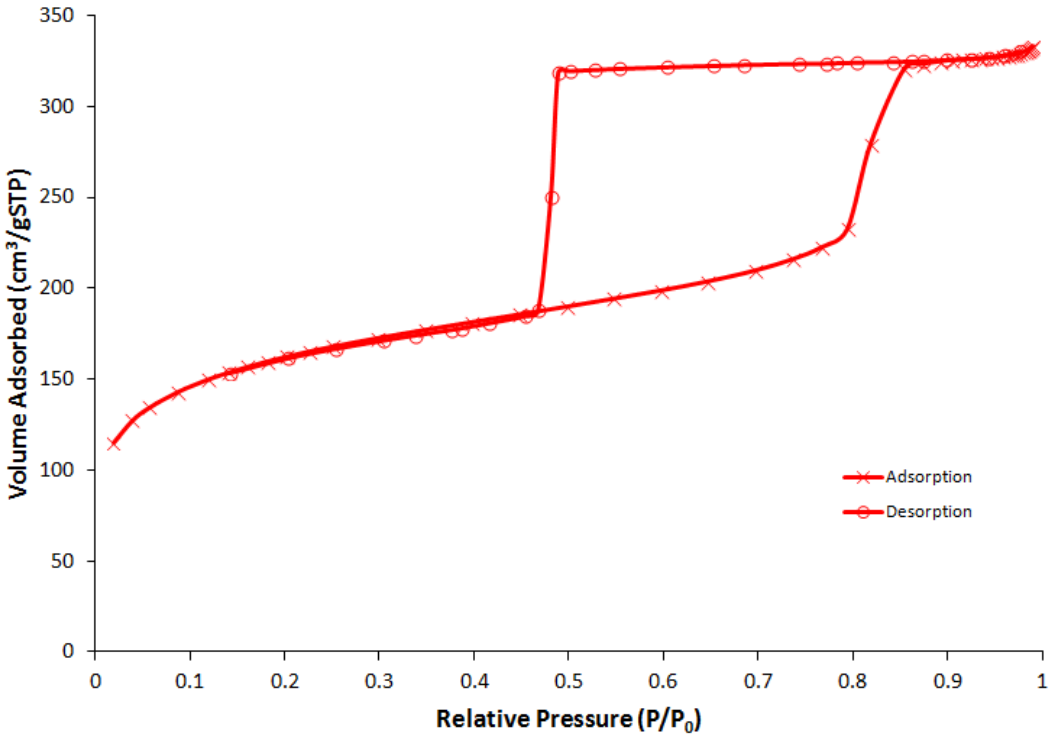

Figure 35: Nitrogen adsorption/desorption isotherm for ethylbenzene swollen ***Meso-SiO_2.***

The PXRD pattern for **Meso-SiO_2** is shown in Figure 36. The observed peaks represent a face-centred cubic pore arrangement, and are assigned in accordance with the literature and the ratios of the d_{hkl}-spacings in accordance with Equation 10 (section 2.2.3c).[209] For the peak at 0.54 ° 2θ, Braggs Law was used to calculate a lattice plane separation of 16.3 nm for the (111) plane, in agreement with the periodicity observed by TEM imaging. The intense peak confirms the high degree of ordering observed by TEM.

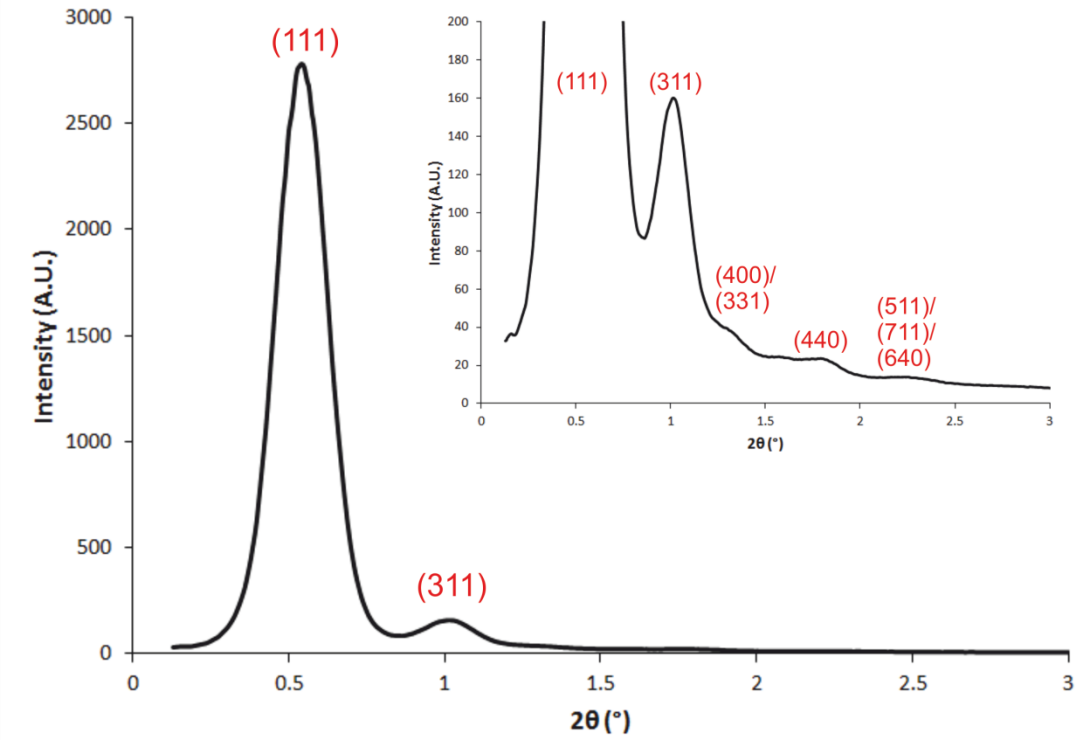

Figure 36: Low angle PXRD pattern for ***Meso-SiO$_2$****, showing peaks corresponding to a face-centred cubic pore arrangement. Inset: Zoomed view of low intensity region.*[209]

2.3: Conclusions and Future Work

Monodisperse polystyrene spheres were synthesised by emulsifier free emulsion polymerisation. Whilst synthetic routes to these materials are reported in the literature, reproducibility was not simple. Holland *et al.* report the synthesis of 421 ± 40 nm and 697 ± 64 nm polystyrene spheres by emulsifier free emulsion polymerisation stirred at 245 rpm and 360 rpm respectively.[180] Following their synthetic method, spheres of diameter 492 ± 21 nm and 601 ± 15 nm were obtained in this study. In comparison to this literature report, the spheres obtained in our system showed a much smaller size distribution. The particle sizes were reproducible between batches. The synthetic method appears to vary greatly depending on the experimental setup. As a result of these differences, the effect of reaction conditions on the sphere size was studied in order to produce a range of template sizes between 200 – 600 nm.

3DOM SiO_2 and ZrO_2 powders with periodicity from 150 – 500 nm were prepared by impregnation of cubic close packed polystyrene spheres, followed by calcination. The powders appear coloured due to Bragg diffraction of light. Characterisation showed phase pure, high quality photonic crystals, as evidenced by electron microscopy, DRUVS and porosimetry. Between batches, small variations in periodicity (± 5 nm), photonic stop band position (± 5 nm) and fill factor (± 2 %) were observed. Sinter funnels were used to infiltrate the templates, which may become clogged due to hydrolysis of the precursors within the porous frit, and hence the time for precursor removal may differ slightly between samples. Future work could attempt to improve the reproducibility, however for comparison of nanoparticle loaded materials in the following section, deposition in materials from the batches with the same or very similar properties will be presented.

In addition to powders, deposition of PS spheres on planar surfaces was used to produce 3DOM FTO films. Mesoporous SiO_2 was synthesised using a triblock copolymer template, swollen by ethylbenzene to increase the periodicity to 16.9 ± 0.8 nm. Deposition of nanoparticles within these hosts will be demonstrated in the next chapter.

Chapter 3

Nanoparticle Deposition in Porous Materials

3.1: Introduction

3.1a: Synthesis of OA-Stabilised Nanoparticles

As described in section 1.1.7, many methods exist in the literature for formation of composite materials consisting of small particles loaded into a porous host. For most of these approaches, simultaneous control over the nanoparticle size, dispersion within the pores, crystal phase and loading is difficult. In the case of methods where control is possible such as ALD, the requirement of specialised equipment limits the universal applicability of the method. By formation of stabilised nanoparticles prior to deposition, the particle size and crystal phase can be predetermined, and loadings can be controlled by variation of the initial mass of nanoparticles. Nanoparticles can be stabilised against aggregation and coagulation by coating the surface with long chain molecules. In many cases, monodisperse nanoparticles < 10 nm can be fabricated. Examples include oleic acid,[214] oleylamine,[215] trioctylphosphine,[216] and polyvinylpyrrolidone capped nanoparticle materials.[217] The structure of oleic acid is shown in Figure 37. When used as a ligand, the carboxyl group binds to the particle surface. Stabilisation of nanoparticles is achieved due to steric repulsion between the hydrophobic fatty acid chains at the particle surface.

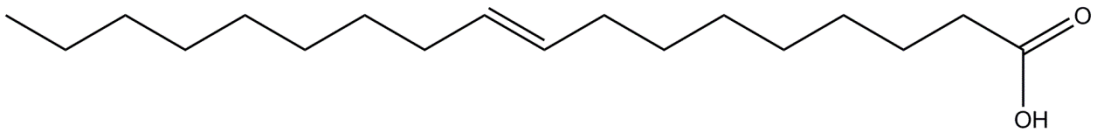

Figure 37: The structure of oleic acid.

To the best of our knowledge, general methods to achieve homogeneous deposition of high loadings (> 5 wt %) of ligand stabilised oxide and sulfide nanoparticles in porous materials have not been reported in the literature. In this chapter, the synthesis and deposition of semiconductor nanoparticles stabilised by oleic acid is investigated. Oleic acid is a liquid at room temperature due to its melting point of 13 °C,[218] and its high boiling point of 360 °C makes it suitable for use as a solvent in the synthesis of nanoparticle materials at elevated

temperatures.[219] Oleic acid can also act as a surfactant[220] and a stabiliser,[221] and literature examples of monodisperse OA stabilised nanoparticles exist for a variety of metals,[222-224] hence the development of a method for deposition of these nanoparticles in high surface area porous materials is of great interest for catalysis applications.

A common route to form OA stabilised nanoparticles is by high temperature decomposition of a metal oleate complex. The decomposition of $Fe(oleate)_3$ in 1-octadecene has been studied by *in situ* IR spectroscopy and TEM, and a mechanism proposed by which nucleation begins at 200 – 240 °C by dissociation of one oleate ligand.[222] Around this temperature slow, anisotropic growth of particles will occur and lead to polydisperse nanoparticles. On heating the solution to 300 °C dissociation of the remaining ligands occurs, and growth is accelerated. The oleate anions in solution act as a surfactant and bind to the surface of the growing particles, stabilising them against coagulation and aggregation. Monodisperse particles can be obtained if the initial nucleation stage is rapid, and is followed by a comparatively slow growth process.[225] Monodisperse metal chalcogenide nanoparticles capped with OA can be formed by injection of chalcogenide sources into metal oleate complexes at high temperature.[214] Monodisperse OA-coated TiO_2 nanorods and spheres have also been formed by slow hydrolysis of $Ti(OiPr)_4$ at 100 °C in an OA solvent, which stabilises the particles throughout the growth process.[219]

3.1b: Chapter Aims

In this chapter, the synthesis and characterisation of ligand stabilised nanoparticles of TiO_2, Fe_3O_4, CdS and CdSe is presented. Deposition of these materials will be presented in 3DOM SiO_2, ZrO_2 and FTO and in mesoporous SiO_2. Initial method development will be presented based on the deposition of TiO_2 in 3DOM SiO_2, with characterisation of the composites by PXRD, electron microscopy and porosimetry. The effect of loading on the photonic structure will be studied by DRUVS.

3.2: Results and Discussion

3.2.1: Nanoparticle Synthesis

3DOM SiO_2 and ZrO_2 powders were fabricated as outlined in chapter 2. For method development, **395-SiO_2** and **271-ZrO_2** samples were used as deposition targets, SEM images of which are displayed in Figure 38. The high quality of the packing and interconnectivity of the porous network can be seen. Deposition of ligand stabilised nanoparticles of TiO_2, Fe_3O_4, CdS and CdSe was targeted, due to the existence of established literature methods for the synthesis of these materials.[214-216, 219, 226, 227] TiO_2 and CdS were chosen especially due to their application as photocatalysts for proton reduction reactions.

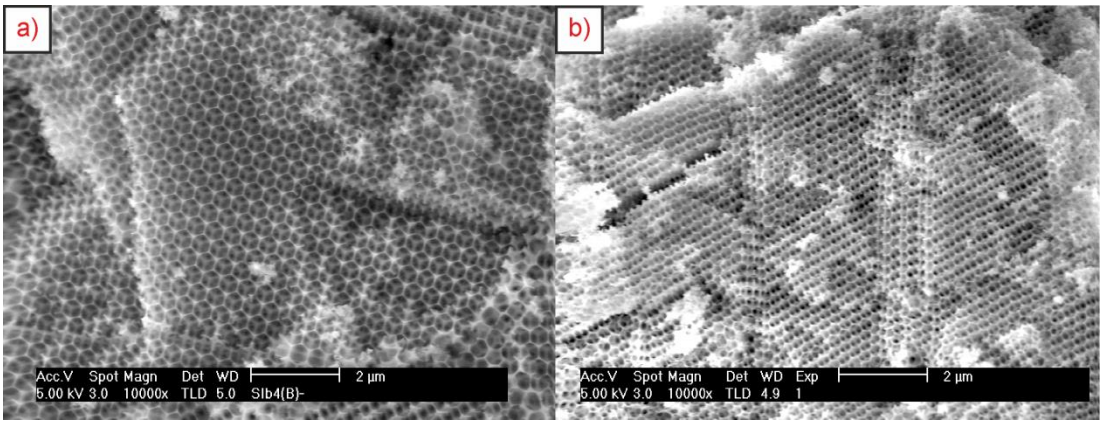

*Figure 38: SEM images of 3DOM SiO_2 and ZrO_2 used for deposition method development (a) **395-SiO_2** and (b) **271-ZrO_2**.*

3.2.1a: Synthesis of OA/TiO_2 Nanoparticles

TiO_2 nanoparticles were formed by a modified literature method.[219] Triethylamine in ethylene glycol (EG) was added to a solution of titanium tetraisopropoxide in oleic acid, acting as both solvent and stabiliser. The titanium precursor was slowly hydrolysed by water released on esterification of OA and EG. The nanoparticles were precipitated by addition of ethanol, isolated by centrifugation, and redispersed in toluene. This process was repeated 3 times to remove residual oleic

acid, and finally the particles were dried at 60 °C overnight. Reactions typically yield around 2.1 g of orange powder. The colour of the powder may be due to residual oleic acid, or other impurities, which are removed during calcination at 500 °C to yield a white powder. The OA/TiO_2 powder was characterised by CHN, TGA, IR, XRD and TEM. The nanoparticles could be readily dispersed in organic solvents such as hexane, chloroform and toluene to give optically transparent dispersions.

The crystal phase of the nanoparticles was analysed using PXRD (Figure 39). The diffractogram shows a single phase with one major peak at 20.4 ° 2θ, which has been attributed to partially condensed hydrous titanium dioxide.[219] In the literature, TiO_2 nanorods exhibiting this phase were observed to convert to the more stable anatase polymorph by extending the reaction time.[219] In this project, increasing the reaction time to 60 hours showed no change in the PXRD pattern, however on calcination at 450 – 500 °C a transformation to the anatase polymorph was observed.

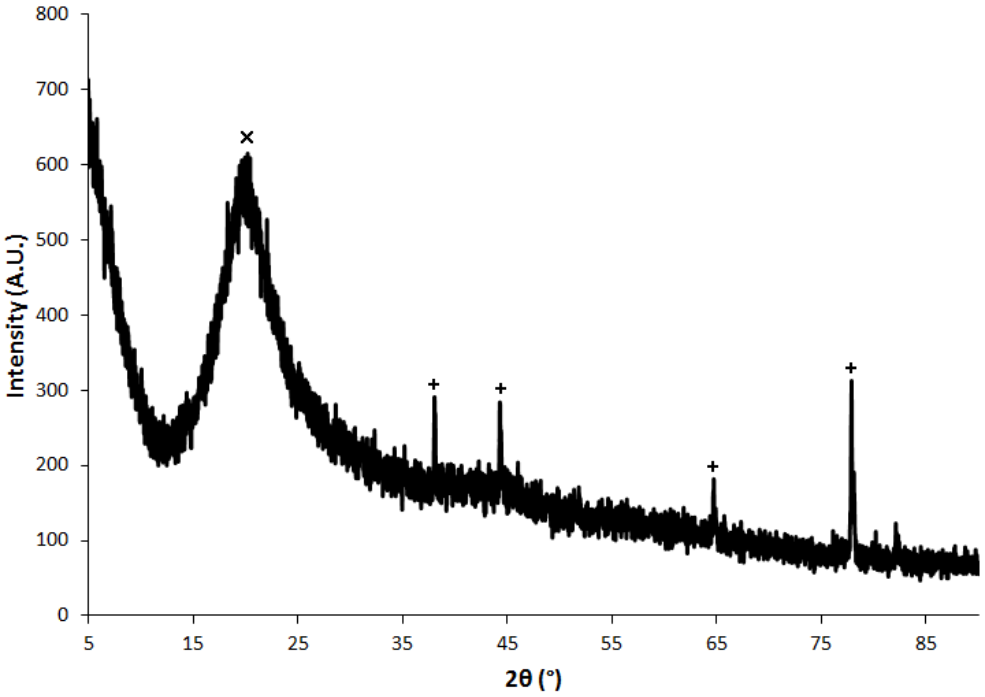

Figure 39: PXRD pattern of OA/TiO_2 nanoparticles. X = TiO_2 (see text),[219] + = Al sample holder.

IR spectroscopy was used to analyse the powder, as shown in Figure 40. The observed spectrum appears similar to the literature,[219] with two peaks at 2923 cm^{-1} and 2854 cm^{-1} representing antisymmetric and symmetric C-H stretches respectively corresponding to oleic acid CH_2 groups, and a peak at 3006 cm^{-1} attributable to the olefinic C-H stretch. The two peaks at 1543 cm^{-1} and 1440 cm^{-1} have been attributed to the antisymmetric and symmetric stretches of COO^- anions bound to Ti centres.[228-230] An additional carbonyl peak is observed in our spectrum at 1734 cm^{-1}, with a low intensity compared to the C-H stretches in the IR spectrum of free oleic acid.[231] This band is close to expected values for ester linkages (1725 – 1750 cm^{-1}),[232] and may correspond to surface bound oleic acid. Alternatively, it could be attributed to crystallised unbound oleic acid as an impurity, which could account for the orange discolouration of the powder.

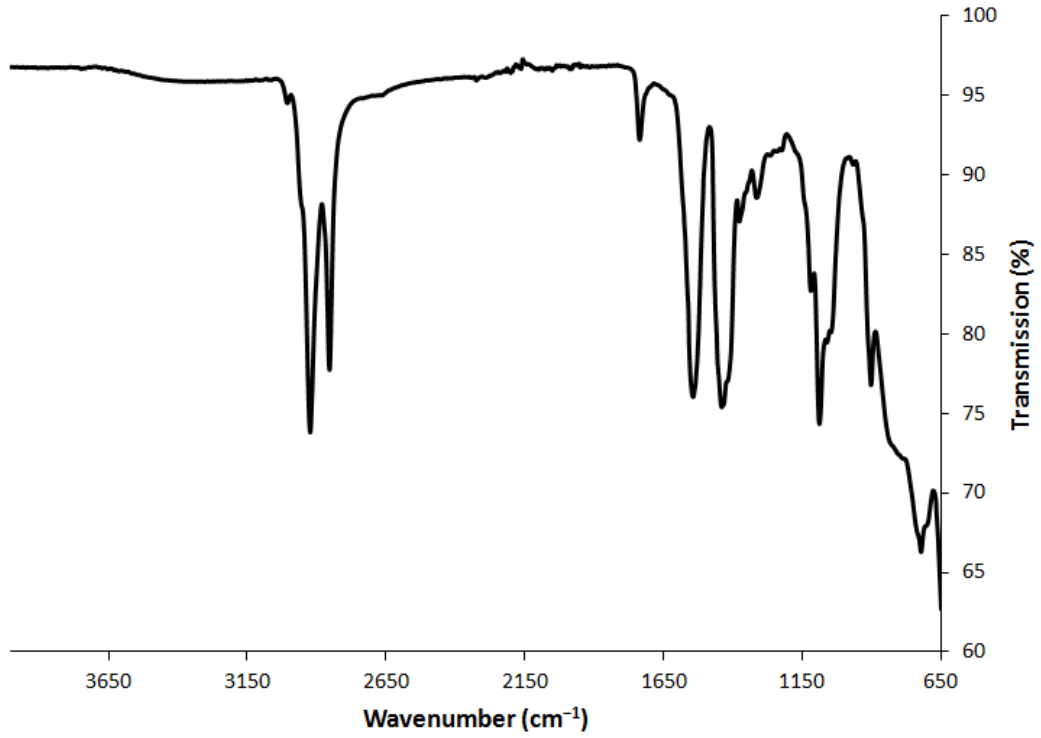

Figure 40: IR spectrum of OA/TiO_2 nanoparticles.

TEM images of TiO_2 nanoparticles are shown in Figure *41*. Single crystalline particles are observed, with an average diameter of 8.9 ± 1 nm.

Combustion analysis was used to quantify the ratio of TiO_2 to ligand. For a particular OA/TiO_2 sample, CHN gave elemental compositions of 62.6 % C, 9.72 % H, and 0 %

N. From these values, the percentage of oxygen contributed from oleic acid was calculated, and subtracted from the residual value. Assuming the residual corresponds to TiO_2, a ratio of 1 TiO_2 molecule to 1.25 oleic acid molecules was calculated, or that the nanoparticles are 18.5 % TiO_2 by mass (see appendix section A1.4 for example calculation). From this, expected elemental compositions of 62.42 % (C), 9.89 % (H), 11.0 % (Ti) and 16.7 % (O) were calculated.

TGA profiles of the nanoparticles showed a mass loss of 79.3 % at 300 °C. Assuming this loss correlates to complete combustion of the organic shell, this suggests a composition of 20.7 % TiO_2 by mass, similar to CHN. As a further control, multiple powder samples were weighed out and calcined. After calcination, all samples contained around 20 % of the initial mass of OA/TiO_2, in support of the CHN analysis.

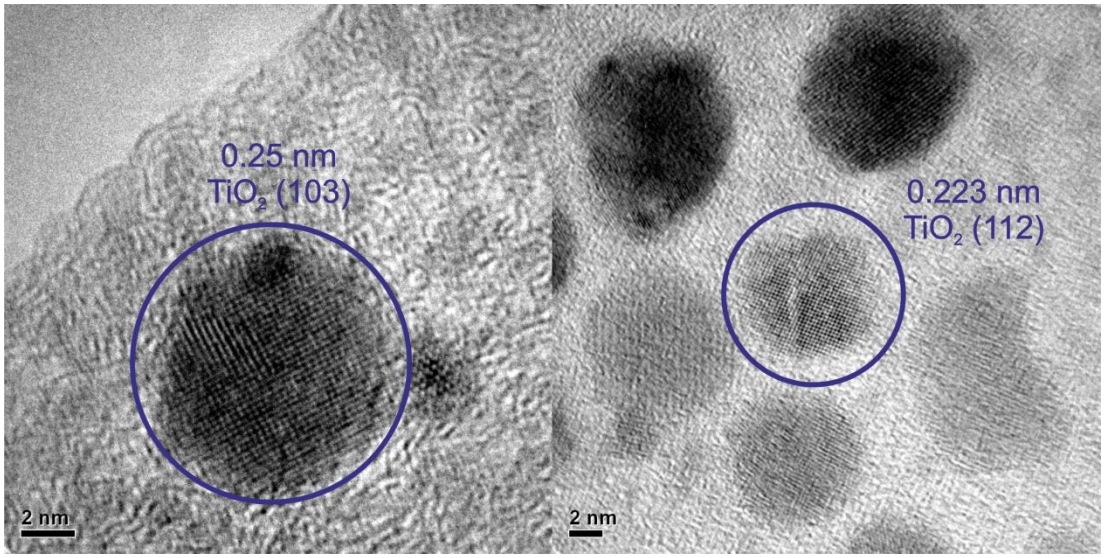

Figure 41: TEM images of OA/TiO_2 nanoparticles.

3.2.1b: Synthesis of OA/Fe_3O_4 Nanoparticles

Oleic acid coated Fe_3O_4 nanoparticles were synthesised by a two step process. Initially, an iron oleate complex was synthesised by reaction of $FeCl_3$ and sodium oleate. OA/Fe_3O_4 nanoparticles were formed by decomposition of this complex at 290 °C in octyl ether.[226, 227] The nanoparticle dispersion was centrifuged, washed

with ethanol and isolated as a powder, typically yielding 0.5 g of a black solid. As with TiO_2, redispersion of the powder in organic solvents gave optically transparent liquids. CHN analysis gave an elemental composition of 54.83 % C, 8.12 % H and 0 % N. A ligand ratio of 1 Fe_3O_4 to 2.01 oleic acid molecules was determined, corresponding to an Fe_3O_4 content of 29 % by mass in the nanoparticles. From this, expected elemental compositions of 54.37 % (C), 8.62 % (H), 21.0 % (Fe) and 16.1 % (O) were calculated.

PXRD was used to analyse the phase of the nanoparticles (Figure 42). In addition to wide angle analysis, longer scans were performed on the 56 – 62 ° 2θ region due to similarities in the diffraction pattern for Fe_3O_4 and other iron oxides. Analysis of the peaks confirmed the presence of single phase cubic Fe_3O_4, JCPDS 01-079-0416. Using the FWHM of the peak at 35.5 ° 2θ, a crystallite size of 6.1 nm was estimated using the Scherrer equation.

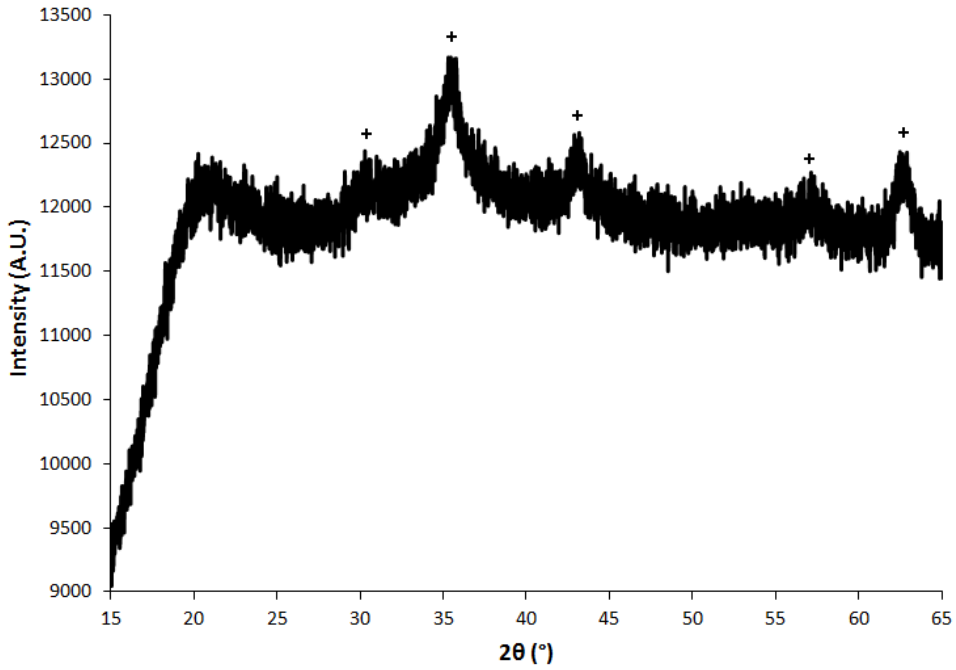

Figure 42: PXRD pattern of OA/Fe_3O_4 nanoparticles. + = cubic Fe_3O_4, JCPDS 01-079-0416.

The IR spectrum of OA/Fe_3O_4 is shown in Figure 43. Similar to OA/TiO_2, peaks at 2924 cm^{-1} and 2854 cm^{-1} can be attributed to C-H stretches, peaks at 1549 cm^{-1}

and 1416 cm^{-1} can be assigned to COO^- anions, and the peak at 1709 cm^{-1} can be assigned as a C=O stretch.

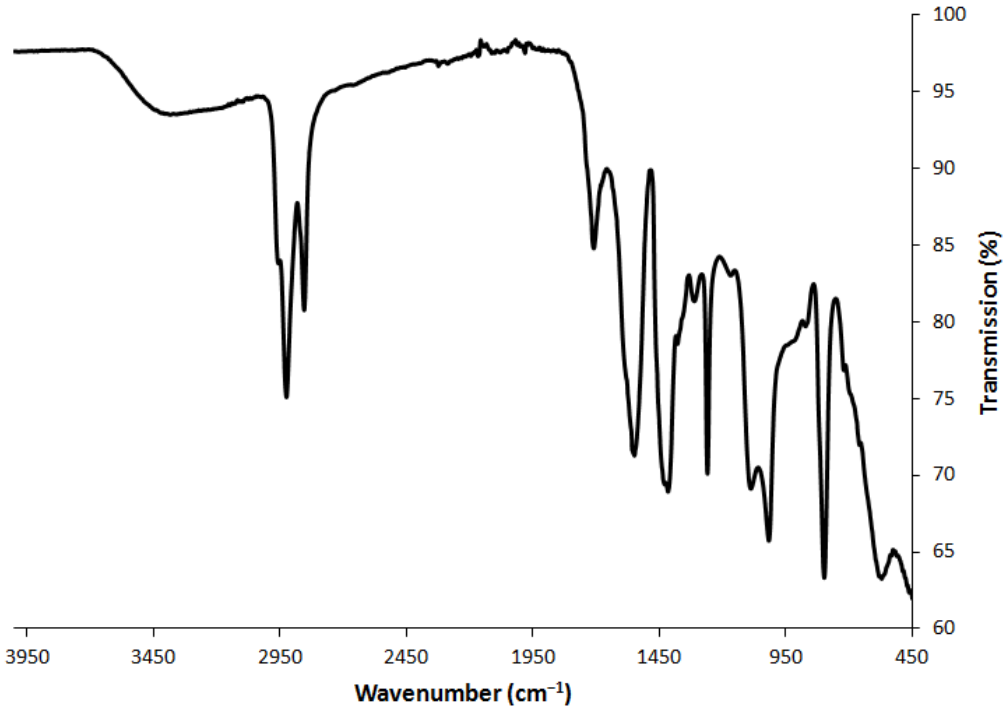

Figure 43: IR Spectrum of OA/Fe_3O_4 nanoparticles.

The nanoparticle size was studied by TEM (Figure 44). A mixture of small (2 – 3 nm) amorphous particles and larger single crystalline particles with an average diameter of 7.3 ± 1.2 nm was observed. For the crystalline particles, the observed particle size is in agreement with values calculated from PXRD. An averaged particle size analysis for the amorphous particles was not possible due to poor contrast between the particles and the amorphous carbon film at high resolution.

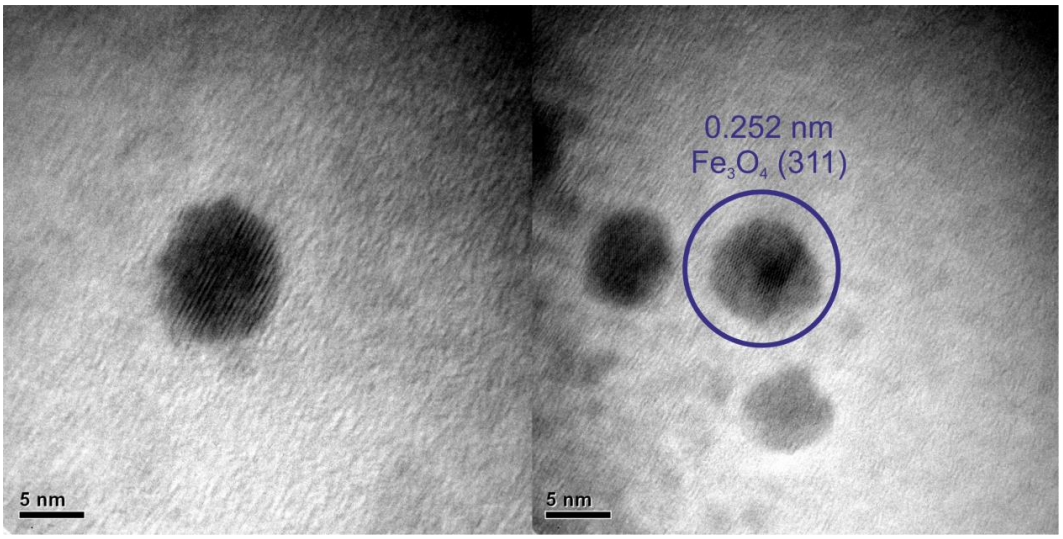

Figure 44: TEM images of OA/Fe_3O_4 nanoparticles.

3.2.1c: Synthesis of OA/CdS Nanoparticles

Initially, CdS nanoparticles functionalised by oleylamine were synthesised by a literature method.[215] Using oleylamine as the solvent and stabiliser, cadmium acetate and sulfur were reacted at 250 °C under argon. After washing, 130 mg of a yellow powder was obtained. Unlike previous samples, the stability of dispersions in organic solvents was short-lived, with some precipitate observed after 4 hours. CHN analysis returned an elemental composition of 25.43 % C, 5.83 % H and 0 % N. A ligand ratio of 1 CdS to 0.25 oleylamine molecules was determined, corresponding to 68.7 % CdS content by mass. From this, expected elemental compositions of 25.57 % (C), 4.41 % (H), 52.3 % (Cd), 14.9 % (S) and 1.6 % (N) were calculated. In comparison to the observed values, the expected hydrogen content is considerably lower, which may be due to impurities in the technical grade oleylamine (70 %). The lack of nitrogen detected by CHN may also suggest that incomplete combustion has occurred. The poor stability of nanoparticle dispersions is likely due to the smaller ligand shell in comparison to TiO_2 and Fe_3O_4. Deposition of these particles was attempted as described previously. Non-homogeneous dispersions were typically yielded, as judged by agglomerates seen by SEM and a reduction in intensity of the

photonic stop bands. To achieve high quality dispersions within the pores, nanoparticles with a higher proportion of ligand were pursued.

A modified literature method was used to fabricate oleic acid functionalised CdS quantum dots.[214] Nanoparticles were formed by injection of sulfur into a hot solution of cadmium oxide and oleic acid in octadecene under argon. Growth of particles proceeded at a constant temperature of 270 °C for 3 minutes, followed by rapid cooling and centrifuge washing. Yields were between 90 – 100 mg of ligand coated nanoparticles. The nanoparticles were stored in toluene, in which they were stable for extended periods of time (> 3 months). Particles were analysed by CHN, UV-Vis spectroscopy, fluorescence and TEM.

CHN analysis gave an elemental composition of 62.3 % C, 10.3 % H and 0 % N. A ligand ratio of 1 CdS to 2.03 oleic acid molecules was determined, corresponding to 18.1 % CdS content by mass in the nanoparticles. From this, expected elemental compositions of 62.61 % (C), 9.93 % (H), 14.1 % (Cd), 9.2 % (O) and 4.0 % (S) were calculated. The higher ligand content than oleyl/CdS contributes to the increased stability of the particles in organic solvents.

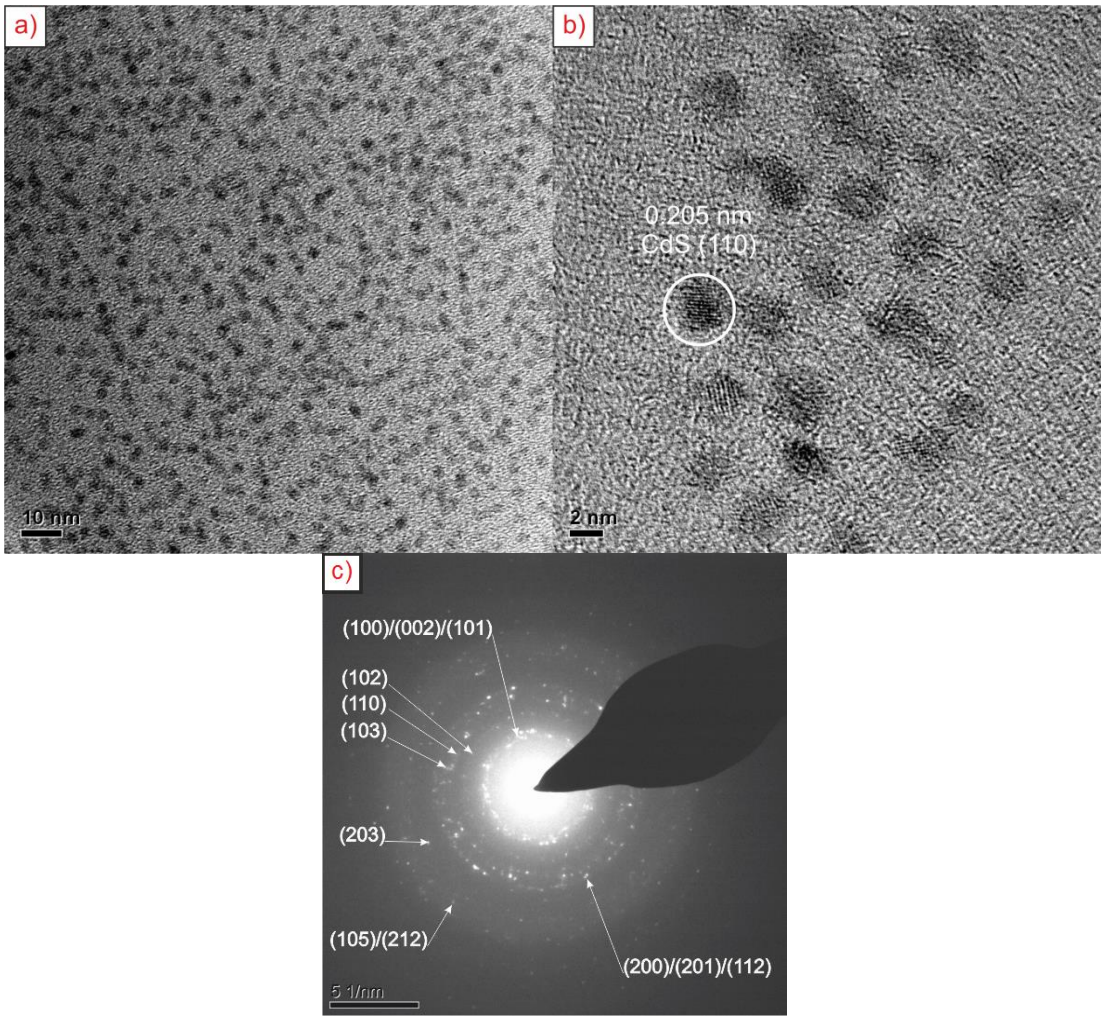

Figure 45: TEM images (a), (b) and electron diffraction pattern (c) of CdS quantum dots grown at 270 °C for 3 minutes. Lattice planes were indexed as hexagonal CdS, JCPDS file 01-075-1545.

TEM images (Figure 45) show single crystalline particles with an average size of 2.84 ± 0.3 nm. The lattice fringes of the circled particle in Figure 45b were measured to be 2.05 Å, corresponding to the (110) crystal plane. Electron diffraction confirmed the chemical identity of the nanoparticles as hexagonal CdS, with d_{hkl}-spacings matching JCPDS file 01-075-1545.

The growth of CdS nanoparticles was studied as a function of reaction time. Aliquots were taken from the reaction mixture approximately every 30 seconds for 3 minutes, and quenched in cold chloroform. The fluorescence spectra of CdS aliquots were measured as a function of reaction time. On increasing the growth time from 37 s to 180 s, the position of the excitation peak shifted from 421 nm to 431 nm,

with corresponding emission peaks at 426 nm and 438 nm respectively. As the particles are below the Bohr radius of CdS (*ca.* 3 nm),[233] the lower emission wavelengths compared to bulk CdS (2.4 eV, 518 nm) are consistent with an increased band separation by quantum confinement. Absorbance and fluorescence spectra for a quenched reaction mixture are shown in Figure 46. The full-width half maximum (FWHM) of the emission peak is around 17 nm, which is comparable to CdS quantum dots in the literature.[234, 235] This specific nanoparticle batch was used for deposition in 3DOM and commercial ZrO_2 powders for photocatalysis. For deposition method development, batches with similar fluorescence emission peak positions were used.

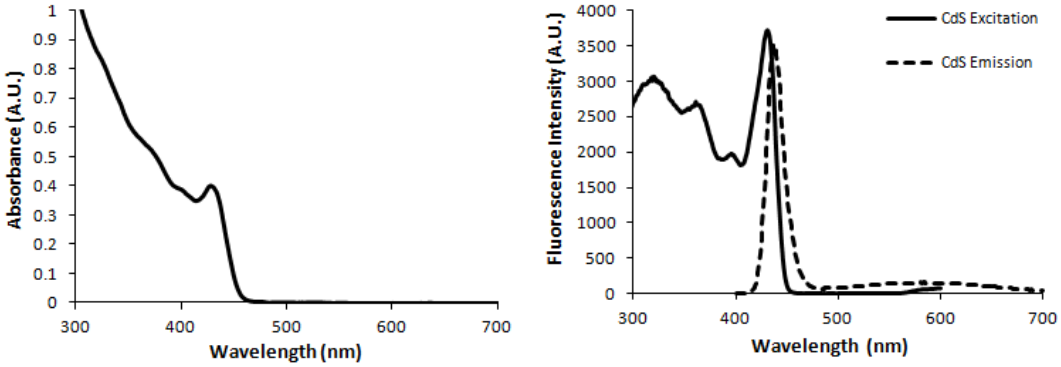

Figure 46: UV-Vis absorbance (left) and fluorescence (right) spectra of CdS quantum dots.

3.2.1d: Synthesis of TOP(O)/CdSe Nanoparticles

CdSe quantum dots were synthesised by injection of a trioctylphosphine (TOP)/selenium solution into a hot solution of trioctylphosphine oxide (TOPO), hexadecylamine (HDA) and CdO.[216] After injection the mixture was held at 270 °C for 7 minutes to allow for particle growth. The reaction was rapidly cooled to room temperature, and the nanoparticles purified as above for CdS. Yields were between 35 – 40 mg of ligand coated nanoparticles. Nanoparticles were stored as toluene dispersions, which were stable for long periods of time (> 3 months).

The particle surface is coated with a mixture of TOPO and TOP in unknown ratios. CHN analysis gave an elemental composition of 39.5 % C, 6.59 % H and 0 % N. Assuming complete TOPO coverage, a ligand ratio of 1 CdSe to 0.55 TOPO molecules was determined, corresponding to a CdSe content of 47.4 % by mass in the nanoparticles. From this, expected elemental compositions of 39.2 % (C), 7.00 % (H), 27.8 % (Cd), 19.6 % (Se), 4.2 % (P) and 2.2 % (O) were calculated.

TEM analysis showed single crystalline particles with an average particle size of 3.75 ± 0.4 nm. The lattice fringes of the circled particle in Figure 47a were measured to be 3.25 Å, corresponding to the (101) crystal plane. Electron diffraction confirmed the chemical identity of the nanoparticles as hexagonal CdSe, with d_{hkl}-spacings matching JCPDS file 01-071-4772.

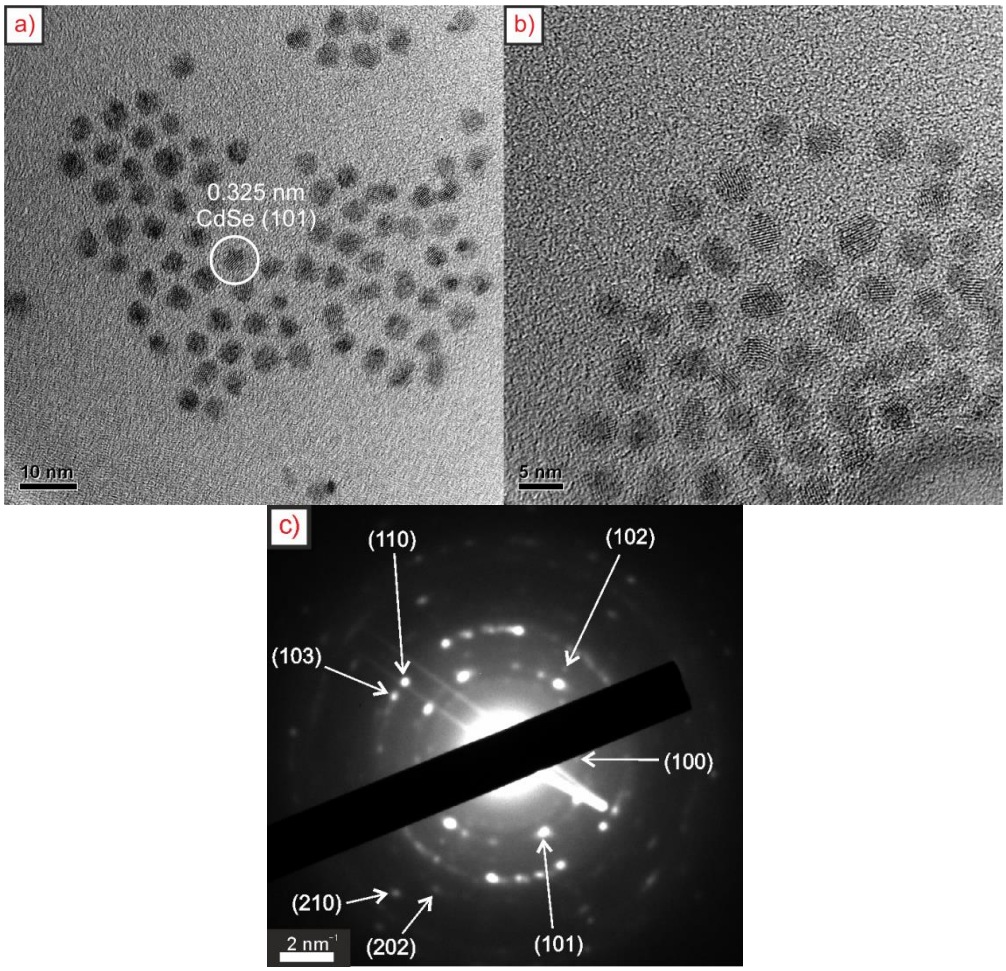

Figure 47: TEM images (a), (b) and electron diffraction pattern (c) of CdSe quantum dots grown at 270 °C for 7 minutes. Lattice planes were indexed as hexagonal CdSe, JCPDS file 01-071-4772.

The growth of CdSe nanoparticles was studied as a function of reaction time. As with CdS, aliquots were regularly taken from the reaction mixture, over a period of 7 minutes. The fluorescence spectra of CdSe aliquots were measured as a function of reaction time. On increasing the growth time from 52 s to 420 s, the position of the excitation peak shifted from 543 nm to 602 nm, with corresponding emission peaks at 545 nm and 608 nm respectively. These values are lower than expected for bulk CdSe (1.7 eV, 730 nm), consistent with quantum confinement of particles which are smaller than the Bohr radius (*ca.* 5.4 nm).[233] The observed peak shift with increased growth time is larger than for CdS, suggesting that particle growth proceeds at an elevated rate. Absorbance and fluorescence spectra for a quenched reaction mixture are shown in Figure 48. The FWHM of the emission peak is around 28 nm, comparable to CdSe quantum dots in the literature.[216, 235] These nanoparticles were used for deposition attempts in 3DOM FTO materials.

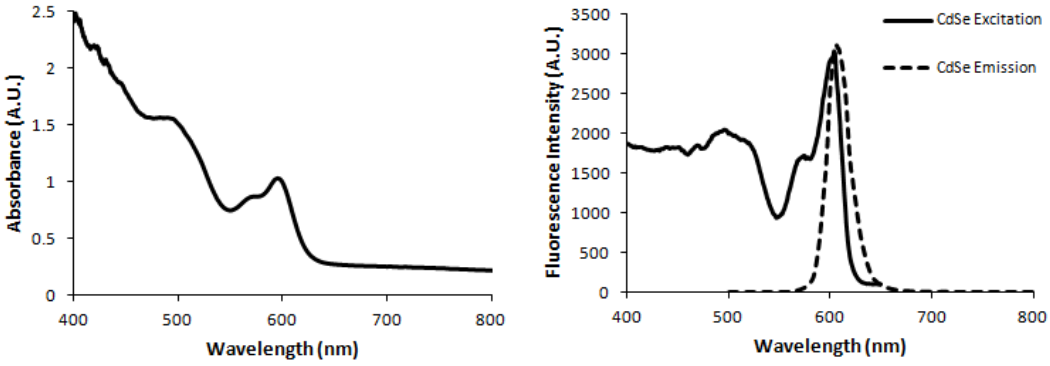

Figure 48: UV-Vis absorbance (left) and fluorescence (right) spectra of CdSe quantum dots.

3.2.2: Deposition of OA/TiO_2 Nanoparticles in 3DOM SiO_2

3.2.2a: Deposition Method Development

To develop a method for deposition of preformed nanoparticles in porous materials, the loading of OA/TiO_2 nanoparticles was attempted in 3DOM SiO_2. Nanoparticle dispersions dispersed in hexane/chloroform were added to the porous support (30 mg) in a glass vial. The solvent (typically 1.5 mL) was then evaporated slowly at elevated temperature. The vial was placed in a furnace and calcined at 500 °C for 5 h (ramp rate 5 °C min^{-1}), to remove the ligands, and promote sintering of the nanoparticles to the support. At no point was the powder transferred from the vial, hence the TiO_2:SiO_2 ratio in the final product is reflective of the targeted loading. The primary goal is to achieve a homogeneous distribution of the added nanoparticles within the pore network.

For all deposition attempts, samples were weighed before and after calcination, as a further check to confirm the quantity of nanoparticles added. Targeted loadings were designated in terms of the weight of nanoparticles in comparison to the weight of support expressed as a percentage, as defined by Equation 11. For TiO_2 in SiO_2, targeted loadings were between 3 and 60 wt% TiO_2. Nanoparticle loaded samples were denoted xx%-NP-yyy-MO_2, where xx% is the added weight of nanoparticles expressed as a percentage of the support mass (wt%), NP is the chemical identity of the nanoparticles, and yyy and MO_2 are the periodicity as measured by SEM and the composition of the support respectively.

Equation 11 $$Added\ Weight\ Percent\ (wt\%) = \frac{mass\ NP}{mass\ Support} x100$$

In initial attempts, no modification was made to the support prior to deposition. DRUVS spectra of the composites showed a decrease in the intensity of the photonic stop band in comparison to the uncoated 3DOM material, with no shift in the stop band position as would be expected on addition of an extra component to the photonic crystal lattice. SEM and TEM analysis showed large aggregates of nanoparticles, confirming the failure of the deposition and the loss of ordering within the material. No change in the periodicity of 3DOM SiO_2 was observed after

calcination, hence the photonic structure is stable under these conditions. To promote interaction between the nanoparticles and the support, modification of the surface groups in the 3DOM materials was investigated.

3.2.2b: Modification of the Support

The surfaces of 3DOM SiO_2 and ZrO_2 used in this study are generally covered with hydrophilic hydroxide groups. Modification of the surface aimed at increasing its hydrophobicity was attempted, to promote interactions with the OA chains on the stabilised nanoparticles and improve the quality of deposition.

Initially, silanes were used to modify the hydroxyl groups on the SiO_2 surface. Dichlorodimethylsilane in toluene was used to treat 3DOM SiO_2 according to literature methods.[236] The surface hydroxyl groups are converted to hydrophobic $OSi(CH_3)_3$ groups. Water was added to a small fraction of the powder to empirically test the wettability, and in all cases the powder was observed to float on top of the liquid in order to minimise its contact, contrary to untreated 3DOM powders which are easily wetted. Nanoparticle dispersions were added to the support, and calcined to remove the ligands as above. Despite the improved contact between the nanoparticles and support, large aggregates were observed in the final product, implying that the interaction between OA surface groups on the nanoparticles and the methyl groups on the substrate are weak in comparison to the nanoparticle-nanoparticle interactions. In some places, individual nanoparticles appeared to have sintered to the support (circled, Figure 49), however these regions were not common, and overall deposition quality was poor.

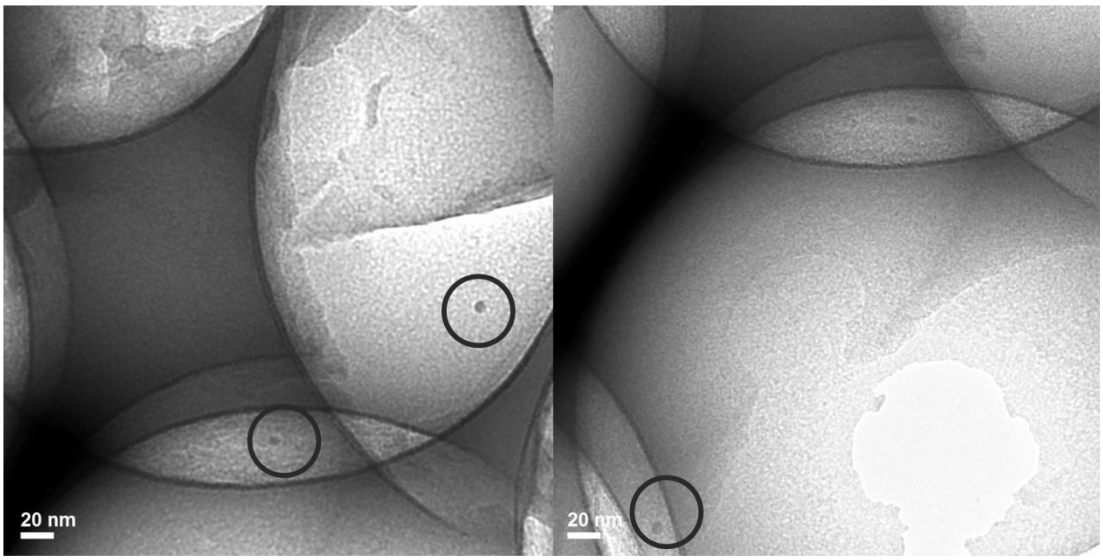

*Figure 49: TEM images of **58%-TiO_2-395-SiO_2**. Nanoparticles were deposited from dispersions in chloroform. Silica was pre-treated with DCDMS.*

3.2.2c: Oleic Acid Coated 3DOM SiO_2

As observed in the previous failed depositions, the strength of nanoparticle-support interactions are important for homogeneous nanoparticle loading. With unmodified SiO_2, the nanoparticle-nanoparticle interaction is greater than the nanoparticle-support interaction, and hence the removal of solvent leads to aggregation of the nanoparticles. Modification of the surface with $OSi(CH_3)_3$ groups did not increase the strength of the nanoparticle-support interaction enough to prevent aggregation. In solution, OA molecules are attracted to each other by van der Waals forces. Hence, it was reasoned that deposition of a layer of OA on the surface of the porous material would promote interactions between the nanoparticles and the support.

Similar approaches have been used for formation of 3DOM CdSe in the literature. SiO_2 template spheres were modified by stearyl alcohol, and immersed in a dispersion of CdSe quantum dots with TOPO/TOP surface ligands. Interaction of the nanocrystals with the surface ligands allowed for formation of a glassy solid by slow removal of the solvent over 1 – 2 months, followed by processing to 3DOM CdSe by etching the silica in HF.[237]

A modified literature method was used to functionalise the SiO_2 surface with oleic acid.[231] 3DOM SiO_2 (40 mg) was soaked in a hexane solution of oleic acid (0.05 M) for 30 minutes. Oleic acid can potentially bind to the surface by covalent interactions, including binding to the acid group by ester linkages, bidentate or bridging configurations or by weaker interactions such as hydrogen bonding to surface SiOH groups.[231] The binding of OA was studied by IR and TGA (see appendix section A1.6a and Figure 115). The IR spectrum of OA/3DOM SiO_2 showed peaks at 2930 cm^{-1} and 2858 cm^{-1} which were not present for uncoated 3DOM SiO_2, corresponding to the symmetric and antisymmetric stretch of OA. The binding mode of OA could not be elucidated solely from the observed peaks. The amount of OA adsorbed was analysed by thermogravimetric analysis (TGA). TGA traces for OA/3DOM SiO_2 showed a mass loss of 7.2 % around 300 °C corresponding to removal of oleic acid. Using the surface area of the 3DOM material and the cross sectional area of oleic acid, 48 $Å^2$, the coverage of OA was calculated, and found to correspond to a monolayer coating of oleic acid on the surface.[238]

3.2.2d: Deposition from Hexane and Chloroform Dispersions

Using OA-coated 3DOM SiO_2, depositions were attempted from OA/TiO_2 dispersions in hexane. After calcination, the powder was analysed by SEM, showing large areas of pristine 3DOM material with some agglomerates of around 3 – 10 µm in length (Figure 50a). SEM/EDX analysis was used to probe the elemental composition of the surface. The EDX spectrum of the whole region of the SEM image in Figure 50a is shown in Figure 50b. EDX Analysis of the red circle regions showed large Ti peaks, confirming the agglomerates are TiO_2. Spectra of the blue square in Figure 50a also showed Ti peaks, with lower intensity than the peaks in Figure 50b, suggesting some incorporation of nanoparticles in the pore network. TEM imaging was used to study the distribution of nanoparticles in the pores.

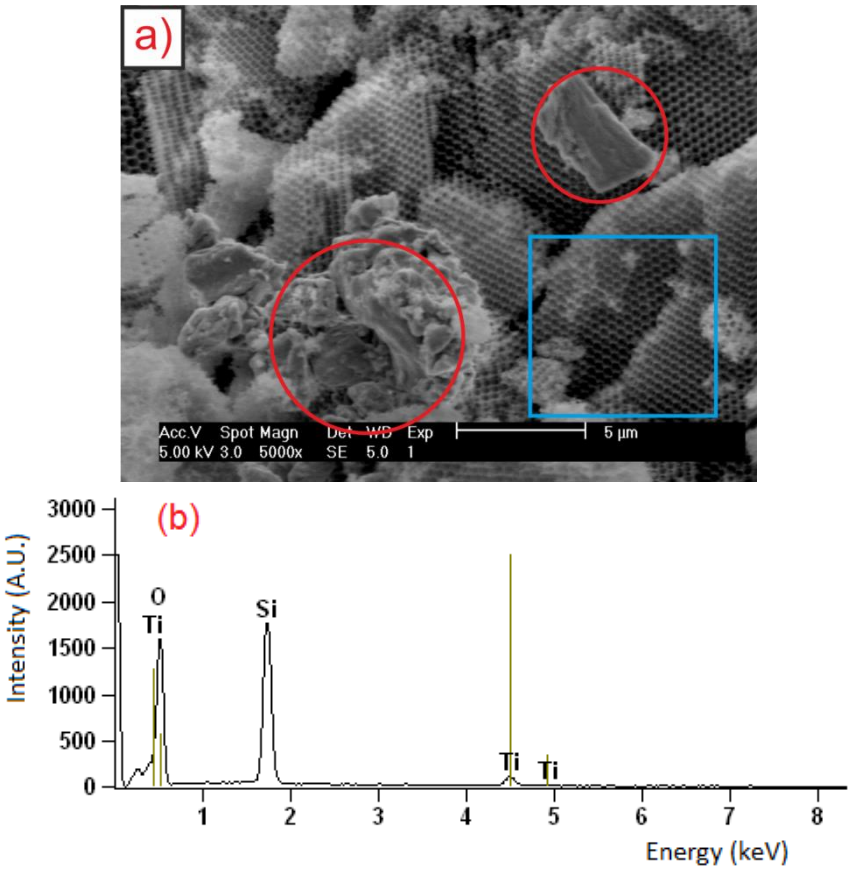

Figure 50: SEM image (a) of ***58%-TiO_2-395-SiO_2*** *sample deposited from hexane dispersions in OA-coated 3DOM SiO_2 showing surface agglomerates (circled), and (b) EDX spectrum of the whole area measured at 10 kV accelerating voltage.*

TEM images of the above sample are shown in Figure 51. A large proportion of the porous surface is coated with nanoparticles, an improvement over previous attempts. However, uncoated SiO_2 (Figure 51a) and agglomerated TiO_2 can still be observed within the sample. For the pores that are coated with nanoparticles, variations in concentration are also observed in places (Figure 51b – d). The composite was characterised further by electron diffraction, dark field imaging and TEM EDX mapping.

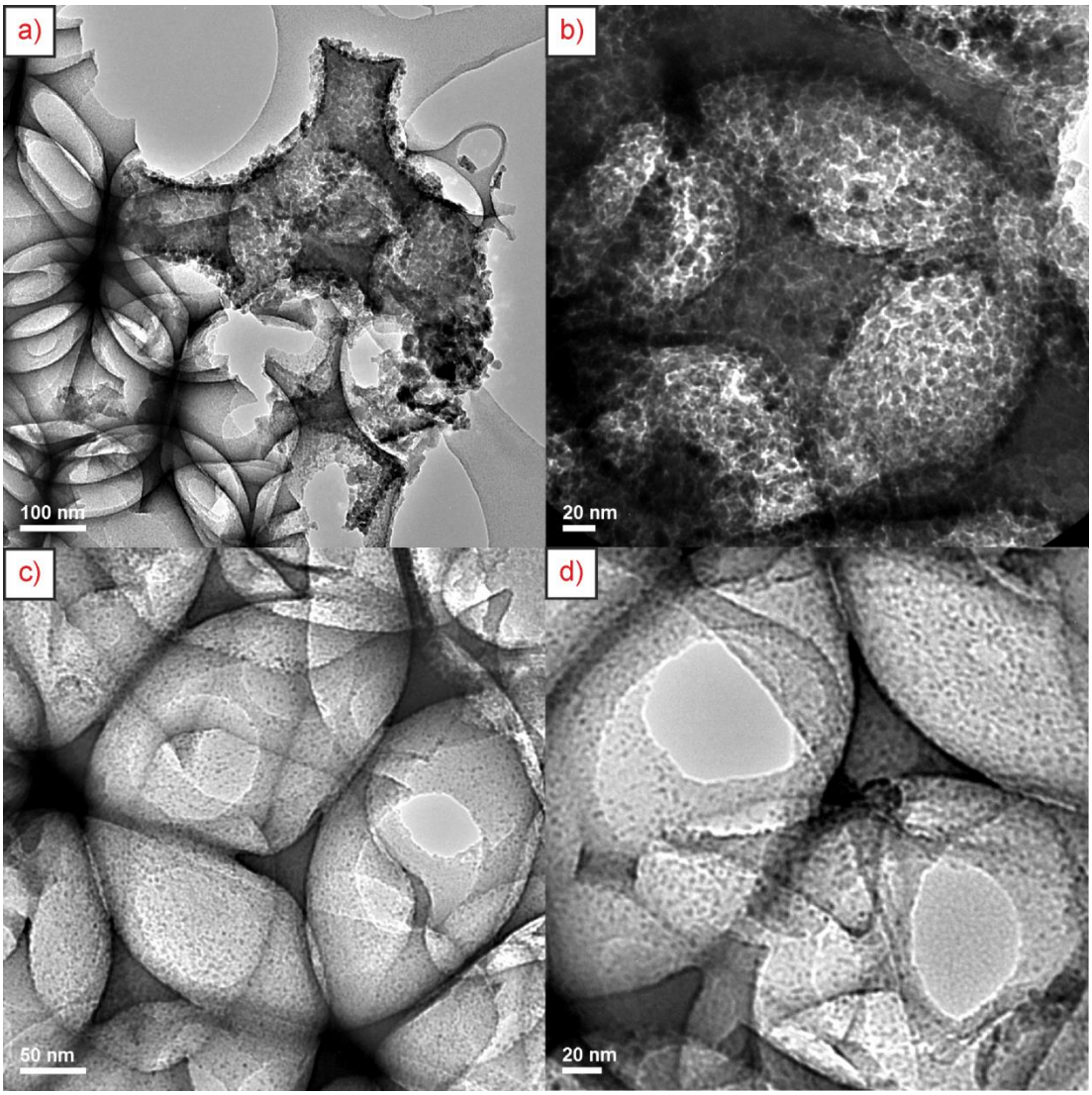

*Figure 51: TEM images of **58%-TiO_2-351-SiO_2** sample. Nanoparticles were deposited from dispersions in hexane. Silica was pre-treated with OA.*

Due to the amorphous nature of the SiO_2 walls, the presence of crystalline TiO_2 nanoparticles within the structure can be confirmed by electron diffraction. An electron diffraction pattern of TiO_2 nanoparticles is shown in Figure 52e. The d_{hkl}-spacings correspond to anatase TiO_2, JCPDS file 01-078-2486. A fully indexed electron diffraction pattern will be presented in section 3.2.2e below (Figure 55d). Dark field imaging was used to analyse the composites. In dark field imaging, the objective aperture of the TEM instrument is moved in order to block the direct beam passing through the specimen, allowing detection of the electrons scattered from individual crystal planes within the sample. Dark field images (Figure 52b and Figure 52d) were formed using scattered electrons from the (101) crystal plane of

TiO_2 (Figure 52e). In this beam orientation, nanoparticles which are positioned such that the (101) plane is perpendicular to the beam show up brightly within the image. Contrast between the TiO_2 nanoparticles and the SiO_2 support can clearly be seen.

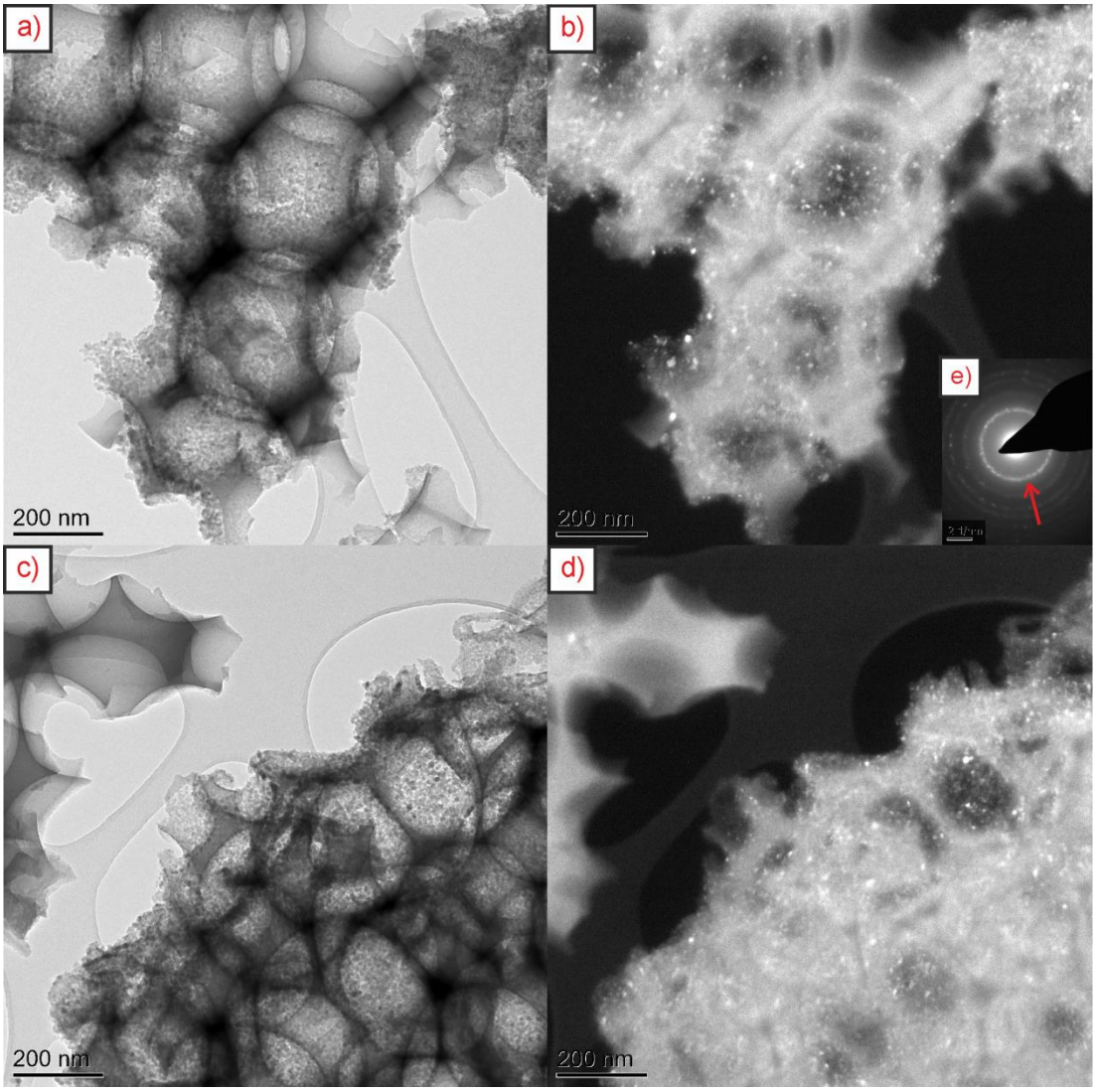

*Figure 52: TEM images of **58%-TiO_2-351-SiO_2** sample. Dark field images (b, d) of corresponding regions (a, c) are shown, indicating the presence of crystalline TiO_2 inside the pores. (e) Electron diffraction pattern of TiO_2 nanoparticles in 3DOM SiO_2. Red arrow indicates (101) plane used for dark field images (Scale bar 2 nm^{-1}).*

The elemental distribution of the region displayed in Figure 52a was probed by EDX mapping. The image does not contain any uncoated porous regions. The chemical identity of the nanoparticle facets was confirmed as TiO_2 by mapping of the

elemental Ti composition. Within the porous region, the coincident signals observed from Ti, Si and O maps showed that the nanoparticles are dispersed evenly across the pore surface (see appendix Figure 116).

The reproducibility of this synthesis was found to vary between batches. Samples aimed at reduced loadings by the same method showed comparatively less coated porous regions, and larger amounts of aggregated TiO_2. The success of the method also varied with the solvent used for nanoparticle dispersion. Attempts to deposit nanoparticles from chloroform dispersions showed slightly better dispersions than hexane, but still with agglomerated regions and uncoated pores.

The stability of a dispersion of nanoparticles in a given solvent appears to play an important role in the formation of homogeneous composite materials. For a given volume of hexane or chloroform used as a solvent for nanoparticle dispersion, a specific mass of nanoparticles can be stably dispersed for a period of time between 10 hours to a day, longer than the time course of deposition. However, as the solvent is evaporated and the effective concentration of nanoparticles is increased, precipitation is more likely to occur.

Initially, it was assumed that on precipitation, the OA chains on the nanoparticle surface would be attracted to those on the support, producing a well dispersed product after calcination. However, experimental results showed that this was not the case, and instead the precipitated nanoparticles form aggregates which are sintered after calcination. To achieve optimal results, additives were mixed with the solvent to increase the initial stability of nanoparticle dispersions.

Solvent suitability for deposition was tested empirically by adding set volumes of various solvent mixtures to a set mass of nanoparticles. The mixtures were sonicated to ensure thorough dispersion, and left to stand until sediment was observed. In particular, solutions of 0.1 M OA in hexane and chloroform formed dispersions stable against precipitation for long periods of time. Evaporation of the solvent was attempted to simulate deposition in 3DOM materials, showing no obvious precipitation as the liquid level dropped. After complete removal of the volatile solvent by evaporation, optically clear liquid remained, suggesting retention

of the nanoparticle dispersion in oleic acid. Deposition in porous materials was attempted from these solutions.

3.2.2e: Deposition from OA/Hexane Dispersions

Solutions of 0.1 M oleic acid in hexane were used as a solvent in order to improve the stability of dispersions. Deposition was attempted by the same methods as previous samples. No precipitation was observed from OA/hexane dispersions of nanoparticles over the deposition timescale. After calcination of the composites, SEM images of the samples showed pristine 3DOM material with no visible agglomerated particles, appearing similar to images prior to deposition. Figure 53 shows TEM images of the TiO_2/3DOM SiO_2 composites. No uncoated porous regions were observed by TEM, however some local agglomeration of nanoparticles can be seen within individual pores (Figure 53d).

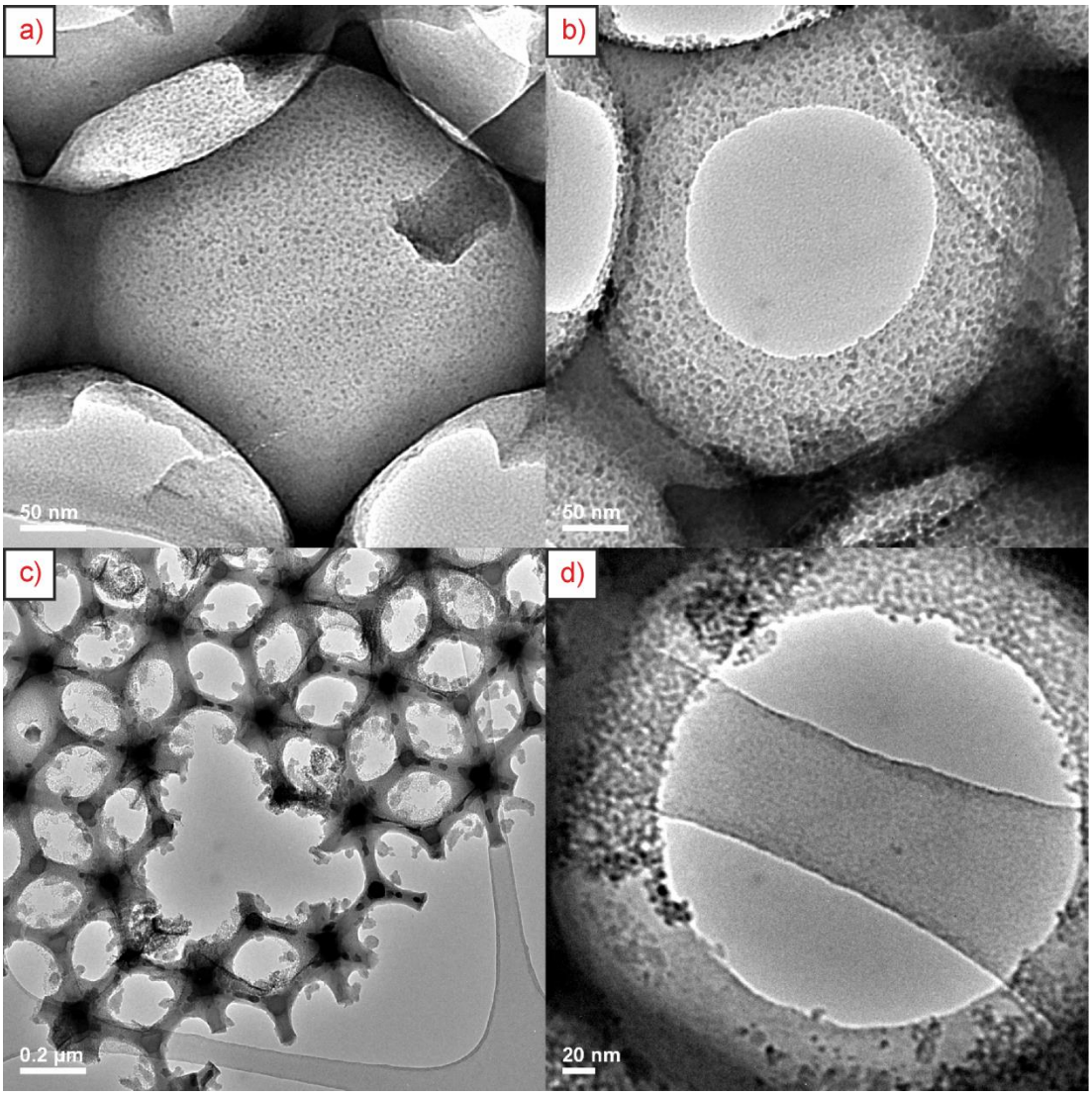

Figure 53: TEM images of TiO_2 loaded 3DOM SiO_2 deposited from nanoparticle dispersions in OA/hexane. (a) ***14.6%-TiO_2-395-SiO_2****, (b)* ***36%-TiO_2-395-SiO_2*** *and (c), (d)* ***58%-TiO_2-395-SiO_2.***

DRUVS was used to analyse the effect of loading on the stop band of the photonic material (Figure 54). As described in section 1.1.4b, for randomly oriented photonic crystal planes, the photonic stop band positions are defined by the Bragg-Snell equation:

Equation 12[99] $\lambda = \frac{2d_{hkl}}{m}[\phi n_{wall} + (1-\phi)n_{void}]$

A red shift of the stop band is observed, as predicted by Equation 12 for addition of a volume of nanoparticles with refractive index greater than that of air (1.00029). In addition to the shift in stop band position, a reduction in intensity of the bands is

observed, due to diminished ordering of the structure as a whole as a result of the local agglomeration. The effect is exacerbated in this sample due to the relatively low stop band of the uncoated 3DOM SiO_2 in comparison to other batches.

Overall, deposition quality from OA/hexane dispersions shows improvement over previous attempts. However, without the addition of OA to the solvent, more homogeneous nanoparticle distributions were observed using chloroform as opposed to hexane. This was attributed to the increased stability of nanoparticle dispersions in chloroform. As the solvent evaporates, OA/chloroform dispersions may be more stable to precipitation than OA/hexane dispersions. As a result, a better dispersion of TiO_2 nanoparticles would be retained in OA when all the solvent is removed, allowing for a more homogeneous deposition. Depositions from dispersions in OA/chloroform were attempted to test this hypothesis.

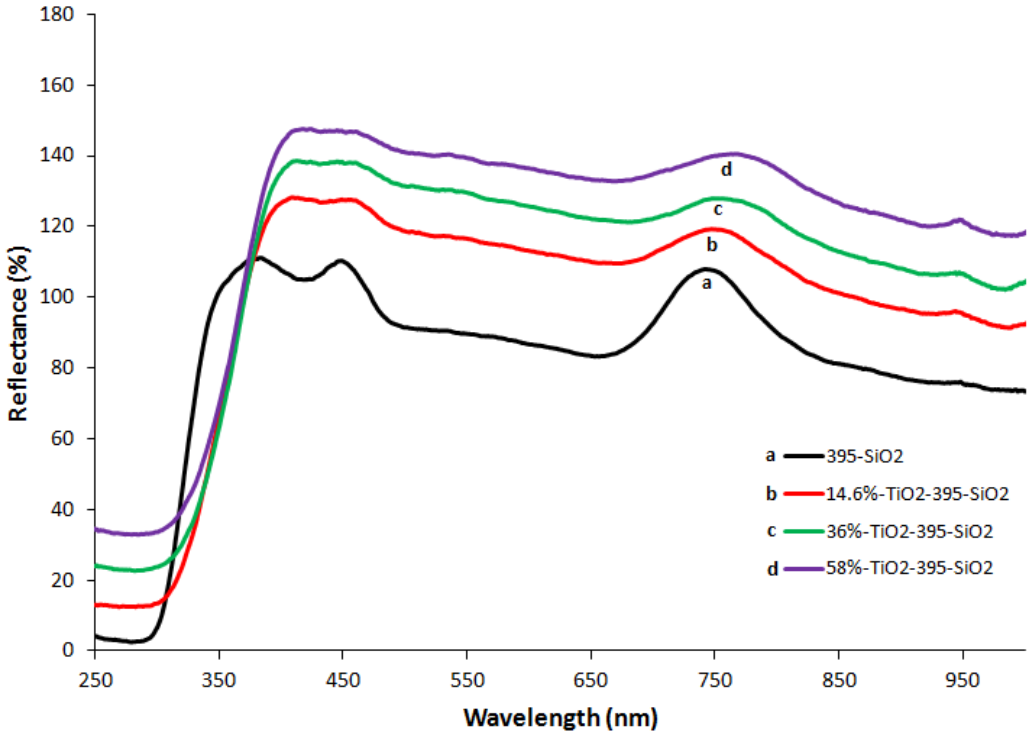

Figure 54: DRUVS spectra of TiO_2 loaded 3DOM SiO_2 deposited from nanoparticle dispersions in OA/hexane. Spectra are vertically offset for clarity.

3.2.2f: Deposition from OA/Chloroform Dispersions

Depositions were attempted using 0.1 M solutions of OA in chloroform as dispersant. After calcination of the composites, all microscopy data showed that high quality dispersions were obtained using this method. SEM images showed no agglomerates, appearing identical to images before deposition. TEM analysis showed a homogeneously coated surface, with no uncoated regions or aggregation of nanoparticles on the nanoscale. Different concentrations of oleic acid in chloroform were investigated, but 0.1 M was found to be optimum for reproducibly producing high quality dispersions of nanoparticles in the pores. Example TEM images and an electron diffraction pattern are shown in Figure 55. Additional TEM images of intermediate loadings are shown in the appendix (Figure 117). TEM images display a 2D representation of a cross section of sample. To evaluate the deposition of nanoparticles around the pores, a series of images as a function of the tilt angle of the TEM sample holder was obtained. Tilt series analysis confirmed that deposition around the entirety of the spherical pores was achieved. The lack of any surface films or agglomerations was also confirmed by tilt series analysis. An average TiO_2 particle size of 8.6 ± 1.5 nm was measured in the composites.

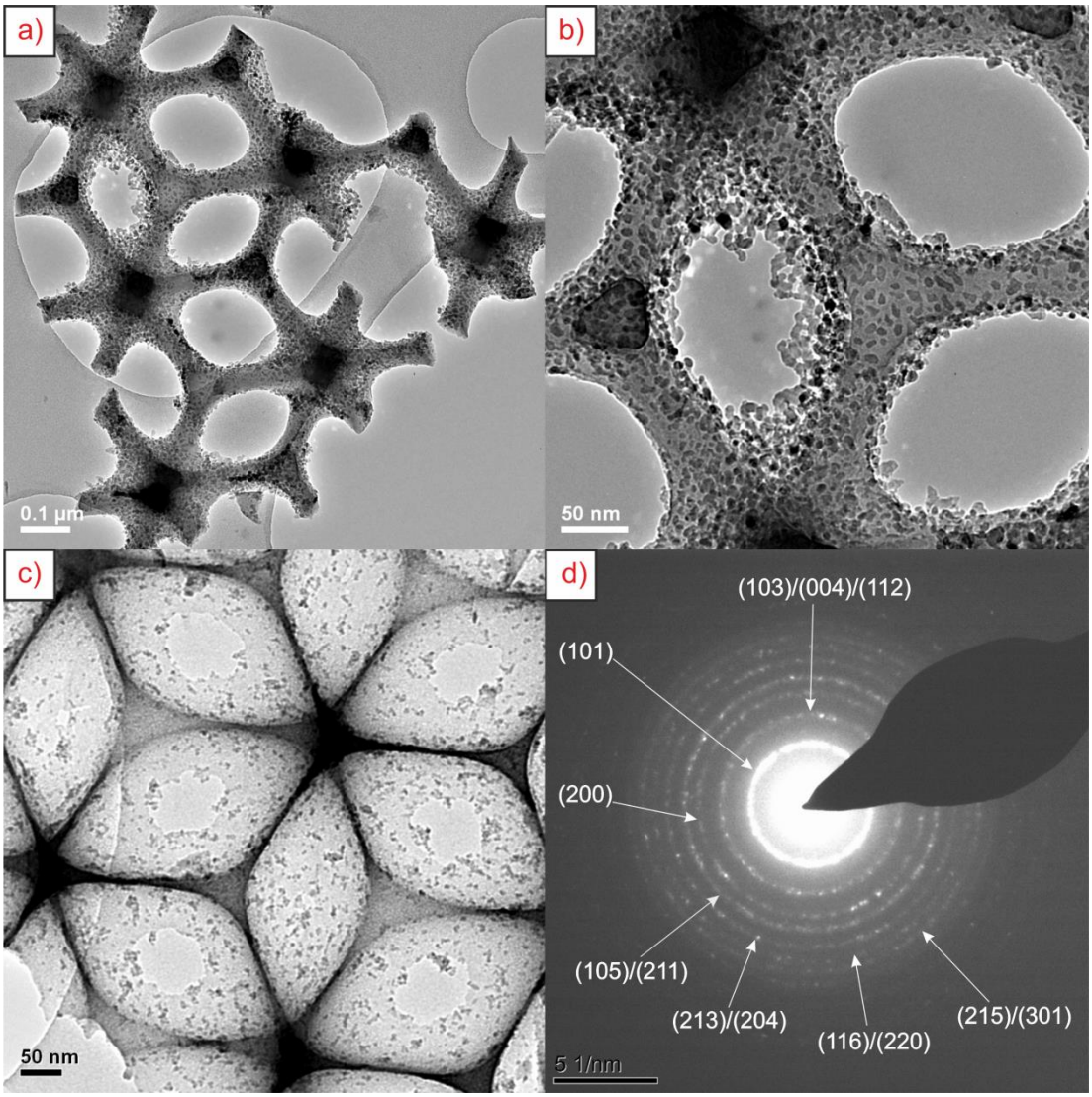

Figure 55: TEM images and electron diffraction of TiO_2 loaded 3DOM SiO_2 deposited from nanoparticle dispersions in OA/chloroform. (a), (b) ***58%-TiO_2-395-SiO_2****, (c)* ***7.3%-TiO_2-395-SiO_2*** *and (d) Electron diffraction pattern of the region in (b) indexed as anatase TiO_2, JCPDS 01-078-2486.*

SEM EDX analysis was used to analyse the elemental compositions of samples after deposition. EDX scans were performed on 10 different 50 x 35 µm areas of the sample containing only porous particles. The experimental average weight % and atom % for TiO_2 loaded 3DOM SiO_2 samples are shown in Table 9. The expected elemental compositions were calculated based on the initial masses of 3DOM SiO_2 and TiO_2, and compared to the experimental values. Good agreement is observed between the experimental data and the calculated values, confirming that all

deposited nanoparticles are loaded into the pores, and further supporting the CHN analysis of the OA/TiO_2 nanoparticles.

Sample	Average Weight %				Average Atom %				EDX TiO_2/SiO_2 wt%[a]
	Ti		Si		Ti		Si		
	Exp	Calc	Exp	Calc	Exp	Calc	Exp	Calc	
3.6%-TiO_2-395-SiO_2	2.1 ±0.6	2.1	47.0 ±5.4	45.1	0.9 ±0.3	0.9	34.3 ±5.0	32.4	3.5 ± 0.7
11%-TiO_2-395-SiO_2	5.8 ±1.5	5.9	40.0 ±2.4	42.1	2.4 ±0.6	2.5	28.9 ±2.0	30.8	11.0 ± 1.6
22%-TiO_2-395-SiO_2	9.2 ±2.1	10.7	38.6 ±5.2	38.4	4.0 ±1.0	4.7	28.6 ±4.9	28.6	18.6 ± 2.6
36%-TiO_2-395-SiO_2	15.2 ±2.1	16.0	34.3 ±2.3	34.3	6.8 ±1.0	7.2	26.0 ±1.8	26.2	34.8 ± 2.1

Table 9: Large area SEM EDX analysis of TiO_2 loaded 3DOM SiO_2 samples. Data was collected at an accelerating voltage of 10 kV on 50 x 35 µm areas of sample. [a]For example calculation, see appendix section A1.5.

In addition to large area compositional analysis via SEM EDX, TEM EDX mapping data was obtained to analyse the elemental distribution within the pores. The elemental maps of a cross section of sample are shown in Figure 56. Ti, Si and O maps were obtained for the region shown. High correlation is observed between the three maps and the base image, confirming the homogeneity of the TiO_2 coating. EDX analysis of other regions of the sample showed the same trends. All electron microscopy data obtained suggests a highly dispersed nanoparticle distribution, observed on all length scales.

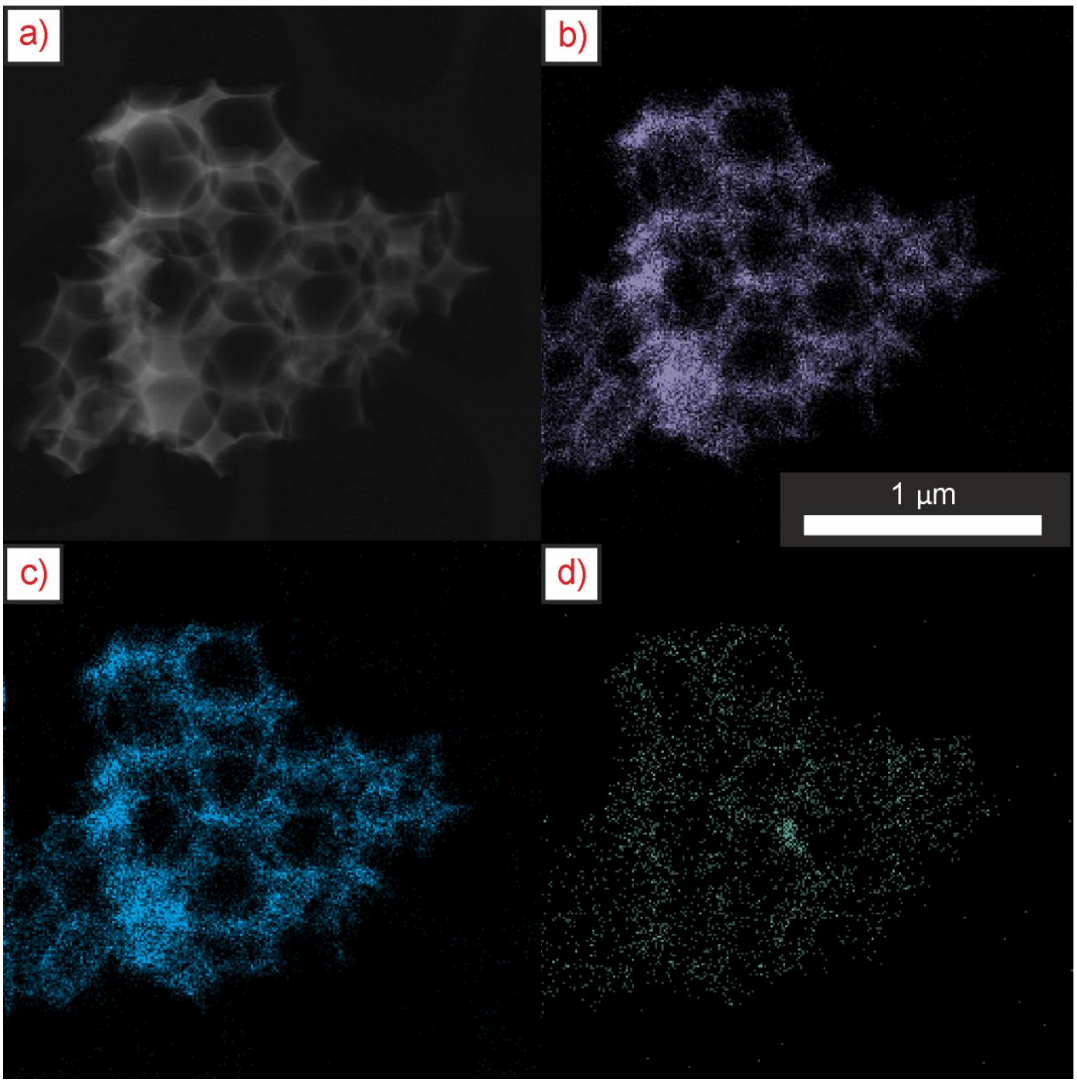

*Figure 56: TEM EDX mapping data for **7.3%-TiO_2-395-SiO_2**. (a) HAADF STEM image, (b) Si map, (c) O map, (d) Ti map. 1 µm scale bar applies to all images.*

PXRD data for the composite sample was obtained, and is shown in Figure 57. All crystalline peaks from the sample can be indexed to tetragonal anatase TiO_2, JCPDS number 01-078-2486. The electron diffraction pattern in Figure 55d confirms this assignment. The oleic acid functionalised nanoparticles showed an orthorhombic TiO_2 phase, hence a phase transition has been effected on calcination to form the tetragonal anatase polymorph. From the FWHM of the peak at 25.2 ° 2θ, an estimated crystallite size of 10.5 nm was calculated using the Scherrer equation. The average size of particles measured from TEM images (8.6 ± 1.5 nm) is in reasonable agreement with this value.

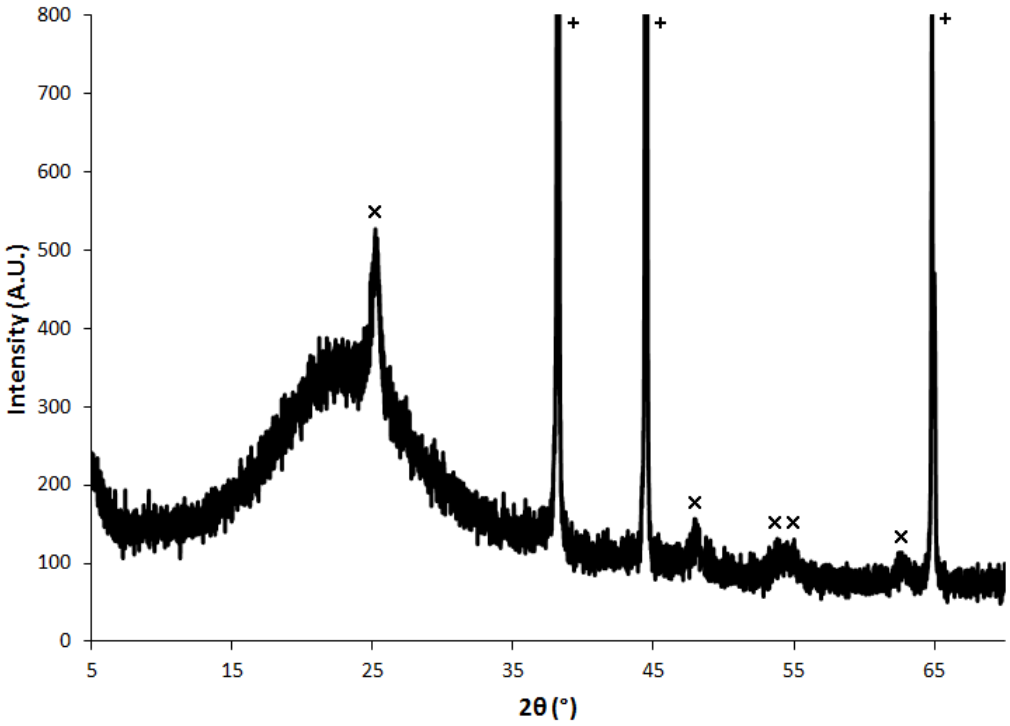

Figure 57: PXRD pattern of ***36%-TiO$_2$-395-SiO$_2$*** *from OA/chloroform dispersions. X = tetragonal anatase TiO$_2$, JCPDS 01-078-2486, + = Al sample holder.*

Analysis of the DRUVS spectra (Figure 58) shows a red shift in the (111) stop band position of 5.5 – 16 nm for **7.3%-TiO$_2$-395-SiO$_2$** – **36.4%-TiO$_2$-395-SiO$_2$**. This is predicted based on Equation 12. Addition of any material with refractive index greater than that of air (1.00029) to the pore surface will increase the value of the brackets in Equation 12 and result in a red shift of the stop band. Hence, this shift confirms that TiO_2 nanoparticles have been deposited at the interface between the SiO_2 wall and the void space and contribute to the photonic structure, as opposed to the formation of outer surface films.

To model the shift, a modification was made to the Bragg-Snell equation to include an additional component for the nanoparticles (Equation 13):

$$\textit{Equation 13} \quad \lambda_{new} = 2d_{hkl}(\varphi\, n_{wall} + \chi_{NP}\, n_{NP} + (1 - \varphi - \chi_{NP}) n_{void})$$

Where χ_{NP} and n_{NP} are the volume fraction and refractive index of the nanoparticles, and λ_{new} is the shifted position of the stop band. The periodicity of each sample was measured from SEM images by averaging of at least 100 measurements from

different regions of the sample, and used to calculate d_{hkl}. The wall fill factor of the composite, ϕ_{total}, is defined by the following expression:

$$\textit{Equation 14} \quad \varphi_{total} = \varphi + \chi_{NP}$$

An expression for χ_{NP} was determined by subtraction of the Bragg-Snell equation (Equation 12) from Equation 13 to give Equation 15:

$$\textit{Equation 15} \quad \chi_{NP} = \frac{\lambda_{new} - \lambda}{2d_{hkl}(n_{NP} - n_{void})}$$

Values of χ_{NP} were calculated for the loading series using λ_{new} values from the experimental data set. To verify the values of χ_{NP}, the new stop band position was modelled based on addition of nanoparticles to the wall material. On nanoparticle loading, an increase in the average refractive index of the wall and total fill factor can be calculated. TiO_2 has a higher refractive index than SiO_2. As TiO_2 is loaded onto the walls of the porous material, the average refractive index of the two components will be higher than for SiO_2 alone. The average wall refractive index, n_{ave} was calculated using Equation 16:

$$\textit{Equation 16} \quad n_{ave} = \frac{n_{wall} + n_{NP}(\%_{NP}.\frac{\rho_{wall}}{\rho_{NP}})}{1 + (\%_{NP}.\frac{\rho_{wall}}{\rho_{NP}})}$$

Where $\%_{NP}$ is the wt% of nanoparticles added and ρ is the density of the components. In the denominator, the 1 represents the initial quantity of host, and the bracket the additional contribution from the nanoparticles. The expected stop band position of the composites was calculated using Equation 17:

$$\textit{Equation 17} \quad \lambda_{calc} = 2d_{hkl}(\varphi_{total} n_{ave} + (1 - \varphi_{total}) n_{void})$$

Alternatively, shifts could be modelled based on addition of nanoparticles to the void space, which would return the same parameters. Addition of a surface film of nanoparticles will slightly reduce the pore size of the materials, however the periodicity of the photonic crystal lattice remains unchanged, and hence d_{hkl} remains constant.

Figure 59 shows the experimentally observed relationship between the weight fraction of nanoparticles loaded into the pores and the position of the stop band maximum. The shift in stop band maximum increases linearly with loading, which confirms that an increase in targeted loading corresponds with an increase in the amount of nanoparticles loaded into the pores. The calculated shifts for each loading are plotted alongside the experimentally observed values. A good agreement is observed, confirming the loading of nanoparticles can be controlled by adjustment of the precursor ratio. This trend allows for prediction of the new stop band position when loading a certain amount of material into the pores or determination of the loading amount for an unknown composition, which are important considerations for optimising the relationship between the photonic stop band of the support and the electronic band gap of the nanoparticles.

For this sample of **395-SiO_2**, a fill factor of ϕ = 8.88 % was calculated using Equation 12. The calculated values of χ_{TiO2}, n_{avg} and ϕ_{total} along with the experimental and calculated stop band shifts are shown in Table 10. As further verification of the calculated data, the volume of nanoparticles added was calculated based on the starting masses of TiO_2 and SiO_2 and their respective densities. The ratio of the volume of nanoparticles added to the volume of SiO_2 was in good agreement with the ratio of χ_{TiO2} to ϕ, representing the volume fraction of TiO_2 and SiO_2, for all samples. This analysis suggests the complete loading of all added nanoparticles into the photonic structure, consistent with the lack of aggregates observed by SEM and TEM. The errors involved in this model will be discussed in appendix section A2.5.

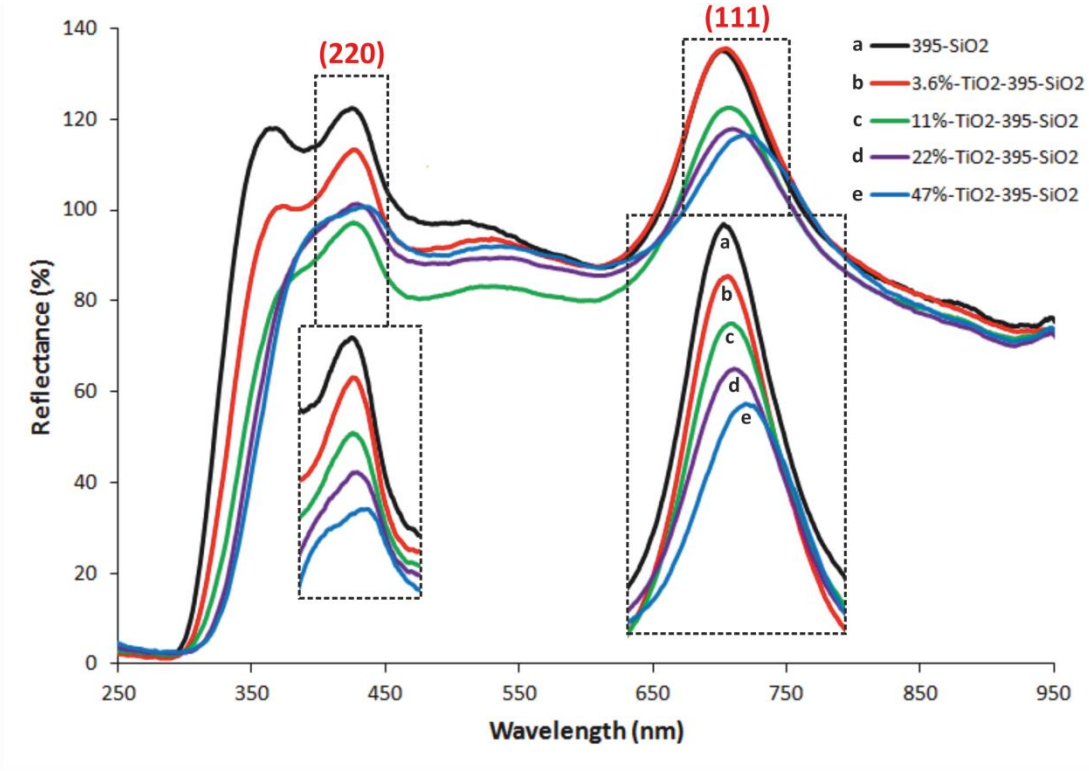

Figure 58: DRUVS spectra of 3DOM SiO_2 and TiO_2 loaded 3DOM SiO_2. Insets: Zoomed view of photonic stop bands, vertically offset for clarity.

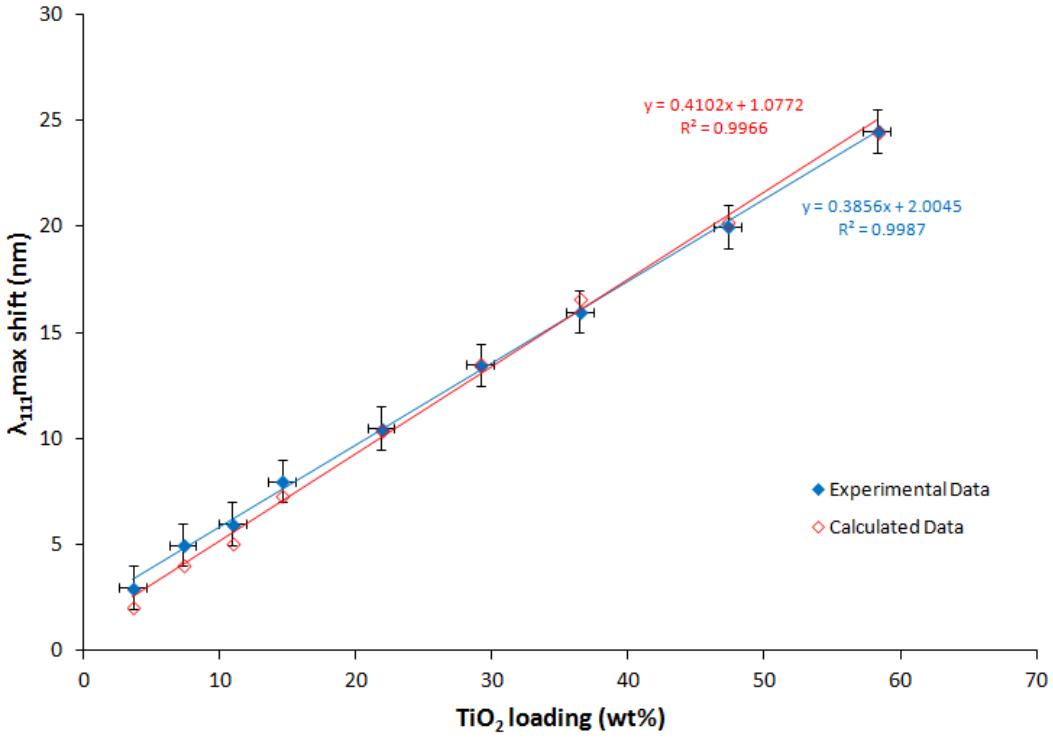

Figure 59: Line plot showing experimental and calculated stop band shift for TiO_2 loaded 3DOM SiO_2 samples.

Sample	χ_{TiO2} / %	n_{avg}	ϕ_{total} / %	Experimental λ_{111} shift[a] / nm	Calculated λ_{111} shift / nm
7.3%-TiO_2-395-SiO_2	0.52	1.493	9.40	5.5	4.05
14.6%-TiO_2-395-SiO_2	0.81	1.528	9.68	8.0	7.33
21.8%-TiO_2-395-SiO_2	1.05	1.561	9.92	10.5	10.41
29.1%-TiO_2-395-SiO_2	1.31	1.591	10.19	13.5	13.53
36.4%-TiO_2-395-SiO_2	1.57	1.620	10.45	16.0	16.63

Table 10: Fill factors, wall refractive indices and stop band shifts for TiO_2 loaded 3DOM SiO_2. [a]Spectrometer resolution 0.5 nm.

In the literature, Zhao *et al.* have shown the deposition of silver nanoparticles in TiO_2 photonic crystals using a chemical bath method.[114] On loading of their materials with nanoparticles, a drop in the stop band intensity is observed as seen in this work. A comparison between the nanoparticle/3DOM material atomic ratio and height of the resultant stop band shown in their work and in Figure 58 is presented in Table 11. Directly comparing the data, their sample ATIO-2 with 0.14 Ag/Ti atom ratio as determined by XPS shows the same loading as the **22%-TiO_2-395-SiO_2** sample reported here (Ti/Si = 0.14 by EDX). The sample **47%-TiO_2-395-SiO_2** is calculated to give a Ti/Si ratio intermediate to the Ag/Ti ratios of the ATIO-5, ATIO-10 and ATIO-20 samples presented in the paper.

For all TiO_2/SiO_2 samples in this work, the reduction in peak height is less marked than for Ag/TiO_2. For the samples with 0.14 nanoparticle/inverse opal atomic ratio, the stop band intensity of the TiO_2/SiO_2 sample is greater than for Ag/TiO_2. The stop band intensity of the highest loading in this study is also greater than the literature samples with similar loadings. As an additional observation, the position of the stop band in the literature work is blue shifted slightly in some samples. Silver has a refractive index less than 1 in the visible region,[239] and hence for incorporation of a volume fraction of nanoparticles into the voids, the term in brackets in Equation 13 will decrease. Alternatively, the blue shift of the stop band could be due to contraction of the walls on heating. For the purposes of this analysis, the primary

consideration is the effect on the ordering of the structure, and hence intensity of the stop band, due to addition of nanoparticles.

Of particular highlight is the consistency of the two methods. Using the chemical bath approach to Ag/TiO_2 composites, a greater intensity loss is observed for the lowest and highest loadings in comparison to the intermediate loadings, suggesting inhomogeneous deposition in these materials. In contrast, TiO_2/SiO_2 samples prepared by the method presented in this work show a progressive decrease in stop band intensity as the loading amount is increased. The use of ligand stabilised nanoparticles for deposition allows for a better quality of dispersion, and an increased control over the position of the stop band on loading, in comparison to an equivalent chemical bath approach.

Sample **(Bold – This work)**	Ag/Ti atom ratio (%)	Ti/Si atom ratio (%)	Stop band height relative to uncoated IO (%)
3.6%-TiO_2-395-SiO_2	**N/A**	**2.6 (EDX)**	**100**
11%-TiO_2-395-SiO_2	**N/A**	**8.3 (EDX)**	**87.4**
22%-TiO_2-395-SiO_2	**N/A**	**14 (EDX)**	**67.8**
ATIO-2	14 (XPS)	N/A	13.2
ATIO-5	31 (XPS)	N/A	52.0
ATIO-10	34 (XPS)	N/A	39.4
47%-TiO_2-395-SiO_2	**N/A**	**35.6 (calc)**	**60.8**
ATIO-20	38 (XPS)	N/A	6.6

Table 11: Comparison of the effect on nanoparticle loading in 3DOM materials in this study and in the work of Zhao et al.[114] Samples are listed in order of increasing NP/host ratio. Peak heights were measured from baseline to maximum using a ruler.

The success of this method appears to lie in the stability of the nanoparticle dispersion. As the chloroform is evaporated to leave an oleic acid/nanoparticle/3DOM SiO_2 composite, the dispersion of nanoparticles within the liquid OA phase is retained. Due to the OA coating on the 3DOM surface, van der Waals forces of attraction between the nanoparticles and support are greater than the nanoparticle-nanoparticle interactions. As the oleic acid is heated above its

boiling point of 360 °C, nanoparticles are deposited onto the OA-coated 3DOM material by capillary forces as the meniscus travels along the surface, in a similar fashion to vertical deposition of PS spheres described in section 2.2.4a. In the literature, deposition of PS spheres and zeolite particles have been demonstrated on curved surfaces by capillary forces.[240, 241] As the temperature is increased, surface bound oleic acid is removed from the nanoparticles as evidenced by TGA. Bonds are formed between the TiO_2 nanoparticles and the SiO_2 support, anchoring them at the surface. Formation of Si-O-Ti bonds has been demonstrated in the synthesis of TiO_2@SiO_2 core shell particles at temperatures greater than 85 °C.[242] The presence of strong Si-Ti interactions is suggested by the stability of the composites on addition of solvents, *ie.* no removal of nanoparticles is observed.

In the case of OA/chloroform dispersions, a more homogeneous distribution of nanoparticles within the pores is observed after calcination compared to deposition from dispersions in OA/hexane. Although dispersions in OA/hexane remained stable for long periods of time if undisturbed, partial sedimentation must occur as the concentration of solvent is decreased, resulting in some agglomeration of nanoparticles. Deposition from OA/toluene was also investigated, and observed to produce high quality composite materials similar to OA/chloroform.

In summary, homogeneous deposition of nanoparticles was achieved through simple modifications to the surface of the 3DOM support and the solvent used for dispersion. In order to investigate the generality of the method, variation in the chemical identity of the support and nanoparticles will be reported in the following sections.

3.2.3: OA/TiO_2 Deposition in ZrO_2 Inverse Opals

Coating of oleic acid onto 3DOM ZrO_2 was attempted using the same method as for 3DOM SiO_2. IR spectroscopy was used to analyse the binding of oleic acid to the surface and determine the optimum time to soak the support for maximal adsorption. After soaking for three hours, clear peaks were observed at 2923 cm^{-1}

and 2856 cm^{-1} attributable to C-H stretches, 1544 cm^{-1} and 1414 cm^{-1} attributable to COO^-, and 1715 cm^{-1} attributable to C=O (see appendix Figure 115) TGA was used to study the quantity of adsorbed OA, showing a mass loss of 2.1 % around 300 °C. Using the cross sectional area of oleic acid and surface area of the 3DOM ZrO_2 sample, this value was found to correspond to a monolayer of OA on the surface.

Using OA/chloroform nanoparticle dispersions, deposition was attempted in OA-coated 3DOM ZrO_2. After calcination using the same conditions as for TiO_2/3DOM SiO_2, the intensity of the colour of the samples was observed to decrease. SEM imaging showed collapse of macropores, suggesting these conditions are too harsh for 3DOM ZrO_2. Instead, samples were calcined at 450 °C for 4 hours (ramp rate 1 °C min^{-1}), in line with the original synthesis of 3DOM ZrO_2. Structural collapse was not observed under these conditions. After calcination, SEM images of the composite materials showed no agglomerates (Figure 60a). No change in the periodicity of 3DOM ZrO_2 was observed after calcination. TEM images of the composite materials are displayed in Figure 60b – d, showing a homogeneous distribution of nanoparticles within the pores.

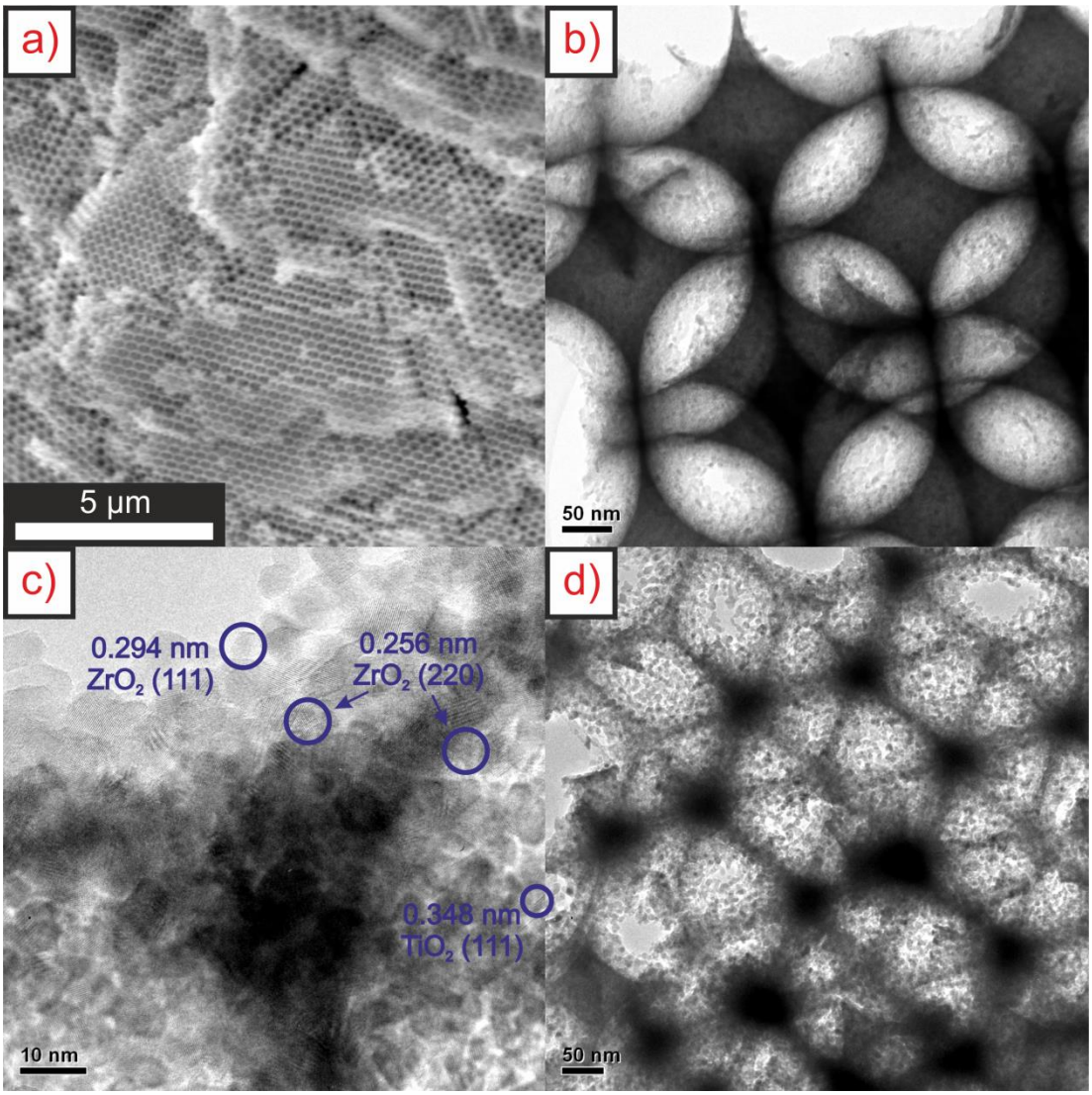

Figure 60: SEM and TEM images of TiO_2 loaded 3DOM ZrO_2 deposited from nanoparticle dispersions in OA/chloroform. (a) SEM and (b), (c) TEM images of ***7.3%-TiO_2-343-ZrO_2****, and (d) TEM image of* ***36%-TiO_2-271-ZrO_2****.*

PXRD analysis showed a two phase product, containing tetragonal anatase TiO_2, JCPDS 01-078-2486 and tetragonal ZrO_2, JCPDS 01-079-1763 (Figure 61). On calcination, the TiO_2 nanoparticles are converted to the anatase polymorph as observed for TiO_2/3DOM SiO_2 samples. From the FWHM of the peak at 25.3 ° 2θ, an estimated crystallite size of 10.7 nm was calculated using the Scherrer equation, similar to the size of TiO_2 nanoparticles in 3DOM SiO_2 (10.5 nm). Analysis of the particle size using TEM images gives a value of 8.8 ± 1.2 nm, in reasonable agreement with PXRD and comparable to the size of TiO_2 particles in 3DOM SiO_2 measured by TEM (8.6 ± 1.5 nm). TEM EDX mapping data was obtained as for

TiO_2/SiO_2 composites. Homogeneous nanoparticle deposition was confirmed by correlation between Ti, Zr and O maps.

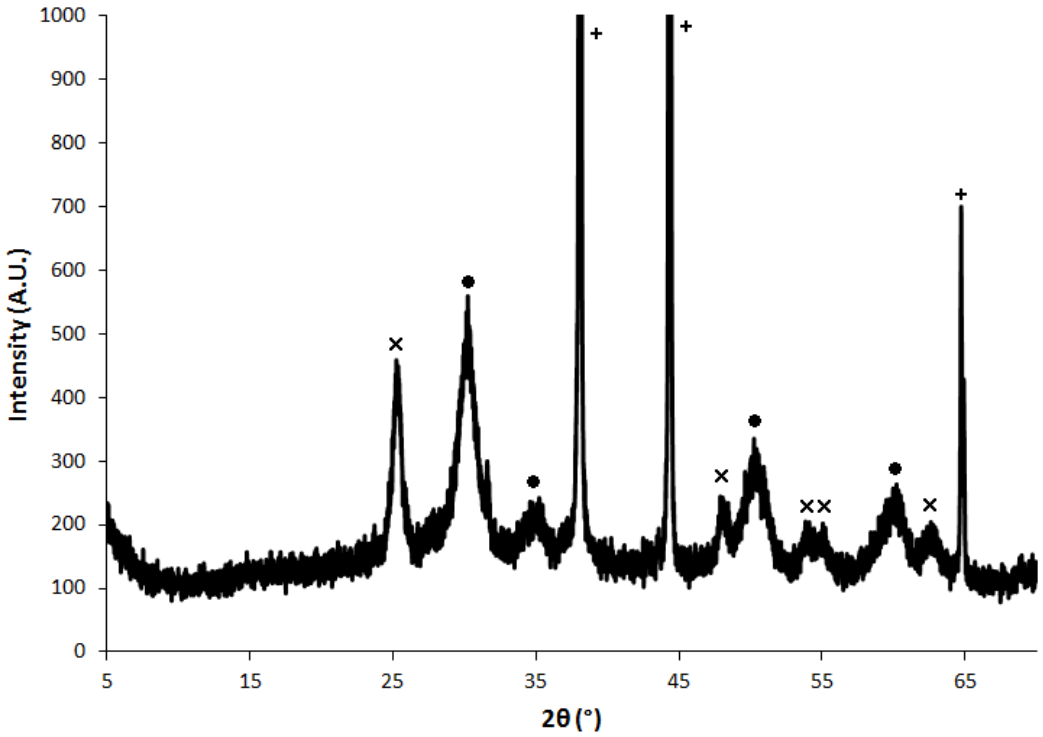

*Figure 61: PXRD pattern of **58%-TiO_2-271-ZrO_2** sample. X = tetragonal anatase TiO_2, JCPDS 01-078-2486, O = tetragonal ZrO_2, JCPDS 01-079-1763.*

The reflectance spectra of TiO_2/3DOM ZrO_2 samples were analysed with respect to the loading of TiO_2. A red shift in the (111) stop band position of 3.5 – 25.5 nm was observed for **3.5%-TiO_2-271-ZrO_2** – **26.5%-TiO_2-271-ZrO_2** (Figure 62). Using the periodicity of 3DOM ZrO_2 from SEM measurements, the fill factor of the uncoated 3DOM ZrO_2 was calculated as ϕ = 15.4 % using Equation 12. From the experimental data, values of χ_{TiO2}, n_{avg} and ϕ_{total} were calculated as a function of the loading amount using Equation 13. Equation 17 was then used to calculate the expected stop band shift as above for TiO_2/3DOM SiO_2 composites. The calculated stop band shift is plotted graphically in Figure 63 and agrees well with the experimentally observed shifts. The values of χ_{TiO2}, n_{avg}, ϕ_{total} and the experimental and calculated stop band shifts are listed in Table 12. The linear relationship between stop band shift and nanoparticle loading confirms the correlation between increased targeted loading and an increase in the amount of nanoparticles loaded into the pores.

Sample	χ_{TiO2} / %	n_{avg}	ϕ_{total} / %	Experimental λ_{111} shift[a] / nm	Calculated λ_{111} shift / nm
3.5%-TiO_2-271-ZrO_2	0.57	2.213	16.0	3.5	3.68
7.0%-TiO_2-271-ZrO_2	1.23	2.225	16.6	7.5	7.75
10.6%-TiO_2-271-ZrO_2	1.80	2.236	17.2	11.0	11.40
14.1%-TiO_2-271-ZrO_2	2.29	2.246	17.7	14.0	14.62
17.6%-TiO_2-271-ZrO_2	2.87	2.255	18.2	17.5	18.24
26.5%-TiO_2-271-ZrO_2	4.18	2.276	19.6	25.5	26.64

Table 12: Fill factors, wall refractive indices and stop band shifts for TiO_2 loaded 3DOM ZrO_2. [a]Spectrometer resolution 0.5 nm.

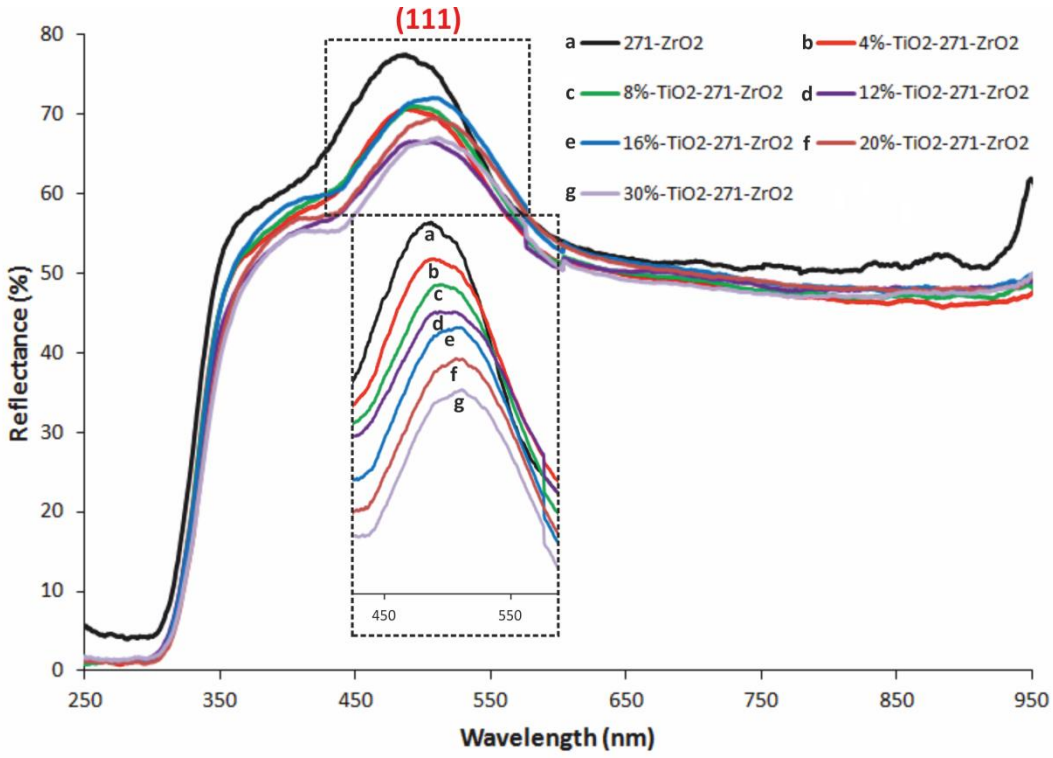

Figure 62: DRUVS spectra of 3DOM ZrO_2 and TiO_2 loaded 3DOM ZrO_2. Inset: Zoomed view of photonic stop bands, vertically offset for clarity.

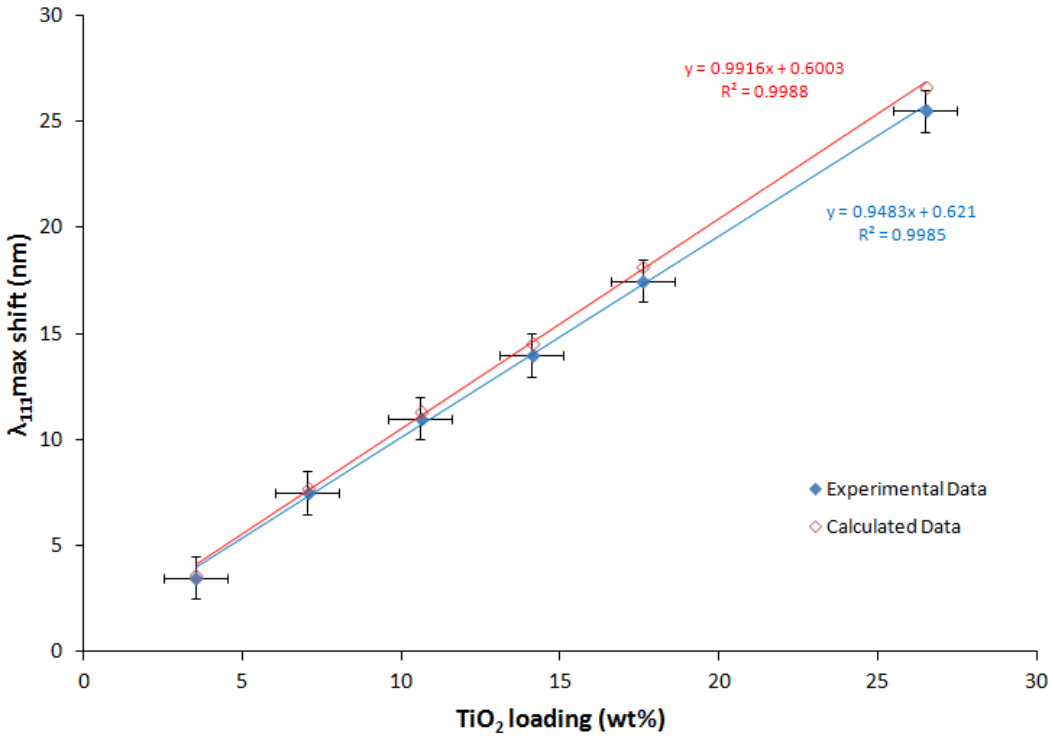

Figure 63: Line plot showing experimental and calculated stop band shift for TiO_2 loaded 3DOM ZrO_2 samples.

The surface area of nanoparticle loaded 3DOM materials was measured by nitrogen adsorption porosimetry. Nitrogen adsorption/desorption isotherms resemble a type II isotherm as classified by IUPAC, and are displayed in Figure 64. Table 13 lists the surface area of uncoated and 10 wt% TiO_2 loaded 3DOM SiO_2 and ZrO_2 materials. For 3DOM SiO_2, a slight decrease in surface area is observed, which suggests that access to hollows in the amorphous walls is blocked. For 3DOM ZrO_2 however, an increase in surface area is observed, which suggests that the roughness of the surface, and hence the overall surface area, is increased by addition of nanoparticles.

Material	Surface area before NP loading / $m^2\ g^{-1}$	Surface area after 10 wt% TiO_2 NP loading / $m^2\ g^{-1}$
395-SiO_2	91 ± 1	83 ± 1
271-ZrO_2	20.6 ± 0.3	29.1 ± 0.3

Table 13: Surface area of 3DOM SiO_2 and ZrO_2 loaded with TiO_2 nanoparticles.

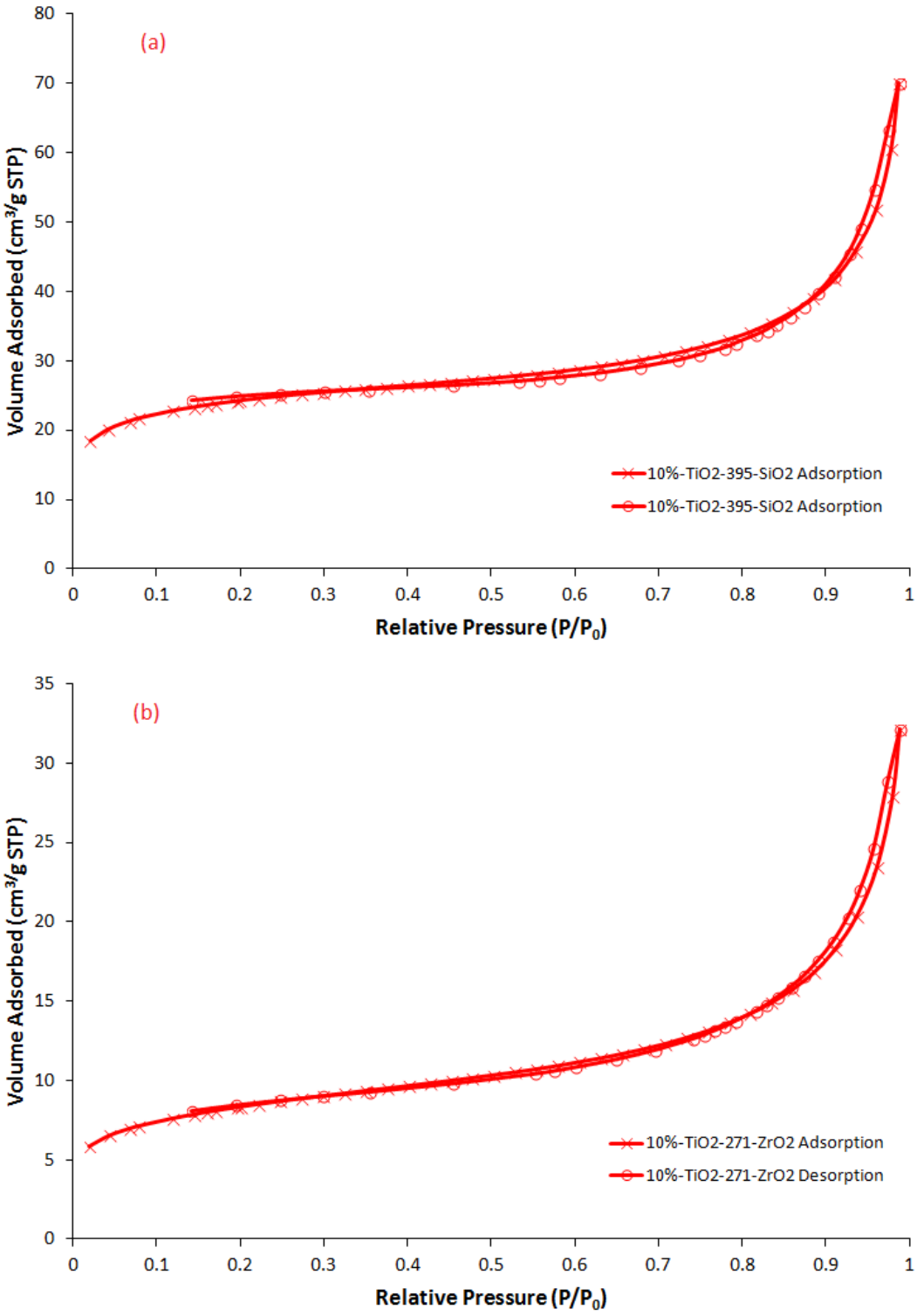

Figure 64: Nitrogen adsorption/desorption isotherm for (a) ***10%-TiO_2-395-SiO_2*** *and (b)* ***10%-TiO_2-271-ZrO_2.***

3.2.4: Deposition of OA/Fe_3O_4 Nanoparticles in 3DOM SiO_2 and ZrO_2

To assess the generality of the deposition technique, its application to the deposition of ligand stabilised nanoparticles of other materials was investigated. Fe_3O_4, or magnetite, is a non-photocatalytically active material with many applications due to its magnetic properties. Magnetite nanoparticles are of interest for MRI imaging,[243, 244] and montmorillonite clay supported magnetite nanoparticles have been used for removal of Cr(VI) from waste water.[245] Using the deposition method developed for OA/TiO_2 nanoparticles, deposition of OA/Fe_3O_4 nanoparticles was investigated in 3DOM SiO_2 and ZrO_2.

Deposition of OA capped Fe_3O_4 nanoparticles in 3DOM SiO_2 and 3DOM ZrO_2 was attempted as outlined above for TiO_2. Nanoparticle dispersions in OA/chloroform were evaporated onto the support, followed by calcination at 500 °C, 5 hours (ramp rate 5 °C min^{-1}) for 3DOM SiO_2 and 450 °C, 4 hours (ramp rate 1 °C min^{-1}) for 3DOM ZrO_2.

SEM images of the composite materials showed no signs of agglomeration, and TEM imaging showed a well dispersed array of nanoparticles of size 2.89 ± 0.42 nm within the pores of 3DOM SiO_2 (Figure 65). These particles are contributed from the smaller amorphous particles observed in TEM images of OA/Fe_3O_4. For high targeted loadings (> 40 wt%), scanning across the surface in the TEM showed some spherical crystalline agglomerates of Fe_3O_4 with diameter around 100 nm, however in comparison to pristinely coated pores their concentration was small. No uncoated regions were observed. The crystal phase of Fe_3O_4 in the composites was analysed by electron diffraction (Figure 65c), showing cubic Fe_3O_4 with low crystallinity as evidenced by the low intensity of the diffraction rings. The elemental composition of a **32.8%-Fe_3O_4-395-SiO_2** sample was analysed using EDX mapping, confirming that the observed nanoparticle species are iron based (Figure 66). In addition, the homogeneity of the dispersion is supported by the correlation in appearance between Si, Fe and O maps.

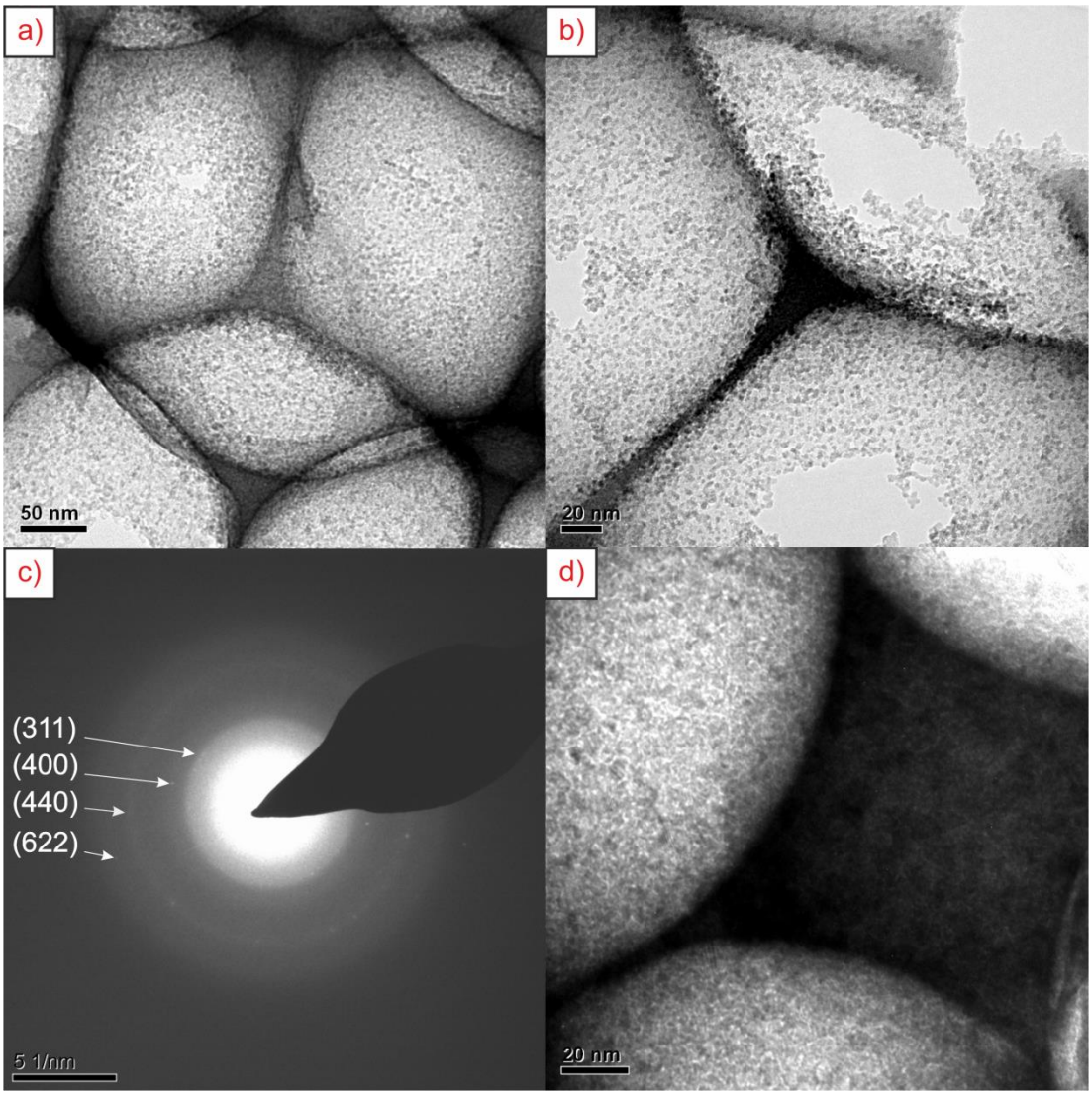

Figure 65: TEM images and electron diffraction for Fe_3O_4 nanoparticles loaded in 3DOM SiO_2 and ZrO_2. (a), (b) ***65.6%-Fe_3O_4-395-SiO_2,*** *(c) Electron diffraction pattern of region in (a) indexed as cubic Fe_3O_4, and (d)* ***41%-Fe_3O_4-271-ZrO_2.***

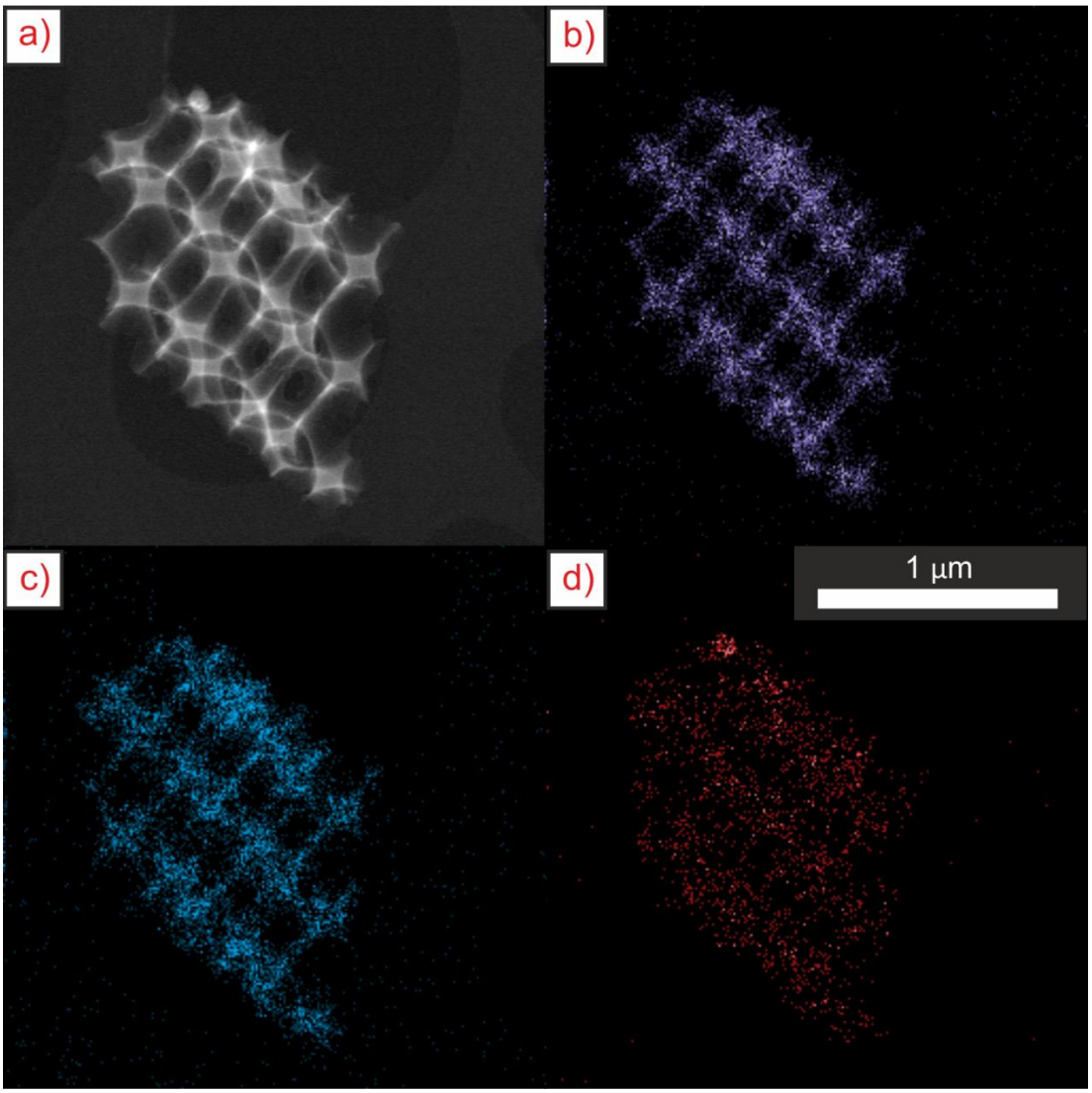

Figure 66: TEM EDX mapping data for ***32.8%-Fe_3O_4-395-SiO_2.*** *(a) HAADF STEM image, (b) Si map, (c) O map, (d) Fe map. 1 µm scale bar applies to all images.*

XRD analysis of **49.2%-Fe_3O_4-395-SiO_2** is shown in Figure 67. The observed peaks are assigned as cubic Fe_3O_4, matching JCPDS 01-088-0866, as with the OA capped nanoparticles. From the peak at 35.3 ° 2θ, the Scherrer equation was used to calculate an Fe_3O_4 crystallite size of 14 nm. The nanoparticle sizes observed from TEM images are much smaller than this value. The intensity of the PXRD peaks are low in comparison to the background, indicating the majority of the incorporated material is amorphous as suggested by TEM imaging. This suggests the crystalline peaks in the PXRD pattern are due to the spherical agglomerates observed by TEM. No crystalline peaks were observed for low loadings of Fe_3O_4 (4 – 40 wt%), confirming this assessment.

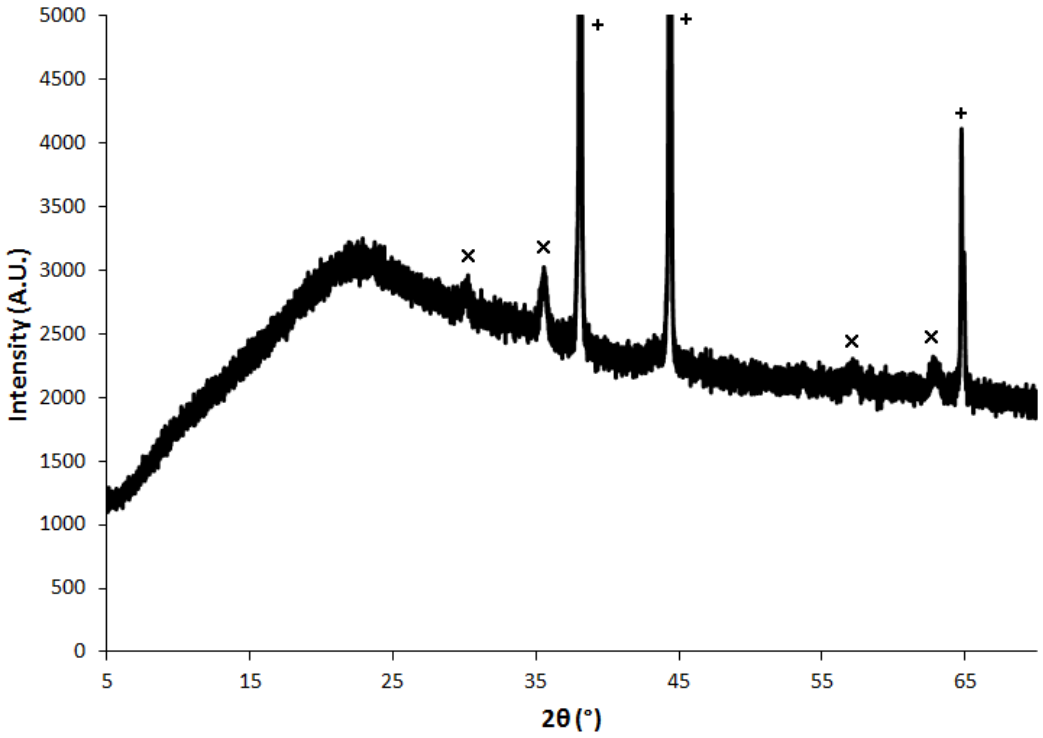

*Figure 67: PXRD pattern of **49.2%-Fe_3O_4-395-SiO_2**. X = cubic Fe_3O_4, JCPDS 01-088-0866, broad feature at 23° = SiO_2, + = Al sample holder.*

As with previous samples, DRUVS spectra of a series of increasing wt% Fe_3O_4 in 3DOM SiO_2 samples showed red shifts in the (111) stop band position of 1.5 – 18 nm for **4.1%-Fe_3O_4-395-SiO_2 – 65.6%-Fe_3O_4-395-SiO_2** (Figure 68a). The stop band shift was plotted as a function of the loading amount (Figure 68b). A linear relationship is observed, confirming the correlation between the targeted loading amount and the amount of material incorporated into the pores. Using the periodicity of 3DOM SiO_2 from SEM measurements, the fill factor of the uncoated 3DOM SiO_2 was calculated as ϕ = 6.64 % using Equation 12. From the experimental data, values of χ_{Fe3O4}, n_{avg} and ϕ_{total} were calculated as a function of the loading amount using Equation 13. Equation 17 was then used to calculate the expected stop band shift as above for TiO_2/3DOM SiO_2 composites. The values of χ_{Fe3O4}, n_{avg}, ϕ_{total} and the experimental and calculated stop band shifts are listed in Table 14. The calculated stop band shift is plotted graphically in Figure 68b, and agrees well with the experimentally observed shifts.

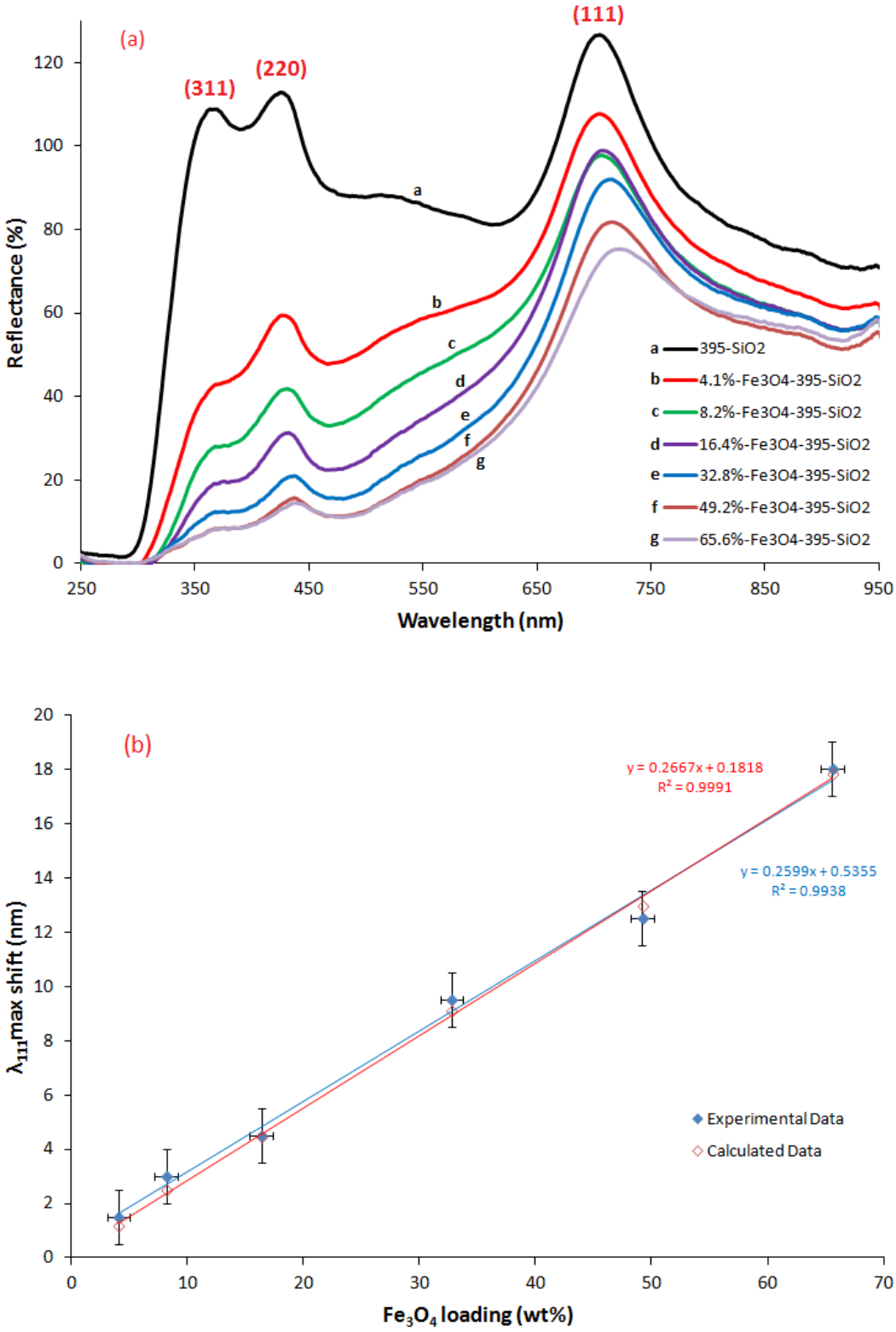

Figure 68: (a) DRUVS spectra of 3DOM SiO_2 and Fe_3O_4 loaded 3DOM SiO_2 and (b) experimentally measured and calculated stop band shift as a function of loading.

Sample	χ_{Fe3O4} / %	n_{avg}	ϕ_{total} / %	Experimental λ_{111} shift[a] / nm	Calculated λ_{111} shift / nm
4.1%-Fe_3O_4-395-SiO_2	0.14	1.471	6.78	1.5	1.19
8.2%-Fe_3O_4-395-SiO_2	0.32	1.487	6.96	3.0	2.54
16.4%-Fe_3O_4-395-SiO_2	0.45	1.518	7.1	4.5	4.45
32.8%-Fe_3O_4-395-SiO_2	0.96	1.573	7.6	9.5	9.10
49.2%-Fe_3O_4-395-SiO_2	1.28	1.621	7.92	12.5	12.99
65.6%-Fe_3O_4-395-SiO_2	1.83	1.665	8.47	18.0	17.82

Table 14: Fill factors, wall refractive indices and stop band shifts for Fe_3O_4 loaded 3DOM SiO_2. [a]Spectrometer resolution 0.5 nm.

Deposition of OA/Fe_3O_4 was also achieved in 3DOM ZrO_2. Samples were calcined at 450 °C for 4 hours (ramp rate 1 °C min^{-1}). The samples were analysed by PXRD, but only single phase tetragonal ZrO_2 could be assigned due to the coincident reflections of ZrO_2 and Fe_3O_4 and the resolution of the instrument. SEM images of the composites after deposition showed no agglomerates, appearing identical to before deposition. TEM images also showed no agglomerates, but differentiation between ZrO_2 and Fe_3O_4 particles was not possible due to similar particle sizes and the poor crystallinity of Fe_3O_4. PXRD, SEM and TEM for this sample are shown in appendix section A3 (Figure 119 and Figure 120) From DRUVS analysis, stop band red shifts were observed on loading as with previous samples (Figure 69). All data suggested homogeneous deposition of Fe_3O_4 within 3DOM ZrO_2.

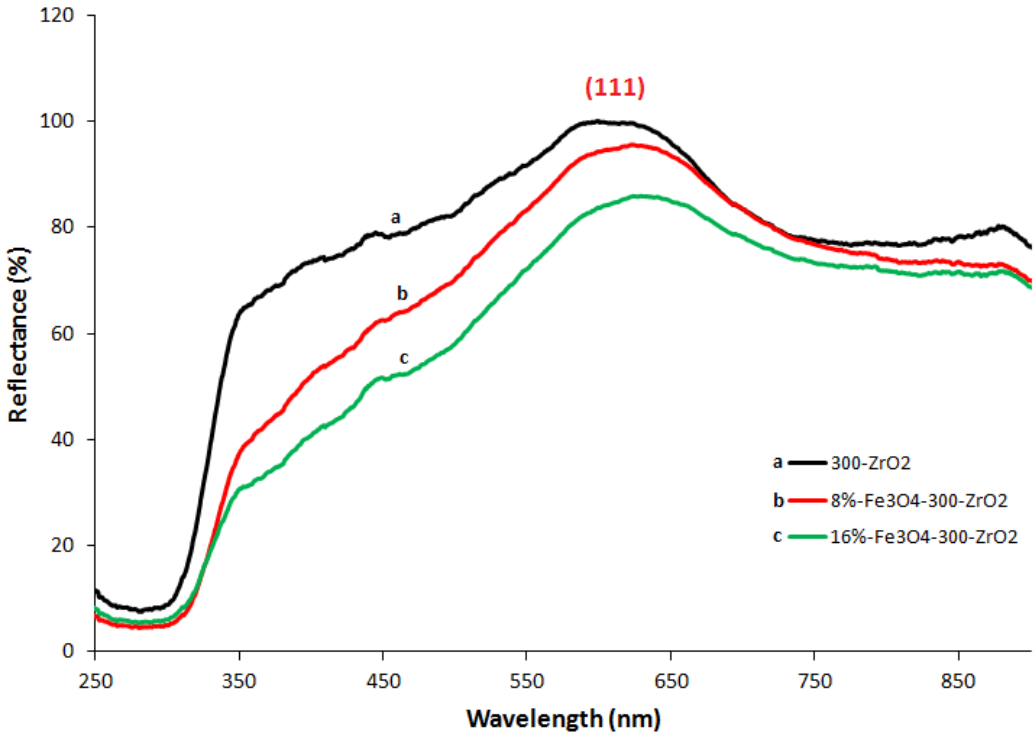

Figure 69: DRUVS spectra of 3DOM ZrO_2 and Fe_3O_4 loaded 3DOM ZrO_2.

3.2.5: Deposition of Nanoparticles in 3DOM FTO Films

3.2.5a: Deposition of TiO_2 in 3DOM FTO

Deposition of TiO_2 nanoparticles in 3DOM FTO films was attempted using similar methods to those described for 3DOM SiO_2. 3DOM FTO was soaked in 0.05 M OA/hexane for 1 hour to adsorb OA molecules on the oxide surface. The slide was placed in a 1.7 cm diameter cylindrical vial, to which nanoparticle dispersions in OA/chloroform were added. On evaporation of the solvent, some nanoparticles are deposited on the pore surface by capillary effects, however unlike in powder materials some deposition was observed to occur on the walls of the slide and the base of the container due to the shape of the slides. Variation in loading amount was controlled by adjusting the concentration of nanoparticles in the dispersion. TiO_2 was deposited from 1.5 mL of OA/chloroform solutions containing 1 – 10 mM dispersed TiO_2 nanoparticles. After evaporation of the solvent, samples were calcined at 450 °C for 4 hours (ramp rate 1 °C min^{-1}).

SEM EDX analysis was used to determine the atom % of Ti and Sn, and used to back calculate the nanoparticle loading obtained. From 1.2 mM and 4.8 mM TiO_2 dispersions, loadings of 15.6 and 19.6 wt% TiO_2 in 3DOM FTO were calculated from EDX measurements. SEM images of **19.6%-TiO_2-289-FTO** are shown in Figure 70. Homogeneous deposition within the pores is indicated by the absence of agglomerated particles. TEM images also showed no blockages of pores on the nanoscale. The relatively small increase in loading amount for a four-fold increase in concentration suggests that the loading amount cannot be directly controlled by concentration alone. The loading amount may potentially be increased by slower evaporation of the solvent front or multiple deposition cycles, and could be investigated as future work.

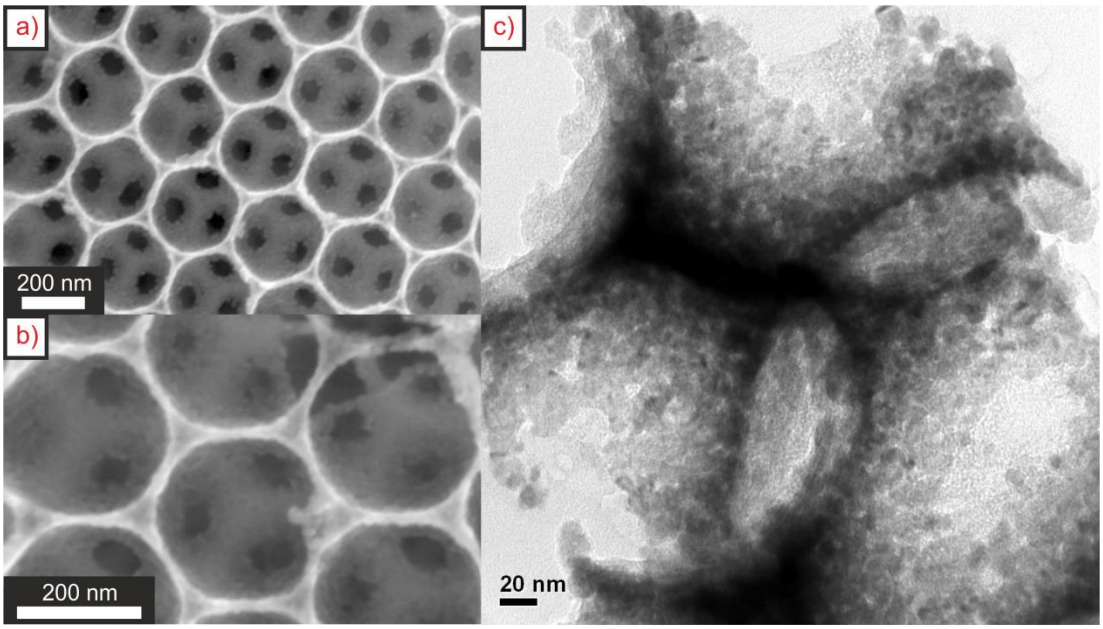

*Figure 70: SEM images (a), (b) and TEM image (c) of **19.6%-TiO$_2$-289-FTO** sample.*

Figure 71 shows the diffuse reflectance spectra of 3DOM FTO samples loaded with TiO_2 nanoparticles. Red shifts in the stop band position are observed on loading as with other 3DOM materials, accompanied by a decrease in the intensity of the stop band. For uncoated **289-FTO**, a value of ϕ = 13.3 % was calculated using Equation 12. From the experimental λ_{111} shift, values of χ_{TiO2}, n_{avg} and ϕ_{total} were calculated using Equation 13. Equation 17 was then used to calculate the expected stop band shift as above for TiO_2/3DOM SiO_2 composites. Good agreement was observed between the calculated and experimental λ_{111} shifts.

Sample	χ_{TiO2} / %	n_{avg}	ϕ_{total} / %	Experimental λ_{111} shift[a] / nm	Calculated λ_{111} shift / nm
15.6%-TiO$_2$-289-FTO	3.43	1.790	16.7	24	24.1
19.6%-TiO$_2$-289-FTO	4.27	1.824	17.6	30	30.1

Table 15: Fill factors, wall refractive indices and stop band shifts for TiO_2 loaded 3DOM FTO. [a]Spectrometer resolution 0.5 nm.

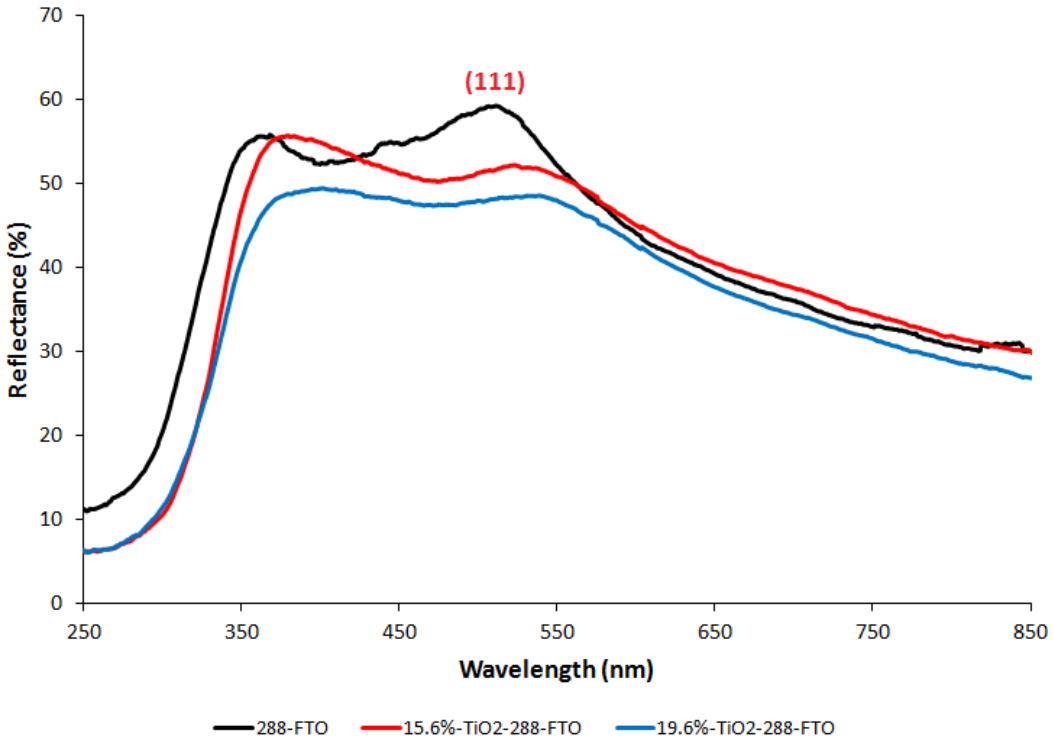

Figure 71: DRUVS spectra of TiO_2 loaded 3DOM FTO on FTO glass samples.

3.2.5b: Deposition of CdS and CdSe in 3DOM FTO

Deposition of CdS and CdSe quantum dots was attempted in 3DOM FTO materials. The 3DOM FTO used in this section was prepared by PhD student Menglong Zhang, by the same techniques described in chapter 2 but using larger PS spheres. Similar to deposition of TiO_2 nanocrystals, FTO was first coated with OA molecules. Stock CdS and CdSe nanoparticle dispersions were diluted down to give an absorbance of around 1 for the first exciton peak by UV-Vis absorption spectroscopy. The concentration of nanoparticles was estimated using extinction coefficients for CdS and CdSe quantum dots from the literature (see appendix section A1.3).[234] Nanoparticle dispersions (1.5 ml) in OA/toluene (0.1 M) were evaporated onto the film as described above for TiO_2. Removal of the ligands was achieved by calcination at 450 °C for 4 h (ramp rate 1 °C min^{-1}) under argon. Photographs of 3DOM FTO and quantum dot loaded samples are shown in Figure 72.

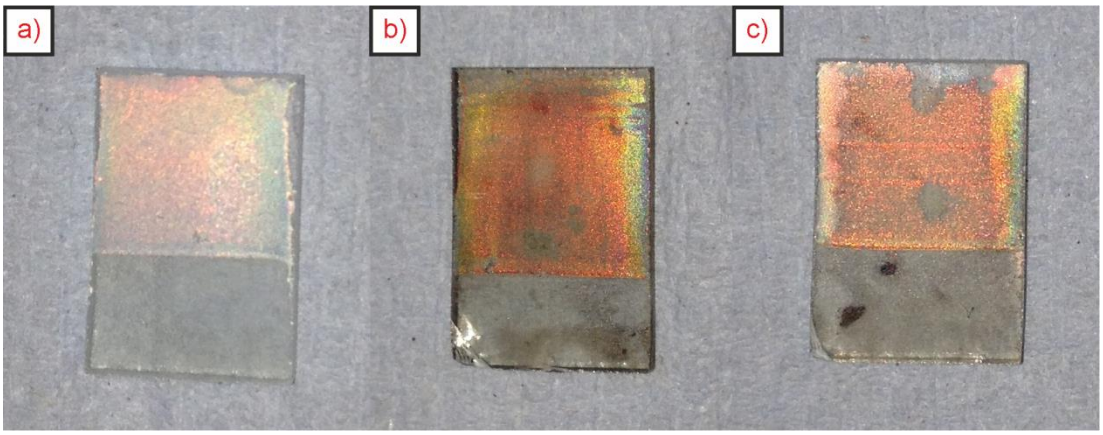

Figure 72: Photographs of 3DOM FTO (a) and quantum dot loaded 3DOM FTO, (b) CdS and (c) CdSe.

SEM images of CdS and CdSe loaded 3DOM FTO are shown in Figure 73. Optimisation of the concentration of nanoparticles in the dispersion is necessary to prevent overloading and subsequent agglomeration of deposited particles. Samples deposited from 7 µM CdS and 6.8 µM CdSe dispersions showed extensive surface agglomerates by SEM (Figure 73a, b). Diffuse reflectance spectra of these samples showed diminished or no photonic stop bands suggesting blockage of pores and agglomeration due to high solution concentrations.

For CdS deposition, reducing the concentration of the dispersion to 0.5 µM produced the samples in Figure 73c and d. Vastly reduced agglomeration is observed compared to deposition attempts from higher concentrations. The photonic stop bands are retained on loading (Figure 75), and red shifted as predicted by Equation 13. From EDX analysis of 50 x 35 µm sample areas a loading of 11.2 wt% CdS was calculated.

TEM images of the CdS and CdSe loaded 3DOM FTO materials deposited from 7 µM and 6.8 µM dispersions respectively showed agglomerates inside the pores due to overloading. For the sample prepared from a 0.5 µM CdS dispersion **(11.2%-CdS-345-FTO)**, pristine macropores were observed by TEM (Figure 74). Differentiation between the lattice fringes of individual nanoparticles was not possible due to the coincident d_{hkl}-spacings of FTO (111)/CdX (101), and FTO (101)/CdX (102) crystal planes.

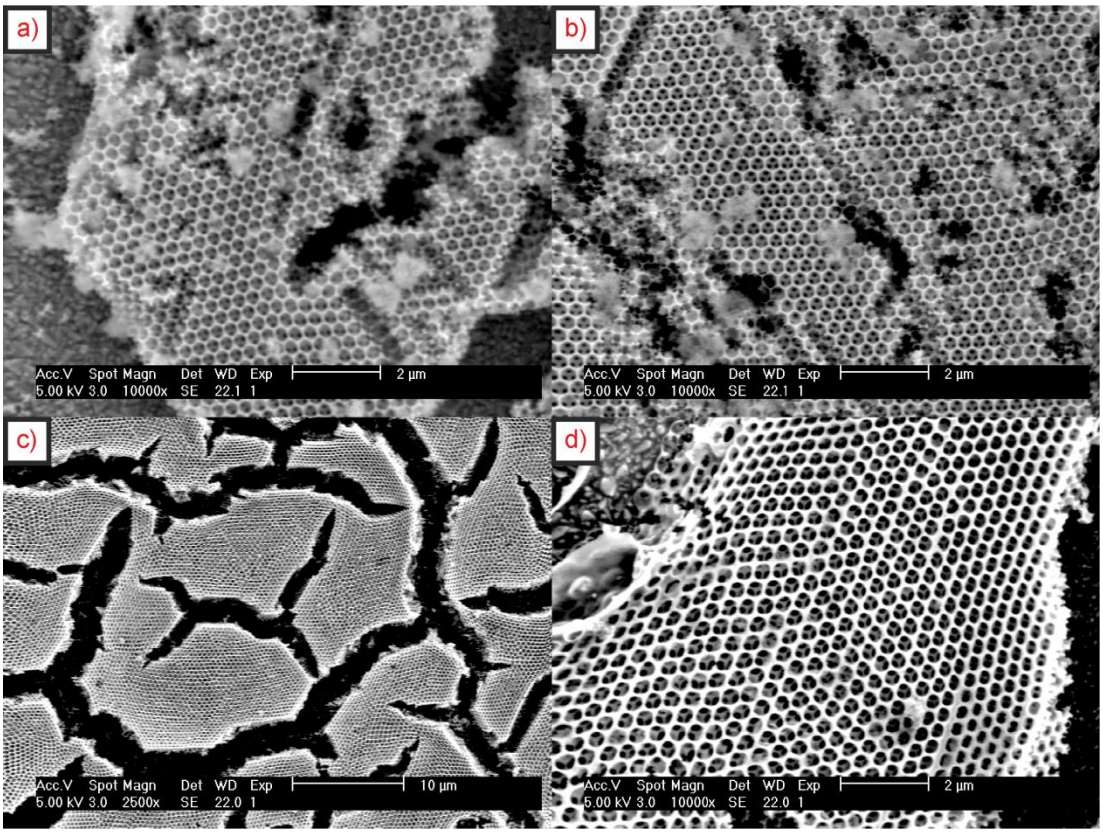

Figure 73: SEM images of CdS and CdSe loaded 3DOM FTO. Composites deposited from 7 µM CdS dispersion (a) and 6.8 µM CdSe dispersion (b), with extensive agglomeration of particles. (c), (d) ***11.2%-CdS-345-FTO*** *deposited from 0.5 µM CdS.*

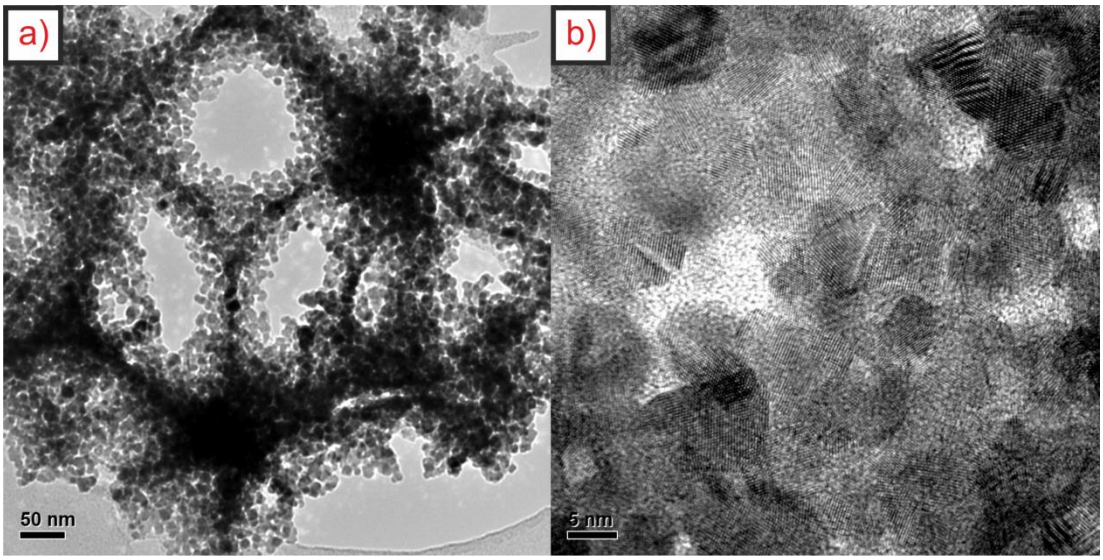

Figure 74: TEM images of ***11.2%-CdS-345-FTO****. Crystal planes in (b) could not be differentiated due to similar* d_{hkl}*-spacings for FTO and CdS.*

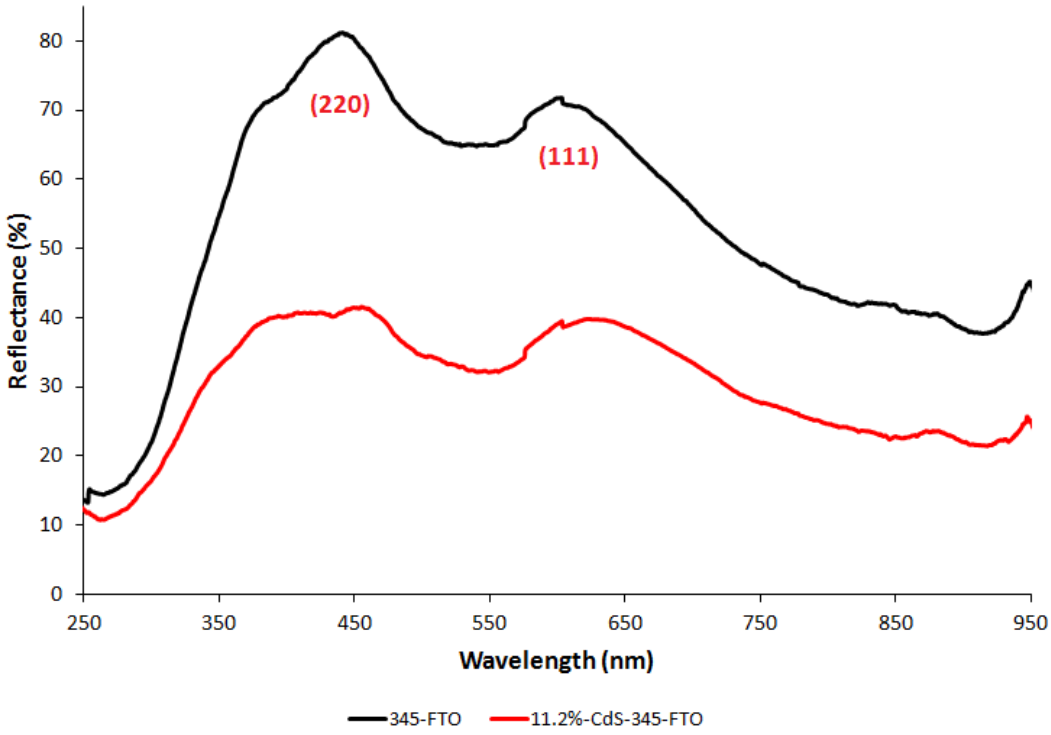

Figure 75: DRUVS spectra of 3DOM FTO and CdS loaded 3DOM FTO.

The fill factor of the **345-FTO** sample was calculated as ϕ = 13.5 % by Equation 12. From the (111) stop band shift of 20 nm, a CdS fill factor of χ_{CdS} = 2.56 % was calculated using Equation 13 to give a total fill factor ϕ_{total} = 16.1 %. Using n_{ave} = 1.72, an expected stop band shift of 18.7 nm was calculated using Equation 17, in reasonable agreement with the experimental shift.

Deposition of CdSe from more dilute dispersions was attempted, but an optimal concentration was not found. Future work could investigate homogeneous loading of CdSe, and increased loading of CdS in 3DOM FTO by multiple depositions and variation in the evaporation rate.

In summary, homogeneous deposition of ligand stabilised TiO_2 and CdS nanoparticles has been achieved in 3DOM FTO films. The quality of dispersion is high as evidenced by SEM, TEM and DRUVS analysis. As opposed to powder materials, the loading amount cannot be directly controlled, but can be influenced by the concentration of nanoparticle dispersion used for deposition. Using the current parameters, a calibration curve could be fabricated, and used to determine

the target loading based on this initial concentration. In future work, variation in the deposition times, nanoparticle concentration and reaction vessel may facilitate more direct control of the loading amount in the final product. Electrochemical characterisation and photoelectrochemical fuel production using these composites is of interest for future work, and is under investigation by other members of the research group.

3.2.6: Deposition of Nanoparticles in Mesoporous SiO_2

Many literature studies have shown the synthesis of mesoporous materials, however comparatively few have reported the homogeneous deposition of nanoparticles within these structures. Using similar methods to 3DOM materials, the deposition of ligand stabilised nanoparticles was investigated in mesoporous SiO_2. The synthesis of **Meso-SiO_2** with periodicity of 16.9 ± 0.8 nm and wall thickness around 4 nm was described in section 2.2.5. Deposition of OA/TiO_2 (8.9 ± 1 nm diameter) and OA/CdS (2.84 ± 0.3 nm diameter) was attempted within the structure. On the basis of size, CdS nanoparticles would be expected to penetrate deeper into the mesoporous network, and cause less occlusion of pores. In the following section, the synthesis and characterisation of the composites by TEM and PXRD is described, and the quality of the samples compared to literature reported materials.

3.2.6a: Deposition of OA/TiO_2 Nanoparticles in Meso-SiO_2

OA/TiO_2 dispersions in 0.1 M OA/chloroform were deposited in **Meso-SiO_2** (30 mg) as described above for 3DOM SiO_2, followed by calcination at 500 °C for 5 h (ramp rate 5 °C min^{-1}). Figure 76 shows TEM images of TiO_2 loaded **Meso-SiO_2**. Individual nanoparticles could be identified by high resolution images (Figure 76d), showing lattice plane separations consistent with tetragonal anatase TiO_2. The anatase polymorph was also confirmed by PXRD and electron diffraction (Figure 76b).

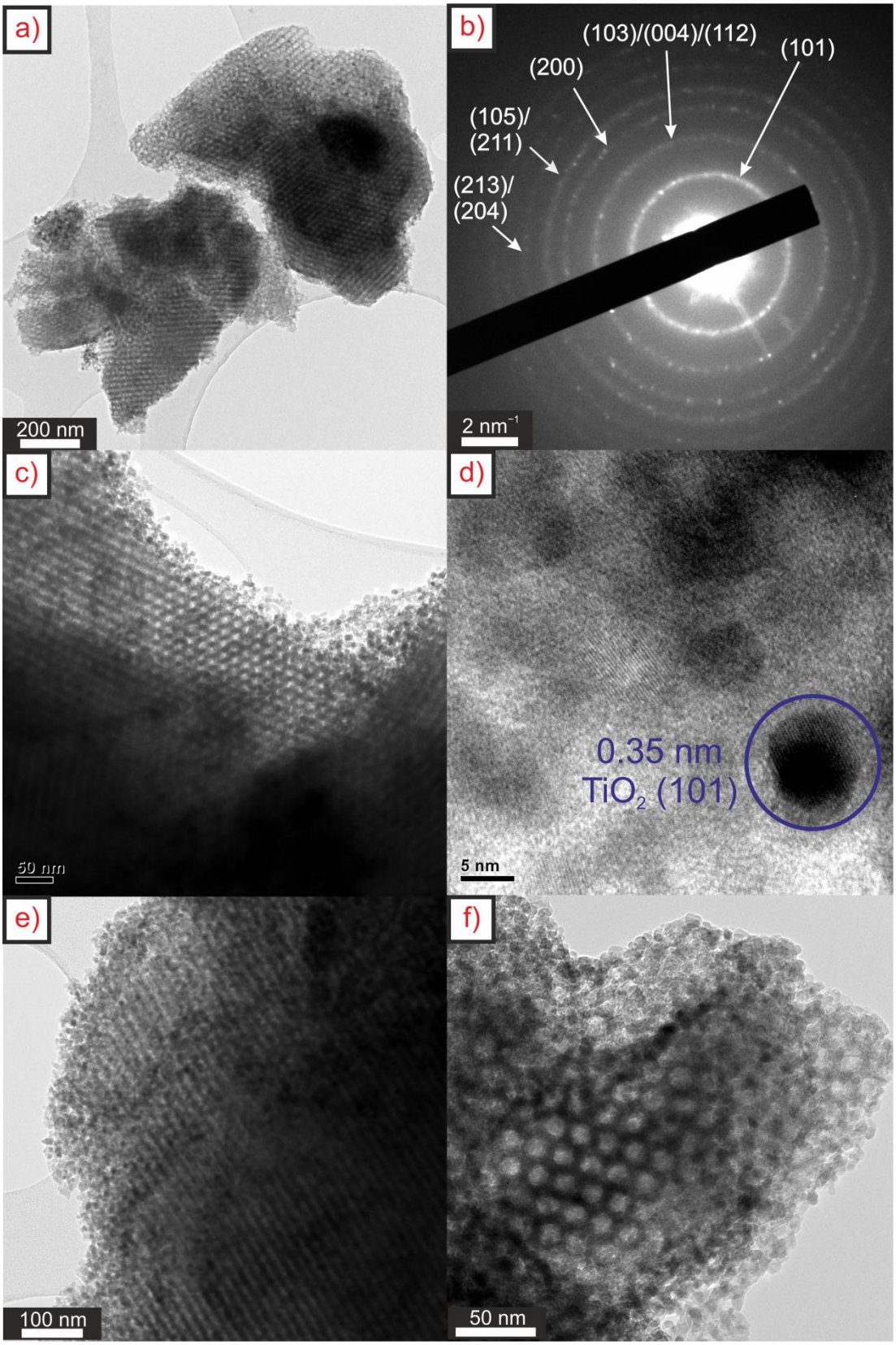

Figure 76: TEM images and electron diffraction of TiO_2 loaded mesoporous SiO_2. (a) TEM image and (b) electron diffraction pattern of ***22%-TiO_2-Meso-SiO_2****, indexed as anatase TiO_2, (c), (d)* ***6.6%-TiO_2-Meso-SiO_2****, (e), (f)* ***36%-TiO_2-Meso-SiO_2****.*

EDX mapping was used to analyse the distribution of particles within the pores (Figure 77). For all regions analysed, an even distribution of nanoparticles around the pores is observed, however it is unclear whether occlusion of the pores occurs on a larger scale.

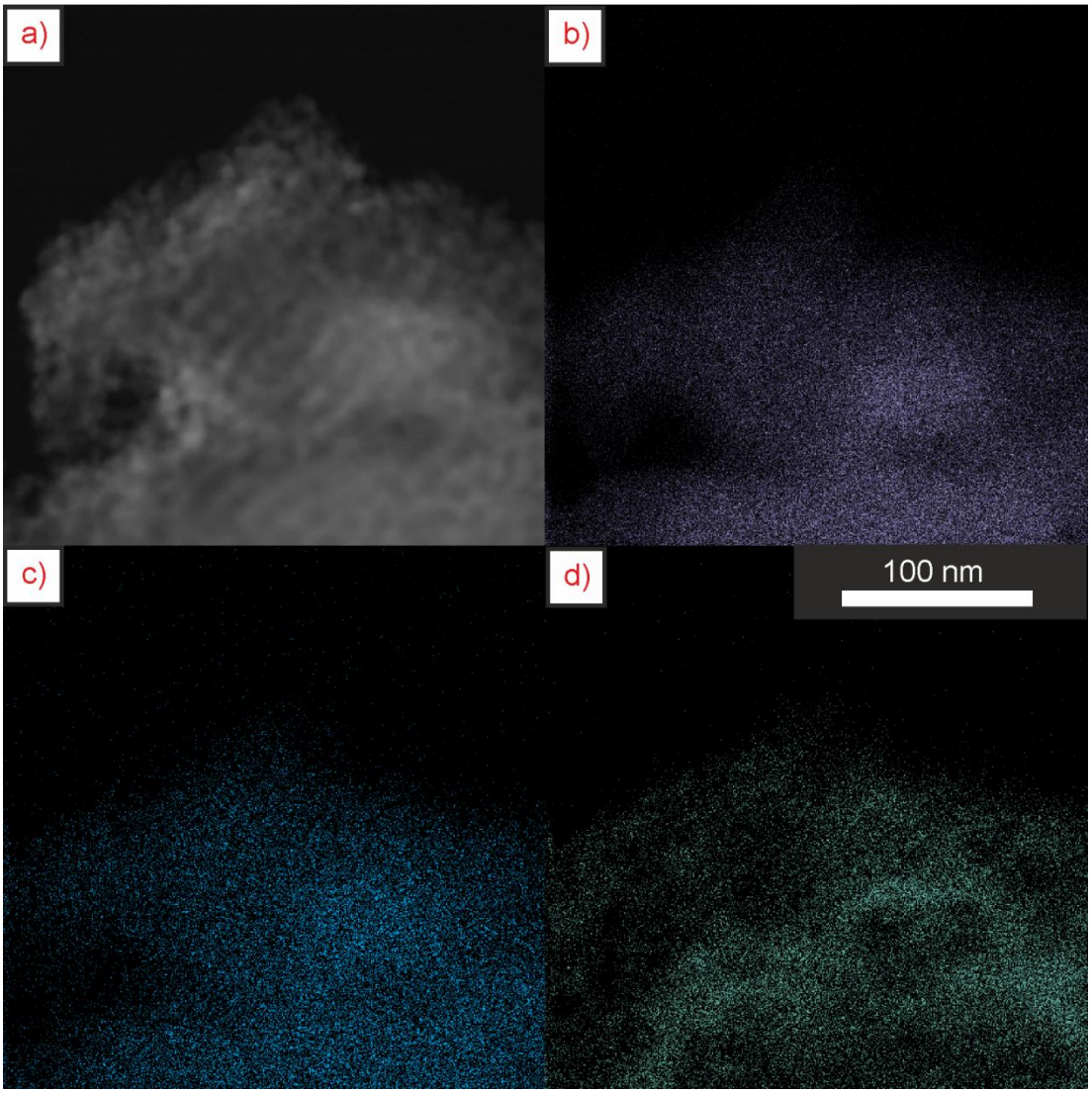

*Figure 77: TEM EDX mapping data for **36%-TiO_2-Meso-SiO_2**. (a) HAADF STEM image, (b) Si map, (c) O map and (d) Ti map. 100 nm scale bar applies to all images.*

3.2.6b: Deposition of OA/CdS Nanoparticles in Meso-SiO_2

OA/CdS dispersions in 0.1 M OA/chloroform were deposited in **Meso-SiO_2** (30 mg) as described above for OA/TiO_2, followed by calcination at 450 °C for 4 h (ramp rate 1 °C min^{-1}). TEM images of the composites are shown in Figure 78. For greater CdS loadings, some agglomeration of particles is observed within the pore channels (Figure 78e), however low magnification images show that large proportions of the pores are not occluded (Figure 78d). For the **4.2%-CdS-Meso-SiO_2** sample no pore blockages were observed. Due to the 2D representation of TEM images, the determination of the exact positions of nanoparticles within the pores was difficult. To further characterise these materials, EDX mapping as shown for TiO_2/**Meso-SiO_2** could be obtained as future work.

Electron diffraction (Figure 78c) showed a ring pattern assignable to cubic CdO (JCPDS 01-075-0592) and hexagonal CdS (JCPDS 01-075-1545). This is consistent with the surface oxidation of CdS by calcination in air.[246] In these composites the primary consideration was to homogeneously distribute nanoparticles within the porous materials, however for photocatalysis applications single phase CdS can be prepared by reaction with Na_2S.[247] The d_{hkl}-spacings of the particles in Figure 78f were measured to be 2.38 Å, however the coincident d_{hkl}-spacings of the CdS (102) and CdO (200) crystal planes prevented assignment of the crystal phase. After reaction of a sample with Na_2S for 6 hours, TEM showed particles containing lattice fringes with d_{hkl}-spacings of 3.2 Å, corresponding to the CdS (101) plane.

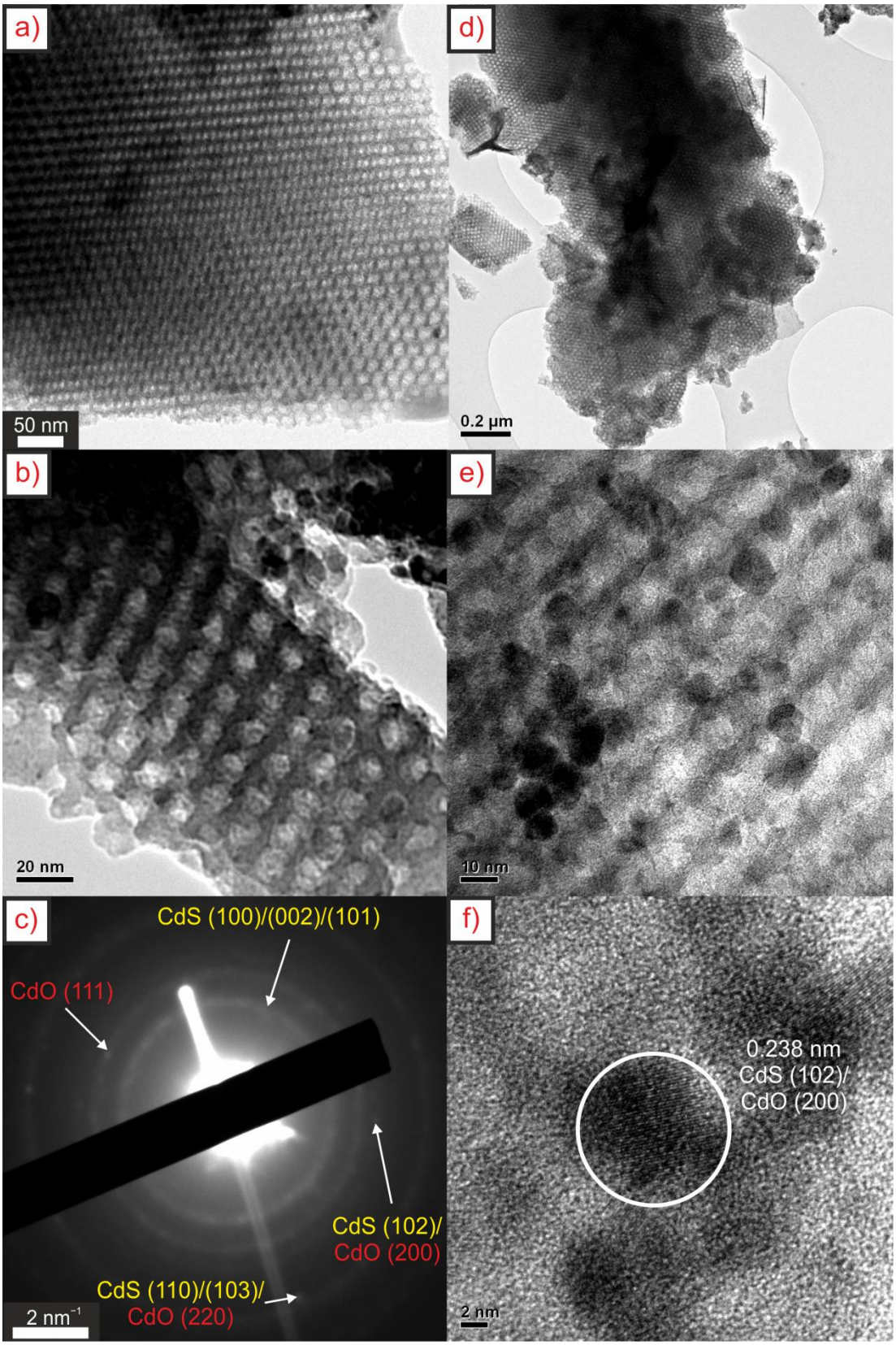

Figure 78: TEM images and electron diffraction of CdS loaded mesoporous SiO_2. (a) – (b) TEM images and (c) electron diffraction of ***4.2%-CdS-Meso-SiO_2****, and (d) – (f) TEM images of* ***29.4%-CdS-Meso-SiO_2.***

3.2.6c: PXRD Analysis of Nanoparticle Loaded Meso-SiO_2

Wide angle PXRD profiles of nanoparticle loaded **Meso-SiO_2** are shown in appendix section A3 (Figure 121). For TiO_2 loaded samples, tetragonal anatase TiO_2 is observed as in 3DOM materials. No peaks attributable to CdO or CdS were observed in the CdS samples, suggesting the nanoparticles are amorphous.

The low angle PXRD profiles of TiO_2 and CdS loaded **Meso-SiO_2** are shown in Figure 79. In section 2.2.5, the (111) peak in the low angle PXRD of **Meso-SiO_2** at a detector angle of 0.54 ° 2θ was calculated to correspond to a periodicity of 16.3 nm. The peak positions are not observed to shift on nanoparticle loading which suggests that the periodicity of the structure is unchanged. In addition, the FWHM of the (111) peaks at 0.54 ° 2θ remain the same in all samples. The peak intensities are decreased in comparison to **Meso-SiO_2**, which could suggest a decrease in the ordering of the structure on nanoparticle loading. However, the capillary tubes used as sample holders may not contain the same thickness of material at the point of exposure to the X-ray source, which could also cause variation in the intensity of the peaks.

For TiO_2 loaded materials, the definition of the (311) peak at 1 ° 2θ is reduced as the loading is increased. This suggests that the crystalline TiO_2 nanoparticles are interfering with the diffraction from (311) planes of Meso-SiO_2. For CdS loaded samples, the (311) peak is well defined as a function of loading. This may be due to homogeneous dispersion of the nanoparticles, or the amorphous nature of the CdO/CdS species may not interfere with diffraction from the mesopore structure.

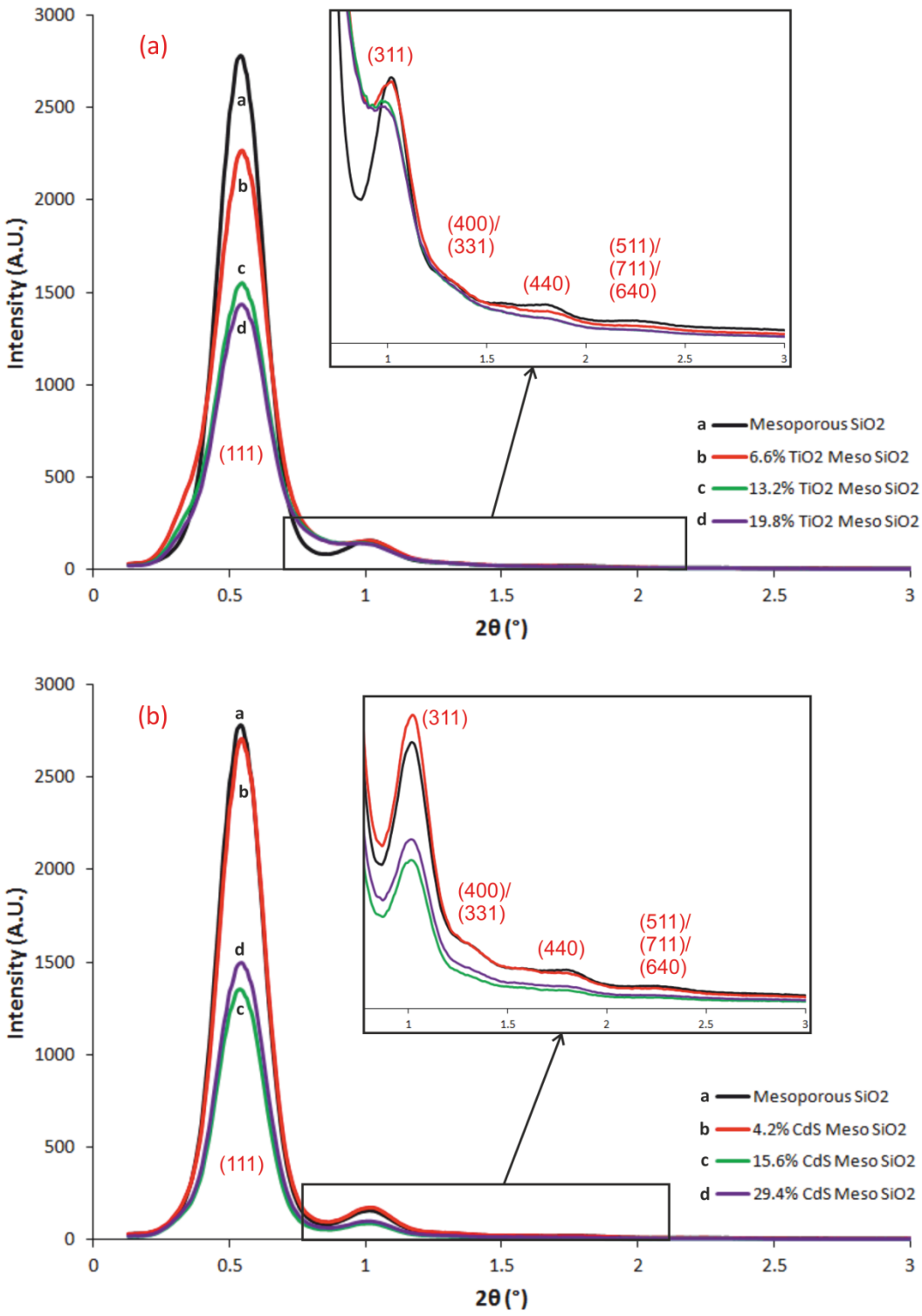

Figure 79: Low angle PXRD analysis of nanoparticle loaded ***Meso-SiO$_2$****. (a) TiO_2 loaded and (b) CdS loaded* ***Meso-SiO$_2$****. Insets: Zoomed view of the 0.8 – 3 ° 2Θ region*

3.2.6d: Surface Area Analysis of Nanoparticle Loaded Meso-SiO_2

The surface areas of the composites were analysed by nitrogen adsorption porosimetry and BET theory, and are compared to the surface area of **Meso-SiO_2** (560.3 ± 7.4 $m^2 g^{-1}$) in Table 16:

	Material	Surface area / $m^2 g^{-1}$
	Meso-SiO_2	560.3 ± 7.4
CdS loaded Meso-SiO_2	**4.2%-CdS-Meso-SiO_2**	548.3 ± 11.3
	15.6%-CdS-Meso-SiO_2	412.7 ± 8.1
	29.4%-CdS-Meso-SiO_2	392.9 ± 7.7
TiO_2 loaded Meso-SiO_2	**6.6%-TiO_2-Meso-SiO_2**	398.2 ± 7.9
	13.2%-TiO_2-Meso-SiO_2	344.7 ± 6.8
	19.8%-TiO_2-Meso-SiO_2	357.4 ± 6.7

Table 16: Surface area of nanoparticle loaded mesoporous materials.

For high nanoparticle loadings a reduction in surface area is observed in comparison to uncoated **Meso-SiO_2**. The magnitude of this reduction is greatest for TiO_2 loaded materials, by factors of 0.29 (6.6 wt% TiO_2) to 0.36 (19.8 wt% TiO_2). For high CdS loadings (> 15 wt%), the reduction factor is smaller (0.26 – 0.30) than for comparable TiO_2 loadings, suggesting access to the mesoporous structure is more restricted for TiO_2 loaded samples as predicted from the comparative sizes of the nanoparticles.

For the lowest loading of CdS (4.2 wt%), within error the surface area is the same as the uncoated **Meso-SiO_2**. As observed from TEM images, CdS is incorporated into the mesoporous structure, and agglomeration is not observed in this composite. The nitrogen adsorption/desorption isotherm (Figure 80) resembles a type IV isotherm with similar shape to **Meso-SiO_2**, however the hysteresis on the desorption trace shows retention of high volumes of adsorbent to lower relative pressures. This may suggest that the windows between pores are smaller, and hence a greater decrease in pressure is required before evaporation of the condensed liquid in the pores will occur. A decrease in the window size is consistent

with deposition of CdS nanoparticles on the pore surface. The retention of high surface area is of particular interest for applications of these materials as catalysts.

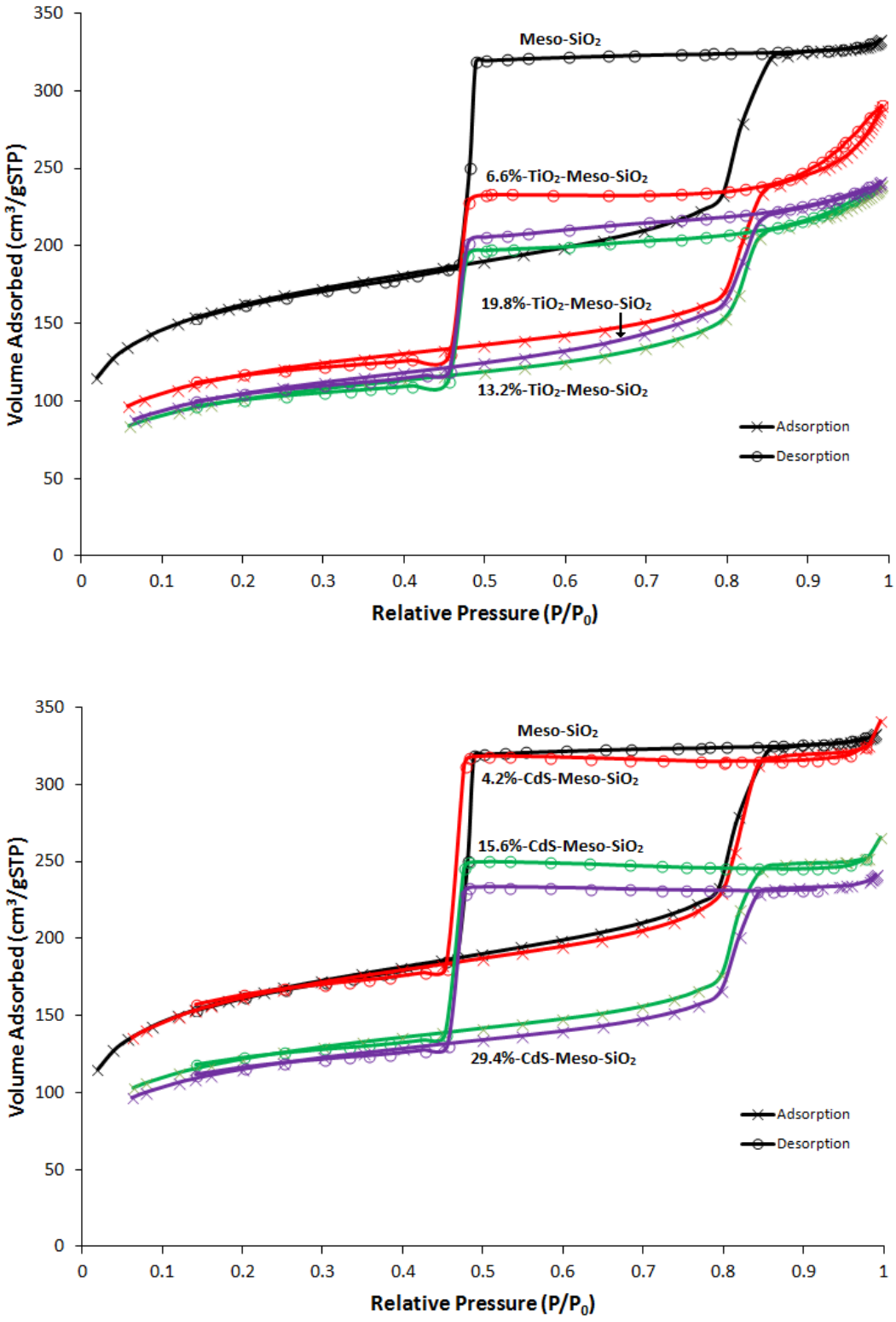

Figure 80: Nitrogen adsorption/desorption isotherms for (top) TiO_2 loaded mesoporous SiO_2 and (bottom) CdS loaded mesoporous SiO_2.

Similar hysteresis curves are observed for higher loadings of CdS. The drop in volume corresponding to evaporation from the pores on the desorption isotherm is similarly shifted to lower relative pressures, which suggests coverage of the pore windows as for **4.2%-CdS-Meso-SiO_2.** The volume adsorbed is lower across the entire isotherm for the higher loadings, which suggests that access to some of the mesopore channels has been blocked. This is consistent with the presence of some agglomerates observed by TEM imaging. For TiO_2 loaded samples, the shapes of the hysteresis loops are the same as **Meso-SiO_2** for all samples, suggesting that deposition of nanoparticles has not occurred on the edges of the windows.

Similar reductions in surface area on nanoparticle loading have been observed in the literature using chemical bath techniques for deposition. An ionic liquid templated mesoporous SiO_2 material shows reduction in surface area from 1127 m^2 g^{-1} to 788 m^2 g^{-1} on TiO_2 loading, and 588 m^2 g^{-1} for TiO_2/PW_{12} loading.[248] The surface area decrease on TiO_2 loading, accompanied by a decrease in pore size from 3.1 nm to 2.96 nm, was attributed to homogeneous coating of TiO_2 on the surface of the pores and in the pore channels. However, TEM evidence was not presented to clarify the nanoparticle distribution. For Co_3O_4 loading in SBA-15 materials, reductions in surface area from 878 m^2 g^{-1} to 596 m^2 g^{-1} and 533 m^2 g^{-1} were observed for 4 and 8 weight % loadings respectively.[207] For these composites, TEM images showed clusters of aggregated particles around 60 – 200 nm in length (Figure 81), coupled with a decrease in the pore size from 8.2 nm (SBA-15) to 7.6 nm (4 weight %) and 7.1 nm (8 weight %). Similarly, growth of WS_2 slabs with an average particle size of 3.6 nm inside SBA-15 (6.5 nm pores) was observed to decrease the surface area from 800 m^2 g^{-1} (SBA-15) to 509 m^2 g^{-1} (20 weight %) and 230 m^2 g^{-1} (60 weight %).[249]

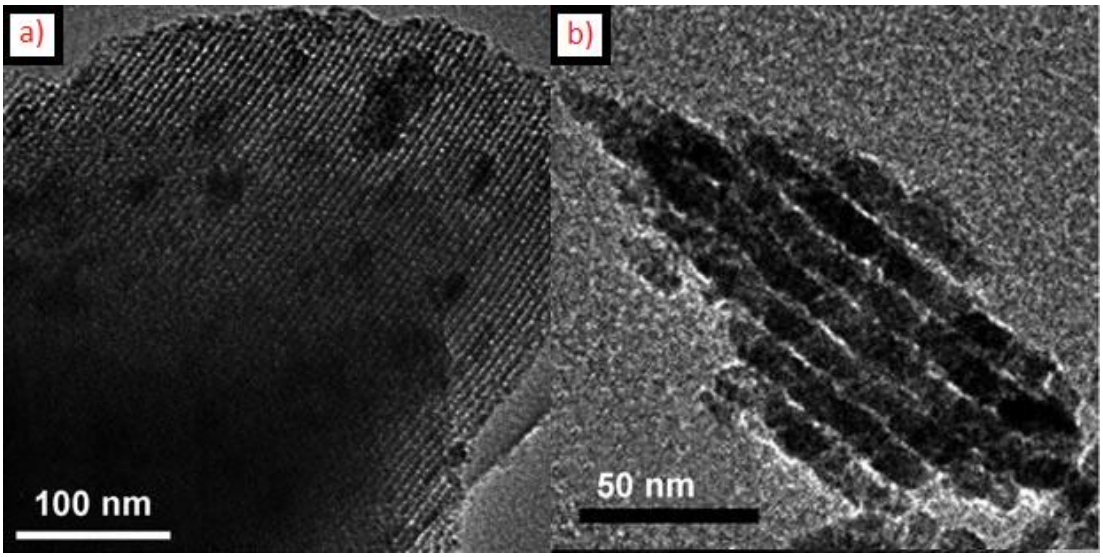

Figure 81: Literature TEM images of (a) 4 weight % Co_3O_4 loaded SBA-15 mesoporous SiO_2 and (b) Co_3O_4 clusters after SiO_2 removal. Adapted from Jiao and Frei.[207]

A decrease in surface area has been observed in $LaCoO_3$ loaded mesoporous SiO_2 from 1095 $m^2\ g^{-1}$ for the uncoated sample, to 750 $m^2\ g^{-1}$ (10.5 weight %), 510 $m^2\ g^{-1}$ (30 weight %) and 340 $m^2\ g^{-1}$ (47.5 weight %).[163] For the composite materials hysteresis loops are not observed in the N_2 adsorption/desorption isotherm, which may suggest the decrease in surface area is due to blocking of the mesopore channels in these materials (Figure 82). NiO has been deposited in mesoporous SiO_2 by atomic layer deposition, showing a slight increase in surface area on nanoparticle loading (2.9 weight %) from 297.6 $m^2\ g^{-1}$ to 302.6 $m^2\ g^{-1}$.

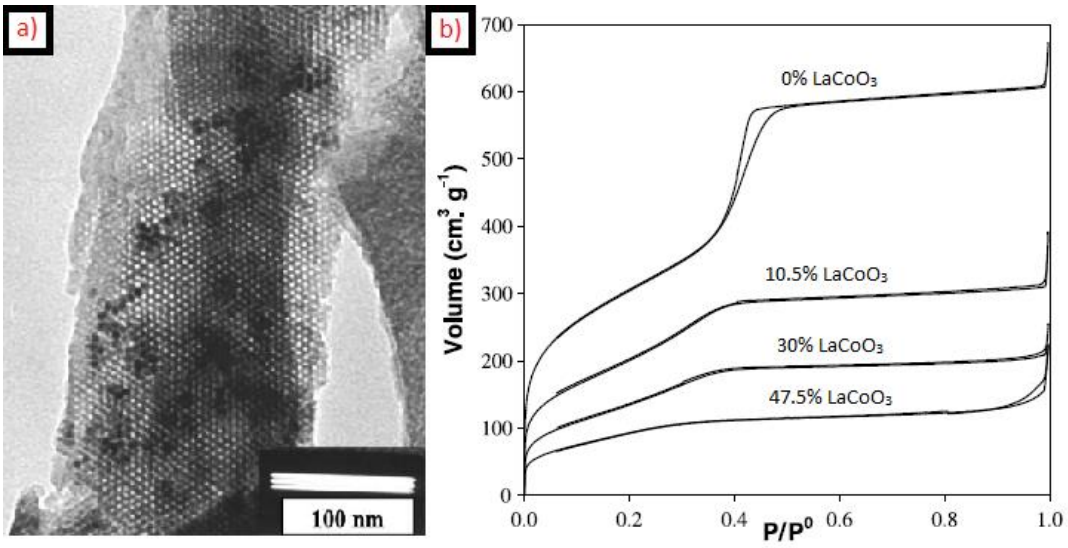

Figure 82: Analysis of $LaCoO_3$ loaded mesoporous SiO_2 from the literature. (a) TEM image of 38.5 weight % $LaCoO_3$ loaded sample and (b) Adsorption/desorption isotherms of $LaCoO_3$ loaded samples. Adapted from Nguyen ***et al.***[163]

The change in surface area on nanoparticle loading observed in this work and in the literature examples discussed is summarised in Table 17. In comparison to chemical bath techniques in the literature, the observed percentage decrease in surface area on nanoparticle loading is of lower magnitude for the samples presented in this work. TEM analysis of the composites shows mostly pristine mesoporous materials, which is reflected in the high surface areas of the composite materials. Some agglomerates are observed for high CdS loadings, the reduction of which could be investigated in future work. Due to the 2D representation of TEM images, the location of nanoparticles within the pores could not be confirmed. To analyse the pore surface, focused ion beam (FIB)/TEM could be used to cut a cross section of the pore structure for imaging. By controlled deposition of ligand stabilised nanoparticles smaller than the mesopore sizes, higher surface area composites can be produced than for an equivalent chemical bath technique, which is of particular interest for catalysis applications.

Weight % Nanoparticle Loading in Mesoporous SiO_2	SiO_2 Surface area / $m^2\ g^{-1}$	Loaded surface area / $m^2\ g^{-1}$	Change in surface area on loading / %
[a]4.0%-CdS (this work)	**560.3**	**548.3**	**−2.1**
[a]22.7%-CdS (this work)	**560.3**	**392.9**	**−29.8**
[a]16.5%-TiO_2 (this work)	**560.3**	**357.4**	**−36.2**
CB: [b]TiO_2[248]	1127	788	−30.1
CB: [b]PW_{12}/TiO_2[248]	1127	588	−47.8
CB: 4%-Co_3O_4[207]	878	596	−32.1
CB: 8%-Co_3O_4[207]	878	533	−39.3
CB: 20%-WS_2[249]	800	509	−36.4
CB: 60%-WS_2[249]	800	230	−71.3
ES: 10.5%-$LaCoO_3$[163]	1095	750	−31.5
ES: 30%-$LaCoO_3$[163]	1095	510	−53.4
ALD: 2.9%-NiO[1]	297.7	302.6	+1.6

Table 17: Surface area change of mesoporous materials on nanoparticle loading in this study and in the literature.[1, 163, 207, 248, 249] [a]weight % values calculated as $mass_{NP}$/total mass for comparison. [b]loading amount not analysed. Key: CB – Chemical bath deposition, ES – Electrostatic stabilisation (citrate) deposition, ALD – Atomic layer deposition.

3.3: Conclusions and Future Work

A method was developed for deposition of preformed, ligand stabilised nanoparticles in porous materials as homogenous monolayers. All nanoparticles used were readily synthesised according to reported literature procedures. The method was optimised through variation in dispersion solvent and modification of the support. Progression of the method is shown by TEM in Figure 83. Adsorption of a monolayer of OA on the support, followed by deposition of a dispersion of nanoparticles in OA/chloroform was found to maximise nanoparticle-support interactions and lead to a homogeneous distribution of nanoparticles after solvent evaporation. On calcination, the ligands are removed from the surfaces, and bonds are formed between the nanoparticles and the support.

The homogeneity of the nanoparticle coating was evidenced by electron microscopy, surface area analysis, and for photonic 3DOM materials, evolution of the stop band position and retention of its intensity. With the exception of high (> 40 wt%) Fe_3O_4 loadings in 3DOM SiO_2, no agglomeration of particles was observed by SEM or TEM. The targeted nanoparticle loadings were confirmed by EDX analysis. In terms of photonic properties, predictable shifts of the stop band were observed on addition of materials with refractive index greater than air. The new stop band position can be predicted based on the loading amount. The fabrication of materials with a defined photonic stop band is of interest for optical sensors.[250] In addition, the wide photonic stop bands observed in these materials can effectively scatter light and modify the absorption of photons by a material within the pores, which has the potential to enhance photocatalysis.[98, 118]

Deposition of OA-coated nanoparticles can achieve a homogeneous dispersion of nanoparticles within porous materials, whilst simultaneously offering control over the loading amount, crystal phase and particle size. The direct influence over all these parameters is not possible in some literature methods, such as the chemical bath deposition. For powder materials, all added material is retained in the final composite, and hence precise control over the loading of nanoparticles is possible by variation of the mass of nanoparticles in the dispersion. The particle size in the

composite is controlled by the initial nanoparticle synthesis, and can be varied by modification of the reaction conditions. In many existing deposition techniques in the literature, the main control over particle size is by variation of the chemical composition of the precursor and its concentration, which requires a trial and error approach to obtain a defined particle size for a specific precursor. In this work, the crystal phase of the nanoparticles can be controlled in the composite materials to an extent, however if the crystal phase of a material can be modified by intermediate temperature transformations (< 400 °C) control may not be possible due to the requirement for calcination to remove the ligands.

The generality of the technique has been demonstrated through its application to a variety of different nanoparticles and supports. In terms of supports, successful deposition has been achieved in 3DOM SiO_2, ZrO_2 and FTO, and in mesoporous SiO_2. Literature methods exist for synthesis of OA-coated nanoparticles with a variety of chemical compositions,[222-224] which could feasibly be deposited in a multitude of porous materials by simple modification of the surface with OA. In the current iteration of the method, control of loading was not directly possible for deposition in 3DOM films. From multiple deposition attempts, a calibration curve could be produced to predict the expected loading based on the dispersion concentration. In future work, modification of the reaction vessel could be investigated to contain deposition within the film and directly correlate the nanoparticle loading with the dispersion concentration.

Currently, the technique has been demonstrated for the deposition of fatty acid stabilised nanoparticles. Future work could be to replicate the same quality of deposition using aqueous phase stable nanoparticles, for example with poly(ethylene glycol) or poly(vinylpyrrolidone) functionality,[217, 251] to extend the applicability of the method to more materials.

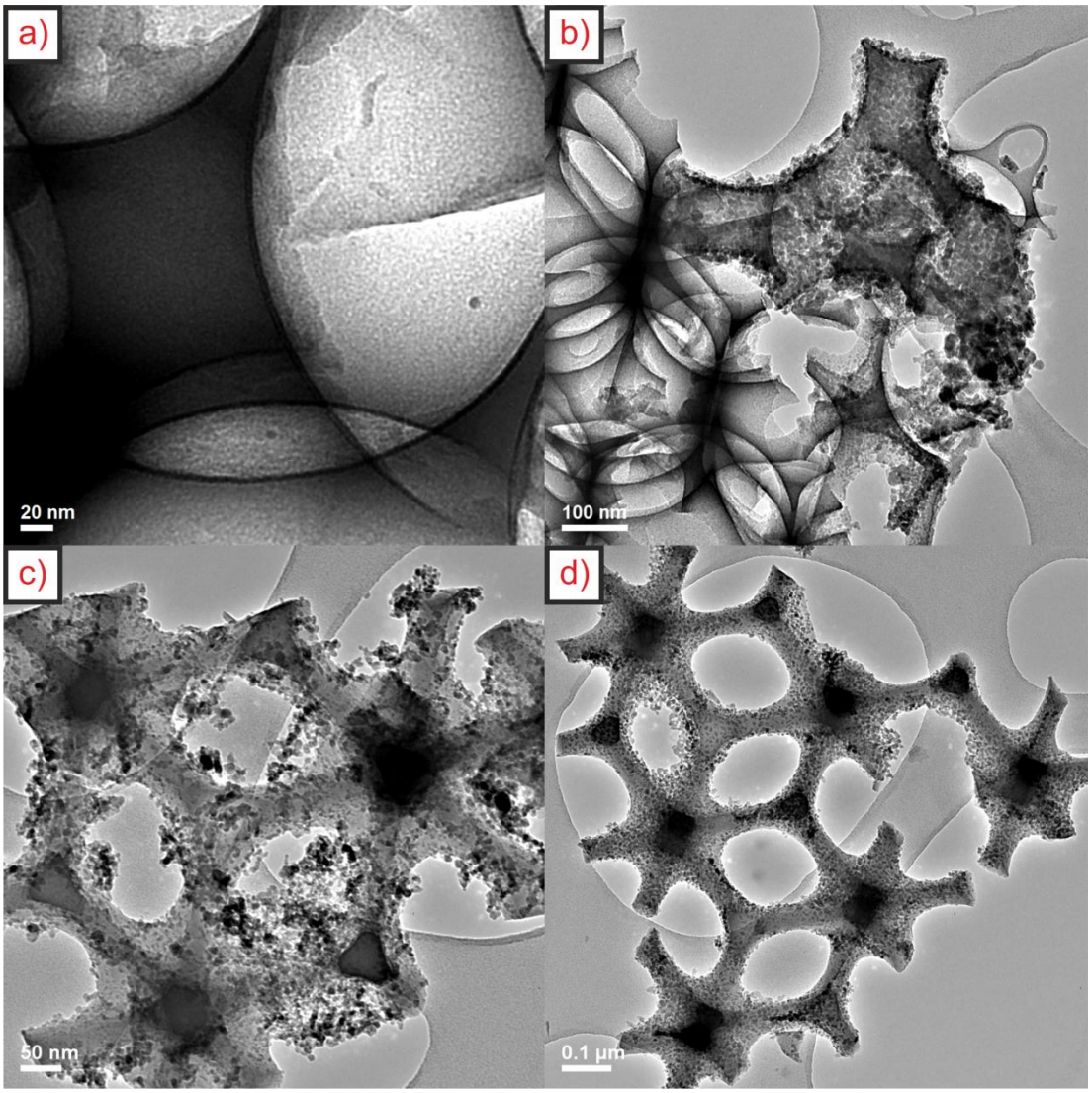

Figure 83: TEM images showing the quality of deposition attained in 3DOM SiO_2 throughout method development. (a) DCDMS-coated SiO_2, hexane NP dispersion, (b) OA-coated SiO_2, hexane NP dispersion, (c) OA-coated SiO_2, OA/hexane NP dispersion, (d) OA-coated SiO_2, OA/chloroform NP dispersion.

Chapter 4

Chalcogenide Nanoparticle Deposition and Photocatalysis

4.1: Introduction

4.1a: Photocatalysis Mechanisms

In this chapter, photocatalytic hydrogen production from CdS and TiO_2 loaded 3DOM ZrO_2 is described. Anatase TiO_2 has an indirect band gap of 3.2 eV, and forms excitons under UV light irradiation. For TiO_2 composites, photocatalytic hydrogen evolution from sacrificial aqueous methanol was studied, in which photogenerated electrons reduce water to hydrogen and methanol is oxidised to formaldehyde by holes, which has been described by the following equations:[252]

Equation 18 $$h^+ + H_2O \rightarrow \bullet OH + H^+$$

Equation 19 $$\bullet OH + CH_3OH \rightarrow \bullet CH_2OH + H_2O$$

Equation 20 $$\bullet CH_2OH \rightarrow HCHO + H^+ + e^-$$

Equation 21 $$2H_2O + 2e^- \rightarrow H_2 + 2OH^-$$

For CdS, to avoid photocorrosion a sacrificial aqueous Na_2S/Na_2SO_3 solution was used. CdS is a direct band gap semiconductor with a band gap of 2.4 eV. CdS shows visible light activity for photocatalytic hydrogen production from pure water, but is degraded over time due to oxidation of the surface under light by photogenerated holes:[252]

Equation 22 $$CdS + 2h^+ \rightarrow Cd^{2+} + S$$

To avoid this degradation, photocatalysis can be performed in solutions of sacrificial S^{2-} (sulfide) and SO_3^{2-} (sulfite) ions. Following exciton formation by band gap excitation, the overall process occurs by the following reactions:[66, 72]

Equation 23 Water Reduction $$2e^- + 2H_2O \rightarrow H_2 + 2OH^-$$

Equation 24 Sulfite Oxidation $$SO_3^{2-} + H_2O + 2h^+ \rightarrow SO_4^{2-} + 2H^+$$

Equation 25 Sulfide Oxidation $2S^{2-} + 2h^{+} \rightarrow S_2^{2-}$

S^{2-} ions in solution are oxidised by holes to form yellow S_2^{2-} (disulfide) ions by Equation 25, preferentially over the decomposition of CdS to elemental S by Equation 22. S_2^{2-} ions can occlude the absorption of light by CdS,[253] however reaction of SO_3^{2-} ions with disulfide forms colourless $S_2O_3^{2-}$ (thiosulfate) ions, which do not interfere with proton reduction or light absorption.[254] SO_3^{2-} ions are also oxidised to SO_4^{2-} (sulfate) ions by photogenerated holes (Equation 24).

The mechanism for hydrogen formation on the CdS surface is described by Equation 26. In water, surface CdS can be reversibly hydrolysed to form CdSH and CdSOH surface species. Reduction of CdSH by two photoexcited electrons forms a reduced state Cd(0)S(0)H, which liberates hydrogen according to Equation 27:[55, 255]

Equation 26 $(CdS)_2 + H_2O \leftrightarrow Cd(+II)SH + S(-II)Cd(+II)OH$

Equation 27 $Cd(0)S(O)H + H^{+} \leftrightarrow Cd(O)S(O)H_2^{+} \rightarrow Cd(+II)S(0)^{+} + H_2$

Following hydrogen release, the CdSH surface species is regenerated. Oxidation of two equivalents of S^{2-} or SO_3^{2-} ions in solution is coupled with the two electron reduction of $Cd(II)S(0)^{+}$ to form $Cd(+II)S(-II)H_2^{+}$. Proton dissociation reforms the CdSH surface species and completes the catalytic cycle.

4.1b: Chapter Objectives

The synthesis and characterisation of CdS nanoparticles was described in section 3.2.1c in chapter 3. Deposition of CdS in 3DOM SiO_2 and ZrO_2 will be investigated using the same methods described previously for TiO_2 and Fe_3O_4.

CdS loaded 3DOM ZrO_2 composites will be investigated for photocatalytic water reduction using Na_2S/Na_2SO_3 as a sacrificial electron donor, and to prevent photocorrosion of CdS. A series of samples is presented with variation in the periodicity, and hence the position of the photonic stop bands. The effect of the optical properties of the material on the rate of hydrogen evolution will be studied.

TiO_2 loaded 3DOM ZrO_2 composites will be studied as photocatalysts for water reduction using sacrificial methanol, and the trends in activity compared to the CdS series for the same 3DOM ZrO_2 materials.

4.2: Results and Discussion

4.2.1: Deposition of CdS Nanoparticles in 3DOM Powders

In the previous chapter, homogeneous deposition of CdS quantum dots was achieved in 3DOM FTO and mesoporous SiO_2 using OA/chloroform as dispersant. CdS loading was attempted in 3DOM materials using the same solvent system. Nanoparticles were dispersed in OA/chloroform (0.1 M) and deposited onto OA-coated supports by evaporation of the solvent at 40 °C overnight. Samples were calcined at 450 °C for 4 h (ramp rate 1 °C min^{-1}) under argon. Initial deposition attempts using oleylamine capped CdS nanoparticles were unsuccessful, resulting in biphasic powders containing large agglomerates as judged by SEM imaging (Figure 84). As observed previously for TiO_2 nanoparticles, the stability of the dispersion is important for high quality deposition. The formation of agglomerates is likely due to sedimentation from dispersion during the evaporation process.

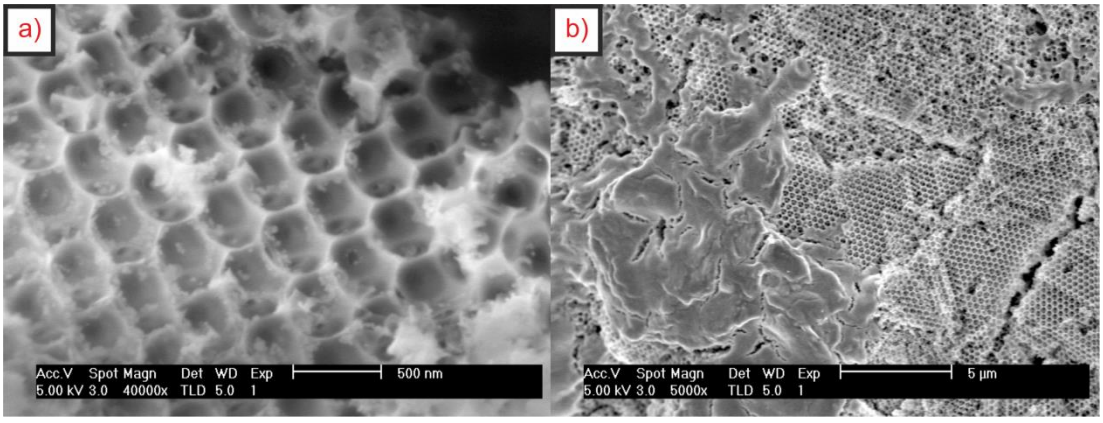

Figure 84: SEM images of CdS loaded 3DOM SiO_2 (left) and 3DOM ZrO_2 (right), deposited from dispersions of oleyl/CdS in OA/chloroform. Clear agglomeration of particles is observed.

To improve the deposition, OA capped CdS quantum dots with long term stability in organic solvents were used. PXRD patterns of CdS loaded 3DOM SiO_2 and ZrO_2 are shown in Figure 85. In both patterns hexagonal CdS matching JCPDS file 01-075-1545 is observed. Electron diffraction confirmed the phase assignment (Figure 86f). SEM images, TEM images and EDX maps of CdS loaded 3DOM SiO_2 and ZrO_2 are shown in Figure 86 and Figure 87. SEM images showed no agglomeration of particles or pore blockages on the macroscale. On the nanoscale, TEM images and EDX maps showed an even distribution of particles within the pores. All microscopy evidence indicates that homogeneous deposition of nanoparticles has been achieved. High resolution TEM images were used to identify the crystal plane and chemical identity of individual nanoparticles (Figure 86b and d). The CdS particle size was measured as 3.51 ± 0.36 nm after calcination. This value is larger than the Bohr radius of CdS (*ca.* 3 nm),[233] hence quantum confinement effects are not exhibited in the composites.

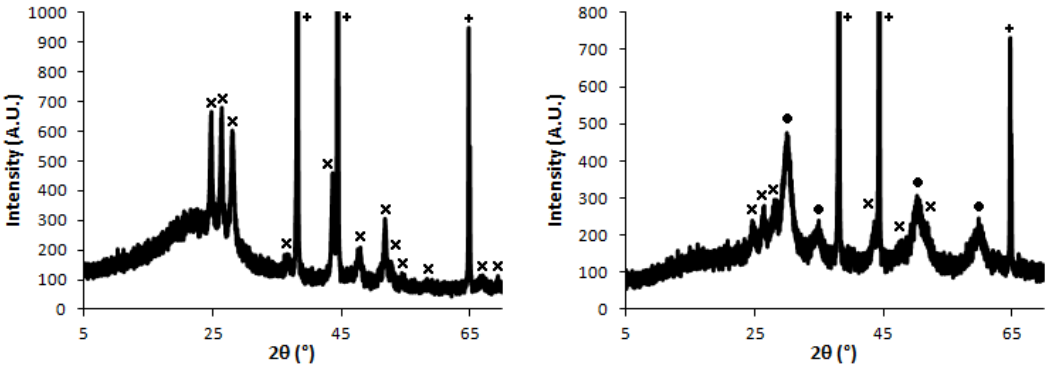

Figure 85: Powder XRD patterns of CdS loaded 3DOM SiO_2 (left) and ZrO_2 (right). + = Al sample holder, ● = tetragonal ZrO_2, JCPDS 01-079-1763, X = hexagonal CdS, JCPDS 01-075-1545.

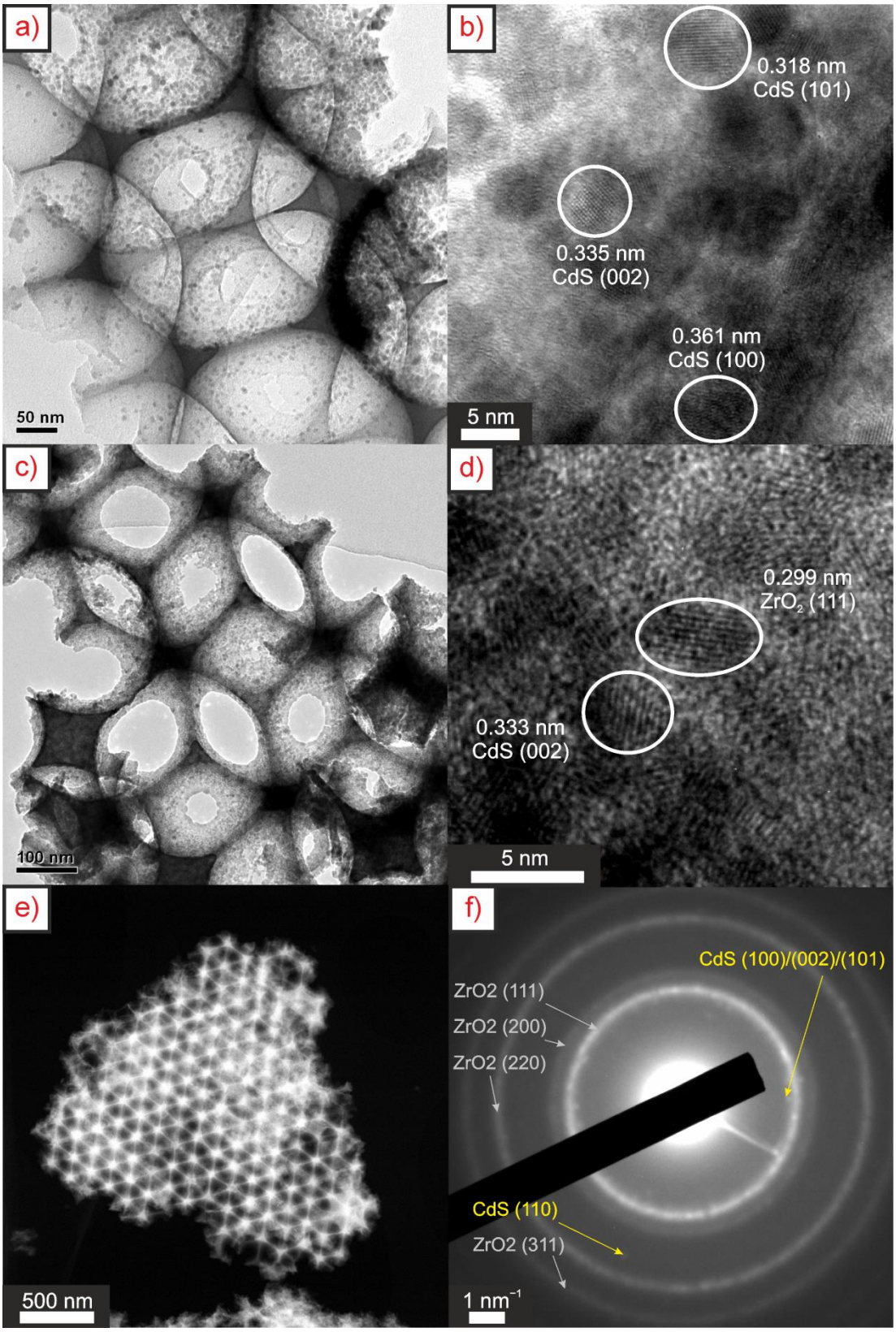

Figure 86: TEM images of CdS loaded 3DOM SiO_2 and ZrO_2. (a), (b) ***93.7%-CdS-316-SiO_2,*** *(c), (d) TEM images of* ***20%-CdS-270-ZrO_2,*** *(e) HAADF STEM image of* ***20%-CdS-270-ZrO_2,*** *and (f) electron diffraction pattern of* ***9.5%-CdS-270-ZrO_2****.*

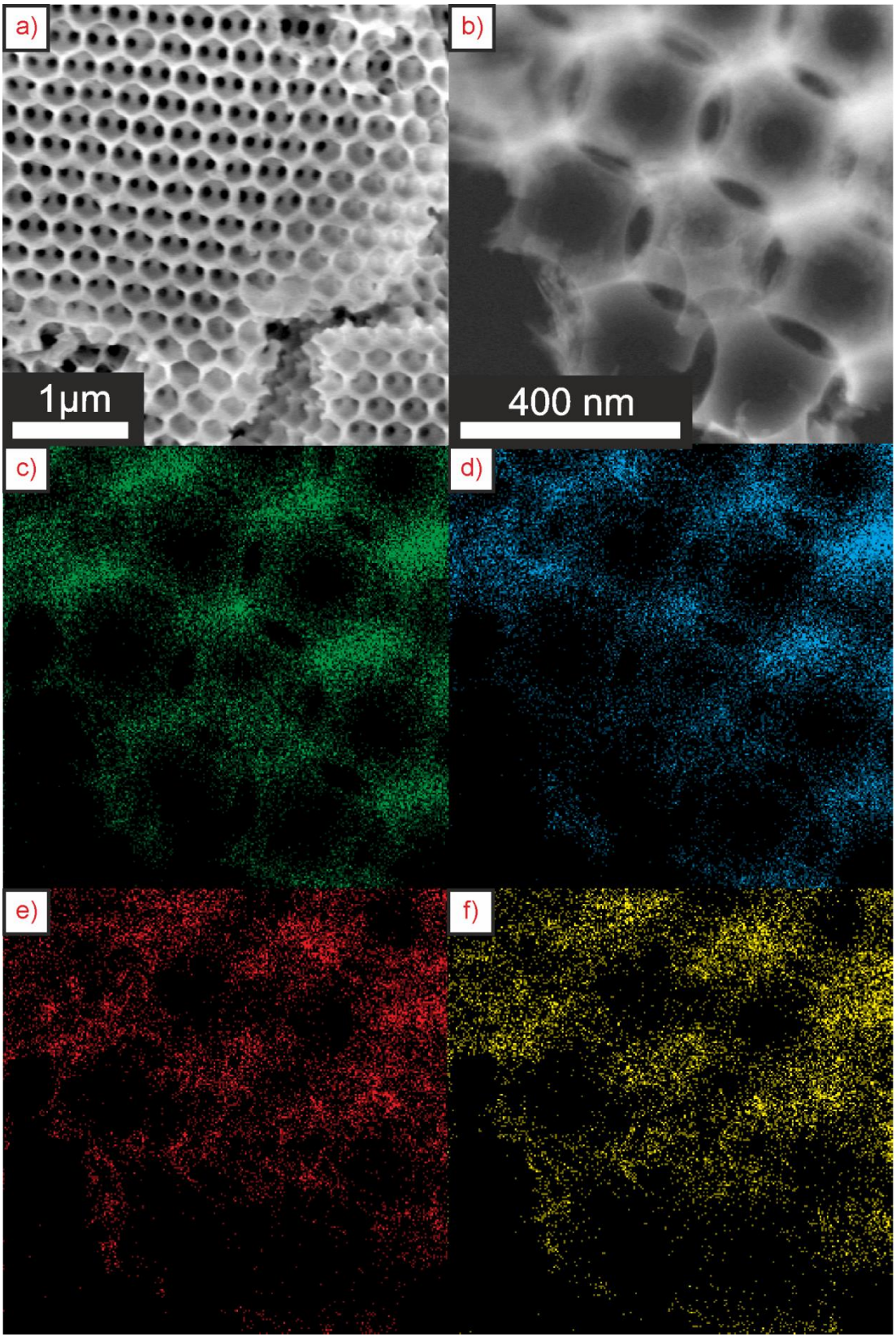

Figure 87: SEM image (a) and TEM EDX mapping of ***20%-CdS-270-ZrO_2****. HAADF STEM image (b), Zr map (c), O map (d), Cd map (e) and S map (f). Scale bar for (b) also applies for (c) – (f).*

Diffuse reflectance spectra of CdS loaded 3DOM SiO_2 and ZrO_2 and stop band shifts as a function of loading are shown in Figure 88 and Figure 89. As with previous composites, a linear red shift in the (111) stop band position is observed as nanoparticle loading is increased. Stop band shifts of 2.5 – 16.5 nm were observed for **15%-CdS-316-SiO_2 – 93.7%-CdS-316-SiO_2**, compared to 6 – 18.5 nm for **4%-CdS-255-ZrO_2 – 16%-CdS-255-ZrO_2.** The linear relationship between stop band shift and nanoparticle loading confirms the correlation between increased targeted loading and an increase in the amount of nanoparticles loaded into the pores.

The fill factors of **316-SiO_2** and **255-ZrO_2** were calculated as 5.27 % and 16.8 % respectively. From the experimental data, values of χ_{CdS}, n_{avg} and ϕ_{total} were calculated as a function of the loading amount using Equation 13 (section 3.2.2f Chapter 3). Equation 17 was then used to calculate the expected stop band shift. The values of χ_{CdS}, n_{avg}, ϕ_{total} and the experimental and calculated stop band shifts are listed in Table 18 (CdS loaded SiO_2) and Table 19 (CdS loaded ZrO_2). The calculated stop band shifts are plotted graphically in Figure 88b and Figure 89b. Good agreement is observed between the experimental and calculated data. Along with the microscopy data, the retention of intense stop bands on nanoparticle loading suggests a homogenous dispersion of nanoparticles within the pores.

Sample	χ_{CdS} / %	n_{avg}	ϕ_{total} / %	Experimental λ_{111} shift[a] / nm	Calculated λ_{111} shift / nm
15%-CdS-316-SiO_2	0.30	1.515	5.57	2.5	2.55
31.4%-CdS-316-SiO_2	0.66	1.573	5.94	5.0	5.39
50.5%-CdS-316-SiO_2	1.27	1.632	6.54	9.5	9.31
93.7%-CdS-316-SiO_2	2.20	1.738	7.47	16.5	16.72

Table 18: Fill factors, wall refractive indices and stop band shifts for CdS loaded 3DOM SiO_2. [a]Spectrometer resolution 0.5 nm.

Sample	χ_{CdS} / %	n_{avg}	ϕ_{total} / %	Experimental λ_{111} shift[a] / nm	Calculated λ_{111} shift / nm
4%-CdS-255-ZrO_2	0.97	2.209	17.77	6.0	5.62
8%-CdS-255-ZrO_2	1.77	2.217	18.58	10.5	10.38
16%-CdS-255-ZrO_2	3.15	2.232	19.95	18.5	18.69

Table 19: Fill factors, wall refractive indices and stop band shifts for CdS loaded 3DOM ZrO_2. [a]Spectrometer resolution 0.5 nm.

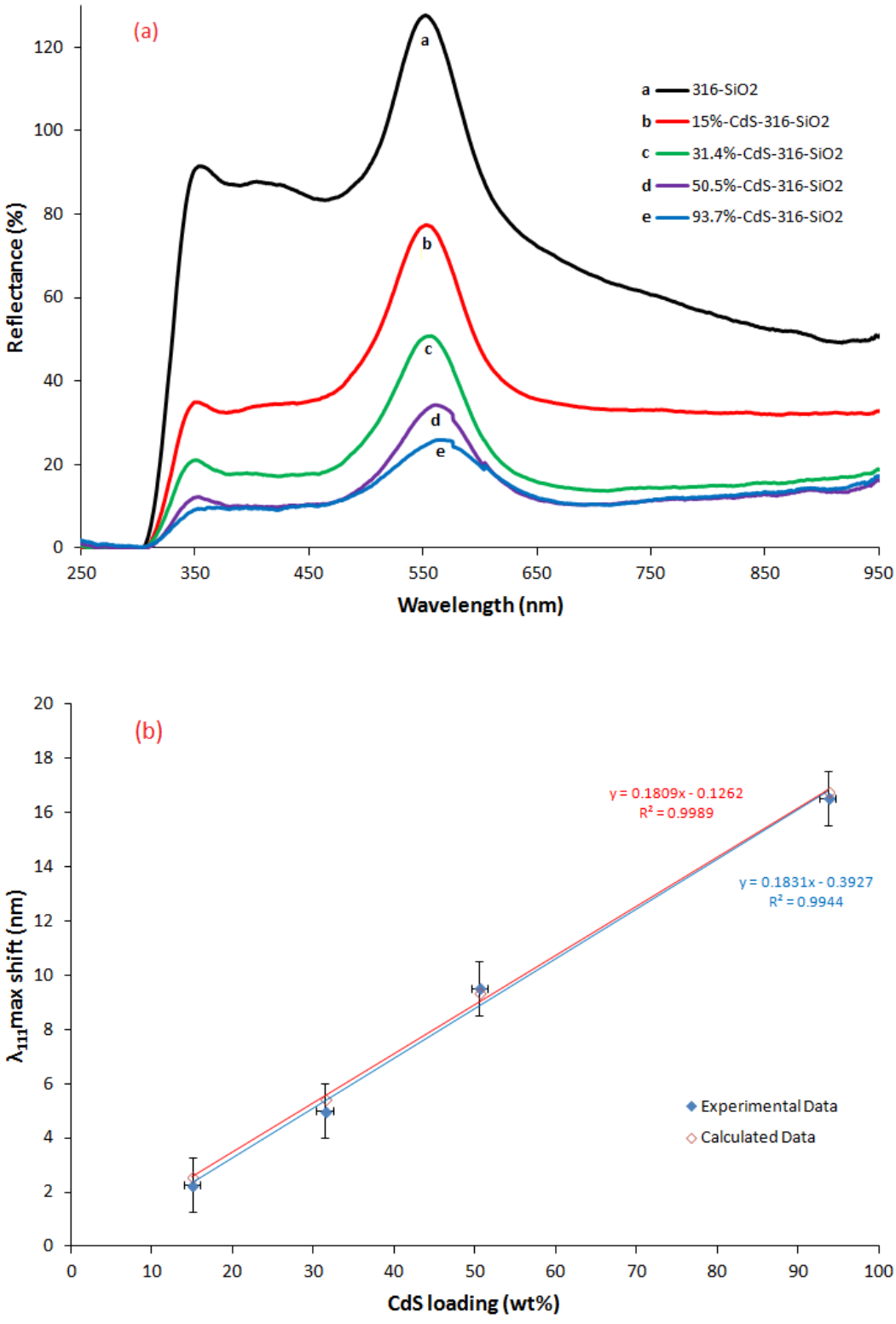

Figure 88: (a) DRUVS spectra of 3DOM SiO_2 and CdS loaded 3DOM SiO_2 and (b) experimentally measured and calculated stop band shift as a function of loading.

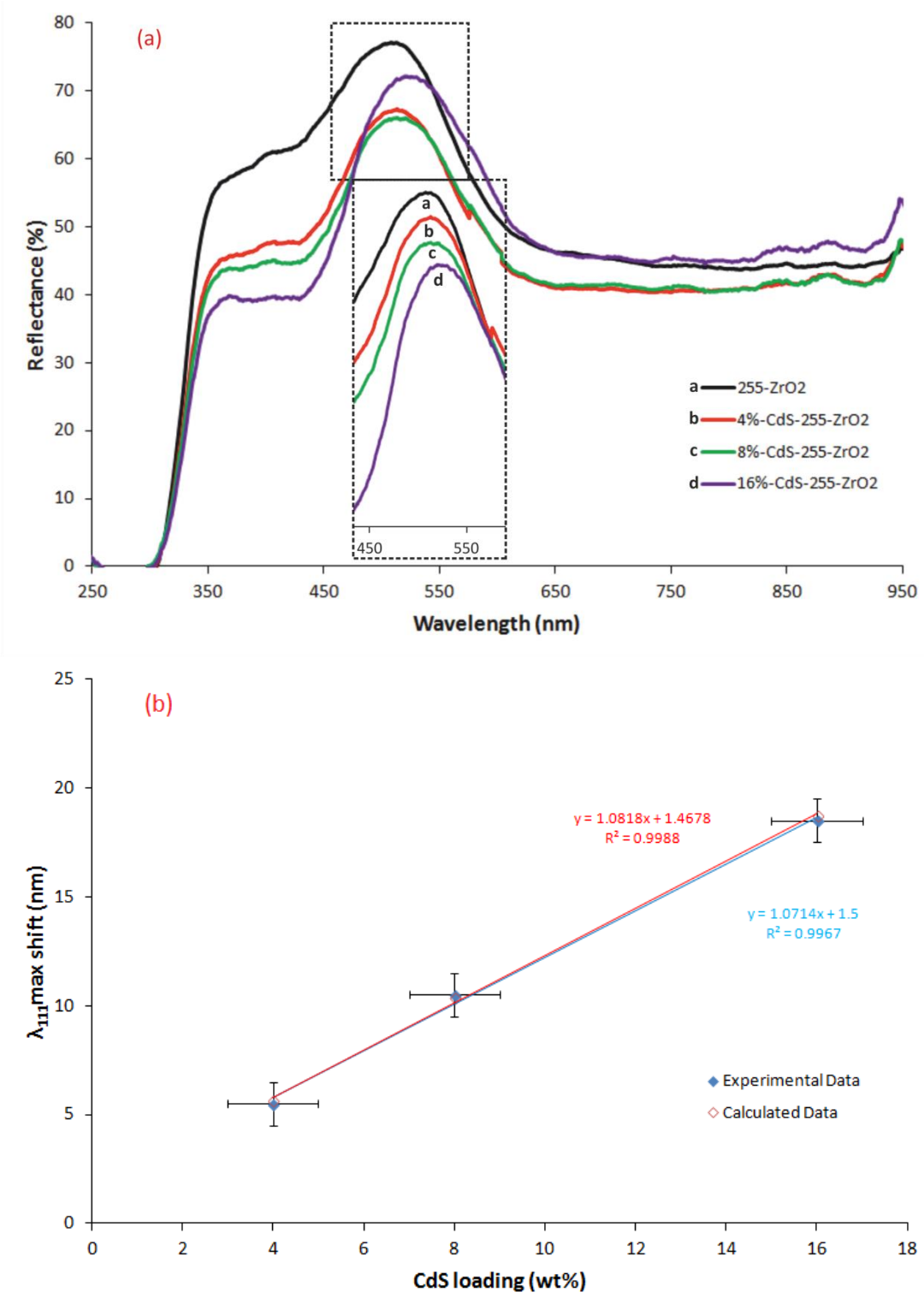

Figure 89: (a) DRUVS spectra of 3DOM ZrO_2 and CdS loaded 3DOM ZrO_2. Inset: Zoomed view of photonic stop bands, vertically offset for clarity. (b) experimentally measured and calculated stop band shift as a function of loading.

4.2.2: 3DOM Photocatalysts

In this section, photocatalytic hydrogen evolution will be demonstrated for 3DOM ZrO_2 supported CdS and TiO_2 nanoparticles. By variation of the periodicity of the support, the effect of overlap between photonic stop bands and electronic absorption will be studied.

4.2.2a: Sample Preparation

3DOM ZrO_2 materials with different periodicities were fabricated as outlined in chapter 2. Four materials with stop bands from 200 nm to 700 nm were chosen as deposition targets (samples **1** – **4**, Table 20), in addition to commercial ZrO_2 powder (sample **5**) as a control. SEM images of **1** – **5** are shown in Figure 91. The particle size of sample **5** was between 150 – 300 nm. Nitrogen adsorption porosimetry and BET theory gave surface areas of *ca.* 25 $m^2 g^{-1}$ for 3DOM ZrO_2 samples **1** – **4**, with no distinct variation due to the pore sizes of the 3DOM structure. The surface area of the non-porous sample **5** was determined to be 3 $m^2 g^{-1}$. Nitrogen adsorption/desorption profiles for these supports are displayed in the appendix (Figure 122 and Figure 123).

The periodicities and wall fill factors of the 3DOM materials are listed in Table 20. Diffuse reflectance spectra of the supports in air and soaked in aqueous Na_2S/Na_2SO_3 solution are shown in Figure 90. For sample **1**, in air the (111) stop band overlaps with the feature centred on *ca.* 325 nm due to absorption of the glass slide used for measurement. Using quartz slides for reflectance measurements, the (111) stop band was observed at 328 nm. On filling the voids with solution, the stop band is red shifted to 427 nm.

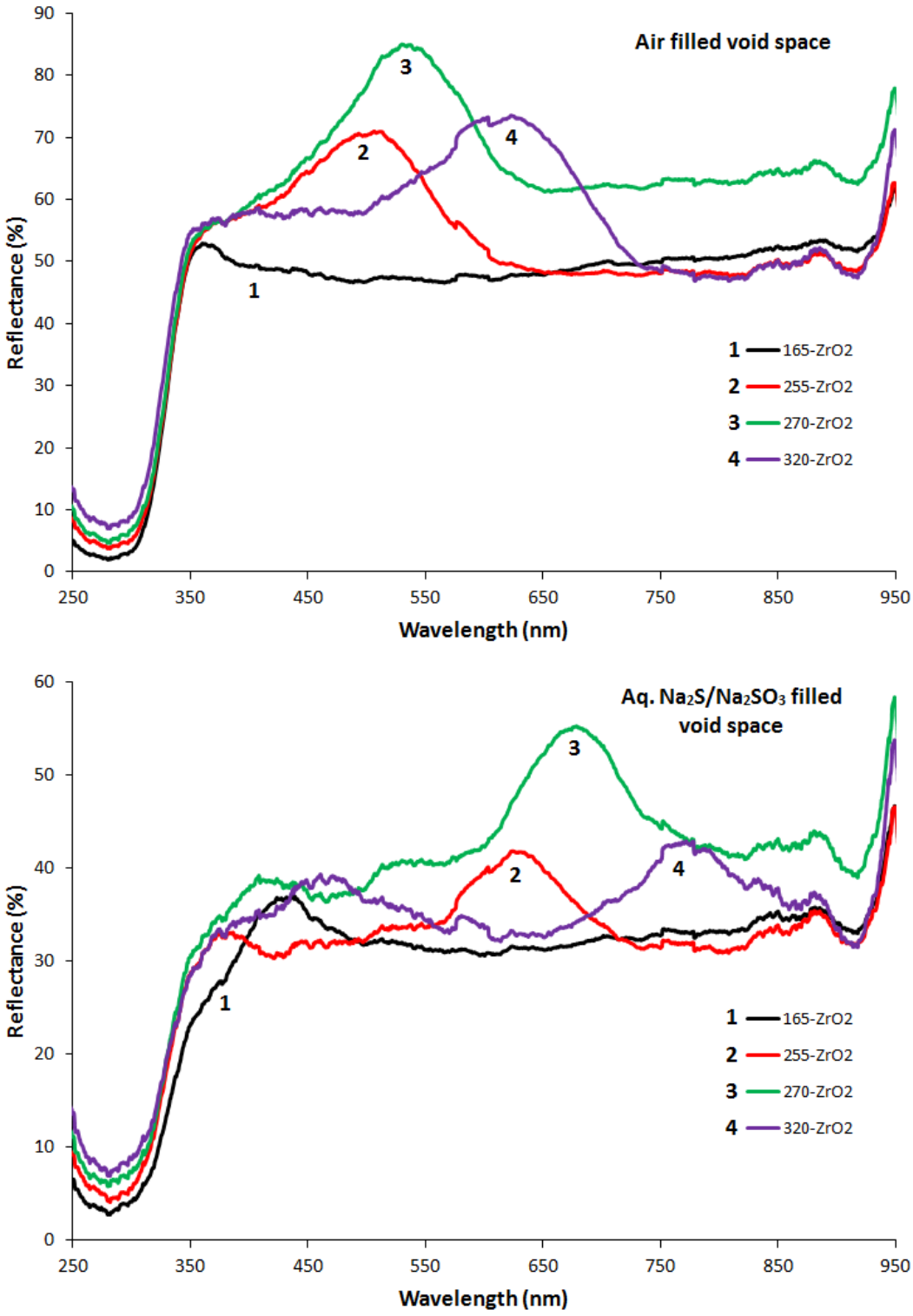

Figure 90: DRUVS spectra of 3DOM ZrO_2 samples used as supports for photocatalyst nanoparticles. Voids were filled with air (top) and aqueous 0.25 M Na_2S/0.35 M Na_2SO_3 (bottom).

Sample	Template Diameter[a] / nm	3DOM ZrO_2 periodicity[a] / nm	Calculated fill factor ϕ / %
1 (165-ZrO_2)	260±20	165±7	17.0
2 (255-ZrO_2)	400±13	255±17	16.8
3 (270-ZrO_2)	430±9	270±12	17.0
4 (320-ZrO_2)	500±17	320±20	17.0

Table 20: Periodicity and filling factors of 3DOM ZrO_2 materials used to support photocatalyst nanoparticles. [a]Measured from SEM.

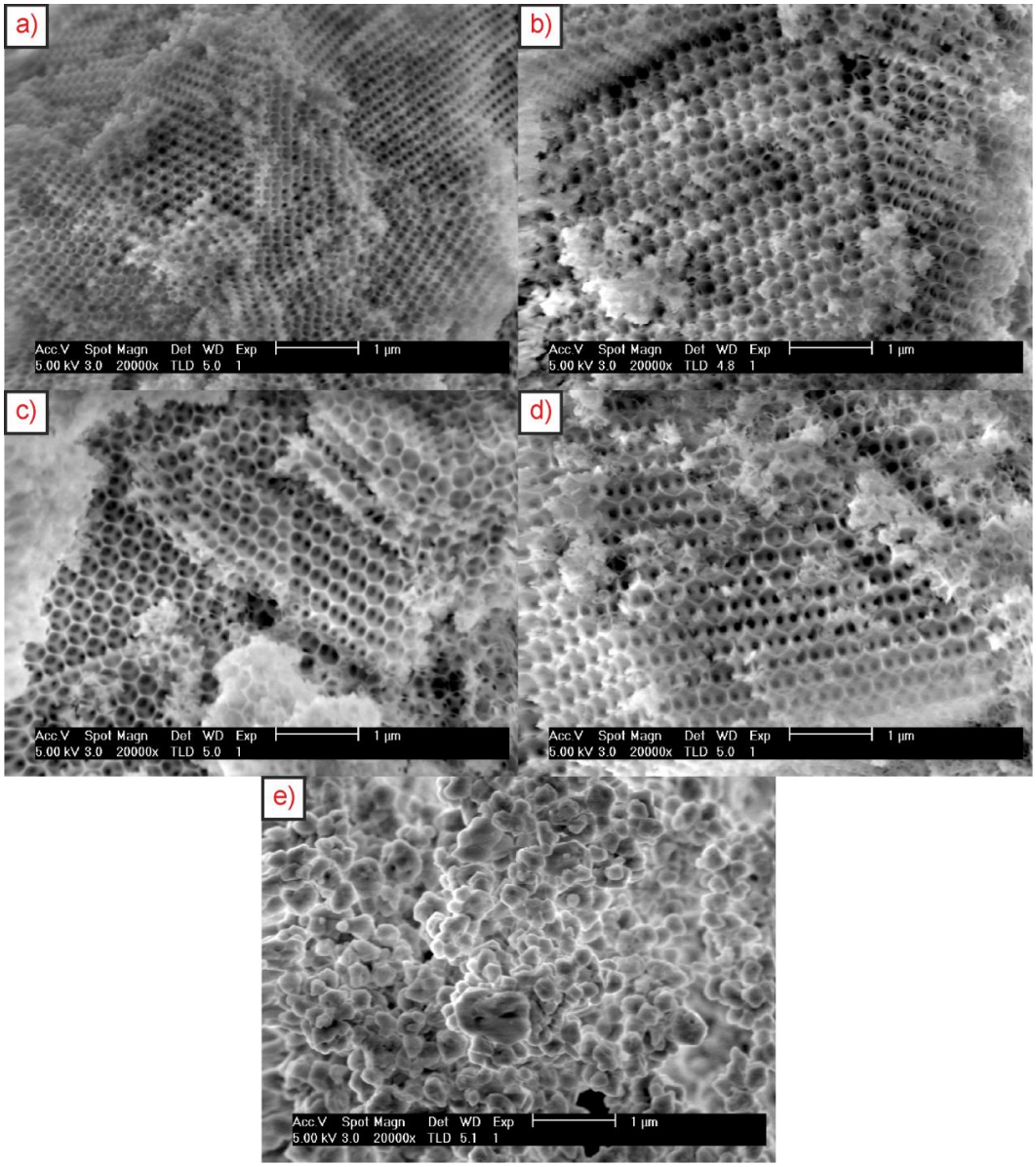

*Figure 91: SEM images of 3DOM and commercial ZrO_2 (**1 – 5**) used as supports. (a) **165-ZrO_2**, (b) **255-ZrO_2**, (c) **270-ZrO_2**, (d) **312-ZrO_2** and (e) commercial ZrO_2.*

In initial attempts at photocatalysis using CdS/3DOM ZrO_2 composites synthesised as described above, poor dispersion of the sample in the sacrificial reagent solution was observed. This was attributed to incomplete combustion of OA under argon, resulting in deposition of a thin layer of carbon on the surface. The formation of carbon films by calcination of organic materials under inert atmosphere has been reported in the literature.[256] For catalysis samples, removal of surface OA was achieved by calcination at 450 °C for 4 hours (ramp rate 1 °C min^{-1}) in air. Under these conditions, partial oxidation of CdS is expected,[246] however as will be described in section 4.2.2b, oxide/sulfide exchange can occur under the conditions used for photocatalysis.[247]

In addition, photocatalysis of Pt loaded CdS/3DOM ZrO_2 composites was attempted. Enhancements of hydrogen evolution activity were observed when 2 wt% (by CdS amount) Pt was loaded onto the CdS/3DOM ZrO_2, by a factor of 3.5 times for a sample with a loading of 25 wt% CdS. Comparable enhancements in activity of photocatalysts by loading of Pt have been reported in the literature.[96] However, to elucidate the effects of the photonic structure on the photocatalytic activity of CdS/3DOM ZrO_2 and TiO_2/3DOM ZrO_2 composites, deposition of a further quantity of nanoparticles adds complexity to the materials that may cloud the results. To ensure a fair test, homogeneous dispersion of Pt preferentially on the CdS nanoparticles rather than the non-photocatalytically active ZrO_2 (under visible light), and complete deposition of the targeted loading with no agglomeration would be required. Pt is also known to cause photoetching of CdS.[254] In the interests of simplicity and to evaluate the effects of the photonic structure, photocatalysis was attempted without the addition of a co-catalyst.

CdS (9.5 wt%) and TiO_2 (47.8 wt%) nanoparticle dispersions in 0.1 M OA/toluene were deposited on 3DOM ZrO_2 samples **1** – **4** and commercial ZrO_2 sample **5**, to form composites **1-CdS** – **5-CdS**, and **1-TiO_2** – **5-TiO_2**. To ensure consistency, photocatalysis samples were prepared in tandem using the same concentration and volume of nanoparticles from the same batch. The volatiles were evaporated at 80 °C overnight, followed by calcination at 450 °C for 4 hours (ramp rate 1 °C min^{-1}) in air. Vials were weighed at each stage of the deposition process to monitor the

nanoparticle deposition. Furthermore, evaporation of nanoparticle dispersions was also performed in separate vials containing no ZrO_2 to analyse the solid content of the dispersion. The masses of CdS and TiO_2 nanoparticles loaded onto ZrO_2 are summarised in Table 21. Photographs of the supports before and after CdS deposition are displayed in Figure 92. For TiO_2 deposition, no noticeable change in the colour of the powder was observed on nanoparticle loading. SEM and TEM analysis showed a homogeneous distribution of nanoparticles within the pores similar to previously displayed microscopy images.

Sample series	Mass support used / mg	Mass nanoparticles added (after calc) / mg	Nanoparticle wt%[a]
CdS / ZrO_2	30 ± 0.1	2.8 ± 0.05	9.5 ± 0.1
TiO_2 / ZrO_2	15.68 ± 0.05	7.35 ± 0.05	47.8 ± 0.1

Table 21: Compositional data for nanoparticle loaded materials. [a]Note OA constitutes 2.1% of pre-calcined support mass.

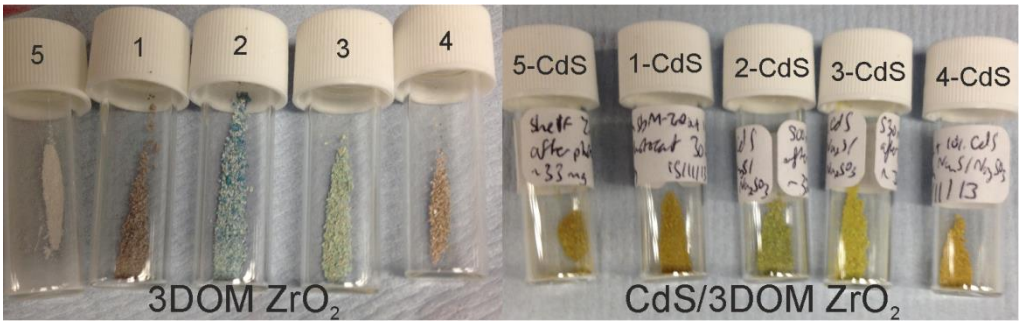

Figure 92: Photographs of commercial and 3DOM ZrO_2 samples. Before deposition (left) and after photocatalysis of 9.5 wt% CdS loaded samples (right). ***165-ZrO₂ (1),*** ***255-ZrO₂ (2),*** ***270-ZrO₂ (3),*** ***320-ZrO₂ (4)*** *and commercial ZrO_2 (**5**).*

Diffuse reflectance spectra for **1-TiO₂** – **5-TiO₂** and **1-CdS** – **5-CdS** are displayed in Figure 93 and Figure 94. In comparison to **1** – **5**, (111) Stop band shifts of 21 – 38 nm and 6 – 11 nm were observed for TiO_2 and CdS loading respectively, consistent with the targeted loadings of 47.8 % TiO_2 and 9.5 % CdS.

Using the fill factors of 3DOM ZrO_2 listed in Table 20, values of χ_{CdS}, χ_{TiO2}, n_{avg} and ϕ_{total} were calculated from the experimental stop band shifts for **1-TiO₂ – 4-TiO₂** and

1-CdS – 4-CdS. An expected stop band shift was calculated from these parameters using Equation 17 (section 3.2.2f). Calculated values of χ_{CdS}, χ_{TiO2}, n_{ave} and ϕ_{total} for the composites are listed in Table 22, in addition to the experimental and calculated stop band shifts.

Sample	χ_{CdS} / %	n_{avg}	ϕ_{total} / %	Experimental λ_{111} shift / nm	Calculated λ_{111} shift / nm
9.5%-CdS-165-ZrO_2 (**1-CdS**)	1.93	2.22	18.91	5.96	5.95
9.5%-CdS-255-ZrO_2 (**2-CdS**)	1.94	2.22	18.78	8.8	8.76
9.5%-CdS-270-ZrO_2 (**3-CdS**)	1.93	2.22	18.94	9.33	9.31
9.5%-CdS-320-ZrO_2 (**4-CdS**)	1.94	2.22	18.88	10.83	10.79

Table 22: Fill factors, wall refractive indices and stop band shifts for 9.5 wt% CdS loaded 3DOM ZrO_2 photocatalysis samples.

Sample	χ_{CdS} / %	n_{avg}	ϕ_{total} / %	Experimental λ_{111} shift / nm	Calculated λ_{111} shift / nm
47.8%-TiO_2-165-ZrO_2 (**1-TiO_2**)	6.22	2.271	23.2	20.5	20.39
47.8%-TiO_2-255-ZrO_2 (**2-TiO_2**)	6.21	2.271	23.1	30.5	29.87
47.8%-TiO_2-270-ZrO_2 (**3-TiO_2**)	6.22	2.271	23.2	32.5	31.90
47.8%-TiO_2-320-ZrO_2 (**4-TiO_2**)	6.22	2.271	23.2	37.5	36.81

Table 23: Fill factors, wall refractive indices and stop band shifts for 47.8 wt% TiO_2 loaded 3DOM ZrO_2 photocatalysis samples.

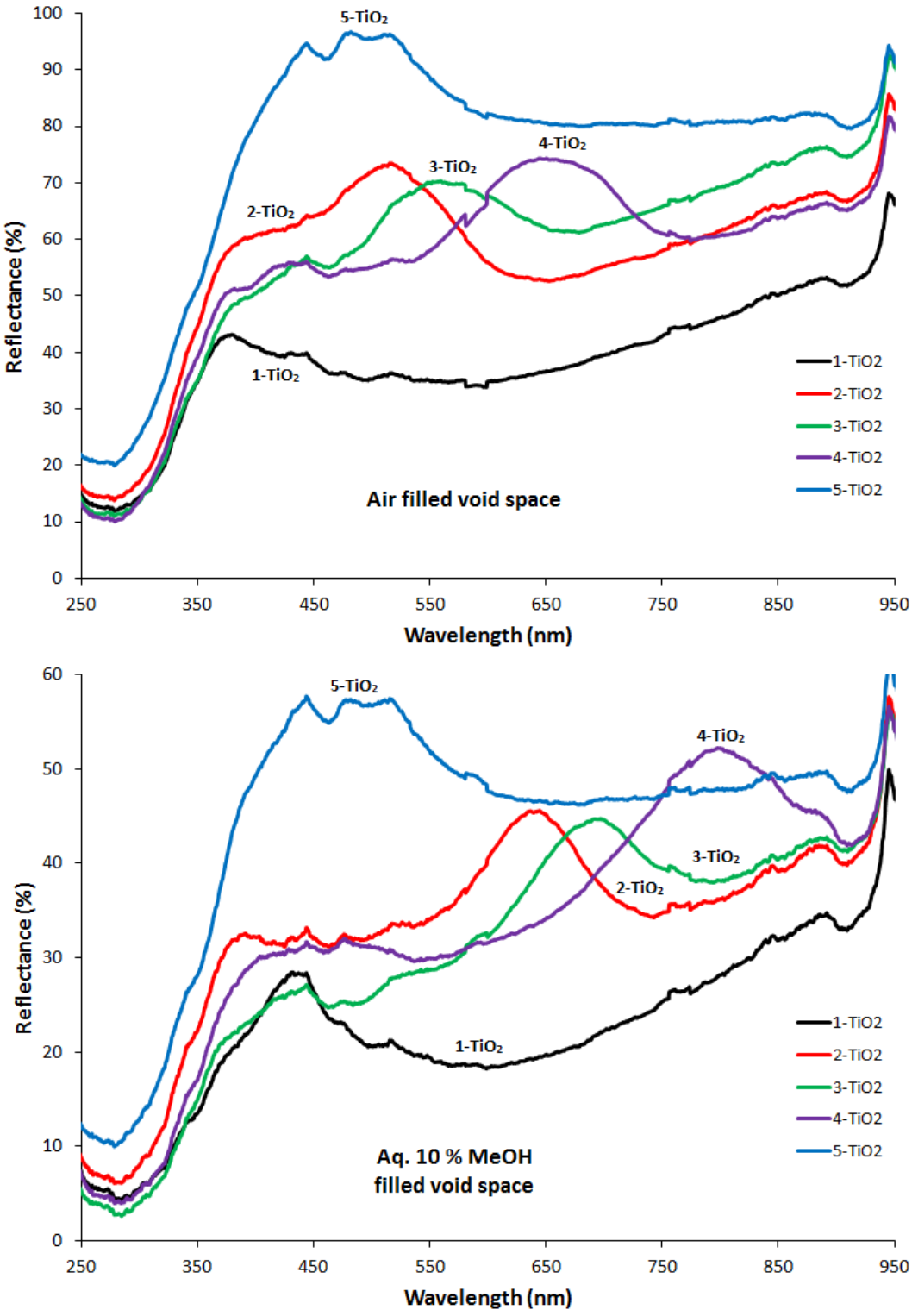

*Figure 93: DRUVS spectra of **1-TiO₂ – 5-TiO₂**. Voids were filled with air (top) and aqueous 10 % methanol (bottom).*

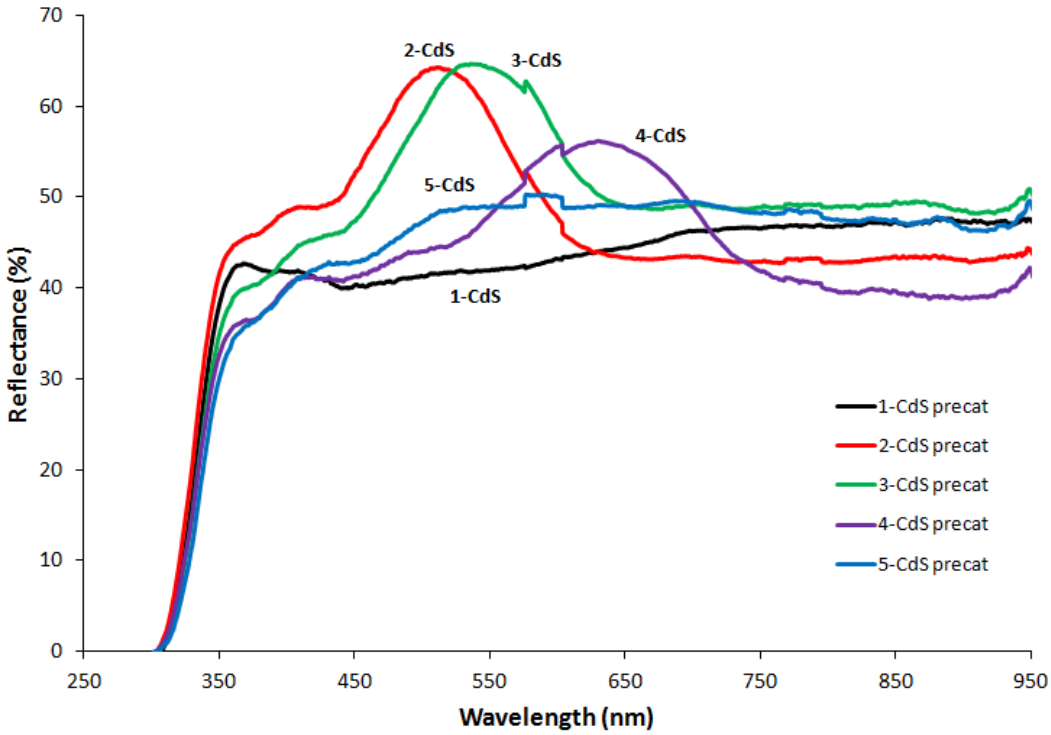

*Figure 94: DRUVS spectra of **1-CdS** – **5-CdS** in air before photocatalysis.*

4.2.2b: Photocatalytic Testing

CdS loaded 3DOM ZrO_2 samples (30 mg) were tested for photocatalytic hydrogen evolution from sacrificial aqueous sodium sulfide (0.25 M) and sodium sulfite (0.35 M) solution (20 mL) under visible light (> 400 nm cutoff). Samples were tested under identical conditions, with 3 initial consecutive runs of 6/14/6 hours for each sample. Finally, each sample was tested for a further 12 hours. Samples were isolated by centrifugation between runs, followed by redispersion in fresh solution. After the initial 6 hour run, catalytic activity was increased, and comparable within 15 % for subsequent reactions. A control reaction of 30 mg Ta_2O_5 in 10 % methanol was run periodically under UV light to check the system calibration.

After the first run, the colour of the powders gained a distinct yellow tinge (Figure 92). Due to calcination in air, partial surface oxidation of the CdS QDs is likely.[246] Before photocatalysis, PXRD analysis of the composites showed single phase ZrO_2 with no additional peaks, suggesting the cadmium species are amorphous. TEM EDX

showed a shoulder on the Zr peak at 2.35 keV corresponding to sulfur (Figure 95). After photocatalysis, this peak showed greater intensity and definition, suggesting reaction with the sacrificial reagent solution. CdS can be prepared by reaction of CdO with Na_2S at room temperature,[247] hence the first catalysis run is likely an important step in formation of the catalyst species. PXRD and electron diffraction of the composites after photocatalysis showed crystalline hexagonal CdS and wide area SEM EDX analysis showed a 1:1 Cd:S atom ratio consistent with sulfurization of surface CdO. In addition, SEM EDX analysis confirmed the CdS loading as 9.5 ± 0.2 wt%. Phase analysis after subsequent reactions showed no change in both loading amount and the Cd:S ratio.

As further confirmation of the loading consistency, the calculated volume fractions of **1-CdS** – **4-CdS** (Table 22) were compared to the volume ratios from the initial mass of CdS and ZrO_2. The ratios of χ_{CdS} to ϕ_{ZrO2} (0.113 – 0.115), representing the additional volume contribution from the nanoparticles, are in good agreement with the expected volume ratio of CdS to ZrO_2 (0.112) from the masses used and their respective densities, confirming identical loadings across the series.

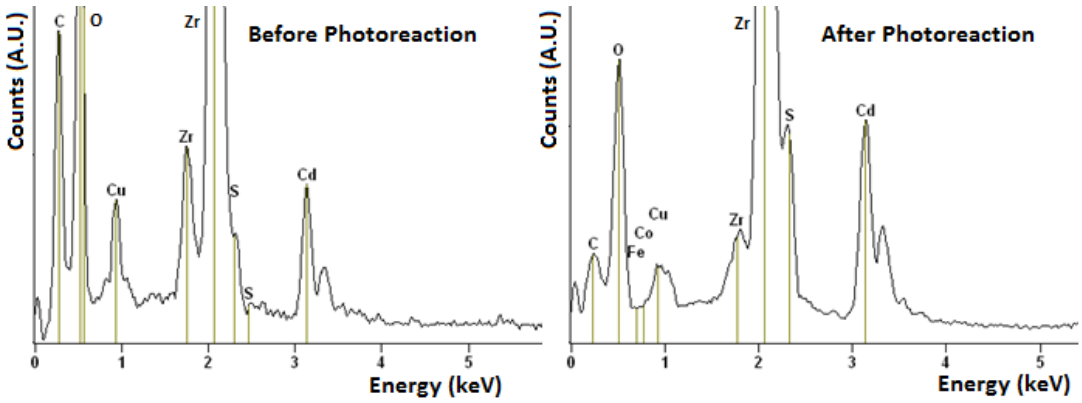

Figure 95: TEM EDX analysis of 9.5 wt% CdS loaded 3DOM ZrO_2 samples before (left) and after (right) photocatalysis.

DRUVs analysis of **1-CdS** – **5-CdS** after photocatalysis (Figure 96) show an enhanced absorption edge with onset around 520 nm in comparison to Figure 94, consistent with the conversion of surface oxide to sulfide. Tauc plots of the reflectance data gave a CdS band gap of 2.4 eV, corresponding to 518 nm, in agreement with literature values for bulk CdS.

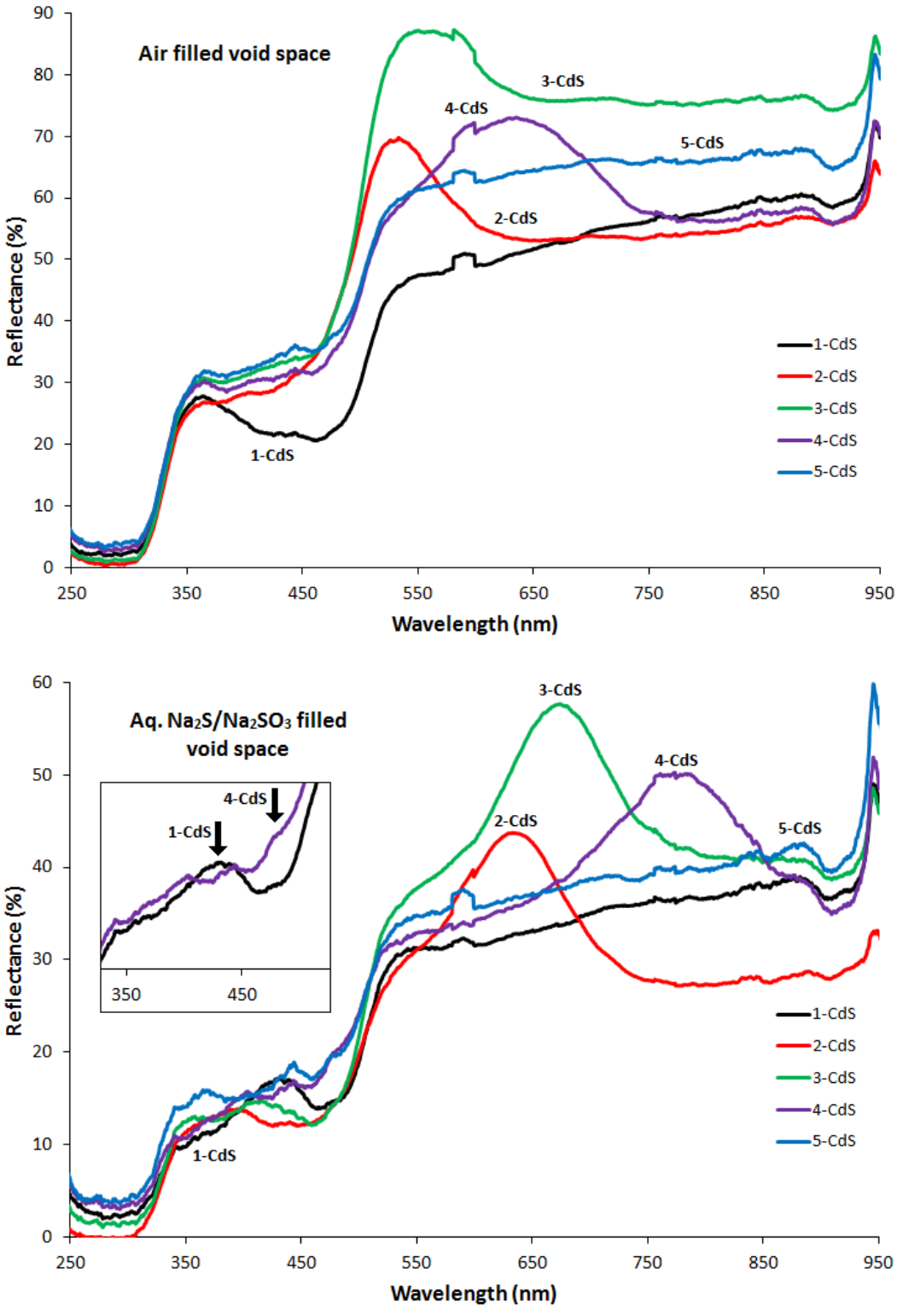

*Figure 96: DRUVS spectra of **1-CdS** – **5-CdS** after photocatalysis. Voids were filled with air (top) and aqueous 0.25 M Na_2S/0.35 M Na_2SO_3 (bottom). Inset: zoomed 350 – 500 nm region, showing **1-CdS** (111) and **4-CdS** (220) stop band positions.*

Photocatalysis data for **1-CdS – 5-CdS** is shown in Figure 97 and Table 24. All samples contain the same amount of active catalyst species, however the rates of hydrogen evolution vary greatly across the series from 220 µmol h^{-1} g^{-1} to 1083 µmol h^{-1} g^{-1}. These values are within the range of activities reported for CdS photocatalysts in the literature. Uncoated 3DOM ZrO_2 showed no activity for hydrogen evolution under visible light, confirming that catalysis is limited to CdS nanoparticles. For **2-CdS**, the reaction was run for sufficient time to form 33 µmol H_2, greater than the number of moles of CdS (18 µmol), confirming that hydrogen production is catalytic.

For all hydrogen evolution rates, an error of 10 % is estimated, which does not account for the observed differences in activity across the sample series. A possible explanation is postulated in the following section, taking into consideration the catalyst dispersion, surface area and photonic properties.

Sample	Activity[a] / µmol h^{-1} g^{-1}
1-CdS	450
2-CdS	1083
3-CdS	220
4-CdS	422
5-CdS	230

*Table 24: Photocatalytic hydrogen evolution of **1-CdS – 5-CdS**. Conditions: [a] 30 mg catalyst (2.6 mg CdS), 20 mL Na_2S (0.25 M) and Na_2SO_3 (0.35 M) in water, λ > 400 nm.*

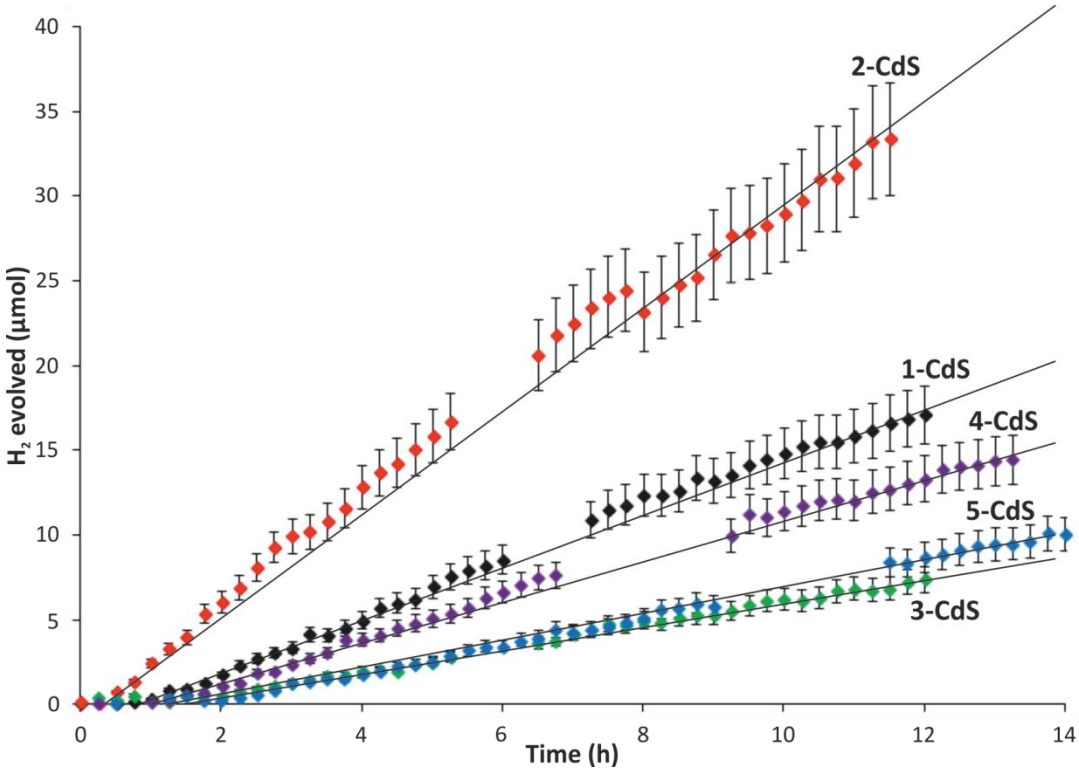

Figure 97: Photocatalytic hydrogen evolution of 9.5 wt% CdS loaded ZrO_2 composites (2.6 mg CdS) ***1-CdS*** *–* ***5-CdS*** *from aqueous solution containing 0.25 M Na_2S and 0.35 M Na_2SO_3 under visible light > 400 nm.*

As a baseline, the non-photonic powder **5-CdS** showed an activity of 230 µmol h^{-1} g^{-1}. The activity of this material was expected to be lower than the 3DOM samples due to the comparatively low surface area of the support (3 m^2 g^{-1} versus 25 m^2 g^{-1}). For **1-CdS** – **4-CdS**, the difference in activity could be attributed to the CdS dispersion, surface area, or diffusion of reagents and products. In terms of dispersion, SEM (Figure 98) and TEM images of the composites showed homogeneously coated CdS nanoparticles, with no evidence of agglomeration. EDX analysis returned identical CdS wt% loadings across the series consistent with the targeted loadings. In addition, the stop band shift observed by DRUVS agreed strongly with the expected shift, and supported the conclusion that full incorporation of the deposited nanoparticles within the 3DOM lattice has been achieved.

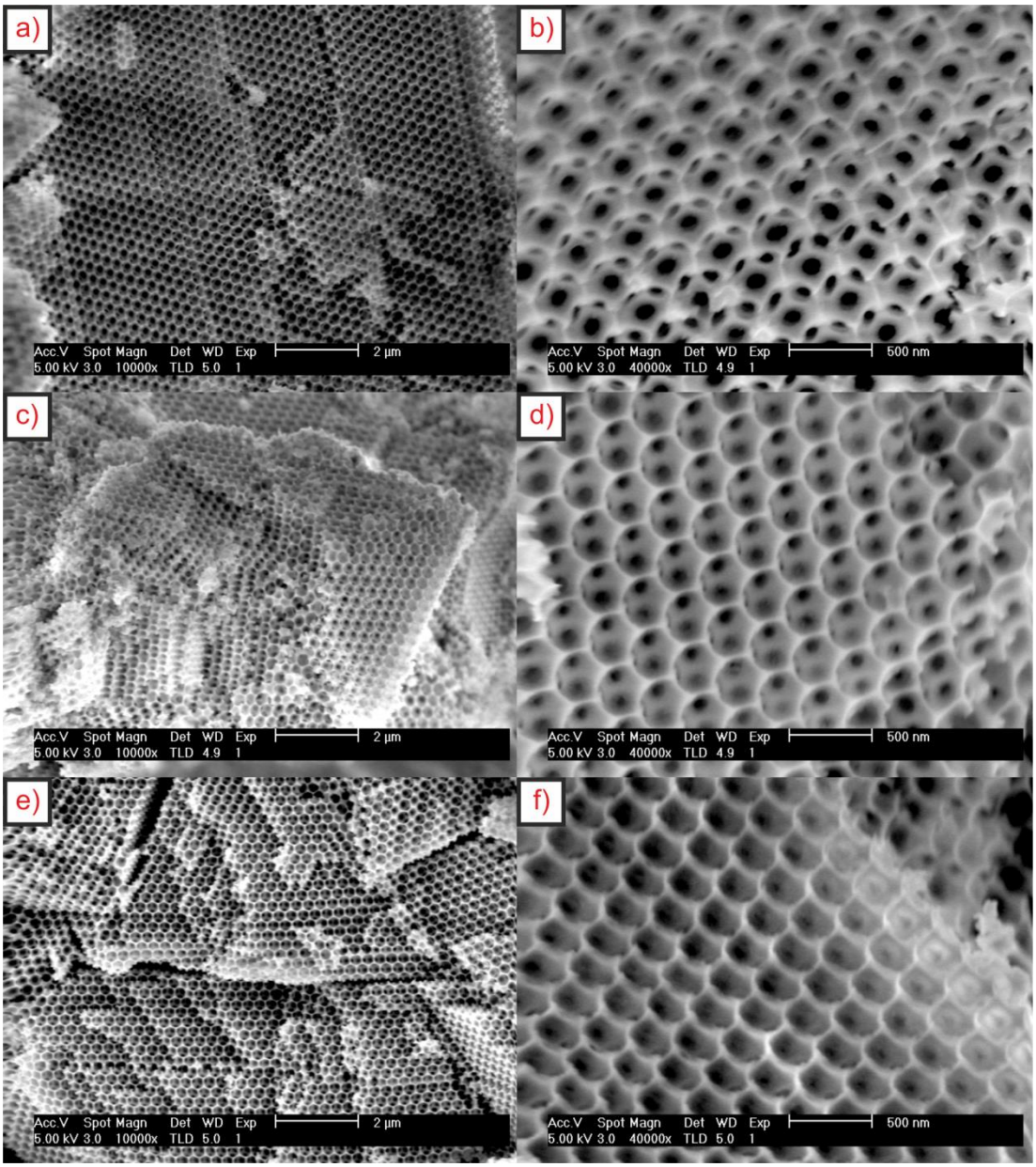

Figure 98: SEM images of photocatalyst samples. (a), (b) ***4-CdS*** *before photocatalysis, (c), (d)* ***4-CdS*** *after photocatalysis, and (e), (f)* ***3-TiO$_2$****.*

The surface area of the supports **1** – **4** were found to be similar (*ca.* 25 m^2 g^{-1}). As discussed in section 3.2.3 in chapter 3, deposition of 10 wt% TiO_2 nanoparticles in 3DOM ZrO_2 was observed to increase the surface area from 20.6 m^2 g^{-1} to 29.1 m^2 g^{-1} by an enhancement of the surface roughness.[257] The mass of **1-CdS** – **5-CdS** obtained was insufficient for surface area measurements, however similar enhancements of surface roughness are likely. Small, if any variations in surface area of **1-CdS** – **4-CdS** are expected as each material contains the same volume of

added nanoparticles. An enhanced surface area would also be expected for **5-CdS** in comparison to **5** due to an increased surface roughness.

If the rate of photocatalysis was limited by diffusion of reagents and products within the 3DOM structure, **5-CdS** would be expected to show the highest activity. As this is not the case, and literature studies have reported that diffusion throughout 3DOM materials is unrestricted,[258] the data does not support this conclusion.

The factors discussed above cannot fully account for the differences in activity of **1-CdS** – **4-CdS**. An explanation for the differences in activity of the materials may be postulated by an analysis of the photonic structure of the composites. A higher activity would be predicted for 3DOM materials compared to bulk powders in the absence of photonic effects due to the increased surface area. For **3-CdS**, a similar, but slightly lower hydrogen evolution rate is observed in comparison to **5-CdS**. The (111) stop band is centred at 673 nm and is unlikely to influence CdS absorption. For the (220) stop band centred at 413 nm, a reduction in the group velocity of photons at the red edge may be observed, leading to enhanced CdS absorption. However, partial reflection of high energy incident photons (400 – 450 nm) will also occur, and may contribute to the decreased activity in comparison to **5-CdS**.

For **1-CdS**, the (111) stop band is centred at 435 nm, and spans from *ca.* 405 – 470 nm. Partial reflection of high energy photons in this region may be expected to reduce the photocatalytic activity. However, the hydrogen evolution rate is enhanced by a factor of *ca.* 2 times is observed in comparison to **5-CdS**. The slow photon region at the red edge of the stop band coincides with the band gap of CdS (Figure 99a), and may account for this enhancement. Photons emitted by e^-/h^+ recombination will be slowed within the photonic crystal. Multiple scattering and diffraction of the emitted photon can lead to light trapping and increases the probability of reabsorption. Enhancements of similar magnitude have been observed for IPCE in CdS/3DOM TiO_2 composites, and photocurrents in 3DOM WO_3 when the absorption band is at the red edge of a stop band.[98, 125] A limit of 2.1 times enhancement in the rate of degradation of methylene blue has been proposed by

overlapping the electronic absorption with the red edge of a stop band in 3DOM TiO_2 in comparison to a film of TiO_2 nanoparticles of the same thickness.[95]

For **4-CdS**, the hydrogen evolution rate is enhanced by a factor of *ca.* 1.8 times in comparison to **5-CdS**. As with **3-CdS** the (111) stop band is outside the absorption region at *ca.* 780 nm and has no effect on CdS absorption. The enhancement in activity is attributed to the (220) stop band centred at 470 nm via slow photon and scattering effects of photons at the red edge of the stop band as with **1-CdS**.

Few literature studies exist on water splitting reactions using photonic crystal based composites. Cui *et al.* have demonstrated overall water splitting with photonic WO_3.[137] Overlap of the red edge of the stop band with the absorption of WO_3 results in enhanced activity due to slow photon effects, to a maximum 1.5 times enhancement compared to a crushed photonic sample. Other studies have also investigated red edge slow photons.[113] In all investigations, red edge enhancements are rationalised due to localisation of the maximum amplitude of electromagnetic radiation in the walls of the 3DOM structure. The magnitude of enhancements in photocatalytic activity observed for **1-CdS** and **4-CdS** are consistent with enhancements observed in the literature by slow photons at the red edge of a photonic stop band.[95, 96, 113, 137]

For **2-CdS,** the hydrogen evolution rate is enhanced by a factor of *ca.* 4.7 times in comparison to **5-CdS**. The (111) stop band centred at 640 nm spans from *ca.* 550 – 735 nm, and the (220) stop band covering *ca.* 365 – 415 nm is centred on 390 nm. At the red edge of the (220) stop band, enhanced CdS absorption is facilitated by a reduction in group velocity and scattering of high energy visible light photons, however partial reflection of incident photons of wavelength 400 – 415 nm is expected. Enhancement is also facilitated by overlap of the blue edge of the (111) stop band with the absorption edge of CdS. Differences in the mechanism by which photons are slowed, but similar magnitudes of reduction in velocity, have been reported for the red and blue edges of a stop band respectively.[94] Blue photons have a reduced velocity within the photonic crystal in comparison to red photons, which leads to a reduced transmission through the lattice. This effect is offset by

enhanced internal scattering of blue photons due to lattice defects. In terms of catalysis, where the blue edge of a photonic stop band overlaps with the absorption edge, enhancements of greater magnitude have been proposed in the literature compared to the red edge. This is explained graphically in Figure 99. In Figure 99a, the stop band is within the absorption edge, and hence reflection by the stop band counters the enhanced semiconductor absorption from slow photons at the red edge. In Figure 99b, the stop band is outside of the absorption band, and the photons which are reflected are too low in energy to promote an electron to the conduction band.

El Harakeh *et al.* have reported a maximum IPCE enhancement of 4.7 times for CdS/3DOM TiO_2 composites with overlap of the stop band blue edge and CdS emission, compared to 1.8 times due to red edge slow photons.[98] The rate of photoconversion of azobenzene has been enhanced by a factor of 1.35 by overlap of the absorption with the blue edge of a stop band in 3DOM SiO_2.[124] However, the low refractive index contrast in this system likely results in the small enhancement in rate. To the best of our knowledge, no enhancements of reactions relevant to water splitting by slow photons at the blue edge of a photonic stop band have been reported in the literature. The magnitude of the increase in hydrogen evolution in our system (4.7 times) is comparable to the IPCE enhancements reported by El Harakeh *et al.*[98]

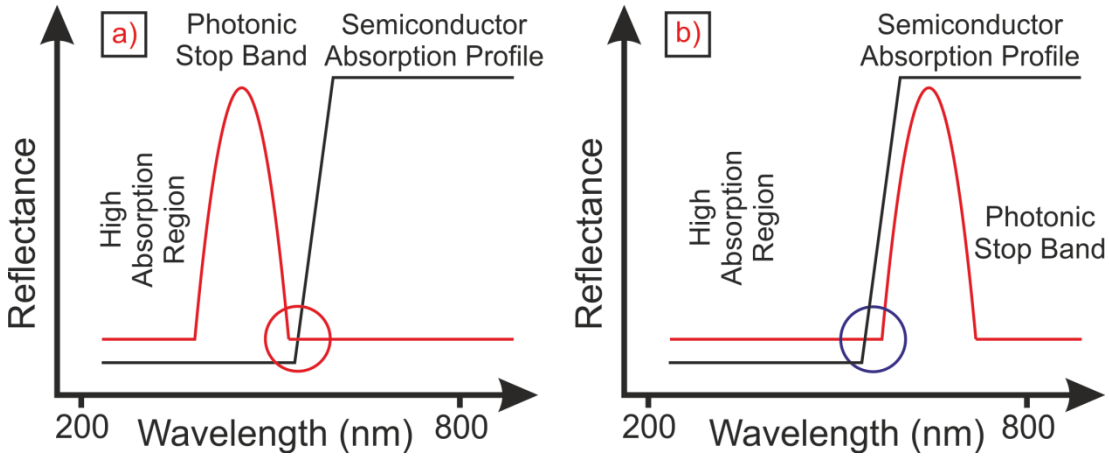

Figure 99: Simulated reflectance spectra in which regions of slow photons at the edge of a stop band overlap with electronic absorption. Circles represent (a) Red edge overlap and (b) Blue edge overlap.

Light at the edges of the photonic band gap has been described as a standing wave.[97, 98] At the red edge of the stop band, the wave maxima are localised in the walls, and the nodes in the voids. The opposite is true for light at the blue edge of the stop band, with the wave maxima in the void spaces. For a 3DOM photonic crystal in which the entirety of the wall is composed of a semiconductor material, slow photons at the red edge are dominant for enhancement as photon absorption corresponds with wave maxima. Photons at the blue edge of the stop band would not be expected to enhance activity as the maximum intensity of the wave is in the voids. In our system, the photocatalyst material is effectively localised on the interface between the wall and the void space. The amplitude of the propagation wave of photons at the blue and red edges of the stop band will be non-zero at this interface. Hence, observed enhancements of activity by slow photons at the blue and red edges of stop bands in our systems are consistent with expectations from theory.

As further control experiments, photocatalysis of TiO_2 nanoparticles loaded onto ZrO_2 samples **1** – **5** was studied. EDX analysis of the composites returned identical TiO_2 wt% loadings across the series consistent with the targeted loadings of 47.8 %. As previously discussed, TiO_2 is active for photocatalytic hydrogen production from water using methanol as a sacrificial hole acceptor. Multiple catalysis runs were

performed under the same conditions, and observed activity was comparable within 15 % for all reactions. The photocatalytic activity of the composites **1-TiO_2** – **5-TiO_2** under UV light from 10 % aqueous methanol over 9 hours is shown in Table 25 and Figure 100. Hydrogen evolution rates of 200 to 326 μmol h^{-1} g^{-1} were observed, with no hydrogen evolved for control samples of **1** – **5** with no TiO_2 present. ZrO_2 has been reported as a photocatalyst under UV light in the literature using a Hg lamp for illumination.[259] The spectral profile of the Xe lamp used in this study, with low intensity below 300 nm (Section 5.2.10d Figure 105), may be responsible for this lack of activity.

The activities of **1-TiO_2** – **5-TiO_2** for hydrogen production are similar. For **2-TiO_2** in which the photonic stop band observed is outside of the absorption region of anatase TiO_2 (380 nm), within error identical activity to **5-TiO_2** is observed. This confirms the enhancements observed for **2-CdS** are due to favourable overlap of CdS absorption and the photonic structure. Small enhancements are observed for **1-TiO_2**, **3-TiO_2** and **4-TiO_2** in comparison to **5-TiO_2**, to a maximum of 1.6 times in **4-TiO_2**. The absorption band of TiO_2 may interact with the blue edge of the (111) stop band of **1-TiO_2**. Compared to the enhancements observed for **2-CdS**, the decreased enhancement in **1-TiO_2** activity could be attributed to the decreased intensity of the (111) stop band reflection. Similar effects may be responsible for the enhancements observed in **3-TiO_2** and **4-TiO_2**.

If typical factors which affect the activity of a catalyst such as surface area, diffusion or dispersion were responsible for the activity differences observed, an identical trend would be expected for **1-TiO_2 – 5-TiO_2** and **1-CdS – 5-CdS**. The observed hydrogen evolution rates across the TiO_2 series are similar, and confirm that this is not the case. Hence, the above explanation for enhancement in activity of **1-CdS – 5-CdS** is supported.

Sample	Activity[a] / µmol h^{-1} g^{-1}
1-TiO_2	261
2-TiO_2	221
3-TiO_2	260
4-TiO_2	326
5-TiO_2	200

*Table 25: Photocatalytic hydrogen evolution of **1-TiO_2 – 5-TiO_2**. Conditions: [a]23 mg catalyst (7.4 mg TiO_2), 20 mL 10 % methanol in water, λ > 325 nm.*

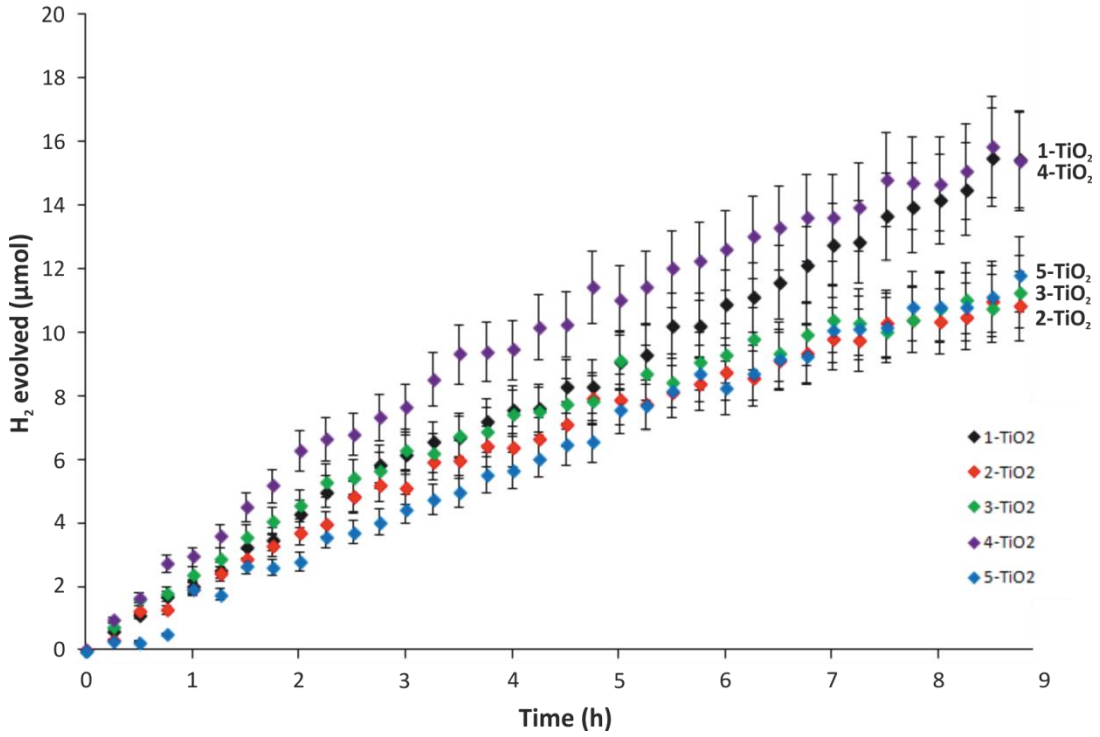

*Figure 100: Photocatalytic hydrogen evolution of 47.8 wt% TiO_2 loaded ZrO_2 composites (7.35 mg TiO_2) **1-TiO_2 – 5-TiO_2** from aqueous solution containing 10 % methanol under UV light > 325 nm.*

4.3: Conclusions and Future Work

The deposition of CdS nanoparticles in 3DOM SiO_2 and ZrO_2 has been demonstrated. Homogeneous deposition was confirmed by electron microscopy and DRUVS analysis. As with CdS supported FTO and mesoporous SiO_2 in the previous chapter, simultaneous ligand removal and Si/Zr/Sn-O-Cd bond formation anchors the nanoparticles to the surface. The generality of the method is extended to non-oxide nanoparticle materials, further enhancing its versatility. Oxidation of CdS nanoparticles was observed under the calcination conditions utilised, however the CdS phase could be reformed by reaction with Na_2S. As future work, the importance of the oxide support in the deposition process could be evaluated by deposition in 3DOM nitride materials such as Ta_3N_5.

Photocatalytic hydrogen evolution has been demonstrated from CdS/3DOM ZrO_2 and TiO_2/3DOM ZrO_2 composites using sacrificial electron donors. For a series of CdS/ZrO_2 samples with different pore sizes the rate of hydrogen evolution varied widely, which could not be explained by typical material properties which affect the activity of a photocatalyst such as surface area, catalyst dispersion and diffusion limitations. The absence of these factors was confirmed by catalysis of TiO_2/ZrO_2 composites, which showed similar activities across the series. An explanation for the variation of activity was postulated based on interaction with the different photonic structures of the materials. For **2-CdS**, an activity enhancement of 4.7 times in comparison to the non-porous control **5-CdS** was observed, attributed to enhanced scattering and slow photons at the blue edge of the (111) stop band. In comparison to **5-CdS**, **1-CdS** and **4-CdS** showed enhancements of 2 and 1.8 times due to slow photons and scattering at the red edge of the (111) and (220) stop bands respectively, which were located within the absorption band of CdS. The potential for both red and blue edge enhancements in these materials is made possible due to the confinement of the light absorber at the surface of the pores.

For overlap of electronic absorption with the red edge of a photonic stop band, water splitting reactions have been demonstrated in literature studies, and the activity enhancements in this work are comparable.[137, 21] For materials in which the

electronic absorption overlaps with the blue edge of a stop band, no reactions relevant to water splitting have been reported in the literature. A 4.7 times enhancement in the conversion efficiency of photons to electrons (IPCE) has been reported.[98] In our system, a 4.7 times enhancement of gaseous product evolution is observed. These enhancements are obviously quoted against a particular control reaction, and hence the actual magnitude of the effect may differ slightly. However, the results are consistent with an increased CdS absorption due to slow photons at the blue edge of the stop band, leading to an efficient conversion of electrons to product in our system, and current in the literature report. These results show the feasibility of increasing the activity and efficiency of a photocatalyst by independent modification of the structural and optical properties.

In all previous literature studies of photonic materials, the walls are constructed entirely of a photocatalyst material. This work represents the first demonstration of photocatalytic reactions relevant to water splitting over nanoparticle monolayers loaded into photonic supports. This approach allows for independent optimisation of the optical properties, particle size and loading in photocatalyst materials. In addition, the mass of photocatalytically active material used is reduced in comparison to a full 3DOM photocatalyst.

As future work, the importance of the stop band position could be evaluated further by formation of composites with slightly different periodicities (± 10 – 30 nm) from **2-CdS**. This could allow elucidation of the correlation between increased activity and the extent of overlap between the stop band and the electronic absorption, and could provide a crucial understanding of the photonic effects.

Concluding Remarks and Future Direction

The aims of this project were to develop a method to homogeneously disperse photocatalyst nanoparticle materials in photonic 3DOM supports, and investigate the effects of the photonic structure on the photocatalytic activity for reactions relevant to water splitting. These aims have been demonstrated, showing the feasibility of utilising photonic crystals to enhance the activity of a photocatalyst. The deposition method was shown to produce homogeneous composites with control over the nanoparticle loading (3 – 65 wt%), particle size and in the absence of intermediate temperature transformations (< 400 °C), the crystal phase. The generality of the method was exhibited by the deposition of a range of nanoparticle materials (TiO_2, Fe_3O_4 and CdS) in ordered porous supports (3DOM SiO_2, ZrO_2, FTO and mesoporous SiO_2). By tuning the nanoparticle-support interactions, it is envisaged that the method could be applied to any combination of ligand stabilised nanoparticles and ligand coated supports.

As a proof of concept this work represents the first example of enhancements of photocatalytic activity by overlap of semiconductor absorption bands with the blue edge of a photonic stop band. As discussed in the previous chapter, the effect of the stop band overlap could be investigated as future work. To improve the catalytic activity further, the addition of a co-catalyst material to reduce e^-/h^+ recombination could also be investigated. In terms of solar fuel research, the deposition of other II-VI and III-V semiconductors within photonic crystals would be of interest, for example GaP, which has been used to photocatalytically reduce CO_2 to methanol.[260] Previous work in our group has investigated ligand stabilised $BiVO_4$ nanoparticles, which could potentially be deposited in these supports as visible light active photocatalysts for water oxidation. The formation of photonic materials with well defined, tunable optical bands also presents applications for these materials as sensors.

The homogeneous deposition of nanoparticles in mesoporous materials presents the opportunity to prepare high surface area materials for traditional catalysis. As an example, oleylamine stabilised Pd nanoparticles have been used as catalysts for

ammonia-borane dehydrogenation.[261] The synthesis and deposition of these materials within mesoporous SiO_2 could enhance the catalytic activity due to the increased surface area for adsorption of reagents.

In conclusion, the nanoparticle deposition method presented in this work shows improvements over existing literature methods, and presents many applications in a wide variety of fields including photocatalysis. The general strategy allows independent optimisation of particle size, morphology and loading of a catalyst. In photocatalysis, the use of photonic crystal materials to effectively trap light has been demonstrated, with a maximum 4.7 times enhancement in activity by overlap of CdS absorption with the blue edge of a stop band.

Chapter 5

Experimental

5.1: Chemicals Used

1-Octadecene ($C_{18}H_{36}$, 90 %), Ammonium fluoride (NH_4F, 98 %), Cadmium acetate dihydrate ($Cd(OCOCH_3)_2.2H_2O$, 98 %), Cadmium oxide (CdO 99.99 %), Ethylbenzene, (C_8H_{10}, 99 %), Hexachloroplatinic acid (H_2PtCl_6, 99.9 %), Hexadecylamine ($C_{16}H_{33}NH_2$, 90 %), Iron (III) chloride ($FeCl_3$, 97 %), Octyl Ether ($(C_8H_{17})_2O$, 99 %), Oleic acid ($C_{18}H_{34}O_2$, 90 % and 99 %), Oleylamine ($C_{18}H_{37}N$, 70 %), Pluronic F127, ($PEO_{106}PPO_{70}PEO_{106}$, Mw = 12600), Polyvinylpyrrolidone (Average molecular weight 40000), Potassium persulfate ($K_2S_2O_8$, 99 %), Selenium (Se, 99.99 %), Sodium oleate ($C_{18}H_{33}O_2Na$, 82 %), Sodium sulfide nonahydrate ($Na_2S.9H_2O$, 98 %), Sodium sulfite (Na_2SO_3, 98 %), Styrene (C_8H_8, 99 %), Sulphur (S, reagent grade), Tetraethyl-orthosilicate ($Si(OC_2H_5)_4$, 99 %), Tin (IV) chloride pentahydrate ($SnO_2.5H_2O$, 98 %), Titanium tetraisopropoxide ($Ti(OiPr)_4$, 97 %), Triethylamine ($C_6H_{15}N$, > 99 %) Trioctylphosphine ($P(C_8H_{17})_3$, 97 %), Trioctylphosphine oxide ($P(C_8H_{17})_3O$, 99 %) and Zirconium acetate solution in dilute acetic acid ($Zr(OCOCH_3)_4$, 16 % Zr) were purchased from Sigma Aldrich and used as received.

Potassium chloride (KCl, 99 %) was purchased from Fisher Scientific and used as received.

Sheets of fluorine doped tin oxide coated glass were purchased from Sigma Aldrich (7 Ω square^{-1}), and cut into 1 x 1.5 cm slides. Before use, slides were sonicated in acetone and propan-2-ol (10 minutes each) to remove surface contaminants.

Holey carbon films on 400 mesh copper grids for mounting TEM samples, and short pin aluminium stubs (0.5 inch) and 12 mm LEIT adhesive carbon tabs for SEM sample preparation were purchased from Agar Scientific.

Where water is mentioned in synthesis, it refers to deionized (DI) water.

5.2: Techniques

5.2.1: Powder X-Ray Diffraction (PXRD)

Wide angle PXRD patterns were recorded on a Bruker-AXS D8 Advance instrument with Lynx eye detector, using Cu Kα radiation (1.54 Å) with a 1 mm slit on the source and 2.5 mm detector slit. Data was collected from 5 – 70 ° 2θ, with 0.02 ° step size and a scan speed of 0.1 seconds per step. Samples were deposited as films on an aluminium sample holder. Peaks were indexed using the Bragg equation:

$$n\lambda = 2d_{hkl}\,sin\,\theta \qquad \textit{Equation 28}$$

Where n is the order of diffraction, d_{hkl} is the lattice plane separation, λ is the X-ray wavelength and θ is the angle of diffraction. The Scherrer equation was used to estimate the minimum crystallite size from the full width half maximum (FWHM) of a diffraction peak:

$$\tau = \frac{K\lambda}{\beta cos\theta} \qquad \textit{Equation 29}$$

where τ is the crystallite size, K is the shape factor of the crystallite (0.89 for spherical crystallites), θ is the angle of diffraction in degrees and β is the FWHM of the diffraction peak in radians.

Low angle PXRD was recorded on a Bruker D8 Discover, with a Vantec 500 detector (1 mm slit, 0.5 mm collimator) and Cu microfocus source (1 mm slit). Samples were packed in 1 mm diameter glass capillary tubes for analysis. Scans were recorded over the 0.1 – 5 ° 2θ range with an acquisition time of 3 minutes.

5.2.2: Scanning Electron Microscopy (SEM)

SEM images were obtained using an FEI Sirion scanning electron microscope. Prior to imaging, samples were supported on an aluminium stub with an adhesive carbon tab and sputter coated with a 10 nm layer of carbon using an Agar auto carbon

coater. For 3DOM materials, the periodicity and wall thicknesses of the structures were analysed by > 100 independent measurements from SEM images.

Energy Dispersive Analysis of X-rays (EDX) was performed using an attached EDAX Phoenix X-ray spectrometer. Scans were recorded at 10 kV accelerating voltage for 1 minute, over regions 50 µm by 35 µm in size. Elemental analyses of samples were averaged over at least 10 of these measurements.

5.2.3: Transmission Electron Microscopy (TEM)

TEM images and electron diffraction patterns were obtained using a JEOL 2011 transmission electron microscope operated at 200 kV accelerating voltage. Dark field imaging and HAADF STEM imaging/EDX mapping were performed at the University of Leeds on a Tecnai TF20 FEGTEM operated at 200 kV. CCD images were extracted using Gatan Digital Micrograph software. Particle size distributions of nanoparticles were evaluated by averaging the diameter of > 100 particles from TEM images.

Prior to analysis, solid samples for TEM imaging were ground in methanol and sonicated for 15 minutes to disperse. One drop of the dispersion was deposited onto 3 mm holey carbon coated copper grids and allowed to dry in air. FTO film samples were scraped off the slide, then ground in methanol/sonicated as above. For ligand stabilised nanoparticle dispersions in organic solvents, TEM samples were prepared by evaporation of a single drop of diluted solution onto a holey carbon copper grid.

5.2.4: Thermogravimetric Analysis (TGA)

TGA measurements were performed on a Rheometric Scientific STA 625 TGA. Approximately 10 mg of sample was weighed into an aluminium crucible and placed on the balance. Samples were heated at a rate of 10 °C min^{-1} to 600 °C under N_2.

5.2.5: Surface Area Measurements

Nitrogen adsorption porosimetry was performed on a Micromeritics Tristar 3000 surface analyser. Approximately 100 mg sample was weighed into a sample tube and degassed under N_2 at 150 °C for 6 h to remove all adsorbed water prior to measurement. The volume of nitrogen adsorbed at 77.4 K per gram of material was measured as a function of the relative pressure P/P_0 within the system. Surface area measurements were calculated from at least 5 data points in the 0.05 to 0.3 P/P_0 region using the Brunauer Emmett Teller (BET) adsorption isotherm equation:[262]

$$\textit{Equation 30} \quad \frac{1}{V_a(\frac{P_0}{P}-1)} = \frac{C-1}{V_m C}.\frac{P}{P_0} + \frac{1}{V_m C}$$

Where V_a is the adsorbed volume of N_2 at STP, P_0 is the saturation pressure of N_2, P is the partial pressure of N_2 in equilibrium with the surface, V_m is the required volume of N_2 adsorbed to form a monolayer on the material surface, and C is a constant. By plotting $1/V_a(P_0/P-1)$ versus P/P_0, V_m was calculated from the gradient and y-intercept of the straight line produced. Specific surface areas were calculated using Equation 31:[210, 263]

$$\textit{Equation 31} \quad S = \frac{V_m N a}{22400}$$

Where N is Avagadro's number, a is the cross sectional area of an N_2 molecule (0.162 nm^2), and 22400 represents the volume of 1 mole of gas in mL.

5.2.6: UV-Vis Absorption and Reflection Spectroscopy

UV-Visible absorption and reflectance spectra were recorded on an Ocean Optics HR2000+ High Resolution Spectrometer with DH-2000-BAL Deuterium/Helium light source (200 – 1100 nm). An R400-7-UV-Vis reflection probe was used to record diffuse reflectance spectra. Powder samples were deposited as a flat layer between two pyrex or quartz slides and placed beneath the reflection probe. Spectra were recorded using Spectra Suite software from an average of 10 scans, an integration time of 20 seconds and box car smoothing width of 20 nm. Solution UV-Visible

absorption spectra were recorded with the same light source, in quartz cuvettes using a solution cell.

5.2.7: Infra-Red Spectroscopy

Attenuated total reflectance Infra-Red spectra were recorded on a Perkin Elmer Spectrum Two FT-IR spectrometer with UATR single reflection diamond accessory. Powdered materials were deposited on the diamond surface. The pressure arm was tightened onto the sample until the force gauge displayed 100 N. Spectra were recorded from 650 to 4000 cm^{-1} over an average of 4 scans.

5.2.8: Fluorescence Spectroscopy

Fluorescence spectra were recorded using a Hitachi F-4500 fluorescence spectrophotometer, with a 150 W Xe lamp light source and photomultiplier tube detector. Scans were recorded using a scan speed of 240 nm min^{-1}, excitation and emission slit widths of 10 nm, and 700 V PMT voltage. The wavelength of the first exciton peak in the UV spectrum was used as an excitation wavelength to record an emission spectrum from 400 – 700 nm. The position of the strongest emission peak was then used as an emission wavelength to record an excitation spectrum from 200 – 600 nm.

5.2.9: CHN Analysis

CHN analysis of solid samples was obtained from the departmental service using an Exeter Analytical CE-440 analyser. Samples were heated to 1500 °C under He, and the elemental composition was determined from the combustion products.

5.2.10: Photocatalytic Testing

5.2.10a: Setup

A gas tight, closed loop setup was used for photoreaction and analysis of products. Previous designs of the apparatus used have been described in published work.[123, 264] A schematic of the loop arrangement is shown in Figure 101.

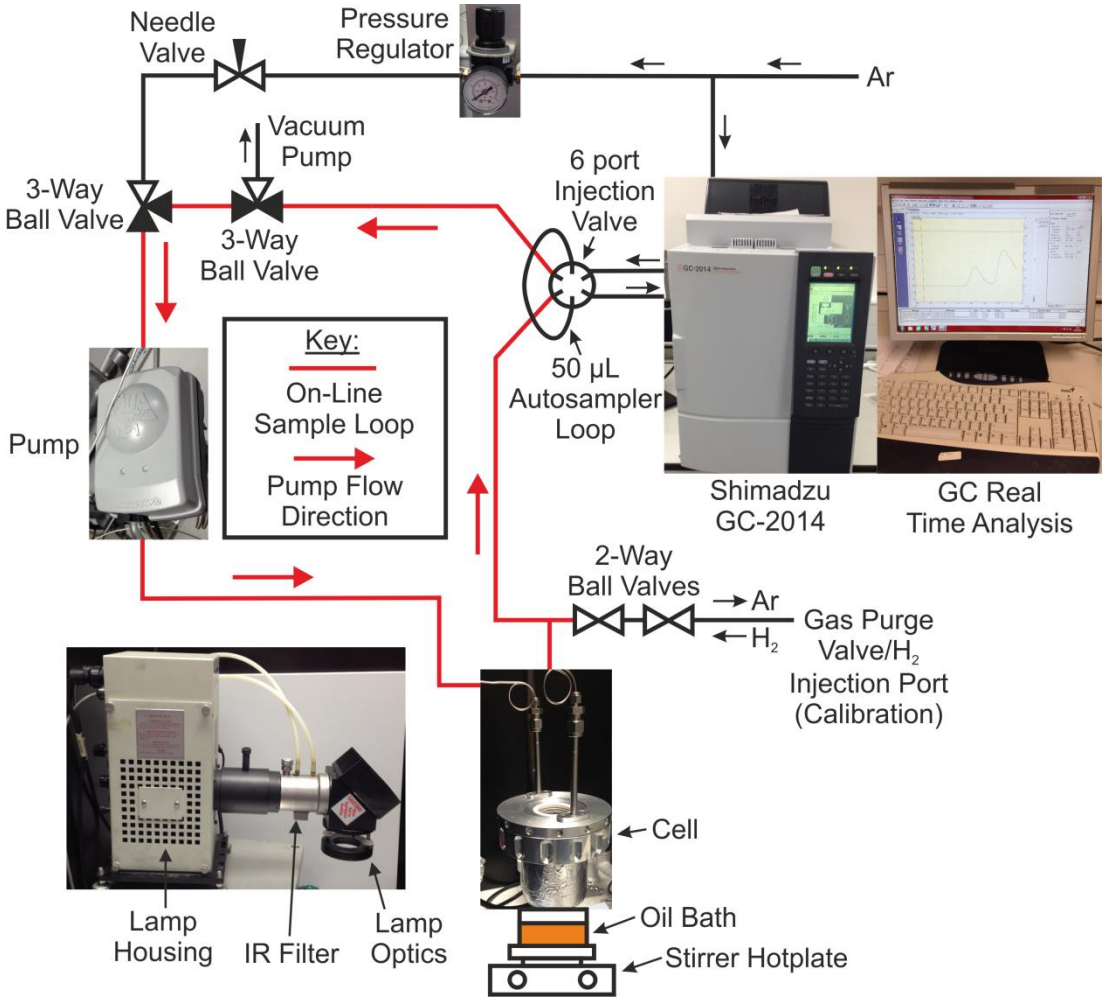

Figure 101: GC loop setup.

Numerous iterations of cell design were trialled throughout the course of the project. The final, leak free design that was used for all photocatalysis experiments in chapter 4 is shown in Figure 102. The design consists of a glass cell with a ground glass rim onto which a metal lid is sealed using an O-ring. A quartz window was encased into the lid to allow illumination. Directly below this, a 50 mL beaker containing sample dispersed in 20 mL sacrificial reagent solution was held central

and rigid within a 100 mL beaker surrounded by glass spacers. A water jacket of 40 mL/10 mL was placed in the cell and 100 mL beaker respectively to allow for efficient heat transfer from the oil bath, hence the total water volume in the cell was 70 mL for all experiments.

The setup was encased in tin foil to minimise loss of photons from the system. Prior to analysis, the loop was purged with Ar (0.5 bar overpressure) for 10 minutes, after which measured chromatograms showed no air peaks. The loop was dried under vacuum (30 minutes) and purged with argon (30 minutes) between runs to prevent buildup of condensation in the tubing.

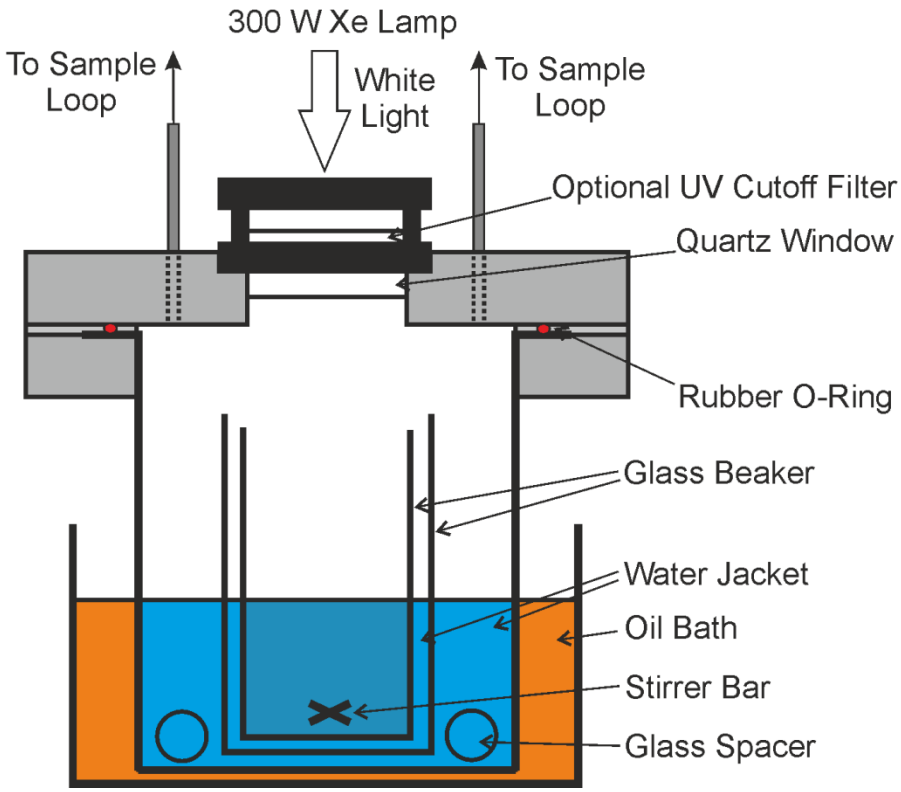

Figure 102: Photocatalyst testing cell setup. The central 50 ml beaker contains sample dispersed in 20 mL aqueous solution of sacrificial reagents, held directly beneath the irradiation source.

The bulk of the loop was constructed from 4.2 m of metal tubing with 1.6 mm external diameter and 0.5 mm internal diameter. Swagelok connections were used to link the metal tubing to 4 mm internal diameter (ID) Clearflex 60 PVC tubing attached to the pump. In addition, 4 mm internal diameter metal tubing was used

for connections to top of the cell, with a total length of all 4 mm tubing of 0.8 m. Hence the volume of loop outside the cell is approximately 11 mL. The empty cell volume is 290 mL, and is reduced to 250 mL with the two beaker inserts and glass spacers. With 70 mL water in the cell, the total gas headspace is approximately 191 mL, the bulk of which is within the cell itself.

5.2.10b: Analysis

Gas analysis was performed using a Shimadzu Corporation GC-2014. Gases were separated on a 25 cm long column packed with 5 Å molecular sieves and detection was performed using a thermal conductivity detector (TCD). 50 µL of gas was autosampled every 15 minutes over a time course of 6 – 24 hours. Gas samples were analysed using the following conditions; 20 mL min^{-1} flow rate of Ar carrier gas, 90 °C column temperature and 120 °C detector temperature. Under these conditions the retention time of H_2 is 1.5 min, O_2 2.3 min and N_2 3 min. An example chromatogram is shown in Figure 103. Peak areas were analysed by integration using Shimadzu GC Solutions – GC Postrun software.

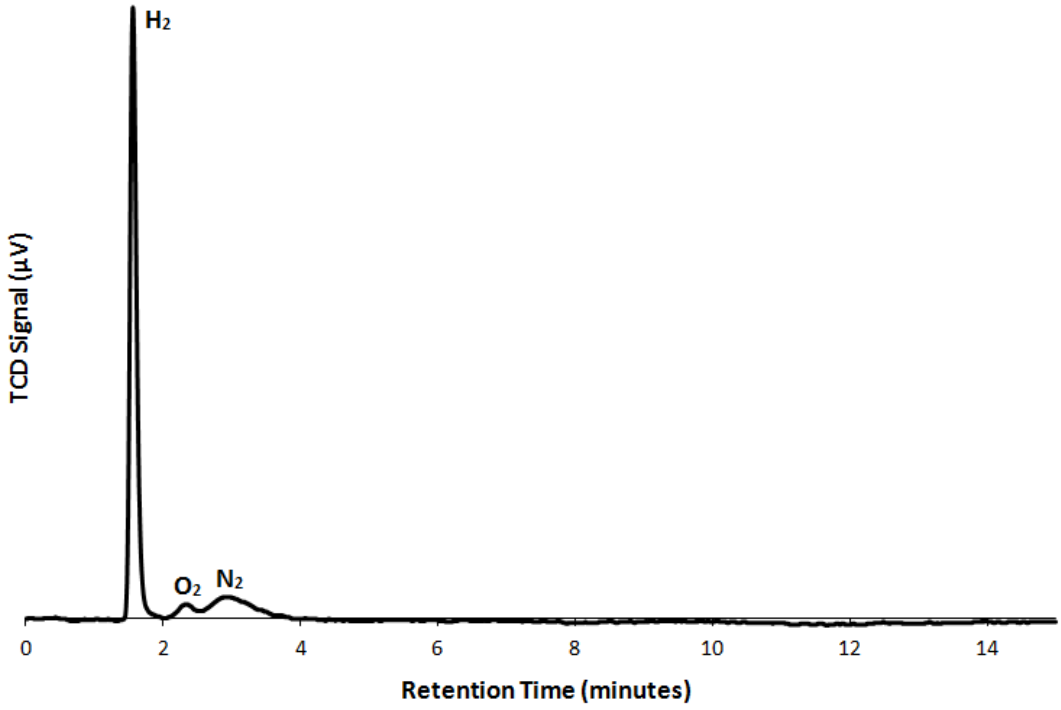

Figure 103: Example chromatogram, showing photogenerated H_2 peak at 1.5 min, and peaks for O_2 and N_2 diffused from solution at 2.3 and 3 mins respectively.

5.2.10c: Calibration

GC calibration for H_2 was performed by a series of injections of known volumes and pressures of gas into the loop. The H_2 source was a BOC 99.99% H_2 cylinder. Using a Schlenk line with mercury manometer, a Schlenk tube with suba seal was evacuated and refilled with argon 3 times. The Schlenk was evacuated again, and the manifold closed off from the vacuum pump to hold a static vacuum. A H_2 balloon was fitted with a needle and inserted into the Schlenk, and removed when the manometer had dropped by an appreciable amount (200 – 500 mm). The pressure of H_2 in the Schlenk was measured from the manometer using a ruler and recorded. H_2 was removed via an argon purged gas syringe and inserted into the loop, and allowed to equilibrate for 10 minutes prior to analysis. Six chromatograms were recorded over a period of 30 minutes, and used to obtain an average H_2 peak area. Using the pressure and volume of gas injected, the number of moles of H_2 in each injection

was calculated. The area of the chromatogram peak at 1.5 min was analysed, and plotted against the number of moles of H_2 to obtain a calibration curve.

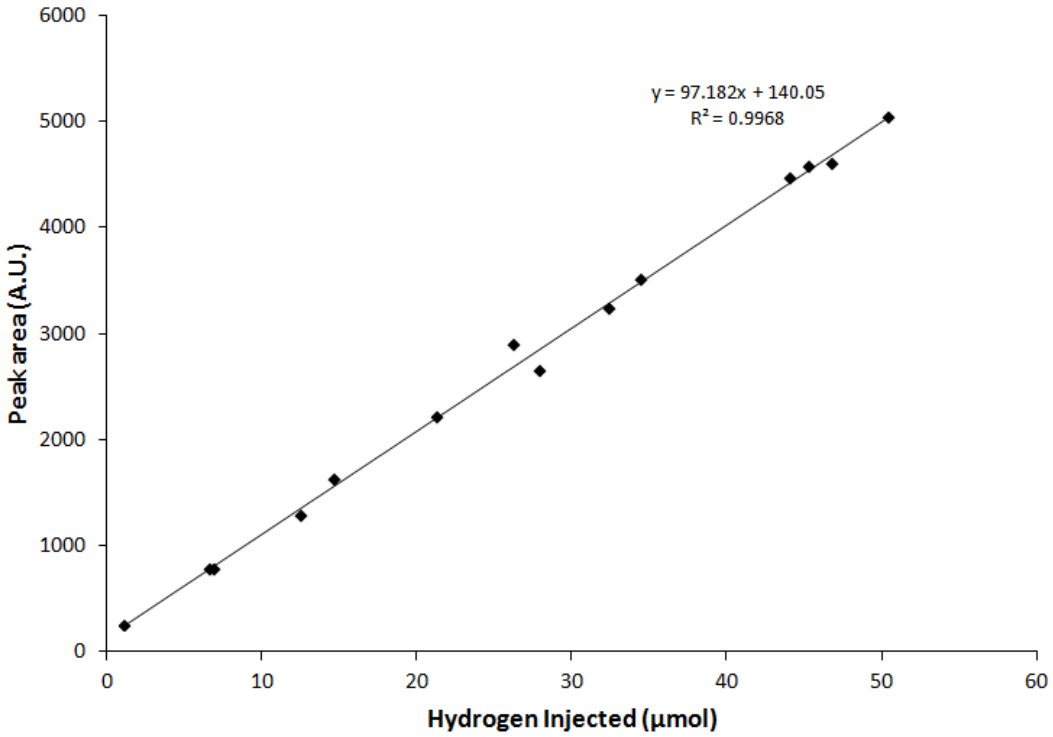

Figure 104: Calibration graph of measured peak area versus the number of moles of H_2 injected.

5.2.10d: Sample Runs

Photocatalysis of powdered samples were tested from colloidal dispersions in 20 mL aqueous solution containing sacrificial reagents. In all reactions the apparatus was maintained at a temperature of 40 °C throughout analysis. For **1-CdS – 5-CdS**, reactions were performed in water containing Na_2S (0.25 M) and Na_2SO_3 (0.35 M) and 30 mg of the photocatalyst. For **1-TiO_2 – 5-TiO_2**, reactions were performed in aqueous 10 % MeOH with 23 mg photocatalyst. Reactions were run three times giving data within 15 %. In addition, a control reaction using Ta_2O_5 (30 mg) in aqueous 10 % MeOH was run periodically to monitor system calibration. Argon/Vacuum purging was used to remove air prior to photoreactions. Illumination was performed using a LOT Oriel 300 W Xe lamp fitted with a 15 cm IR

filter and a wideband $AlMgF_2$ coated mirror. For CdS containing samples, a 400 nm band pass filter was used to exclude UV light. The emission profile of the Xe bulb is displayed in Figure 105.

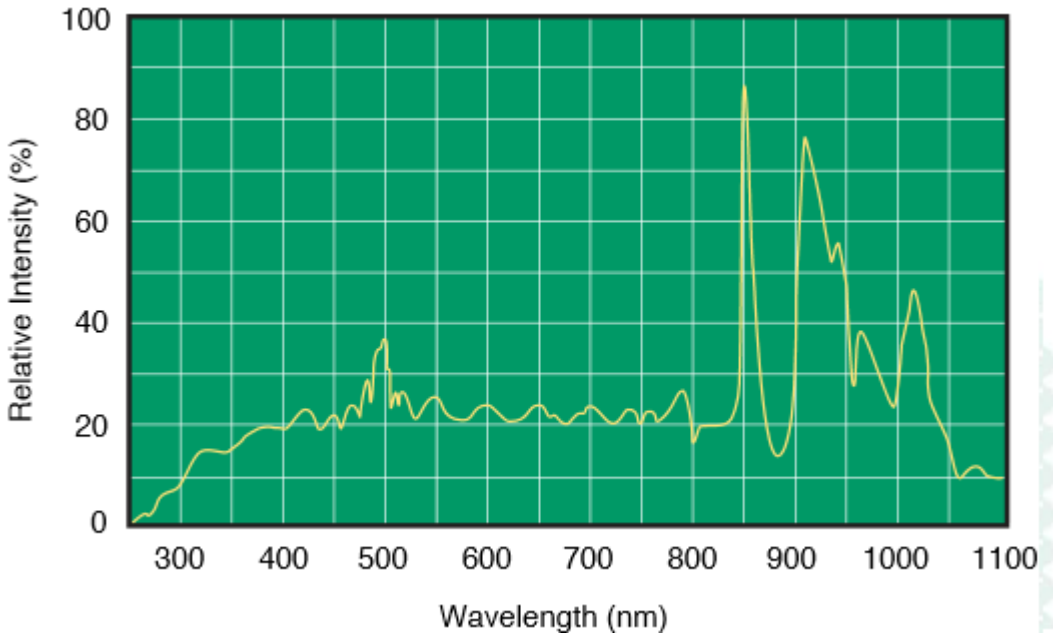

Figure 105: Spectral emission profile of the Xe light source used for irradiation.[265]

The irradiance from the lamp was periodically monitored by intensity measurements directly below the lamp optics using an International Light Technologies ILT 1400-A radiometer/photometer. Normal lamp output was 1.5 W cm^{-2}, which was reduced to 1 W cm^{-2} through the quartz window on the cell lid and 700 mW cm^{-2} through both the quartz window and 400 nm cutoff filter.

5.3: Synthetic Methods

5.3.1: Synthesis of 3DOM Powders by Colloidal Crystal Templating

5.3.1a: Polystyrene Synthesis

Polystyrene spheres of diameter 300 - 600 nm were synthesised by emulsifier free emulsion polymerisation by a modified literature method.[180] A 3-necked round bottom flask was fitted with reflux condenser, overhead motorised stirrer, temperature controller and dropping funnel for addition of reagents. Reactions were stirred at constant speed between 180 – 360 rpm. Water (1133 mL) was added to the flask and heated to 70 – 90 ± 2 °C under flowing N_2. Styrene (140 mL, 1.218 mol) was washed 4 times with NaOH (0.1 M, 140 mL) and 4 times with water (140 mL) in a separating funnel to remove inhibitors. Inhibitor free styrene (133 mL, 1.157 mol) was added and the temperature stabilised. After N_2 purging for 30 minutes, $K_2S_2O_8$ (0.442 g, 1.635 mmol) dissolved in 66 ml water was added, and the reaction allowed to proceed for 28 – 48 hours. The colloid dispersion was cooled to room temperature, and filtered through glass wool to remove polymer agglomerates.

Spheres of diameter < 300 nm were synthesised by emulsifier free emulsion polymerisation using polyvinylpyrrolidone as a stabiliser as described in a literature method.[191] Water (100 mL) was added to a 3-necked round bottom flask and degassed under N_2. Inhibitor removed styrene (13 mL, 0.113 mol) and PVP (0.1 – 1 g) were added, and the mixture stirred at 300 rpm for 15 minutes. $K_2S_2O_8$ (0.3 g, 1.11 mmol) dissolved in 20 mL water was added, followed by heating to 70 – 80 ± 2 °C for 24 hours. The colloid dispersion was cooled to room temperature, and filtered through glass wool to remove polymer agglomerates.

5.3.1b: Template Preparation

Cubic close packed polystyrene spheres were isolated by centrifugation of the colloidal solution (4000 rpm, 3 hours). The spheres were dried in an oven at 66 °C

overnight before use to give the template as a white brittle solid. From 50 mL colloid, around 4 g of PS was obtained, giving a concentration of 80 g L^{-1} for the stock solution. Sphere size of the templates was determined by averaging > 100 independent measurements of particles from SEM images.

Impregnation of polystyrene spheres was achieved by an optimised version of a literature method.[99, 138] Polystyrene spheres (1 g) were crushed using a pestle and mortar to a fine powder and layered on filter paper in a glass sinter funnel (Porosity 3, 16 – 40 μm). The template was soaked with ethanol for 15 minutes, and then dried under reduced pressure immediately prior to infiltration.

5.3.1c: 3DOM SiO_2 Formation

Tetraethyl-orthosilicate (TEOS, 3 mL, 13.4 mmol), ethanol (2 mL), water (1.5 mL) and HCl (1 M, 0.5 mL) were mixed in this order and stirred at RT for 15 minutes. The solution was transferred via pipette onto the template and allowed to soak for 30 minutes, followed by removal of excess solution under reduced pressure. The impregnated template was dried at room temperature for 24 hours in air. The template was removed by calcination in air at 550 °C for 10 hours (ramp rate 2 °C min^{-1}) to yield opalescent 3DOM SiO_2 powders (50 – 150 mg). Alternate precursor solutions using neat alkoxide (7 mL), or a mixture of TEOS (3.5 mL) and ethanol (3.5 mL) were also attempted.

5.3.1d: 3DOM ZrO_2 Formation

Zirconium acetate in acetic acid (16 wt % Zr, 3 mL) and methanol (3 mL) were stirred at RT for 15 minutes. The solution was transferred via pipette onto the template and allowed to soak for 1 hour, followed by removal of excess solution under reduced pressure. The impregnated template was dried at room temperature for 24 hours in air. The template was removed by calcination in air at 450 °C for 4 hours (ramp rate 1 °C min^{-1}) to yield coloured 3DOM ZrO_2 powders (150 – 250 mg).

3DOM materials were denoted yyy-MO_2, where yyy and MO_2 are the periodicity as measured by SEM and the composition of the support respectively.

5.3.2: Synthesis of 3DOM Films by Colloidal Crystal Templating

5.3.2a: Deposition of Polystyrene Films on FTO glass

Polystyrene films were deposited on FTO glass by evaporation of a colloidal polyvinylpyrrolidone (PVP)/PS solution at constant temperature.[125] Prior to deposition, FTO coated glass slides were cleaned by sonication in acetone (10 mins) and isopropanol (10 mins) and dried under N_2, then made hydrophilic by soaking in 3:1 H_2SO_4/H_2O_2 solution (Piranha solution, 1 h). The slides were rinsed with water and dried under N_2 ready for use. Stock solutions of polystyrene colloids prepared as described above contained around 80 g L^{-1}. A solution of PVP (20 mg L^{-1}) and PS (2 g L^{-1}) in water was prepared by dilution of the stock. Piranha-treated FTO slides were mounted vertically in glass vials, into which PVP/PS solution was pipetted until the meniscus was 1 mm from the top of the slide. The solvent was evaporated at temperatures from 40 – 80 °C over 1 – 3 days. The best results were obtained by evaporation at 50 °C over 3 days, giving an opalescent, uniform film. Under these conditions, packed colloidal crystal films of 10 – 12 µm thickness corresponding to 20 – 24 layers of spheres were observed.

5.3.2b: Formation of 3DOM FTO on FTO glass

An FTO precursor solution was prepared according to literature methods.[204] A saturated aqueous solution of NH_4F (4.53 g, 0.122 mol) was prepared by dissolution in water (10 mL). 0.24 g (2 mmol NH_4F) of this solution was added to a solution of $SnCl_4 \cdot 5H_2O$ (1.40 g, 4 mmol) in ethanol (20 mL), and sonicated for 20 min until the solution became clear. The FTO sol was stored in a plastic container until use.

Two methods were used for formation of 3DOM FTO films. In the first, PS films on FTO were placed directly in FTO solution (5 mL) and soaked for 3 hours (direct

infiltration). The slides were then removed and dried vertically over 1 hour. Finally, the slides were calcined in air at 500 °C for 2 hours (ramp rate 1 °C min^{-1}) to yield opalescent 3DOM FTO films.

In the second method, a reduced pressure infiltration technique was used to form 3DOM FTO films (forced impregnation technique).[197] PS films on FTO glass were carefully placed in methanol and allowed to soak for 1 hour. The slides were removed from the solvent and another slide placed adjacent so as to sandwich the PS film, held together loosely with an elastic band. If too much pressure was applied, transferral of the film to the adjacent slide could occur. The sandwiched slide was placed directly in a vial of FTO solution (5 mL) as shown in Figure 106, and placed in a vacuum desiccator. The slides were allowed to soak for 30 minutes, after which a partial vacuum was applied to the desiccator. With the tap half open, the air was slowly removed over a period of 1 minute, until slight effervescence was observed in the vial. At this point the tap was closed to retain a static partial vacuum in the desiccator and draw the sol into the interstitial sites in the PS film. After 3 hours, the slides were removed, allowed to dry vertically over 1 hour, and finally calcined in air at 500 °C for 2 hours (ramp rate 1 °C min^{-1}) to yield opalescent 3DOM FTO films.

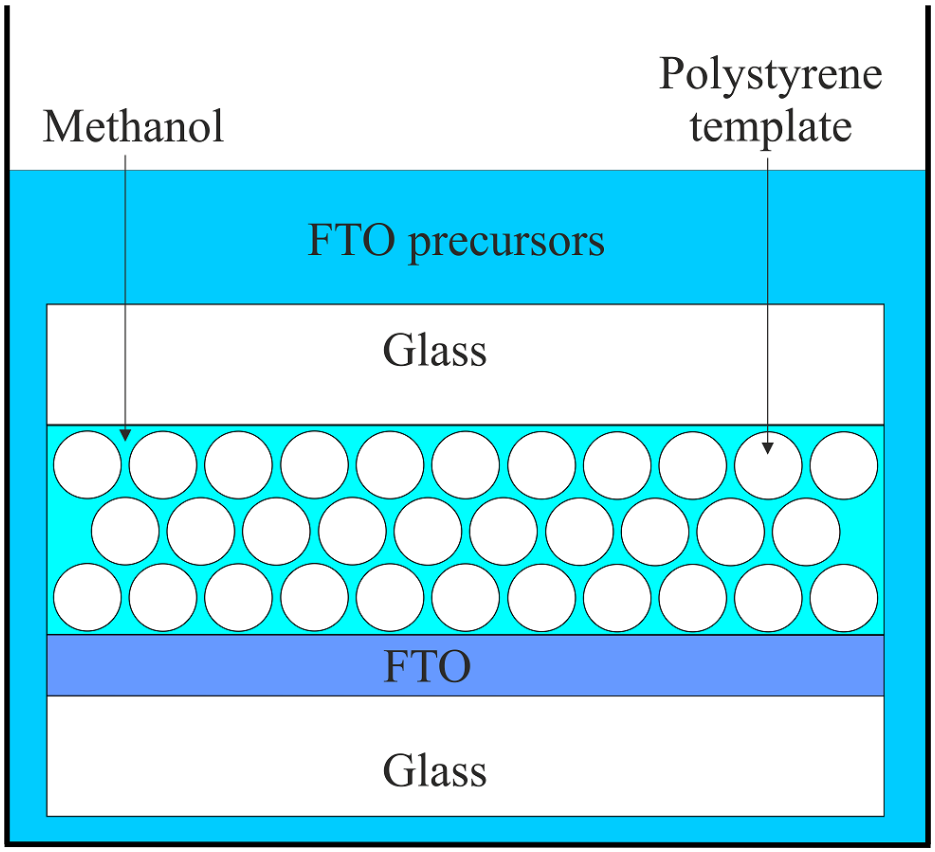

Figure 106: Schematic of setup used for sandwich vacuum deposition to form 3DOM FTO.

5.3.3: Synthesis of Mesoporous Silica

Mesoporous silica was synthesised according to a literature method.[209] Pluronic F127 (1 g) and KCl (2.5 g, 33.5 mmol) were dissolved in HCl (2 M, 60 mL) at room temperature. Ethylbenzene (5.2 g, 49 mmol) was added, and the mixture stirred at 350 rpm for 24 hours. Tetraethyl-orthosilicate (4.5 g, 21.6 mmol) was added, and the mixture stirred for a further 24 hours. The mixture was then transferred into a polypropylene bottle and heated to 100 °C for 24 hours. The resultant white powder was filtered, dried at 60 °C, and then calcined to remove the template at 550 °C for 5 hours (ramp rate 2 °C min^{-1}), to yield mesoporous SiO_2 as a white solid (1.13 g, 87 %).

5.3.4: Nanoparticle Synthesis

In all nanoparticle syntheses, removal of residual solvent and surfactant was achieved by centrifugation. Nanocrystals were precipated by addition of excess ethanol (60 – 100 mL) followed by centrifugation (4000 rpm, 30 mins). The supernatant was discarded and the nanocrystals twice redispersed in toluene (5 mL), crashed with ethanol (40 mL) and centrifuged (4000 rpm, 30 mins). The precipitate was then dried or redispersed as required.

5.3.4a: OA/TiO_2

Oleic acid functionalised TiO_2 nanoparticles were synthesised by a modified literature procedure.[219] Oleic acid (90 %, 35 g, 0.124 mol) was degassed under N_2 in a 3-neck round bottom flask and heated to 100 °C. Titanium isopropoxide (2.84 g, 10 mmol) was added and the solution stirred for 5 minutes. Triethylamine (1.01 g, 10 mmol) in ethylene glycol (6.4 g, 0.103 mol) was subsequently added, and the mixture refluxed at 100 °C for 48 hours. After cooling the solution, nanoparticles were precipated by addition of excess ethanol (100 ml), followed by centrifugation (4000 rpm, 30 minutes). The nanocrystals were purified by a further two centrifuge cycles as described above. The product was dried at 60 °C overnight to yield OA/TiO_2 as an orange powder (2.1 g). Elemental Analysis found (%) C 62.6; H 9.72; N 0; Calc. C 62.42; H 9.89; Ti 11.0; O 16.7. Corresponding ligand ratio TiO_2:1.25$C_{18}H_{34}O_2$, or 18.5 % TiO_2 content by mass.

5.3.4b: OA/Fe_3O_4

Oleic acid functionalised Fe_3O_4 nanoparticles were synthesised by a modified literature procedure.[226, 227] In a 2-necked round bottom flask, Fe(oleate)$_3$ was synthesised by reaction of $FeCl_3$ (6.49 g, 40 mmol) dissolved in a water:ethanol (60:80 mL) solution and sodium oleate (36.5 g, 120 mmol) dissolved in hexane (140 mL). With stirring, the biphasic solution was refluxed with stirring at 65 °C for 4

hours. After cooling the organic phase was separated and washed 3 times with water (30 mL), and dried over $MgSO_4$. The volatiles were removed under reduced pressure to yield a red/brown viscous liquid (24.2 g, 67 %).

$Fe(oleate)_3$ (1 g, 1.1 mmol), oleic acid (99 %, 0.35 mL, 1.1 mmol) and octyl ether (20 mL) were added to a 2-necked round bottom flask. With vigorous stirring, the mixture was heated to 290 °C (ramp rate 5 °C min^{-1}), and refluxed for 1 hour. After cooling to room temperature, nanoparticles were precipitated by addition of ethanol (50 mL) followed by centrifugation (4000 rpm, 30 min). The nanocrystals were purified by a further two centrifuge cycles as described above. The product was dried at 60 °C overnight to yield OA/Fe_3O_4 as a black powder (0.5 g). Elemental Analysis found (%) C 54.83; H 8.12; N 0; Calc. C 54.37; H 8.62; Fe 21.0; O 16.1. Corresponding ligand ratio Fe_3O_4:2.01$C_{18}H_{34}O_2$, or 29 % Fe_3O_4 content by mass.

5.3.4c: Oleyl/CdS

Oleylamine capped CdS nanocrystals were prepared using a literature procedure.[215] In a 3-necked round bottom flask, cadmium acetate dihydrate (200 mg, 0.75 mmol) and sulphur powder (120 mg, 3.75 mmol) were added to oleylamine (10 mL) under flowing nitrogen. With vigorous stirring, the mixture was heated to 250 °C (5 °C min^{-1}), and refluxed for 4 h. Methanol (50 mL) was added to precipitate CdS, followed by centrifugal separation (4000 rpm, 30 mins). The supernatant was discarded and the nanocrystals redispersed in toluene (5 mL), crashed with methanol (40 mL) and centrifuged (4000 rpm, 30 mins) a further four times. The product was dried at 60 °C overnight to yield oleyl/CdS as a yellow solid (130 mg). Elemental Analysis found (%) C 25.43; H 5.83; N 0; Calc. C 25.57; H 4.41; Cd 52.3; S 14.9; N 1.6. Corresponding ligand ratio CdS:0.25$C_{18}H_{37}N$, or 68 % CdS content by mass.

5.3.4d: CdS Quantum Dots

CdS quantum dots were synthesised by a modified literature method.[214] CdO (38.4 mg, 0.3 mmol), oleic acid (2.5422 g, 9 mmol) and 1-octadecene (13.4194 g) were added to a 3 neck round bottom flask under Ar, and heated to 300 °C (5 °C min^{-1}). A solution of sulphur (4.8 mg, 0.15 mmol) in 1-octadecene (1.9952 g) was rapidly injected into the reaction mixture, and the temperature held at 270 °C for nanocrystal growth. To monitor the growth of particles, aliquots were taken from the reaction mixture and quenched in cold chloroform. After 3 minutes the reaction was quenched by submerging the flask in an ice bath. The nanocrystals were precipated by addition of excess ethanol (60 mL) followed by centrifugation (4000 rpm, 30 mins). The nanocrystals were purified by a further two centrifuge cycles as described above. Finally, nanocrystals were dispersed in toluene (4 – 5 mL). The aliquots were worked up by the same procedures and redispersed in toluene. Through deposition of CdS/OA (described below), the total yield of nanoparticles in a batch was found to between 90 – 100 mg OA/CdS. Elemental Analysis found (%) C 62.3; H 10.3; N 0; Calc. C 62.61; H 9.93; Cd 14.1; O 9.2; S 4.0. Corresponding ligand ratio CdS:2.3$C_{18}H_{34}O_2$, or 18.1 % CdS content by mass.

5.3.4e: CdSe Quantum Dots

CdSe quantum dots were synthesised by a literature method.[216] All manipulations were performed under Schlenk conditions. Selenium (0.79 g, 10 mmol) was dissolved in trioctylphosphine (25 mL) with constant stirring in a nitrogen filled glovebox. The ampoule of clear liquid was then removed from the glovebox for use. In a 3-neck round bottom flask, trioctylphosphine oxide (9 g, 23.4 mmol), hexadecylamine (3 g, 12.4 mmol) and CdO (16 mg, 0.125 mmol) were degassed at 150 °C under vacuum for 20 minutes. The flask was filled with argon and heated to 325 °C to dissolve CdO. The temperature was then stabilised at 300 °C, and 2.5 mL of Se/TOP solution (1 mmol Se) rapidly injected. To monitor the growth of particles, aliquots were taken from the reaction mixture and quenched in cold chloroform. After 7 minutes the reaction was quenched by submerging the flask in an ice bath.

The nanocrystals were precipated by addition of excess ethanol (60 mL) followed by centrifugation (4000 rpm, 30 mins). The nanocrystals were purified by a further two centrifuge cycles as described above. Finally, nanocrystals were dispersed in toluene (4 – 5 mL) for further processing. The aliquots were worked up by the same procedures and redispersed in toluene. The total yield of nanoparticles was found to be 35 – 40 mg TOP(O)/CdSe. Elemental Analysis found (%) C 39.5; H 6.59; N 0; Calc. C 39.24; H 7.00; Cd 27.8; Se 19.6; P 4.2; O 2.2 (Assuming TOPO shell). Corresponding ligand ratio CdSe:0.55$C_{24}H_{51}PO$, or 47.4 % CdSe content by mass.

5.3.5: Deposition of Nanoparticles in Pores

5.3.5a: Nomenclature of Composite Samples

The loading of nanoparticles in all materials was analysed by SEM/EDX in addition to gravimetric analysis of the starting materials. Nanoparticle loaded samples were denoted xx%-NP-yyy-MO_2, where xx% is the added weight of nanoparticles expressed as a percentage of the support mass (wt%) as defined by Equation 32, NP is the chemical identity of the nanoparticles, and yyy and MO_2 are the periodicity as measured by SEM and the composition of the support respectively.

Equation 32 $$Added\ Weight\ Percent\ (wt\%) = \frac{mass\ NP}{mass\ Support} x100$$

5.3.5b: DCDMS Treatment of 3DOM SiO_2

3DOM SiO_2 was made hydrophobic by treatment with dichlorodimethylsilane (DCDMS) using a literature method.[236] A solution of DCDMS (0.535 g, 4.15 mmol) in toluene (10 mL total volume) was added to 3DOM SiO_2 (30 mg) and the mixture stirred at RT for 40 minutes. The mixture was then heated to 100 °C for 30 minutes. After cooling, the solid was filtered, washed twice with ethanol (20 mL) and dried at 60 °C. Deposition of TiO_2 nanoparticles was attempted within 30 mg of modified porous material.

5.3.5c: Surface Modification with OA

Oleic acid modification of powdered 3DOM and mesoporous materials was achieved by dispersion of 40 mg sample in a hexane solution of oleic acid (0.05 M, 40 mL).[231, 266] Deposition times of 30 minutes and 3 hours were used for SiO_2 and ZrO_2 respectively. After these times the solid was collected by vacuum filtration, washed twice with hexane (20 mL), and dried at 60 °C for 1 h. Typically deposition was attempted in 30 mg of OA-coated material. For surface area analysis of loaded 3DOM SiO_2 and ZrO_2, 100 mg OA-coated material was used.

For 3DOM FTO, slides were carefully placed in a vial containing a hexane solution of oleic acid (0.05 M, 5 mL). After 1 hour, the slides were removed, dipped in hexane (5 mL) three times to remove residual surfactant, and dried at 60 °C for 1 hour.

5.3.5d: Deposition of OA/TiO_2

Development of the deposition method was attempted in powdered 3DOM SiO_2 using OA/TiO_2. Nanocrystals corresponding to a loading of 3 – 60 wt% TiO_2 were dispersed in 1.5 mL hexane, chloroform or toluene, or solutions of oleic acid (0.1 M) in these solvents. Nanocrystals were dispersed by sonication, and added to uncoated, DCDMS treated or OA-coated porous supports (30 mg) in a 2 mL, 10 mm diameter vial. The volatiles were evaporated at 40 °C (chloroform), 50 °C (hexane) or 80 °C (toluene) overnight.

For TiO_2 loading in 3DOM ZrO_2 and mesoporous SiO_2, nanocrystals were dispersed in a solution of oleic acid in chloroform (0.1 M, 1.5 mL). Nanocrystals were dispersed by sonication, and added to OA-coated porous supports (30 mg) in a 2 mL, 10 mm diameter vial. The volatiles were evaporated at 40 °C overnight.

For TiO_2 loading in 3DOM FTO, nanocrystals dispersions containing 1 – 10 mM TiO_2 were prepared in a solution of oleic acid in chloroform (0.1 M, 1.5 mL). OA-coated 3DOM FTO films were placed in the base of cylindrical vials with an internal

diameter of 1.7 cm. The dispersion was added to the film, and the volatiles were evaporated at 40 °C overnight.

For the synthesis of TiO_2 loaded 3DOM SiO_2 and mesoporous SiO_2 composites, samples were calcined at 500 °C for 5 hours (ramp rate 5 °C min^{-1}). For 3DOM ZrO_2 and FTO, samples were calcined at 450 °C for 4 hours (ramp rate 1 °C min^{-1}). For deposition in 3DOM FTO films, nanoparticle loadings were calculated from large area SEM/EDX analysis.

5.3.5e: Deposition of OA/Fe_3O_4

An optimised version of the deposition method used for OA/TiO_2 nanoparticles was used for deposition of OA/Fe_3O_4 in 3DOM SiO_2 and ZrO_2. Nanocrystals corresponding to a loading of 4 – 65 wt% Fe_3O_4 were dispersed in a solution of oleic acid in chloroform (0.1 M, 1.5 mL). Nanocrystals were dispersed by sonication, and added to OA-coated porous supports (30 mg) in a 2 mL, 10 mm diameter vial. The volatiles were evaporated at 40 °C overnight.

For the synthesis of Fe_3O_4 loaded 3DOM SiO_2 composites, samples were calcined at 500 °C for 5 hours (ramp rate 5 °C min^{-1}). For 3DOM ZrO_2, samples were calcined at 450 °C for 4 hours (ramp rate 1 °C min^{-1}).

5.3.5f: Deposition of Oleyl/CdS

Deposition of oleyl/CdS was attempted using the same method as for OA/Fe_3O_4. Nanocrystals corresponding to a loading of 10 – 50 wt% CdS were dispersed in a solution of oleic acid in chloroform (0.1 M, 1.5 mL). Nanocrystals were dispersed by sonication, and added to OA-coated porous supports (30 mg) in a 2 mL, 10 mm diameter vial. The volatiles were evaporated at 40 °C overnight.

For the synthesis of CdS loaded 3DOM SiO_2 and ZrO_2 composites, samples were calcined at 450 °C for 4 hours (ramp rate 1 °C min^{-1}) under flowing Ar (60 mL min^{-1}).

5.3.5g: Deposition of OA/CdS

For OA/CdS deposition, nanoparticles were not isolated as powders prior to deposition. Instead, different loadings of nanoparticles were obtained by dilution of the stock dispersion in toluene or chloroform. All volumes of liquid used were measured out by difference using a 1 mL syringe. Aliquots of OA/CdS dispersions (0.1 – 1.45 mL) were added to an empty vial, and made up to 1.45 mL total volume with additional solvent (toluene or chloroform). OA (0.05 mL) was added to the vials to form a dispersion containing OA/CdS in 0.1 M oleic acid in chloroform or toluene. The mixture was sonicated to disperse.

For deposition in powder materials, OA-coated porous supports (30 mg) were added to a preweighed 2 mL, 10 mm diameter vial for deposition. In addition, two empty vials per sample set were preweighed for deposition with no porous material present. Stock nanoparticle dispersion (0.5 mL, no added OA) was added to the empty vials. The CdS/OA dispersions were added to the vials containing OA-coated support. The volatiles in the vials were evaporated overnight at 40 °C (chloroform) or 80 °C (toluene).

For deposition of OA/CdS in 3DOM FTO, dispersions containing 0.5 – 7 μM CdS and 0.1 M OA were prepared by dilution of stock dispersions in toluene (concentrations were determined by the absorbance of the first exciton peak in the UV-Visible spectrum and the calculated molar absorption coefficient for CdS – see appendix section A1.3).[234] OA-coated 3DOM FTO films were placed in the base of cylindrical vials with an internal diameter of 1.7 cm. The OA/CdS dispersion (1.5 mL) was added to the film, and the volatiles were evaporated at 80 °C overnight.

Initially, all CdS loaded porous composites were calcined at 450 °C for 4 hours (ramp rate 1 °C min^{-1}) under flowing Ar (60 mL min^{-1}). However, the incomplete combustion of OA was observed under these conditions, and hence the composites were instead calcined at the same temperatures in air.

For powder materials, all vials were reweighed after calcination and used to calculate the amount of CdS added, the CdS wt%, and the concentration of

nanoparticles in the initial stock dispersion. As a further control, an empty vial was weighed before and after calcination under the same conditions, showing no change in mass due to heating. For deposition in 3DOM FTO films, nanoparticle loadings were calculated from large area SEM/EDX analysis.

5.3.5h: Deposition of TOP(O)/CdSe

For deposition of TOP(O)/CdSe in 3DOM FTO, dispersions containing 6.8 μM CdSe and 0.1 M OA were prepared by dilution of stock dispersions in toluene (concentrations were determined by the absorbance of the first exciton peak in the UV-Visible spectrum and the calculated molar absorption coefficient for CdSe – see appendix section A1.3).[234] OA-coated 3DOM FTO films were placed in the base of cylindrical vials with an internal diameter of 1.7 cm. The TOP(O)/CdSe dispersion (1.5 mL) was added to the film, and the volatiles were evaporated at 80 °C overnight. Ligand removal was achieved by calcination at 450 °C for 4 hours (ramp rate 1 °C min^{-1}) under flowing Ar (60 mL min^{-1}). Nanoparticle loadings were calculated from large area SEM/EDX analysis.

5.3.6: Conversion of Surface CdO to CdS

In photocatalysis samples, surface CdO formed during calcination in air was converted to CdS by Na_2S present in the sacrificial solution. Complete conversion was achieved after 6.5 hours. For mesoporous SiO_2 loaded with OA/CdS and calcined in air, conversion of CdO to CdS was achieved by dispersion of the composites (30 mg) in 0.2 M aqueous Na_2S (50 mL) with stirring for 6 hours.[247] The solid was isolated by centrifugation (4000 rpm, 30 minutes), and residual Na_2S removed by a further two washes with water (45 mL) and isolation by centrifugation. Finally, the powder was dried at 60 °C overnight to yield CdS/mesoporous SiO_2.

5.3.7: Pt loading on CdS/3DOM ZrO_2 Composites

Example for 25 wt% CdS loaded 3DOM ZrO_2: 7.5 mg CdS was loaded into 30 mg 3DOM ZrO_2, therefore 30 mg of the composite sample contains 6 mg CdS. Addition of 0.12 mg Pt corresponds to 2 wt% Pt loading. Hexachloroplatinic acid hydrate (10.5 mg, 24.6 μmol) was dissolved in water (10 mL). This solution was diluted down by a factor of 4, and 1 mL solution (0.62 mM) added to the composite. The solvent was evaporated at 110 °C overnight. Reduction to form Pt(0) was achieved by calcination at 200 °C for 1 hour (ramp rate 1 °C min^{-1}) under flowing H_2 (60 mL min^{-1}).

Appendix

A1: Example Calculations

A1.1: Estimation of Crystallite Size from PXRD

The Scherrer equation was used to estimate the crystallite size from PXRD patterns:

$$\textit{Equation 33} \quad \tau = \frac{K\lambda}{\beta cos\theta}$$

As an example, for **36%-TiO_2-395-SiO_2** (Figure 57 section 3.2.2f) the FWHM of the peak at 25.2 ° 2θ is 0.77 °. For spherical particles the shape factor K = 0.89, using a Cu $K\alpha_1$ X-ray source with wavelength λ = 1.54 x 10^{-10} nm, with the FWHM β = 1.34 x 10^{-2} radians and cos θ = 0.976, a value of τ = 10.5 nm is obtained using Equation 33.

A1.2: Example Filling Factor Calculation

The Bragg-Snell equation was used to calculate the filling factor of 3DOM materials:

$$\textit{Equation 34} \quad \lambda = \frac{2d_{hkl}}{m}[\phi n_{wall} + (1-\phi)n_{void}]$$

$$\textit{Equation 35} \quad D = \frac{a}{\sqrt{2}}$$

$$\textit{Equation 36} \quad d_{hkl} = \frac{a}{\sqrt{h^2+k^2+l^2}}$$

As an example, for 3DOM ZrO_2 in section 2.2.3d the periodicity D was measured from SEM images as 319 ± 12 nm. From the diffuse reflectance spectrum (Figure 25), the (111) peak is centred on λ = 618 nm. The refractive indices of ZrO_2 and air are n_{ZrO2} = 2.2 and n_{void} = 1.00, and the order of diffraction m = 1. Using Equation 35 and Equation 36 with h = k = l = 1, the lattice plane separation d_{hkl} = 260.2 nm. The wall fill factor was calculated by rearrangement of Equation 34 to give ϕ = 15.6 %.

A1.3: Calculation of QD concentration from UV-Vis Absorption Spectrum

The concentrations of dispersions of CdS and CdSe quantum dots were estimated from the absorbance of the first exciton peak in the UV-Vis spectrum. Extinction coefficients for CdS (2.84 nm) and CdSe (3.75 nm) quantum dots were calculated by a literature method using the following equations:[234]

Equation 37 *CdS* $\varepsilon = 21536\ (D)^{2.3}$

Equation 38 *CdSe* $\varepsilon = 5857\ (D)^{2.65}$

Where D is the nanoparticle diameter in nm, and ε is the extinction coefficient in M^{-1} cm^{-1}. Extinction coefficients were calculated as 2.38 x 10^5 M^{-1} cm^{-1} (CdS) and 1.94 x 10^5 M^{-1} cm^{-1} (CdSe). Nanoparticle concentrations (c) were calculated using the Beer Lambert law:

Equation 39 $A = \varepsilon c l$

Where A is the absorbance of the first exciton peak, and l is the path length (1 cm). As an example, the corresponding concentrations of solutions with 1 absorbance for the first exciton peaks were calculated as 5.1 µM (CdS) and 4.2 µM (CdSe).

A1.4: Determination of Nanoparticle Composition from CHN Analysis

CHN elemental analysis was used to calculate the inorganic content of OA-coated nanoparticles. As an example, TiO_2/OA nanoparticles returned a composition of 62.6 % C, 9.72 % H, 0 % N. The composition % was divided by Mr to get values of 5.21 for C and 9.64 for H. To find expected O, these ratios were divided by 9 (C) or 17 (H) to relate the number of atoms of C and H to O in oleic acid ($C_{18}H_{34}O_2$). This value was multiplied by Mr_O to get 9.27 % O. Subtracting the C, H and O percentages from 100 gives a TiO_2 composition of 18.5 %. To work out the ratio of TiO_2 : OA, the TiO_2 % was divided by Mr_{TiO2} to give a ratio of 0.23, from which a composition of 1 TiO_2 : 22.5 C : 41.6 H : 2.52 O was calculated, or 1 TiO_2 : 1.25 OA.

Expected elemental compositions for each sample were recalculated using these ratios.

Calculated elemental analysis values are listed below for reference:

OA/TiO_2: CHN Analysis found (%) C 62.6; H 9.72; N 0; Calc. C 62.42; H 9.89; Ti 11.0; O 16.7.

OA/Fe_3O_4: CHN Analysis found (%) C 54.83; H 8.12; N 0; Calc. C 54.37; H 8.62; Fe 21.0; O 16.1.

Oleyl/CdS: CHN Analysis found (%) C 25.43; H 5.83; N 0; Calc. C 25.57; H 4.41; Cd 52.3; S 14.9; N 1.6.

OA/CdS: CHN Analysis found (%) C 62.3; H 10.3; N 0; Calc. C 62.61; H 9.93; Cd 14.1; O 9.2; S 4.0.

TOPO/CdSe: CHN Analysis found (%) C 39.5; H 6.59; N 0; Calc. C 39.24; H 7.00; Cd 27.8; Se 19.6; P 4.2; O 2.2.

A1.5: Example Added Weight Percent Calculations

Using the calculated OA/TiO_2 composition above, loadings were targeted based on the mass ratio of nanoparticle:support. For a target loading of 30 wt% TiO_2 in 30 mg 3DOM SiO_2, a mass of 9 mg TiO_2 is required, which requires 48.6 mg OA/TiO_2. This mass of powder was weighed out and dispersed in OA/chloroform for deposition.

From EDX analysis, the weight fractions in the composites were analysed in comparison to the target loading. For **36%-TiO_2-395-SiO_2**, the average atom percentages in the composite were found to be 6.8 % (Ti) and 26.0 % (Si). These values were multiplied by the Mr of the corresponding oxide to give a relative mass of 5.43 g (TiO_2) and 15.62 g (SiO_2). The ratio of these masses gives the weight fraction of nanoparticles in the composite, equal to 34.8 wt%.

A1.6a: TGA Analysis of OA Surface Coverage on 3DOM SiO_2

The surface coverage of OA on 3DOM SiO_2 was analysed by TGA. OA-coated 3DOM SiO_2 (8.2 mg) was heated to 600 °C under N_2, and the mass recorded as a function of temperature (Figure 107). Taking 300 °C as the onset of oleic acid loss, a percentage mass change from 90.6 % to 83.4 % is observed. Assuming the mass loss is due to removal of oleic acid, this corresponds to 0.59 mg OA (2.1 µmol), with 6.84 mg SiO_2 remaining. The surface area of 3DOM SiO_2 was measured to be 91 m^2 g^{-1}, hence 6.84 mg has a surface area of 0.62 m^2.

The number of moles of OA was multiplied by Avagadro's number to obtain a value of 1.26 x 10^{18} molecules of OA. The cross-sectional area of a single OA molecule has been reported in the literature (48 $Å^2$),[238] and hence this number of molecules would occupy an area of 0.60 m^2. Hence, this quantity of OA molecules corresponds to a monolayer coverage of OA on 3DOM SiO_2.

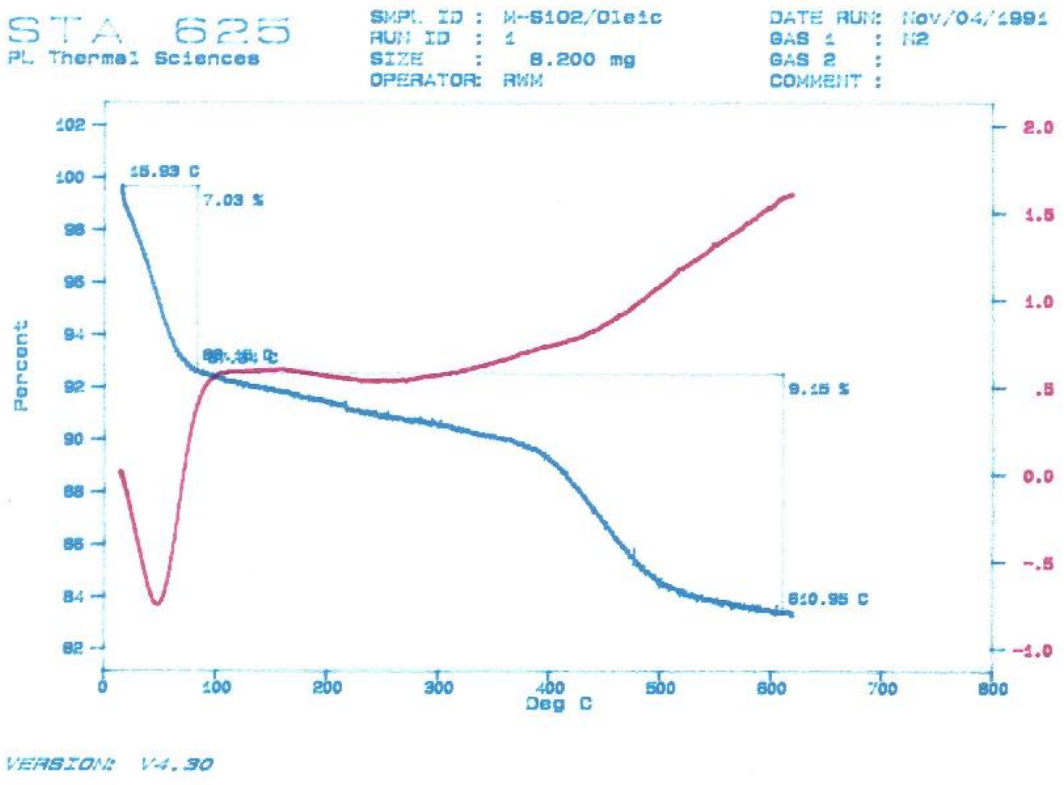

Figure 107: TGA (blue line) and DSC (red line) plots for OA-coated 3DOM SiO_2.

A1.6b: TGA Analysis of OA Surface Coverage on 3DOM ZrO_2

The surface coverage of OA on 3DOM ZrO_2 was analysed by TGA. OA-coated 3DOM ZrO_2 (11.6 mg) was heated to 600 °C under N_2, and the mass recorded as a function of temperature (Figure 108). Taking 300 °C as the onset of oleic acid loss, a percentage mass change from 99.8 % to 97.75 % is observed. Assuming the mass loss is due to removal of oleic acid, this corresponds to 0.24 mg OA (0.8 µmol), with 11.34 mg ZrO_2 remaining. The surface area of 3DOM ZrO_2 was measured to be 20.6 $m^2\ g^{-1}$, hence 11.34 mg has a surface area of 0.23 m^2.

The number of moles of OA was multiplied by Avagadro's number to obtain a value of 5.24 x 10^{17} molecules of OA. Multiplying by the cross-sectional area of OA (48 $Å^2$) gives an area of 0.25 m^2. Hence, this quantity of OA molecules corresponds to a monolayer coverage of OA on 3DOM ZrO_2

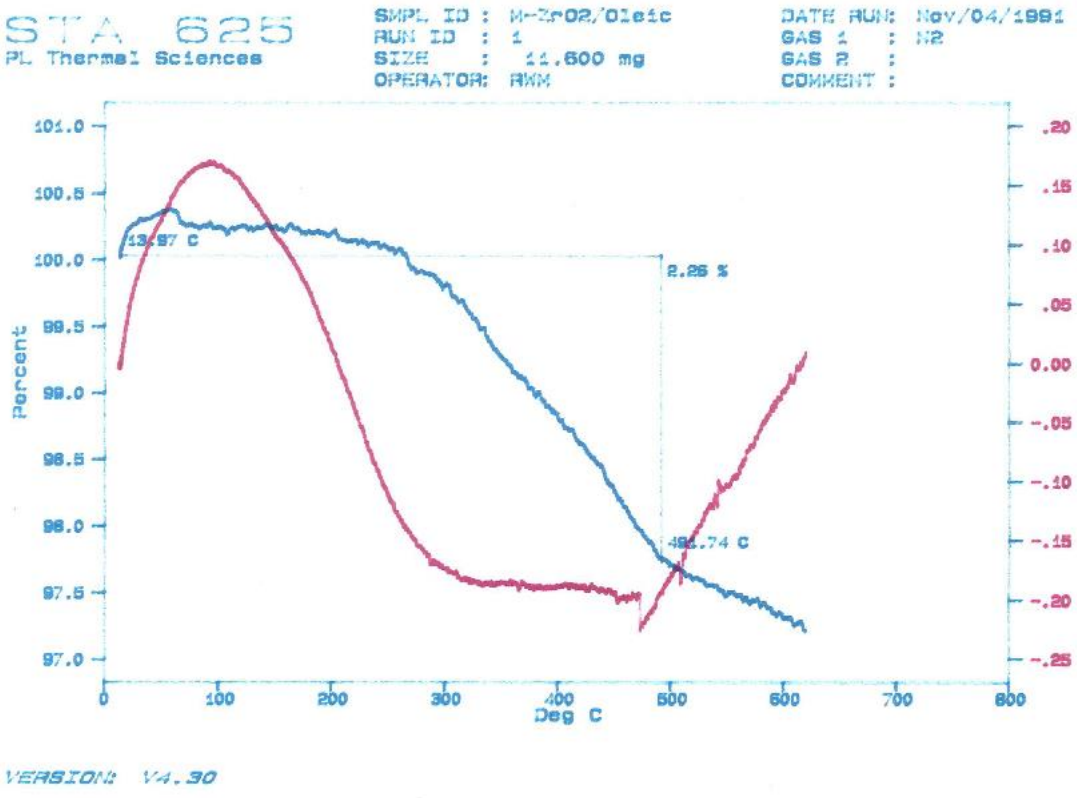

Figure 108: TGA (blue line) and DSC (red line) plots for OA-coated 3DOM ZrO_2.

A2: Modelling of Nanoparticle Fill Factor Contributions

A2.1: Refractive Index and Density List

DRUVS was used to analyse the stop band shift in nanoparticle loaded materials. The refractive index of materials varies with wavelength, and hence averaged values were used for the modelling of reflectance data. The average refractive indices and densities used within this work are listed in Table 26:

Material	Average Refractive Index	Density / g cm^{-3}
Amorphous SiO_2	1.455[99]	2.2
Tetragonal ZrO_2	2.2[267]	5.68
FTO	1.61[204]	6.95
Anatase TiO_2	2.49[99]	4.23
Cubic Fe_3O_4	2.42[268]	5.2
Hexagonal CdS	2.4[269]	4.83
Air	1.00029	N/A

Table 26: Refractive indices and densities of materials studied in this work.

A2.2: Equations

The equations used to model the reflectance data are collected here. As described in chapter 3 section 3.2.2f, a modification was made to the Bragg-Snell equation to describe the stop band red shift (Equation 40):

$$\textit{Equation 40} \quad \lambda_{new} = 2d_{hkl}(\varphi\, n_{wall} + \chi_{NP}\, n_{NP} + (1 - \varphi - \chi_{NP}) n_{void})$$

Where χ_{NP} and n_{NP} are the volume fraction and refractive index of the nanoparticles, and λ_{new} is the shifted position of the stop band. χ_{NP} values were calculated using Equation 41:

$$\textit{Equation 41} \quad \chi_{NP} = \frac{\lambda_{new} - \lambda}{2d_{hkl}(n_{NP} - n_{void})}$$

From the calculated χ_{NP} values, the predicted stop band position in the composite (λ_{calc}) was calculated using the following equation:

$$\textit{Equation 42} \quad \lambda_{calc} = 2d_{hkl}(\varphi_{total} n_{ave} + (1 - \varphi_{total}) n_{void})$$

Where ϕ_{total} is the wall fill factor of the composite, defined by the following expression:

$$\textit{Equation 43} \quad \varphi_{total} = \varphi + \chi_{NP}$$

The average wall refractive index, n_{ave} was calculated using Equation 44:

$$\textit{Equation 44} \quad n_{ave} = \frac{n_{wall} + n_{NP}(\%_{NP}.\frac{\rho_{wall}}{\rho_{NP}})}{1 + (\%_{NP}.\frac{\rho_{wall}}{\rho_{NP}})}$$

Where $\%_{NP}$ is the wt% of nanoparticles added and ρ is the density of the wall and nanoparticles. In the denominator, the 1 represents the initial quantity of host, and the bracket the amount of added nanoparticles.

A2.3: Chi Tables

The modelled reflectance data sets for the composites in the main text are collected here for reference.

Sample	χ_{TiO2} / %	n_{avg}	ϕ_{total} / %	Experimental λ_{111} shift / nm	Calculated λ_{111} shift / nm
7.3%-TiO_2-395-SiO_2	0.52	1.493	9.40	5.5	4.05
14.6%-TiO_2-395-SiO_2	0.81	1.528	9.68	8.0	7.33
21.8%-TiO_2-395-SiO_2	1.05	1.561	9.92	10.5	10.41
29.1%-TiO_2-395-SiO_2	1.31	1.591	10.19	13.5	13.53
36.4%-TiO_2-395-SiO_2	1.57	1.620	10.45	16.0	16.63

Table 27: Modelled reflectance data for TiO_2 loaded 3DOM SiO_2.

Sample	χ_{TiO2} / %	n_{avg}	ϕ_{total} / %	Experimental λ_{111} shift / nm	Calculated λ_{111} shift / nm
3.5%-TiO_2-271-ZrO_2	0.57	2.213	16.0	3.5	3.68
7.0%-TiO_2-271-ZrO_2	1.23	2.225	16.6	7.5	7.75
10.6%-TiO_2-271-ZrO_2	1.80	2.236	17.2	11.0	11.40
14.1%-TiO_2-271-ZrO_2	2.29	2.246	17.7	14.0	14.62
17.6%-TiO_2-271-ZrO_2	2.87	2.255	18.2	17.5	18.24
26.5%-TiO_2-271-ZrO_2	4.18	2.276	19.6	25.5	26.64

Table 28: Modelled reflectance data for TiO_2 loaded 3DOM ZrO_2.

Sample	χ_{Fe3O4} / %	n_{avg}	ϕ_{total} / %	Experimental λ_{111} shift / nm	Calculated λ_{111} shift / nm
4.1%-Fe_3O_4-395-SiO_2	0.14	1.471	6.78	1.5	1.19
8.2%-Fe_3O_4-395-SiO_2	0.32	1.487	6.96	3.0	2.54
16.4%-Fe_3O_4-395-SiO_2	0.45	1.518	7.1	4.5	4.45
32.8%-Fe_3O_4-395-SiO_2	0.96	1.573	7.6	9.5	9.10
49.2%-Fe_3O_4-395-SiO_2	1.28	1.621	7.92	12.5	12.99
65.6%-Fe_3O_4-395-SiO_2	1.83	1.665	8.47	18.0	17.82

Table 29: Modelled reflectance data for Fe_3O_4 loaded 3DOM SiO_2.

Sample	χ_{CdS} / %	n_{avg}	ϕ_{total} / %	Experimental λ_{111} shift / nm	Calculated λ_{111} shift / nm
1-CdS	1.93	2.22	18.91	5.96	5.95
2-CdS	1.94	2.22	18.78	8.8	8.76
3-CdS	1.93	2.22	18.94	9.33	9.31
4-CdS	1.94	2.22	18.88	10.83	10.79

Table 30: Modelled reflectance data for 9.5 wt% CdS loaded 3DOM ZrO_2 photocatalysis samples.

Sample	χ_{CdS} / %	n_{avg}	ϕ_{total} / %	Experimental λ_{111} shift / nm	Calculated λ_{111} shift / nm
1-TiO_2	6.22	2.271	23.2	20.5	20.39
2-TiO_2	6.21	2.271	23.1	30.5	29.87
3-TiO_2	6.22	2.271	23.2	32.5	31.90
4-TiO_2	6.22	2.271	23.2	37.5	36.81

Table 31: Modelled reflectance data for 47.8 wt% TiO_2 loaded 3DOM ZrO_2 photocatalysis samples.

Sample	χ_{CdS} / %	n_{avg}	ϕ_{total} / %	Experimental λ_{111} shift / nm	Calculated λ_{111} shift / nm
15%-CdS-316-SiO_2	0.30	1.595	5.48	2.5	2.49
31.4%-CdS-316-SiO_2	0.67	1.648	5.84	5.0	5.29
50.5%-CdS-316-SiO_2	1.27	1.701	6.45	9.5	9.23
93.7%-CdS-316-SiO_2	2.21	1.797	7.38	16.5	16.55

Table 32: Modelled reflectance data for CdS loaded 3DOM SiO_2.

Sample	χ_{CdS} / %	n_{avg}	ϕ_{total} / %	Experimental λ_{111} shift / nm	Calculated λ_{111} shift / nm
4%-CdS-255-ZrO_2	0.97	2.209	17.77	6.0	5.62
8%-CdS-255-ZrO_2	1.77	2.217	18.58	10.5	10.38
16%-CdS-255-ZrO_2	3.15	2.232	19.95	18.5	18.69

Table 33: Modelled reflectance data for CdS loaded 3DOM ZrO_2.

Sample	χ_{TiO2} / %	n_{avg}	ϕ_{total} / %	Experimental λ_{111} shift / nm	Calculated λ_{111} shift / nm
15.6%-TiO_2-289-FTO	3.43	1.790	16.7	24	24.1
19.6%-TiO_2-289-FTO	4.27	1.824	17.6	30	30.1

Table 34: Modelled reflectance data for TiO_2 loaded 3DOM FTO.

A2.4: Experimental Stop Band Shift Analysis

The gradients of the plots of stop band shift *vs.* nanoparticle loading vary between the different materials used in this study. As an example, for CdS loading in SiO_2 and TiO_2 loading in ZrO_2 the gradients of these plots for the experimental data are 0.18 and 0.95 respectively. The loadings are calculated in wt%, and hence a large proportion of this difference is due to the increased density of ZrO_2 (5.68 g cm^{-3}) compared to SiO_2 (2.2 g cm^{-3}). The densities of TiO_2 and CdS are 4.23 and 4.83 g cm^{-3} respectively. For a loading of 20 wt%, the volume ratio of CdS/SiO_2 and TiO_2/ZrO_2 are 0.09 and 0.27 respectively, hence the added volume of TiO_2 nanoparticles in ZrO_2 is three times higher than CdS in SiO_2 for a given loading.

The rest of the difference is accounted for by variation in refractive index, fill factor, and periodicity of the two materials. The average refractive index of the wall space, n_{ave}, is much lower for CdS/SiO_2 compared to TiO_2/ZrO_2 due to the low refractive index of SiO_2 (1.46) in comparison to ZrO_2 (2.2). The left hand side of the brackets in Equation 13 will be larger for TiO_2/ZrO_2, by a factor dependent on the fill factors for a given material, hence the stop band shift for a given nanoparticle loading will be larger than in CdS/SiO_2.

A2.5: Estimated Errors

The main sources of error in the determination of the modelled data are the measured periodicity, the measured stop band shift, and the loading amount. The periodicity of **319-ZrO_2** discussed above was measured to be 319 ± 12 nm, which translates to a d_{hkl} value of 260.2 ± 10 nm, or around a 4 % error. The error in the calculated values of the fill factor from this are 15.6 ± 4 %, showing the sensitivity of the fill factor calculation. The percentage error in the fill factor is 25 % for this example, and can approach 50 % for 3DOM SiO_2 which has a lower value of ϕ. However, ϕ values are linked to specific d_{hkl} values and hence the percentage error does not extend to the modelled shift data.

For measurement of reflectance data, the resolution of the spectrometer used was 0.47 nm, and hence for two measurements of the stop band position (uncoated and NP loaded) the error in the shift value is a minimum of 0.94 nm. Some peaks are asymmetrical which complicates the determination of the centre, and may further increase this error. Taking ± 0.94 nm as the error for a stop band shift, it is clear that for low loadings the percentage error is much higher than for high loadings. From the trendlines of stop band shift as a function of loading, larger deviations are observed for low loading values in agreement with this analysis. From EDX measurements, the error in the loading amount was observed to be around 20 % for low loadings, decreasing to around 10 % for higher loadings. The error bars on the plots attempt to convey some of this information. As a general conclusion, taking into account the errors in the measurements, the experimental stop band shift shows a linear increase for all materials as a function of nanoparticle loading, and the calculated shifts agree well with the experimental trends.

For the modelled shift data, the calculated values of χ_{NP} do not involve the fill factor. For the TiO_2/ZrO_2 series the periodicity of the porous structure was measured as 271 ± 20 nm. Changing the periodicity by ± 20 nm changes the values of χ_{TiO2} by ± 7.5 %. This corresponds to a maximum 6.5 % error in the calculated shift values. The ϕ_{total} values reported are subject to large errors intrinsic to the ϕ values of the 3DOM material, however the rest of the tabulated values (χ_{NP}, calculated shift) are not expected to deviate by more than around 10 %.

A3: Supplementary Figures

The figures in this section are listed here for reference:

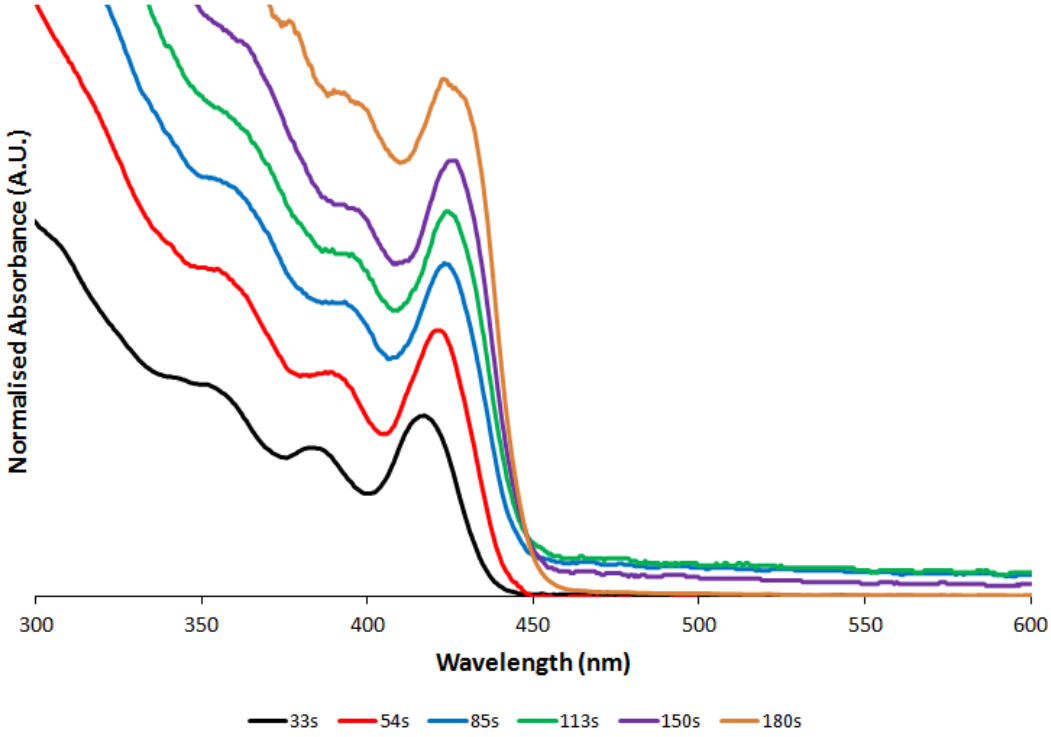

Figure 109: UV-Vis absorption spectra of CdS quantum dot aliquots extracted as a function of reaction time. Intensity of peaks are normalised for comparison.

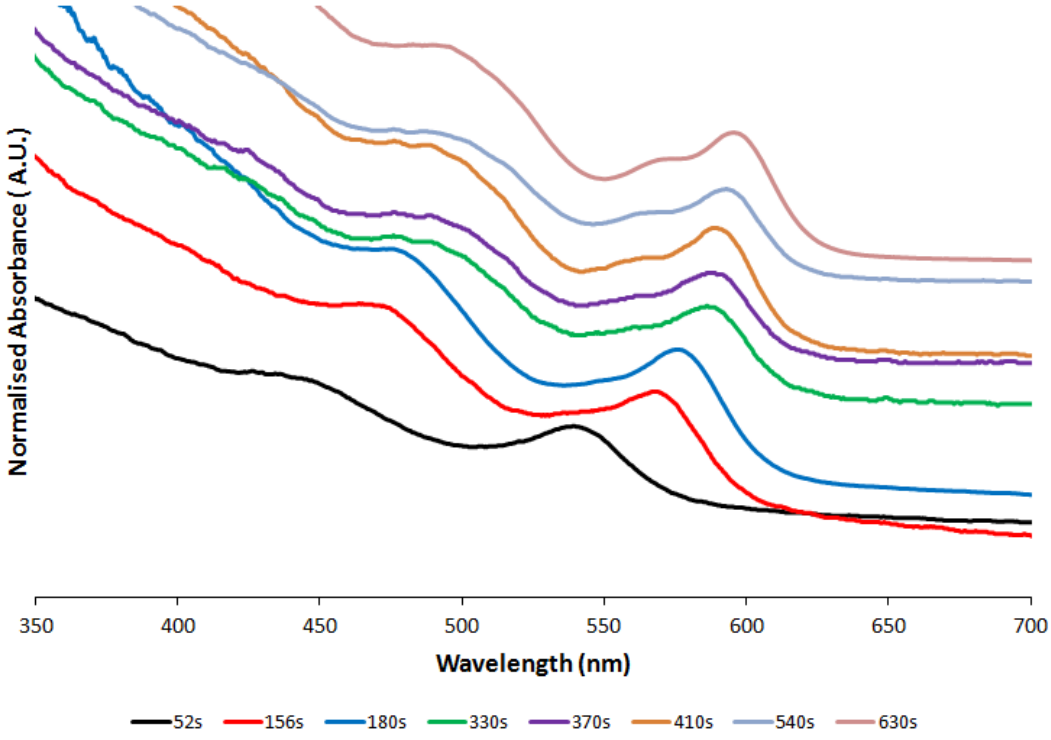

Figure 110: UV-Vis absorption spectra of CdSe quantum dot aliquots extracted as a function of reaction time. Intensity of peaks are normalised for comparison.

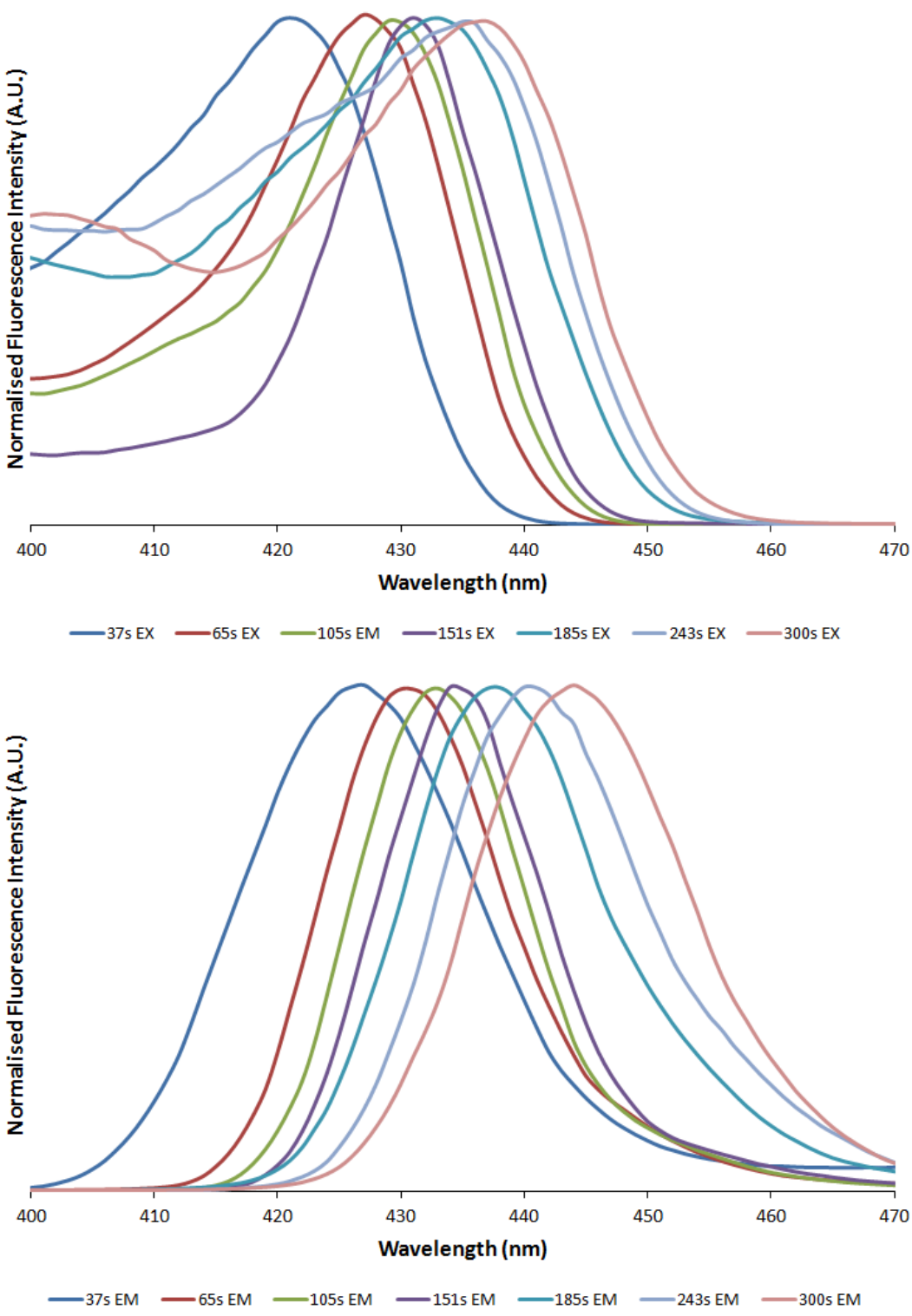

Figure 111: Fluorescence excitation (top) and emission (bottom) spectra of CdS quantum dot aliquots extracted as a function of reaction time. Intensity of peaks are normalised for comparison.

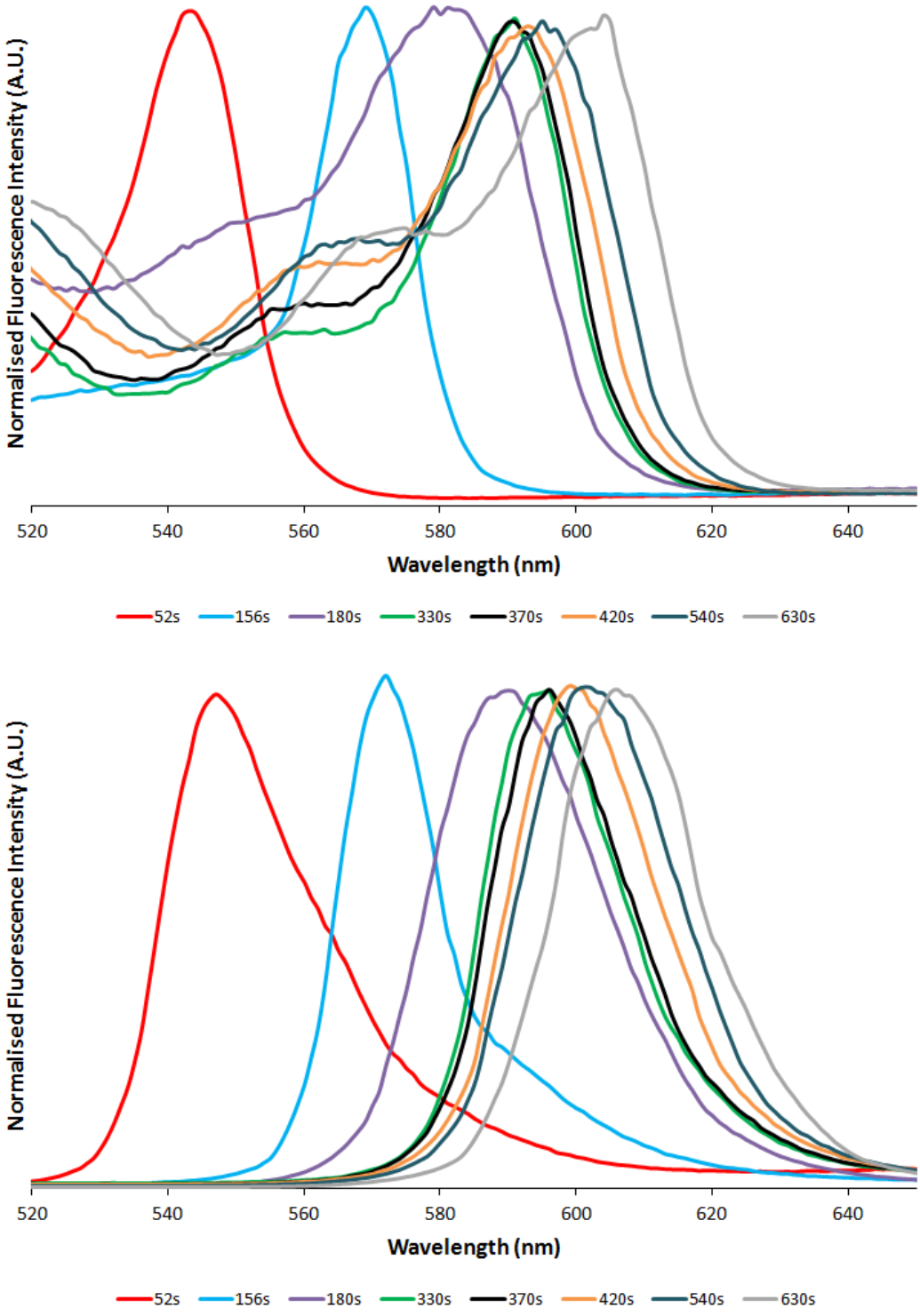

Figure 112: Fluorescence excitation (top) and emission (bottom) spectra of CdSe quantum dot aliquots extracted as a function of reaction time. Intensity of peaks are normalised for comparison.

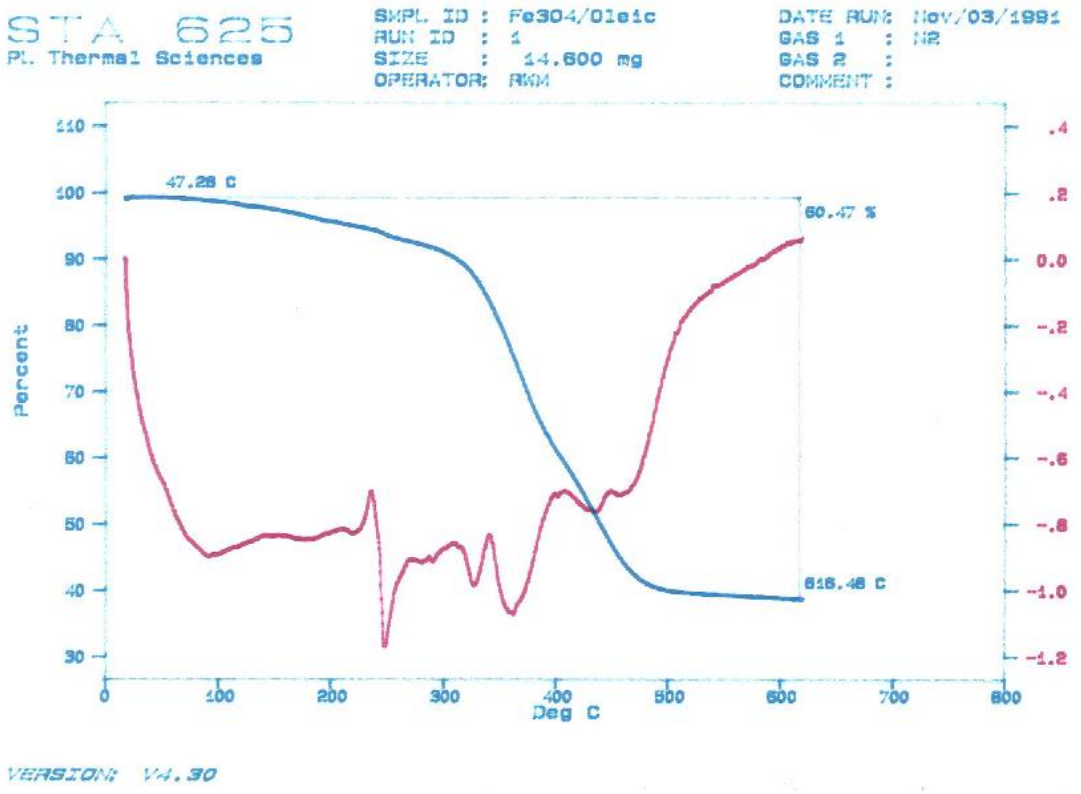

Figure 113: TGA (blue) and DSC (red) plots for OA/Fe_3O_4 nanoparticles.

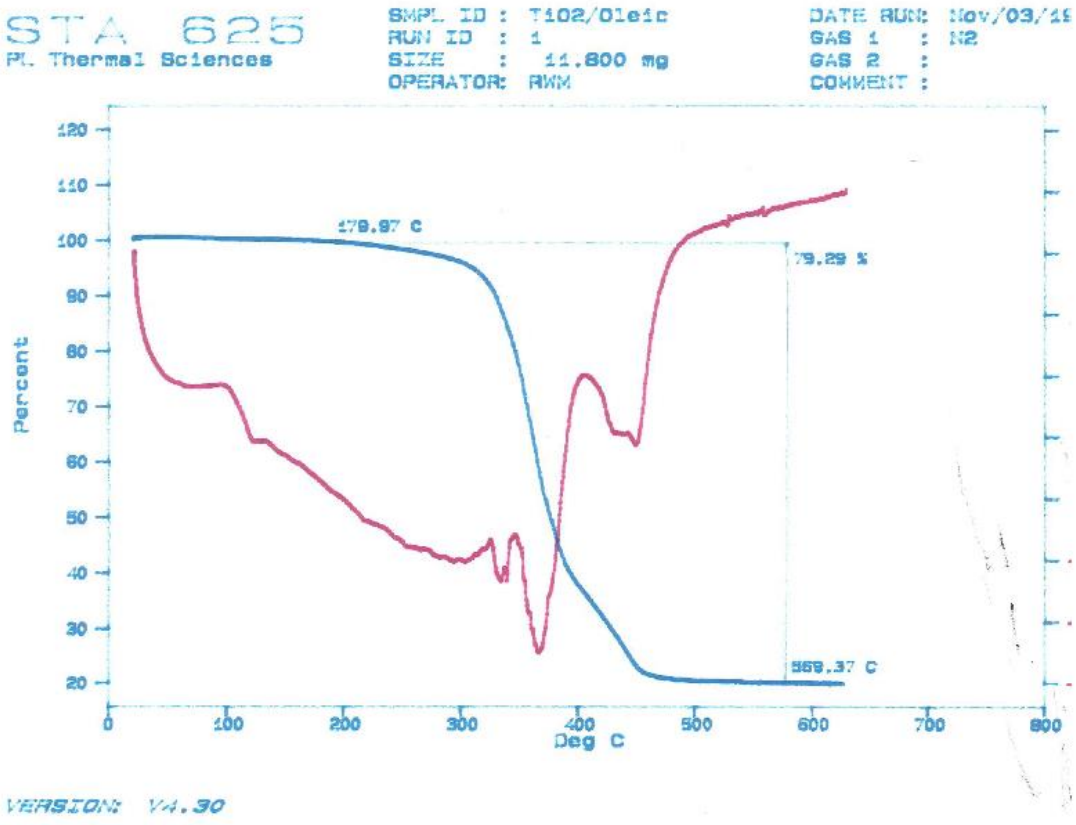

Figure 114: TGA (blue) and DSC (red) plots for OA/TiO_2 nanoparticles.

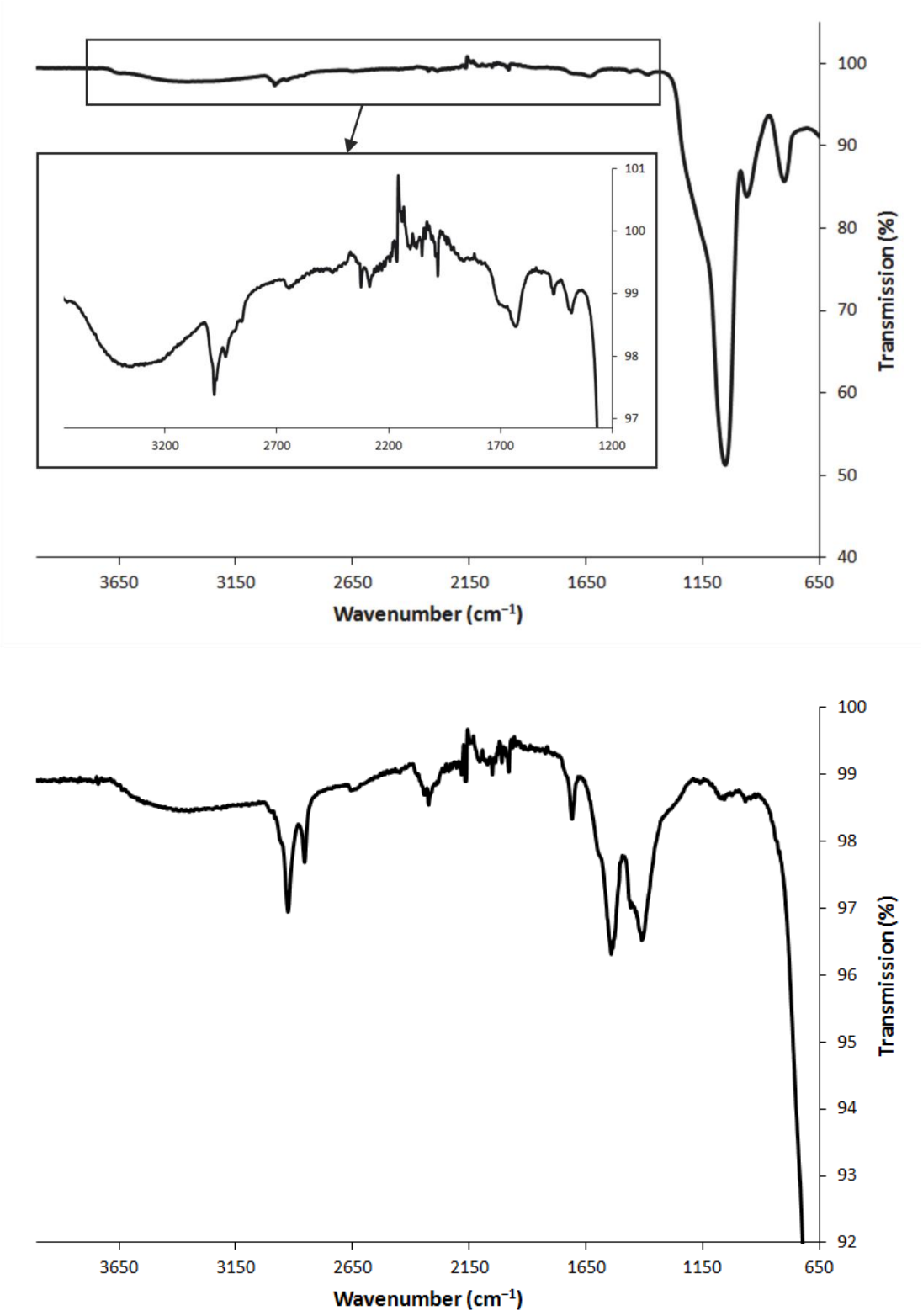

Figure 115: IR spectra of OA-coated 3DOM SiO_2 (top) and OA-coated 3DOM ZrO_2 (bottom).

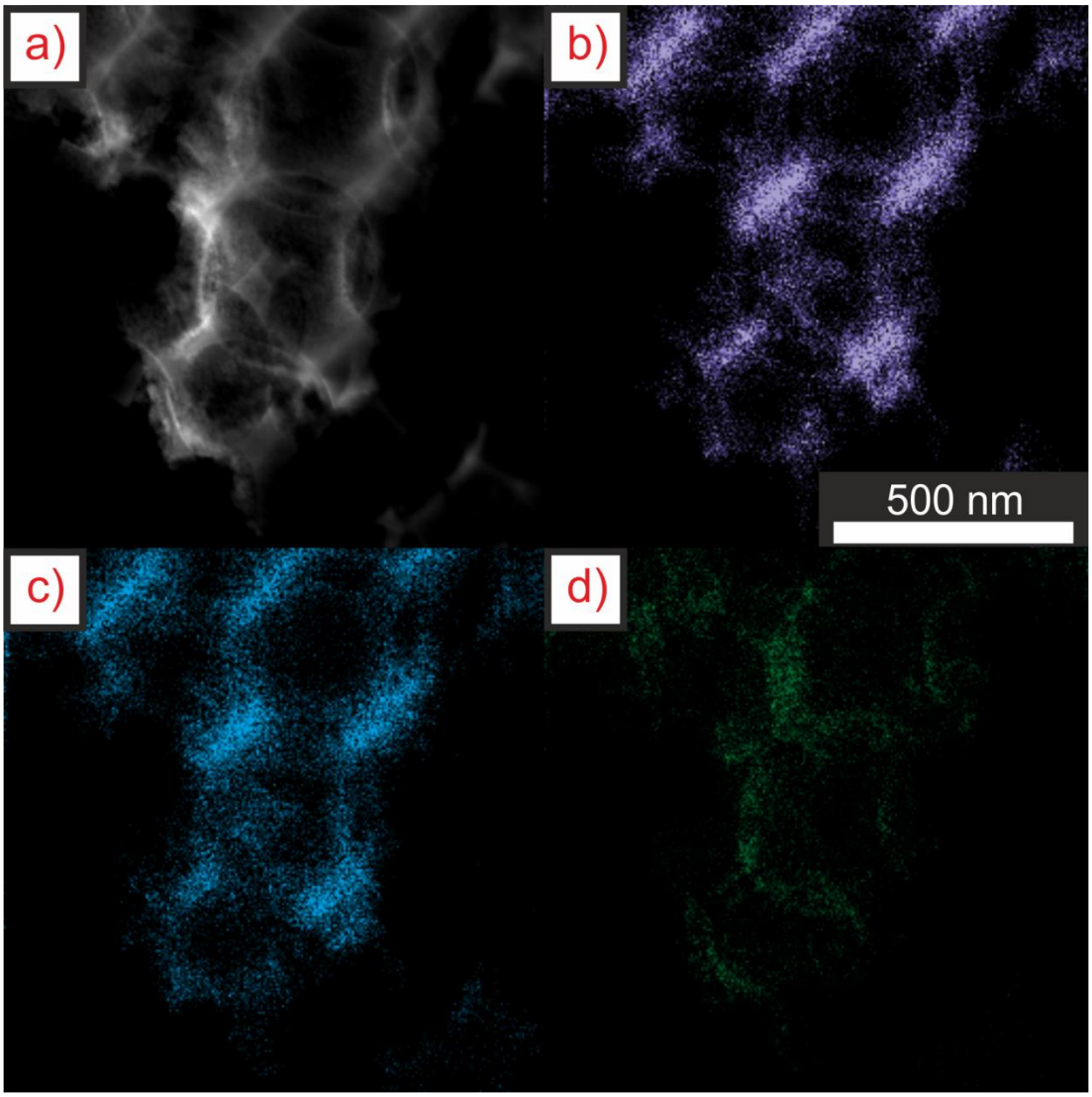

Figure 116: TEM EDX mapping data for ***58%-TiO_2-351-SiO_2*** *fabricated by deposition in OA-coated* ***351-SiO_2*** *from nanoparticle dispersions in hexane. (a) HAADF STEM image, (b) Si map, (c) O map, (d) Ti map. 500 nm scale bar applies to all images.*

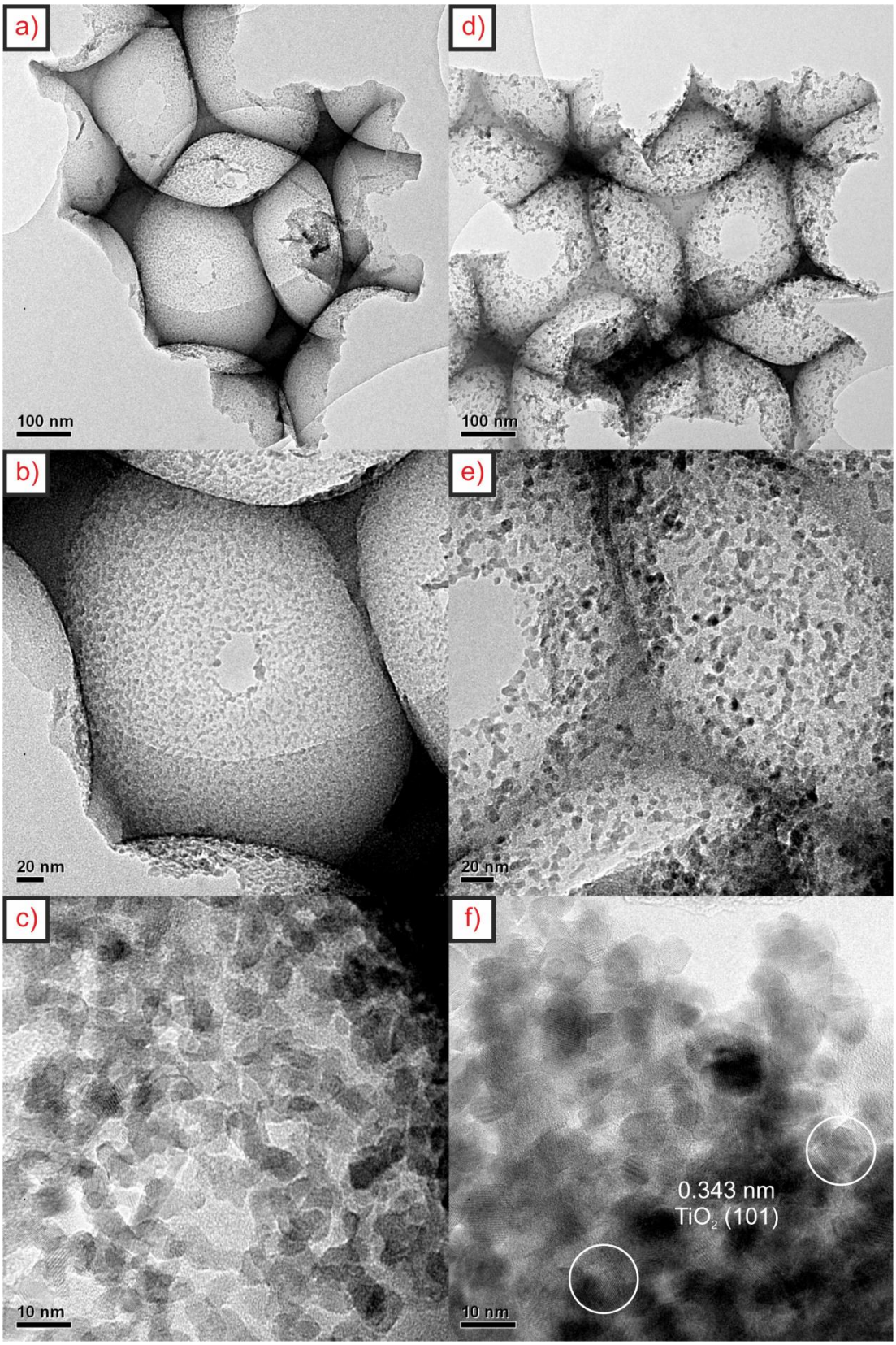

Figure 117: TEM images of TiO_2 loaded 3DOM SiO_2 deposited from OA/chloroform dispersions into OA-coated supports. (a) – (c) ***14.6%-TiO_2-395-SiO_2*** *and (d) – (f)* ***36.4%-TiO_2-395-SiO_2.***

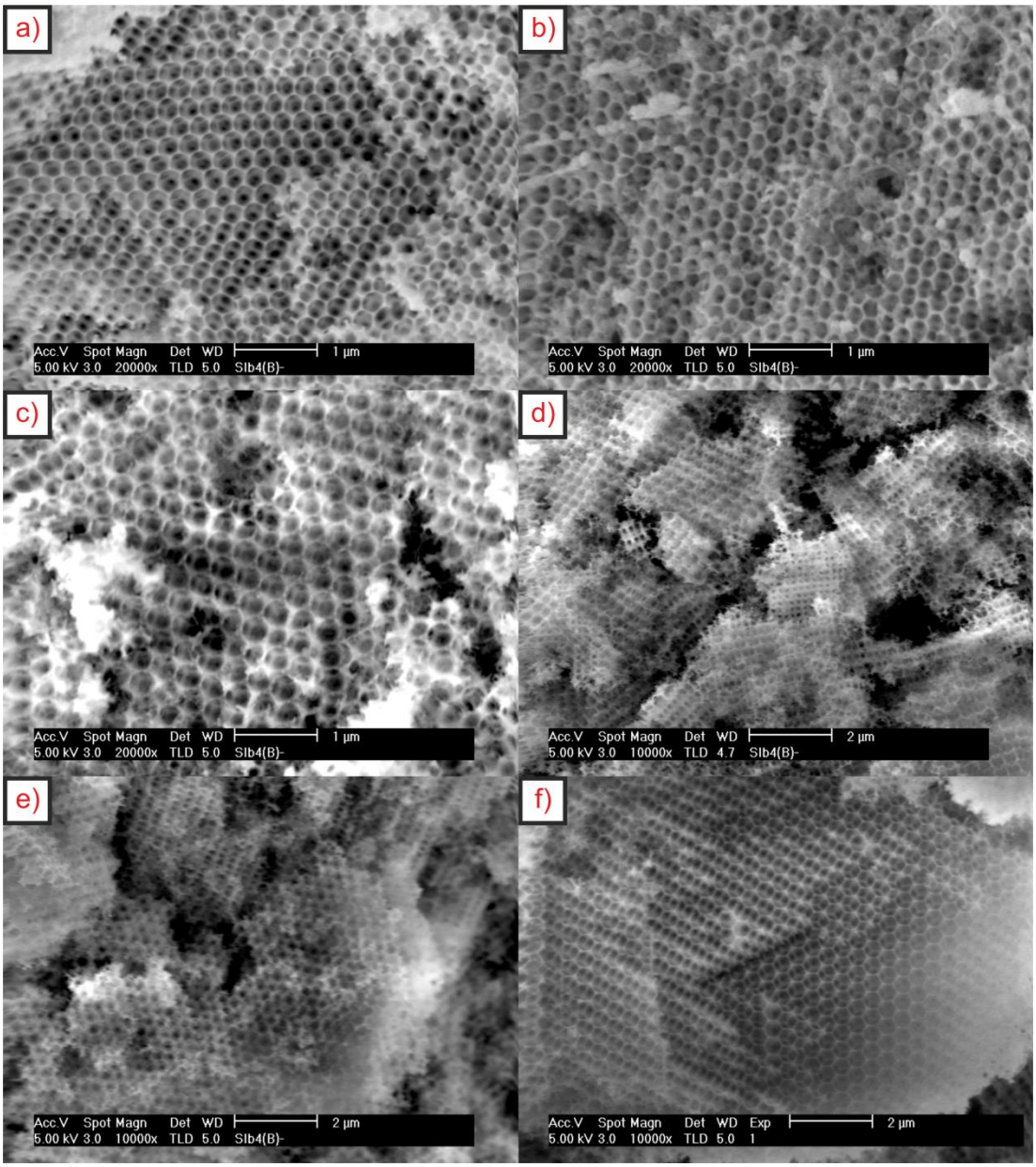

Figure 118: SEM images of nanoparticle loaded 3DOM SiO_2 and ZrO_2 composites deposited from OA/toluene dispersions. (a) ***11.5%-TiO_2-271-ZrO_2****, (b)* ***28.8%-TiO_2-271-ZrO_2****, (c)* ***22%-TiO_2-351-SiO_2****, (d)* ***15%-CdS-351-SiO_2****, (e)* ***93.7%-CdS-351-SiO_2*** *and (f)* ***4.1%-Fe_3O_4-395-SiO_2****.*

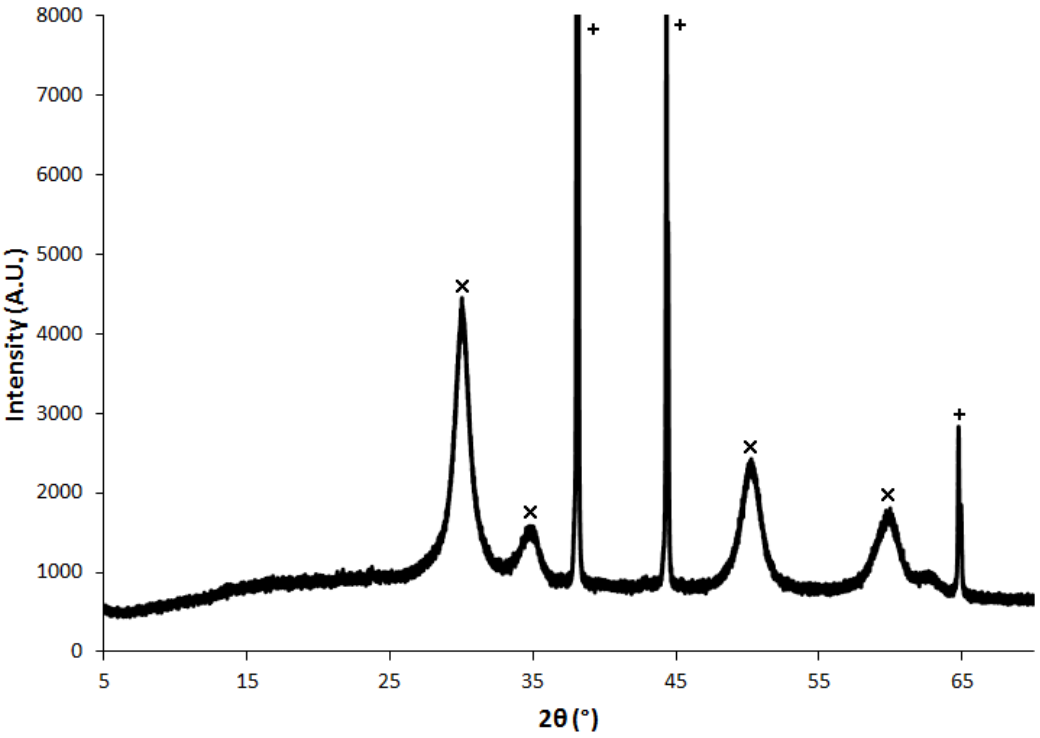

Figure 119: PXRD pattern for Fe_3O_4 loaded 3DOM ZrO_2. x = tetragonal ZrO_2, JCPDS 01-079-1763, + = Al sample holder. Peaks for ZrO_2 and Fe_3O_4 are coincident at this resolution.

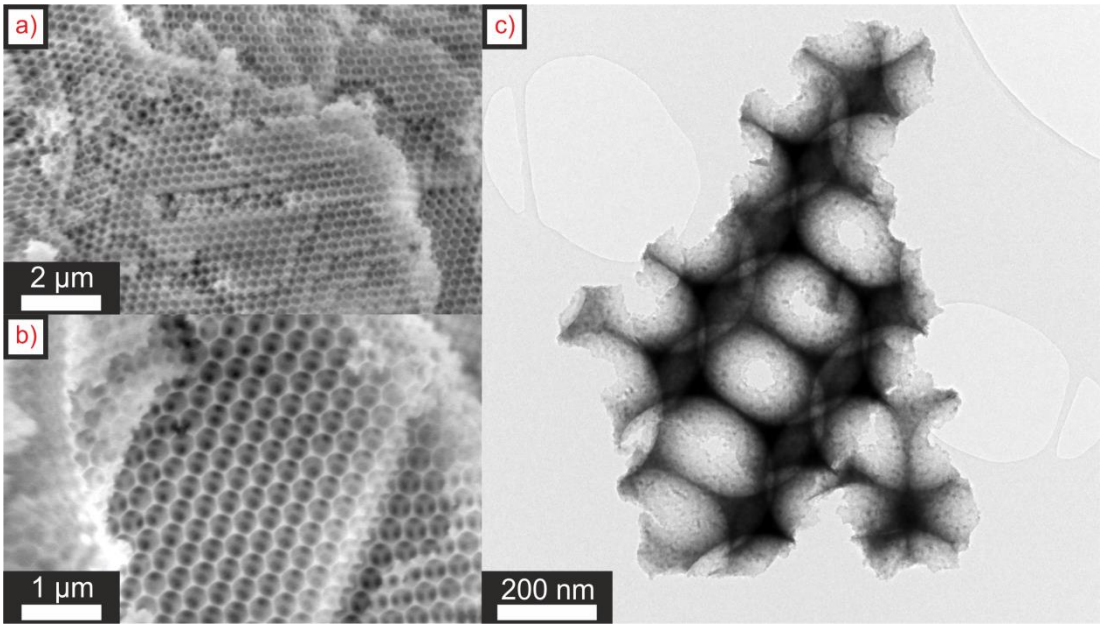

*Figure 120: SEM and TEM images of Fe_3O_4 loaded 3DOM ZrO_2. (a), (b) SEM images of **8.2%-Fe_3O_4-343-ZrO_2**, and (c) TEM image of **16.4%-Fe_3O_4-343-ZrO_2**.*

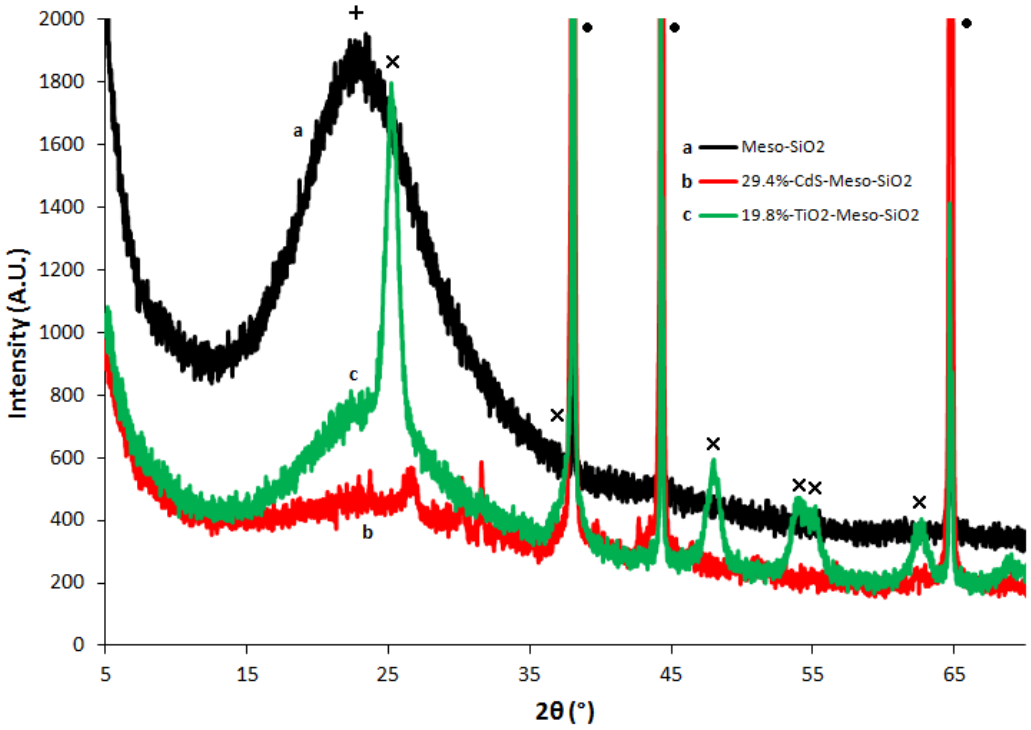

Figure 121: PXRD patterns for ***Meso-SiO$_2$, 29.4%-CdS-Meso-SiO$_2$,*** *and* ***19.8%-TiO$_2$-Meso-SiO$_2$****. + = Amorphous SiO$_2$, X = tetragonal anatase TiO$_2$, JCPDS 01-078-2486, ● = Al sample holder.*

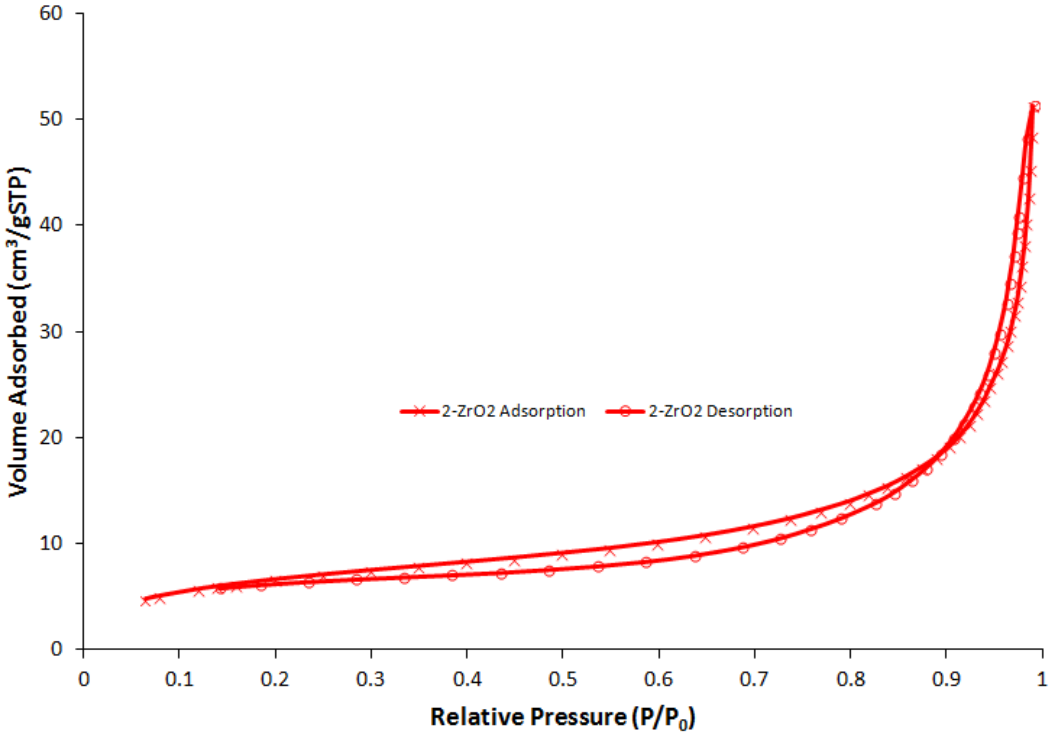

Figure 122: Nitrogen adsorption/desorption isotherm for ***255-ZrO$_2$*** *sample* ***2****.*

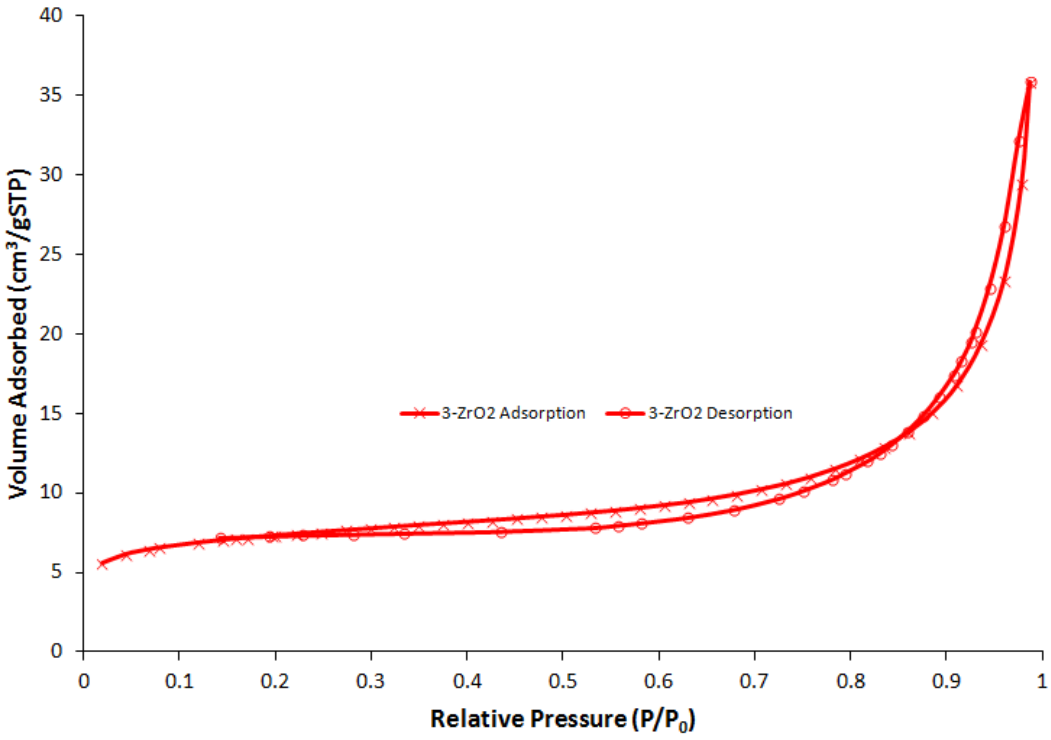

*Figure 123: Nitrogen adsorption/desorption isotherm for **270-ZrO_2** sample **3**.*

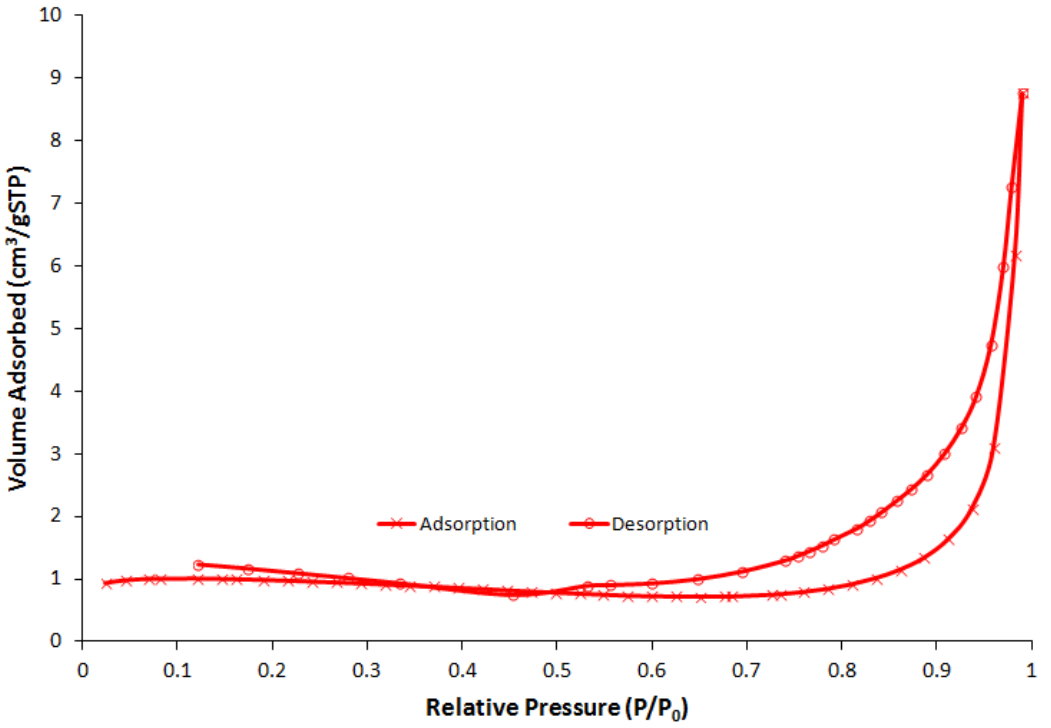

*Figure 124: Nitrogen adsorption/desorption isotherm for commercial ZrO_2 powder **5**.*

Abbreviations

3DHNS – Three Dimensionally Ordered Hollow Nanospheres

3DOM – Three Dimensionally Ordered Macroporous Material

AACVD – Aerosol Assisted Chemical Vapour Deposition

Ac – Acetate

ALD – Atomic Layer Deposition

AQY – Apparent Quantum Yield

A.U. – Arbitrary Units

BET – Brunauer Emmett Teller

CB – Conduction Band

CCP – Cubic Close Packed

CVD – Chemical Vapour Deposition

DCDMS – Dichlorodimethylsilane

DRUVS – Diffuse Reflectance UV-Visible Spectroscopy

DSSC – Dye Sensitised Solar Cell

EDTA – Ethylenediaminetetraacetic acid

EDX – Energy Dispersive Analysis of X-rays

EQE – External Quantum Efficiency

E_g – Band Gap

EG – Ethylene Glycol

EPR – Electron Paramagnetic Resonance

ET – Exotemplating

FCC – Face Centred Cubic

FDU – Class of Mesoporous Material

FTO – Fluorine Doped Tin Oxide

GC – Gas Chromatography

HNS – Hollow Nanospheres

ID – Internal Diameter

IO – Inverse Opal

IPCE – Incident Photon to Current Conversion Efficiency

iPr – Isopropyl

IQE – Internal Quantum Efficiency

IR – Infra Red

ITO – Tin Doped Indium Oxide

Macroporous – > 50 nm Pores

MCM – Mobil Crystalline Material Class Porous Material

Mesoporous – 2 – 50 nm Pores

Microporous – < 2 nm Pores

NP – Nanoparticle

OA – Oleic acid

P25 – 80:20 mixture of Anatase:Rutile TiO_2

PC – Photonic Crystal

PEO – Poly(ethylene oxide)

PL – Photoluminescence

PMMA – Poly(methyl methacrylate)

PPO – Poly(propylene oxide)

PS – Polystyrene

PVP – Poly(vinyl pyrrolidone)

PXRD – Powder X-Ray Diffraction

QDs – Quantum Dots

QE – Quantum Efficiency

QY – Quantum Yield

RT – Room Temperature

SBA – Santa Barbara Amorphous Type Mesoporous Material

SEM – Scanning Electron Microscopy

SILAR – Successive Ionic Layer Adsorption and Reaction

SPR – Surface Plasmon Resonance

SSR – Solid State Reaction

STP – Standard Temperature and Pressure

TCO – Transparent Conducting Oxide

TEM – Transmission Electron Microscopy

TGA – Thermogravimetric Analysis

UV – Ultraviolet Light

UV-Vis – Ultraviolet and Visible Light

VB – Valence Band

wt% – Weight Percentage of Nanoparticles as a Ratio to the Support Mass

List of References

1. M.-G. Jeong, E. J. Park, B. Jeong, D. H. Kim and Y. D. Kim, *Chem. Eng. J.*, 2014, **237**, 62
2. A. Fujishima and K. Honda, *Nature*, 1972, **238**, 37
3. A. J. Bard, *J. Phys. Chem.*, 1982, **86**, 172
4. J. Li, Y. Qiu, Z. Wei, Q. Lin, Q. Zhang, K. Yan, H. Chen, S. Xiao, Z. Fan and S. Yang, *Energy Environ. Sci.,* 2014, **7**, 3651
5. M. Hasanzadeh, A. Bahrami, M. Alizadeh and N. Shadjou, *RSC Adv.*, 2013, **3**, 24237
6. N. S. Lewis and D. G. Nocera, *Proc. Natl. Acad. Sci. USA*, 2006, **103**, 15729
7. T. R. Cook, D. K. Dogutan, S. Y. Reece, Y. Surendranath, T. S. Teets and D. G. Nocera, *Chem. Rev.*, 2010, **110**, 6474
8. W. M. Haynes, *Handbook of Chemistry and Physics, 94th ed.*, CRC Press, Boca Raton, Florida, 2013
9. H. Kisch, *Angew. Chem. Int. Ed.*, 2013, **52**, 812
10. Z. Zhang and J. T. Yates, *Chem. Rev.*, 2012, **112**, 5520
11. W. Stumm, *Chemistry of the Solid-Water Interface*, Wiley, New York, 1992
12. F. E. Osterloh, *Chem. Mater.*, 2008, **20**, 35
13. H. Kato and A. Kudo, *Chem. Phys. Lett.*, 1998, **295**, 487
14. R. M. Navarro, M. C. Alvarez-Galvan, J. A. Villoria de la Mano, S. M. Al-Zahrani and J. L. G. Fierro, *Energy Environ. Sci.*, 2010, **3**, 1865
15. A. Mills, R. H. Davies and D. Worsley, *Chem. Soc. Rev.*, 1993, **22**, 417
16. S. Chen and L.-W. Wang, *Chem. Mater.*, 2012, **24**, 3659
17. L. Chai, R. T. White, M. T. Greiner and Z. H. Lu, *Phys. Rev. B*, 2014, **89**, 035202
18. S. Sayan, R. A. Bartynski, X. Zhao, E. P. Gusev, D. Vanderbilt, M. Croft, M. Banaszak Holl and E. Garfunkel, *Phys. Status Solidi B*, 2004, **241**, 2246
19. K. Maeda and K. Domen, *J. Phys. Chem. C*, 2007, **111**, 7851
20. C. M. Fang, E. Orhan, G. A. de Wijs, H. T. Hintzen, R. A. de Groot, R. Marchand, J. Y. Saillard and G. de With, *J. Mater. Chem.*, 2001, **11**, 1248
21. G. Hitoki, T. Takata, J. N. Kondo, M. Hara, H. Kobayashi and K. Domen, *Chem. Commun.*, 2002, 1698
22. G. Hitoki, A. Ishikawa, T. Takata, J. N. Kondo, M. Hara and K. Domen, *Chem. Lett.*, 2002, **31**, 736
23. A. Kasahara, K. Nukumizu, T. Takata, J. N. Kondo, M. Hara, H. Kobayashi and K. Domen, *J. Phys. Chem. B*, 2003, **107**, 791
24. D. Yamasita, T. Takata, M. Hara, J. N. Kondo and K. Domen, *Solid State Ionics*, 2004, **172**, 591
25. M. Liu, W. You, Z. Lei, G. Zhou, J. Yang, G. Wu, G. Ma, G. Luan, T. Takata, M. Hara, K. Domen and C. Li, *Chem. Commun.*, 2004, 2192
26. A. Ishikawa, T. Takata, J. N. Kondo, M. Hara, H. Kobayashi and K. Domen, *J. Am. Chem. Soc.*, 2002, **124**, 13547
27. H. Irie, Y. Watanabe and K. Hashimoto, *J. Phys. Chem. B*, 2003, **107**, 5483
28. H.-L. Qin, G.-B. Gu and S. Liu, *Mater. Chem. Phys.*, 2008, **112**, 346

29. Y. Liu, L. Xie, Y. Li, R. Yang, J. Qu, Y. Li and X. Li, *J. Power Sources*, 2008, **183**, 701
30. X. Qiu, M. Miyauchi, H. Yu, H. Irie and K. Hashimoto, *J. Am. Chem. Soc.*, 2010, **132**, 15259
31. N. Serpone, *J. Photochem. Photobiol. A*, 1997, **104**, 1
32. N. Serpone and A. Salinaro, *Pure Appl. Chem.*, 1999, **71**, 303
33. T. Maschmeyer and M. Che, *Angew. Chem. Int. Ed.*, 2010, **49**, 1536
34. H. Kato, K. Asakura and A. Kudo, *J. Am. Chem. Soc.*, 2003, **125**, 3082
35. J. F. Reber and K. Meier, *J. Phys. Chem.*, 1984, **88**, 5903
36. K. Maeda and K. Domen, *Chem. Mater.*, 2010, **22**, 612
37. T. Hisatomi, K. Maeda, K. Takanabe, J. Kubota and K. Domen, *J. Phys. Chem. C*, 2009, **113**, 21458
38. K. Maeda, K. Teramura and K. Domen, *J. Catal.*, 2008, **254**, 198
39. Z. Zou, J. Ye, K. Sayama and H. Arakawa, *Nature*, 2001, **414**, 625
40. K. Sayama, K. Mukasa, R. Abe, Y. Abe and H. Arakawa, *Chem. Commun.*, 2001, 2416
41. H. Yan, J. Yang, G. Ma, G. Wu, X. Zong, Z. Lei, J. Shi and C. Li, *J. Catal.*, 2009, **266**, 165
42. J. Yang, H. Yan, X. Wang, F. Wen, Z. Wang, D. Fan, J. Shi and C. Li, *J. Catal.*, 2012, **290**, 151
43. F. L. Souza, K. P. Lopes, E. Longo and E. R. Leite, *Phys. Chem. Chem. Phys.*, 2009, **11**, 1215
44. H. Ohta, M. Orita, M. Hirano, H. Tanji, H. Kawazoe and H. Hosono, *Appl. Phys. Lett.*, 2000, **76**, 2740
45. S. Y. Reece, J. A. Hamel, K. Sung, T. D. Jarvi, A. J. Esswein, J. J. H. Pijpers and D. G. Nocera, *Science*, 2011, **334**, 645
46. D. G. Nocera, *Acc. Chem. Res.*, 2012, **45**, 767
47. R. E. Rocheleau, E. L. Miller and A. Misra, *Energ. Fuel.*, 1998, **12**, 3
48. O. Khaselev and J. A. Turner, *Science*, 1998, **280**, 425
49. D. Zhao, S. Budhi, A. Rodriguez and R. T. Koodali, *Int. J. Hydrogen Energy*, 2010, **35**, 5276
50. F. Amano, O.-O. Prieto-Mahaney, Y. Terada, T. Yasumoto, T. Shibayama and B. Ohtani, *Chem. Mater.*, 2009, **21**, 2601
51. Y. Li, W.-N. Wang, Z. Zhan, M.-H. Woo, C.-Y. Wu and P. Biswas, *Appl. Cat. B*, 2010, **100**, 386
52. K. Sivaranjani and C. S. Gopinath, *J. Mater. Chem.*, 2011, **21**, 2639
53. H. G. Kim, P. H. Borse, J. S. Jang, C. W. Ahn, E. D. Jeong and J. S. Lee, *Adv. Mater.*, 2011, **23**, 2088
54. A. Vaneski, A. S. Susha, J. Rodríguez-Fernández, M. Berr, F. Jäckel, J. Feldmann and A. L. Rogach, *Adv. Funct. Mater.*, 2011, **21**, 1547
55. S. Y. Ryu, W. Balcerski, T. K. Lee and M. R. Hoffmann, *J. Phys. Chem. C*, 2007, **111**, 18195
56. K. Onozuka, Y. Kawakami, H. Imai, T. Yokoi, T. Tatsumi and J. N. Kondo, *J. Solid State Chem.*, 2012, **192**, 87
57. J. B. Joo, I. Lee, M. Dahl, G. D. Moon, F. Zaera and Y. Yin, *Adv. Funct. Mater.*, 2013, **23**, 4246

58. S. B. Narendranath, A. K. Yadav, D. Bhattacharyya, S. N. Jha and R. N. Devi, *ACS Appl. Mater. Interfaces,* 2014, **6**, 12321
59. K. Maeda, N. Nishimura and K. Domen, *Appl. Cat. A*, 2009, **370**, 88
60. Q. Zhang and L. Gao, *Langmuir*, 2004, **20**, 9821
61. T. Grewe, K. Meier and H. Tüysüz, *Catal. Today*, 2014, **225**, 142
62. T. Meyer, J. B. Priebe, R. O. da Silva, T. Peppel, H. Junge, M. Beller, A. Brückner and S. Wohlrab, *Chem. Mater.,* 2014, **26**, 4705
63. Q. Li, B. Guo, J. Yu, J. Ran, B. Zhang, H. Yan and J. R. Gong, *J. Am. Chem. Soc.*, 2011, **133**, 10878
64. W. Wang, P. Serp, P. Kalck and J. L. Faria, *Appl. Cat. B*, 2005, **56**, 305
65. M. Krissanasaeranee, S. Wongkasemjit, A. K. Cheetham and D. Eder, *Chem. Phys. Lett.*, 2010, **496**, 133
66. I. Tsuji, H. Kato, H. Kobayashi and A. Kudo, *J. Am. Chem. Soc.*, 2004, **126**, 13406
67. D. Jing and L. Guo, *J. Phys. Chem. B*, 2006, **110**, 11139
68. S. Kambe, M. Fujii, T. Kawai, S. Kawai and F. Nakahara, *Chem. Phys. Lett.*, 1984, **109**, 105
69. F. Andrew Frame, E. C. Carroll, D. S. Larsen, M. Sarahan, N. D. Browning and F. E. Osterloh, *Chem. Commun.*, 2008, 2206
70. M. A. Holmes, T. K. Townsend and F. E. Osterloh, *Chem. Commun.*, 2012, **48**, 371
71. J. Zhao, M. A. Holmes and F. E. Osterloh, *ACS Nano*, 2013, **7**, 4316
72. N. Bao, L. Shen, T. Takata and K. Domen, *Chem. Mater.*, 2008, **20**, 110
73. J. F. Reber and M. Rusek, *J. Phys. Chem.*, 1986, **90**, 824
74. H. N. Kim, T. W. Kim, I. Y. Kim and S.-J. Hwang, *Adv. Funct. Mater.*, 2011, **21**, 3111
75. Y. Ebina, T. Sasaki, M. Harada and M. Watanabe, *Chem. Mater.*, 2002, **14**, 4390
76. K. Domen, J. Yoshimura, T. Sekine, A. Tanaka and T. Onishi, *Catal. Lett.*, 1990, **4**, 339
77. S. Ikeda, M. Hara, J. N. Kondo, K. Domen, H. Takahashi, T. Okubo and M. Kakihana, *Chem. Mater.*, 1998, **10**, 72
78. M. D. Kelzenberg, S. W. Boettcher, J. A. Petykiewicz, D. B. Turner-Evans, M. C. Putnam, E. L. Warren, J. M. Spurgeon, R. M. Briggs, N. S. Lewis and H. A. Atwater, *Nat. Mater.*, 2010, **9**, 239
79. J. Y. Lee, S. Lee, J.-K. Park, Y. Jun, Y.-G. Lee, K. M. Kim, J. H. Yun and K. Y. Cho, *Opt. Express*, 2010, **18**, A522
80. K. S. Lee, J. H. Yun, Y.-H. Han, J.-H. Yim, N.-G. Park, K. Y. Cho and J. H. Park, *J. Mater. Chem.*, 2011, **21**, 15193
81. Z. Xuming, C. Yu Lim, L. Ru-Shi and T. Din Ping, *Rep. Prog. Phys.*, 2013, **76**, 046401
82. W. Hou and S. B. Cronin, *Adv. Funct. Mater.*, 2013, **23**, 1612
83. C. Gomes Silva, R. Juárez, T. Marino, R. Molinari and H. García, *J. Am. Chem. Soc.*, 2010, **133**, 595
84. O. Rosseler, M. V. Shankar, M. K.-L. Du, L. Schmidlin, N. Keller and V. Keller, *J. Catal.*, 2010, **269**, 179

85. F. F. Abdi, A. Dabirian, B. Dam and R. van de Krol, *Phys. Chem. Chem. Phys.*, 2014, **16**, 15272
86. T. Torimoto, H. Horibe, T. Kameyama, K. Okazaki, S. Ikeda, M. Matsumura, A. Ishikawa and H. Ishihara, *J. Phys. Chem. Lett.*, 2011, **2**, 2057
87. S. Guldin, S. Hüttner, M. Kolle, M. E. Welland, P. Müller-Buschbaum, R. H. Friend, U. Steiner and N. Tétreault, *Nano Lett.*, 2010, **10**, 2303
88. D.-K. Hwang, B. Lee and D.-H. Kim, *RSC Adv.*, 2013, **3**, 3017
89. P. Bermel, C. Luo, L. Zeng, L. C. Kimerling and J. D. Joannopoulos, *Opt. Express*, 2007, **15**, 16986
90. E. Yablonovitch, *Phys. Rev. Lett.*, 1987, **58**, 2059
91. S. John, *Phys. Rev. Lett.*, 1987, **58**, 2486
92. M. Aloshyna, S. Sivakumar, M. Venkataramanan, A. G. Brolo and F. C. J. M. van Veggel, *J. Phys. Chem. C*, 2007, **111**, 4047
93. C.-T. Dinh, H. Yen, F. Kleitz and T.-O. Do, *Angew. Chem.*, 2014, **126**, 6736
94. A. Imhof, W. L. Vos, R. Sprik and A. Lagendijk, *Phys. Rev. Lett.*, 1999, **83**, 2942
95. J. I. L. Chen, G. von Freymann, S. Y. Choi, V. Kitaev and G. A. Ozin, *Adv. Mater.*, 2006, **18**, 1915
96. J. I. L. Chen, E. Loso, N. Ebrahim and G. A. Ozin, *J. Am. Chem. Soc.*, 2008, **130**, 5420
97. S. Nishimura, N. Abrams, B. A. Lewis, L. I. Halaoui, T. E. Mallouk, K. D. Benkstein, J. van de Lagemaat and A. J. Frank, *J. Am. Chem. Soc.*, 2003, **125**, 6306
98. M. El Harakeh and L. Halaoui, *J. Phys. Chem. C*, 2010, **114**, 2806
99. R. C. Schroden, M. Al-Daous, C. F. Blanford and A. Stein, *Chem. Mater.*, 2002, **14**, 3305
100. M. A. McLachlan, N. P. Johnson, R. M. D. L. Rue and D. W. McComb, *J. Mater. Chem.*, 2004, **14**, 144
101. Y. Xia, B. Gates, Y. Yin and Y. Lu, *Adv. Mater.*, 2000, **12**, 693
102. P. D. García, Á. Blanco, A. Shavel, N. Gaponik, A. Eychmüller, B. Rodríguez-González, L. M. Liz-Marzán and C. López, *Adv. Mater.*, 2006, **18**, 2768
103. A. Blanco, C. López, R. Mayoral, H. Míguez, F. Meseguer, A. Mifsud and J. Herrero, *Appl. Phys. Lett.*, 1998, **73**, 1781
104. S. V. Gaponenko, V. N. Bogomolov, E. P. Petrov, A. M. Kapitonov, D. A. Yarotsky, I. I. Kalosha, A. A. Eychmueller, A. L. Rogach, J. McGilp, U. Woggon and F. Gindele, *J. Lightwave Technol.*, 1999, **17**, 2128
105. S. G. Romanov, A. V. Fokin and R. M. De La Rue, *Appl. Phys. Lett.*, 1999, **74**, 1821
106. J. Zhou, Y. Zhou, S. Buddhudu, S. L. Ng, Y. L. Lam and C. H. Kam, *Appl. Phys. Lett.*, 2000, **76**, 3513
107. P. Lodahl, A. Floris van Driel, I. S. Nikolaev, A. Irman, K. Overgaag, D. Vanmaekelbergh and W. L. Vos, *Nature*, 2004, **430**, 654
108. D. Gaillot, T. Yamashita and C. J. Summers, *Phys. Rev. B*, 2005, **72**, 205109
109. M. D. Leistikow, A. P. Mosk, E. Yeganegi, S. R. Huisman, A. Lagendijk and W. L. Vos, *Phys. Rev. Lett.*, 2011, **107**, 193903
110. D. J. Norris and Y. A. Vlasov, *Adv. Mater.*, 2001, **13**, 371
111. E. Graugnard, V. Chawla, D. Lorang and C. J. Summers, *Appl. Phys. Lett.*, 2006, **89**, 211102

112. A. Frölich, J. Fischer, T. Zebrowski, K. Busch and M. Wegener, *Adv. Mater.*, 2013, **25**, 3588
113. J. Liu, G. Liu, M. Li, W. Shen, Z. Liu, J. Wang, J. Zhao, L. Jiang and Y. Song, *Energy Environ. Sci.*, 2010, **3**, 1503
114. Y. Zhao, B. Yang, J. Xu, Z. Fu, M. Wu and F. Li, *Thin Solid Films*, 2012, **520**, 3515
115. Q. Yang, M. Li, J. Liu, W. Shen, C. Ye, X. Shi, L. Jiang and Y. Song, *J. Mater. Chem. A*, 2013, **1**, 541
116. J. Liu, M. Li, J. Wang, Y. Song, L. Jiang, T. Murakami and A. Fujishima, *Environ. Sci. Technol.*, 2009, **43**, 9425
117. G. Liao, S. Chen, X. Quan, H. Chen and Y. Zhang, *Environ. Sci. Technol.*, 2010, **44**, 3481
118. J. I. L. Chen and G. A. Ozin, *J. Mater. Chem.*, 2009, **19**, 2675
119. H. Chen, S. Chen, X. Quan and Y. Zhang, *Environ. Sci. Technol.*, 2009, **44**, 451
120. S. Meng, D. Li, X. Zheng, J. Wang, J. Chen, J. Fang, Y. Shao and X. Fu, *J. Mater. Chem. A*, 2013, **1**, 2744
121. S. Sun, W. Wang, L. Zhang and J. Xu, *Appl. Cat. B*, 2012, **125**, 144
122. L. Zhang, C. Baumanis, L. Robben, T. Kandiel and D. Bahnemann, *Small*, 2011, **7**, 2714
123. M.-Y. Tsang, N. E. Pridmore, L. J. Gillie, Y.-H. Chou, R. Brydson and R. E. Douthwaite, *Adv. Mater.*, 2012, **24**, 3406
124. J. I. L. Chen and G. A. Ozin, *Adv. Mater.*, 2008, **20**, 4784
125. X. Chen, J. Ye, S. Ouyang, T. Kako, Z. Li and Z. Zou, *ACS Nano*, 2011, **5**, 4310
126. J. Moir, N. Soheilnia, P. O'Brien, A. Jelle, C. M. Grozea, D. Faulkner, M. G. Helander and G. A. Ozin, *ACS Nano*, 2013, **7**, 4261
127. Y. Zhang, J. Wang, Y. Zhao, J. Zhai, L. Jiang, Y. Song and D. Zhu, *J. Mater. Chem.*, 2008, **18**, 2650
128. C. Cheng, S. K. Karuturi, L. Liu, J. Liu, H. Li, L. T. Su, A. I. Y. Tok and H. J. Fan, *Small*, 2012, **8**, 37
129. S. K. Karuturi, J. Luo, C. Cheng, L. Liu, L. T. Su, A. I. Y. Tok and H. J. Fan, *Adv. Mater.*, 2012, **24**, 4157
130. S. K. Karuturi, C. Cheng, L. Liu, L. Tat Su, H. J. Fan and A. I. Y. Tok, *Nano Energy*, 2012, **1**, 322
131. Z. Zhang, X. Yang, M. N. Hedhili, E. Ahmed, L. Shi and P. Wang, *ACS Appl. Mater. Interfaces*, 2013, **6**, 691
132. K. Kim, M.-J. Kim, S.-I. Kim and J.-H. Jang, *Sci. Rep.*, 2013, **3**,
133. X. Shi, K. Zhang, K. Shin, J. H. Moon, T.-W. Lee and J. H. Park, *Phys. Chem. Chem. Phys.*, 2013, **15**, 11717
134. M. Zhou, H. B. Wu, J. Bao, L. Liang, X. W. Lou and Y. Xie, *Angew. Chem. Int. Ed.*, 2013, **52**, 8579
135. Y. Lu, H. Yu, S. Chen, X. Quan and H. Zhao, *Environ. Sci. Technol.*, 2012, **46**, 1724
136. X. Zhang, Y. Liu, S.-T. Lee, S. Yang and Z. Kang, *Energy Environ. Sci.*, 2014, **7**, 1409
137. X. Cui, Y. Wang, G. Jiang, Z. Zhao, C. Xu, Y. Wei, A. Duan, J. Liu and J. Gao, *RSC Adv.*, 2014, **4**, 15689

138. M. Sadakane, R. Kato, T. Murayama and W. Ueda, *J. Solid State Chem.*, 2011, **184**, 2299
139. A. S. Amalraj and G. Senguttuvan, *J. Mater. Sci.: Mater. Electron.*, 2014, **25**, 2035
140. F. Bayansal, T. Taşköprü, B. Şahin and H. Çetinkara, *Metall. Mater. Trans. A*, 2014, **45**, 3670
141. L. Wenjun, W. Zhiqiang, W. Lijuan, L. Zhaosheng, Y. Tao and Z. Zhigang, *J. Phys. D: Appl. Phys.*, 2010, **43**, 405402
142. M. A. Becker, J. G. Radich, B. A. Bunker and P. V. Kamat, *J. Phys. Chem. Lett.*, 2014, **5**, 1575
143. F. Zhang, A. Yamakata, K. Maeda, Y. Moriya, T. Takata, J. Kubota, K. Teshima, S. Oishi and K. Domen, *J. Am. Chem. Soc.*, 2012, **134**, 8348
144. M. Li, W. Luo, D. Cao, X. Zhao, Z. Li, T. Yu and Z. Zou, *Angew. Chem. Int. Ed.*, 2013, **52**, 11016
145. D. R. Baker and P. V. Kamat, *Adv. Funct. Mater.*, 2009, **19**, 805
146. Y. Li, J. Du, S. Peng, D. Xie, G. Lu and S. Li, *Int. J. Hydrogen Energy*, 2008, **33**, 2007
147. B. Kraeutler and A. J. Bard, *J. Am. Chem. Soc.*, 1978, **100**, 4317
148. L. Yuliati, J.-H. Yang, X. Wang, K. Maeda, T. Takata, M. Antonietti and K. Domen, *J. Mater. Chem.*, 2010, **20**, 4295
149. F. Zhang, K. Maeda, T. Takata, T. Hisatomi and K. Domen, *Catal. Today*, 2012, **185**, 253
150. S. C. Chan and M. A. Barteau, *Langmuir*, 2005, **21**, 5588
151. X. Chen, W. Chen, P. Lin, Y. Yang, H. Gao, J. Yuan and W. Shangguan, *Catal. Commun.*, 2013, **36**, 104
152. L. Zhang, Y. Zhong, Z. He, J. Wang, J. Xu, J. Cai, N. Zhang, H. Zhou, H. Fan, H. Shao, J. Zhang and C.-N. Cao, *J. Mater. Chem. A*, 2013, **1**, 4277
153. C. Li, S. Zhang, B. Zhang, D. Su, S. He, Y. Zhao, J. Liu, F. Wang, M. Wei, D. G. Evans and X. Duan, *J. Mater. Chem. A*, 2013, **1**, 2461
154. H. Zhou, L. Ding, T. Fan, J. Ding, D. Zhang and Q. Guo, *Appl. Cat. B*, 2014, **147**, 221
155. Y. Kang, K. Song, J. H. Park, Y. C. Kim and S. G. Oh, *J. Ceram. Process. Res.*, 2013, **14**, 419
156. A. V. Korzhak, N. I. Ermokhina, A. L. Stroyuk, V. K. Bukhtiyarov, A. E. Raevskaya, V. I. Litvin, S. Y. Kuchmiy, V. G. Ilyin and P. A. Manorik, *J. Photochem. Photobiol. A*, 2008, **198**, 126
157. P. Nagpal, D. P. Josephson, N. R. Denny, J. DeWilde, D. J. Norris and A. Stein, *J. Mater. Chem.*, 2011, **21**, 10836
158. E. Borgarello, J. Kiwi, E. Pelizzetti, M. Visca and M. Graetzel, *J. Am. Chem. Soc.*, 1981, **103**, 6324
159. P. A. Brugger, P. Cuendet and M. Graetzel, *J. Am. Chem. Soc.*, 1981, **103**, 2923
160. D. Duonghong, E. Borgarello and M. Graetzel, *J. Am. Chem. Soc.*, 1981, **103**, 4685
161. D. Connolly, B. Twamley and B. Paull, *Chem. Commun.*, 2010, **46**, 2109
162. H. Yang, H. Wang, H. Li, S. Ji, M. W. Davids and R. Wang, *J. Power Sources*, 2014, **260**, 12

163. S. V. Nguyen, V. Szabo, D. Trong On and S. Kaliaguine, *Micropor. Mesopor. Mater.*, 2002, **54**, 51
164. Z. Wang, M. A. Al-Daous, E. R. Kiesel, F. Li and A. Stein, *Micropor. Mesopor. Mater.*, 2009, **120**, 351
165. Z. Wang, N. S. Ergang, M. A. Al-Daous and A. Stein, *Chem. Mater.*, 2005, **17**, 6805
166. P. C. Hiemenz and R. Rajagopalan, *Principles of Colloid and Surface Science*, 3rd ed., Marcel Dekker Inc., New York, 1997
167. N. Zheng and G. D. Stucky, *J. Am. Chem. Soc.*, 2006, **128**, 14278
168. J. Zhao, M. Spasova, Z.-A. Li and M. Zharnikov, *Adv. Funct. Mater.*, 2011, **21**, 4724
169. C. Y. Cummings, F. Marken, L. M. Peter, K. G. Upul Wijayantha and A. A. Tahir, *J. Am. Chem. Soc.*, 2011, **134**, 1228
170. S. Sun and H. Zeng, *J. Am. Chem. Soc.*, 2002, **124**, 8204
171. C. R. Crick, J. C. Bear, P. Southern and I. P. Parkin, *J. Mater. Chem. A*, 2013, **1**, 4336
172. G. Collins, M. Blömker, M. Osiak, J. D. Holmes, M. Bredol and C. O'Dwyer, *Chem. Mater.*, 2013, **25**, 4312
173. F. Pena-Pereira, R. M. B. O. Duarte and A. C. Duarte, *TrAC - Trend. Anal. Chem.*, 2012, **40**, 90
174. M. Santiago, A. Restuccia, F. Gramm and J. Pérez-Ramírez, *Micropor. Mesopor. Mater.*, 2011, **146**, 76
175. Y.-C. Lee, T.-J. Kuo, C.-J. Hsu, Y.-W. Su and C.-C. Chen, *Langmuir*, 2002, **18**, 9942
176. K. E. R. Brown and K.-S. Choi, *Chem. Commun.*, 2006, 3311
177. S. Kim, H. Chong, R. M. D. L. Rue, J. H. Marsh and A. C. Bryce, *Nanotechnology*, 2003, **14**, 1004
178. L. Liu, S. K. Karuturi, L. T. Su and A. I. Y. Tok, *Energy Environ. Sci.*, 2011, **4**, 209
179. Y. G. Seo, K. Woo, J. Kim, H. Lee and W. Lee, *Adv. Funct. Mater.*, 2011, **21**, 3094
180. B. T. Holland, C. F. Blanford, T. Do and A. Stein, *Chem. Mater.*, 1999, **11**, 795
181. Y. Fu, Z. Jin, Z. Liu and W. Li, *J. Eur. Ceram. Soc.*, 2007, **27**, 2223
182. W. Stöber, A. Fink and E. Bohn, *J. Colloid Interface Sci.*, 1968, **26**, 62
183. Q.-B. Meng, Z.-Z. Gu, O. Sato and A. Fujishima, *Appl. Phys. Lett.*, 2000, **77**, 4313
184. Q. B. Meng, C. H. Fu, Y. Einaga, Z. Z. Gu, A. Fujishima and O. Sato, *Chem. Mater.*, 2001, **14**, 83
185. Z.-Z. Gu, A. Fujishima and O. Sato, *Chem. Mater.*, 2002, **14**, 760
186. A. Stein, F. Li and N. R. Denny, *Chem. Mater.*, 2008, **20**, 649
187. F. Li, Z. Wang, N. S. Ergang, C. A. Fyfe and A. Stein, *Langmuir*, 2007, **23**, 3996
188. R. Arshady, *Colloid. Polym. Sci.*, 1992, **270**, 717
189. P. K. Sahoo and R. Mohapatra, *Eur. Polym. J.*, 2003, **39**, 1839
190. L. V. Woodcock, *Nature*, 1997, **385**, 141
191. X. Du and J. He, *J. Appl. Polym. Sci.*, 2008, **108**, 1755
192. A. Stein, B. E. Wilson and S. G. Rudisill, *Chem. Soc. Rev.*, 2013, **42**, 2763
193. X.-J. Xu, K.-S. Siow, M.-K. Wong and L.-M. Gan, *J. Polym. Sci. Part A*, 2001, **39**, 1634

194. C. E. Reese and S. A. Asher, *J. Colloid Interface Sci.*, 2002, **248**, 41
195. Z.-Z. Gu, H. Chen, S. Zhang, L. Sun, Z. Xie and Y. Ge, *Colloid Surface A*, 2007, **302**, 312
196. J. Q. Li and R. Salovey, *J. Polym. Sci. Part A*, 2000, **38**, 3181
197. X. Chen, Z. Li, J. Ye and Z. Zou, *Chem. Mater.*, 2010, **22**, 3583
198. G. T. D. Shouldice, G. A. Vandezande and A. Rudin, *Eur. Polym. J.*, 1994, **30**, 179
199. C. F. Blanford, H. Yan, R. C. Schroden, M. Al-Daous and A. Stein, *Adv. Mater.*, 2001, **13**, 401
200. G. Subramania, K. Constant, R. Biswas, M. M. Sigalas and K. M. Ho, *Adv. Mater.*, 2001, **13**, 443
201. K. S. W. Sing, D. H. Everett, R. A. W. Haul, L. Moscou, R. A. Pierotti, J. Rouquerol and T. Siemieniewska, *Pure Appl. Chem.*, 1985, **57**, 603
202. H. Yan, C. F. Blanford, B. T. Holland, W. H. Smyrl and A. Stein, *Chem. Mater.*, 2000, **12**, 1134
203. E. Arsenault, N. Soheilnia and G. A. Ozin, *ACS Nano*, 2011, **5**, 2984
204. Z. Z. Yang, S. M. Gao, W. Li, V. Vlasko-Vlasov, U. Welp, W. K. Kwok and T. Xu, *ACS Appl. Mater. Interfaces*, 2011, **3**, 1101
205. A. S. Dimitrov and K. Nagayama, *Langmuir*, 1996, **12**, 1303
206. M. Kanehara, H. Koike, T. Yoshinaga and T. Teranishi, *J. Am. Chem. Soc.*, 2009, **131**, 17736
207. F. Jiao and H. Frei, *Angew. Chem. Int. Ed.*, 2009, **48**, 1841
208. M. Kitahara and K. Kuroda, *RSC Adv.*, 2014, **4**, 27201
209. L. Huang and M. Kruk, *J. Colloid Interface Sci.*, 2012, **365**, 137
210. S. Lowell and J. E. Shields, *Powder Surface Area and Porosity*, 2nd ed., Chapman and Hall Ltd., London, 1984
211. J. W. McBain, *J. Am. Chem. Soc.*, 1935, **57**, 699
212. A. Grosman and C. Ortega, *Langmuir*, 2008, **24**, 3977
213. L. Huang, X. Yan and M. Kruk, *Langmuir*, 2010, **26**, 14871
214. W. W. Yu and X. Peng, *Angew. Chem. Int. Ed.*, 2002, **41**, 2368
215. N. Li, X. Zhang, S. Chen, X. Hou, Y. Liu and X. Zhai, *Mater. Sci. Eng. B*, 2011, **176**, 688
216. R. E. Bailey and S. Nie, *J. Am. Chem. Soc.*, 2003, **125**, 7100
217. R. C. Merrifield, Z. W. Wang, R. E. Palmer and J. R. Lead, *Environ. Sci. Technol.*, 2013, **47**, 12426
218. J. A. Young, *J. Chem. Educ.*, 2002, **79**, 24
219. P. D. Cozzoli, A. Kornowski and H. Weller, *J. Am. Chem. Soc.*, 2003, **125**, 14539
220. R. M. de Silva, V. Palshin, K. M. N. de Silva, L. L. Henry and C. S. S. R. Kumar, *J. Mater. Chem.*, 2008, **18**, 738
221. N. Li, X. Zhang, S. Chen and X. Hou, *J. Phys. Chem. Solids*, 2011, **72**, 1195
222. J. Park, K. An, Y. Hwang, J.-G. Park, H.-J. Noh, J.-Y. Kim, J.-H. Park, N.-M. Hwang and T. Hyeon, *Nat. Mater.*, 2004, **3**, 891
223. M. Yin, C.-K. Wu, Y. Lou, C. Burda, J. T. Koberstein, Y. Zhu and S. O'Brien, *J. Am. Chem. Soc.*, 2005, **127**, 9506
224. Z. Chen, A. Xu, Y. Zhang and N. Gu, *Curr. Appl. Phys.*, 2010, **10**, 967
225. Y. Zhang, J. Zhu, X. Song and X. Zhong, *J. Phys. Chem. C*, 2008, **112**, 5322

226. A. Demortiere, P. Panissod, B. P. Pichon, G. Pourroy, D. Guillon, B. Donnio and S. Begin-Colin, *Nanoscale*, 2011, **3**, 225
227. M. Pauly, B. P. Pichon, A. Demortière, J. Delahaye, C. Leuvrey, G. Pourroy and S. Bégin-Colin, *Superlattice Microst.*, 2009, **46**, 195
228. P. J. Thistlethwaite, M. L. Gee and D. Wilson, *Langmuir*, 1996, **12**, 6487
229. P. J. Thistlethwaite and M. S. Hook, *Langmuir*, 2000, **16**, 4993
230. M. Nara, H. Torii and M. Tasumi, *J. Phys. Chem.*, 1996, **100**, 19812
231. G. Blyholder, C. Adhikar and A. Proctor, *Colloid Surface A*, 1995, **105**, 151
232. S. Duckett and B. Gilbert, *Foundations of Spectroscopy*, Oxford University Press, New York, 2000
233. A. D. Yoffe, *Adv. Phys.*, 1993, **42**, 173
234. W. W. Yu, L. Qu, W. Guo and X. Peng, *Chem. Mater.*, 2003, **15**, 2854
235. J. Ouyang, M. Vincent, D. Kingston, P. Descours, T. Boivineau, M. B. Zaman, X. Wu and K. Yu, *J. Phys. Chem. C*, 2009, **113**, 5193
236. A. Quintanilla, J. J. W. Bakker, M. T. Kreutzer, J. A. Moulijn and F. Kapteijn, *J. Catal.*, 2008, **257**, 55
237. Y. A. Vlasov, N. Yao and D. J. Norris, *Adv. Mater.*, 1999, **11**, 165
238. I. Langmuir, *Proc. Natl. Acad. Sci. USA*, 1917, **3**, 251
239. P. B. Johnson and R. W. Christy, *Phys. Rev. B*, 1972, **6**, 4370
240. M. Abkarian, J. Nunes and H. A. Stone, *J. Am. Chem. Soc.*, 2004, **126**, 5978
241. J. Li, X. Liu, X. Lv and B. Zhang, *Mater. Lett.*, 2014, **124**, 299
242. J. W. Lee, M. R. Othman, Y. Eom, T. G. Lee, W. S. Kim and J. Kim, *Micropor. Mesopor. Mater.*, 2008, **116**, 561
243. E. D. Smolensky, M. C. Neary, Y. Zhou, T. S. Berquo and V. C. Pierre, *Chem. Commun.*, 2011, **47**, 2149
244. L. Xiao, J. Li, D. F. Brougham, E. K. Fox, N. Feliu, A. Bushmelev, A. Schmidt, N. Mertens, F. Kiessling, M. Valldor, B. Fadeel and S. Mathur, *ACS Nano*, 2011, **5**, 6315
245. P. Yuan, M. Fan, D. Yang, H. He, D. Liu, A. Yuan, J. Zhu and T. Chen, *J. Hazard. Mater.*, 2009, **166**, 821
246. R. I. Dimitrov and B. S. Boyanov, *J. Therm. Anal. Calorim.*, 2000, **61**, 181
247. G.-S. Li, D.-Q. Zhang and J. C. Yu, *Environ. Sci. Technol.*, 2009, **43**, 7079
248. D. S. Gopala, R. R. Bhattacharjee and R. Richards, *Appl. Organomet. Chem.*, 2013, **27**, 1
249. L. Vradman, M. V. Landau, M. Herskowitz, V. Ezersky, M. Talianker, S. Nikitenko, Y. Koltypin and A. Gedanken, *J. Catal.*, 2003, **213**, 163
250. C. Pacholski, *Sensors*, 2013, **13**, 4694
251. P. Šimáková, J. Gautier, M. Procházka, K. Hervé-Aubert and I. Chourpa, *J. Phys. Chem. C*, 2014, **118**, 7690
252. X. Chen, S. Shen, L. Guo and S. S. Mao, *Chem. Rev.*, 2010, **110**, 6503
253. Y. Bessekhouad, M. Mohammedi and M. Trari, *Sol. Energy Mater. Sol. Cells*, 2002, **73**, 339
254. N. Buehler, K. Meier and J. F. Reber, *J. Phys. Chem.*, 1984, **88**, 3261
255. L. A. Silva, S. Y. Ryu, J. Choi, W. Choi and M. R. Hoffmann, *J. Phys. Chem. C*, 2008, **112**, 12069
256. R. Kostecki, B. Schnyder, D. Alliata, X. Song, K. Kinoshita and R. Kötz, *Thin Solid Films*, 2001, **396**, 36
257. R. Mitchell, R. Brydson and R. E. Douthwaite, *Nanoscale*, 2014, **6**, 4043

258. T. Cherdhirankorn, M. Retsch, U. Jonas, H.-J. Butt and K. Koynov, *Langmuir*, 2010, **26**, 10141
259. K. Sayama and H. Arakawa, *J. Phys. Chem.*, 1993, **97**, 531
260. E. E. Barton, D. M. Rampulla and A. B. Bocarsly, *J. Am. Chem. Soc.*, 2008, **130**, 6342
261. O. Metin, S. Duman, M. Dinç and S. Özkar, *J. Phys. Chem. C*, 2011, **115**, 10736
262. S. Brunauer, P. H. Emmett and E. Teller, *J. Am. Chem. Soc.*, 1938, **60**, 309
263. BET Surface Area Analysis, http://particle.dk/methods-analytical-laboratory/surface-area-bet/surface-area-bet-theory/, (Accessed September 2014)
264. N. Hondow, Y.-H. Chou, K. Sader, R. Brydson and R. E. Douthwaite, *J. Phys. Chem. C*, 2010, **114**, 22758
265. USHIO Lighting-Edge Technologies Xenon Short Arc Lamp Data Sheet, http://www.ushio.com/files/specs/Xenonshortarc.pdf, (Accessed September 2014)
266. E. R. Garland, E. P. Rosen, L. I. Clarke and T. Baer, *Phys. Chem. Chem. Phys.*, 2008, **10**, 3156
267. R. H. French, S. J. Glass, F. S. Ohuchi, Y. N. Xu and W. Y. Ching, *Phys. Rev. B*, 1994, **49**, 5133
268. G. Buxbaum, *Industrial Organic Pigments*, 2nd ed., Wiley, New York, 1998
269. E. F. Schubert, 2004 - Refractive Index Data, http://homepages.rpi.edu/~schubert/Educational-resources/Materials-Refractive-index-and-extinction-coefficient.pdf, (Accessed September 2014)